DATA ASSIMILATION AND DYNAMICAL DOWNSCALING OF REMOTELY-SENSED PRECIPITATION AND SOIL MOISTURE FROM SPACE

A Thesis
Presented to
The Academic Faculty

by

Liao-Fan Lin

In Partial Fulfillment
of the Requirements for the Degree
Doctor of Philosophy in the
School of Civil and Environmental Engineering

Georgia Institute of Technology
May 2016

DATA ASSIMILATION AND DYNAMICAL DOWNSCALING OF REMOTELY-SENSED PRECIPITATION AND SOIL MOISTURE FROM SPACE

Approved by:

Dr. Rafael L. Bras, Advisor
School of Civil and Environmental
Engineering
Georgia Institute of Technology

Dr. Aris P. Georgakakos
School of Civil and Environmental
Engineering
Georgia Institute of Technology

Dr. Jingfeng Wang
School of Civil and Environmental
Engineering
Georgia Institute of Technology

Dr. Emanuele Di Lorenzo
School of Earth and Atmospheric
Sciences
Georgia Institute of Technology

Dr. Alejandro N. Flores
Department of Geosciences
Boise State University

Date Approved: March 4, 2016

To my parents and my wife

ACKNOWLEDGEMENTS

Finally, and mostly importantly, I want to thank my family, my wife, Tzu-Jung Huang, and my parents, Yun-Chiao Huang and Liao-Wen Lin. Their love, support, and patience encouraged and helped to overcome the difficult times. Last but not least, I would like to thank my son George, whose arrival brings so much joy to my daily life.

TABLE OF CONTENTS

LIST OF TABLES

LIST OF FIGURES

xiv

SUMMARY

Environmental monitoring of Earth from space has provided invaluable information for understanding the land-atmosphere water and energy exchanges. However, the use of satellite observations in hydrologic applications is often limited by coarse space-time resolutions. This study aims to develop a data assimilation system that integrates remotely-sensed precipitation and soil moisture observations into physically-based models to produce fine-scale precipitation, soil moisture, and other relevant hydrometeorological variables. This is particularly useful with the active Global Precipitation Measurement and Soil Moisture Active Passive missions. The system consists of two major components: (1) a framework for dynamic downscaling of satellite precipitation products using the Weather Research and Forecasting (WRF) model with four-dimensional variational data assimilation (4D-Var) and (2) a variational data assimilation system using spatio-temporally varying background error covariance for directly assimilating satellite soil moisture data into the Noah land surface model coupled with the WRF model. The WRF 4D-Var system can effectively assimilate and downscale six-hour precipitation products of a spatial resolution of about 20 km (i.e., those derived from the National Centers for Environmental Prediction Stage IV data and the Tropical Rainfall Measuring Mission (TRMM) 3B42 dataset) to hourly precipitation with a spatial resolution of less than 10 km. The system is able to assimilate and downscale daily soil moisture products at a gridded 36-km resolution obtained from the Soil Moisture and Ocean Salinity (SMOS) mission to produce hourly 4-by-4 km surface soil moisture forecasts with a reduction of mean absolute error by 35% on average. The results from the system with coupled components show that assimilation of the TRMM 3B42 precipitation improves the quality of both downscaled precipitation and soil moisture analyses, while the effect of SMOS soil moisture data assimilation is largely on the soil moisture analyses. The downscaled WRF precipitation, with and without assimilation of TRMM precipitation, was preliminarily tested with a spatially distributed simulation of streamflow using the TIN

(Triangular Irregular Network)-based Real-time Integrated Basin Simulator (tRIBS).

CHAPTER I

INTRODUCTION

1.1 Introduction and Motivation

Among the wide variety of earth observations available from satellites, precipitation and soil moisture are perhaps the most important for hydrological applications and the most complementary. Soil moisture is a direct expression of precipitation. The Global Precipitation Measurement (GPM) is an on-going mission providing remotely-sensed precipitation measurements at a nearly global coverage, while global soil moisture measurements are available from two operational missions, the Soil Moisture and Ocean Salinity (SMOS) and the Soil Moisture Active Passive (SMAP). The satellites are used to (1) provide accurate estimates of hydrometeorological variables, particularly precipitation and soil moisture; and (2) integrate remotely-sensed measurements into atmospheric or hydrologic models for improving predictions. The former one, known as retrievals, is critical for climate studies, drought monitoring, and modeling development. The latter one, often referred to as data assimilation, is crucial for applications such as flood and landslide predictions.

The Tropical Rainfall Measuring Mission (TRMM) Multi-satellite Precipitation Analysis (TMPA) provides quasi-global precipitation retrieval data in space-time resolutions of $0.25°\times0.25°$ every three hours (*Huffman et al.*, 2007). As a successor of TRMM, the GPM currently provides precipitation data at a spatially gridded resolution of $0.1°\times0.1°$ and a temporal resolution of 30 minutes (*Hou et al.*, 2014). SMAP, without its nonoperational radar, and SMOS provide global soil moisture observations at a resolution of approximately 40 km every two to three days (*Kerr et al.*, 2010; *Entekhabi et al.*, 2010; *Brown et al.*, 2013). In addition to precipitation and soil moisture, hydrologic applications and high-resolution distributed hydrologic models often require other forcing inputs such as near-surface temperature, humidity, and wind speeds. To account for such needs, NASA has developed land data assimilation systems that use reanalysis datasets as forcing to simulate land surface

states at finer space-time resolutions than their forcing. On a global scale, the Global Land Data Assimilation System (GLDAS) provides data at a gridded spatial resolution of $0.25°$ every 3 hours (*Rodell et al.*, 2004), while over the United States, data from the North American Land Data Assimilation System (NLDAS) are available at finer resolutions (i.e., $0.125° \times 0.125°$ and hourly (*Xia et al.*, 2012)).

Data assimilation, the integration of observations into a dynamic model, has been widely used in numerical weather predictions for estimating more accurate state estimates (also known as analyses) of atmospheric models. Operationally, global weather forecast systems such as the National Centers for Environmental Prediction (NCEP) Global Forecast System (GFS) and the European Centre for Medium-Range Weather Forecasts (ECMWF) system commonly assimilate a variety of data such as in-situ, radiosonde, and satellite measurements. Well-known products produced by these systems include the NCEP final analysis (FNL) and ECMWF-Interim reanalysis (*Dee et al.*, 2011). Regional climate models equipped with data assimilation techniques are also commonly used for improving precipitation forecasts and analyses at a fine scale. For example, the Weather Research and Forecasting (WRF) Ensemble Data Assimilation System (WRF-EDAS) was developed for assimilating radiances from partner satellites of the GPM constellation for providing downscaled precipitation fields (*Zupanski et al.*, 2011; *Chambon et al.*, 2013; *Zhang et al.*, 2013). For soil moisture, the SMAP level 4 soil moisture product available at a resolution of 9 km is produced by assimilating its radiances and freeze/thaw conditions into the NASA Catchment land surface model (*Entekhabi et al.*, 2010).

This thesis aims to develop a framework that is capable of assimilating both precipitation and soil moisture data and to produce forecasts and analyses at fine time (e.g., hourly or less) and space scales (e.g., less than 10 km). We develop a framework to assimilate remotely-sensed precipitation data based on the WRF four-dimensional variational data assimilation (4D-Var) system and a 1D-Var system to assimilate remotely-sensed soil moisture data into the WRF-Noah model. The background error of both atmospheric states (e.g., stream function, velocity potential, temperature, surface pressure, and relative humidity) and the soil moisture states are estimated using the National Meteorological Center (NMC)

method. Furthermore, we study the relative impacts of precipitation and soil moisture data assimilation on hydrologic and atmospheric predictions. Specifically, this research addresses the following scientific questions:

1. How does the assimilation of only precipitation observations into the WRF-Noah model improve the predictability of precipitation and soil moisture?

2. How does the assimilation of precipitation and soil moisture observations into the WRF-Noah model improve the estimation of both fields?

In addition, we have begun to quantify the usefulness of downscaled precipitation produced by the WRF 4D-Var system on streamflow simulations.

1.2 Outline of the Thesis

The thesis is structured as follows. Chapter 2 introduces a framework that uses the WRF model with the 4D-Var algorithm to downscale precipitation. Preliminary results show that the WRF 4D-Var system can effectively downscale a six-hour precipitation product with a gridded spatial resolution of 20 km to hourly precipitation with a gridded spatial resolution of 9 km. Chapter 3 extends the development by assimilating six-hour TRMM 3B42 precipitation data into the WRF model. Chapter 4 is devoted to the characterization of soil moisture background error covariance over the contiguous United States and the development of a soil moisture variational data assimilation system with a coupled land-atmosphere model. Chapter 5 explains the framework of a joint precipitation and soil moisture data assimilation system and demonstrates the relative impacts of assimilating TRMM precipitation and SMOS soil moisture on the estimates of both fields. Chapter 6 summarizes the main findings and recommendations for future work. Appendix A includes the preliminary work of the comparison of the downscaled WRF precipitation analyses with and without data assimilation with several other precipitation products and quantify their impacts on streamflow simulations using a distributed hydrologic model over the Turkey River basin, Iowa.

CHAPTER II

PRECIPITATION DATA ASSIMILATION AND DOWNSCALING I: A PROOF OF CONCEPT

This chapter describes a data assimilation and modeling framework for downscaling remotely-sensed precipitation from the Global Precipitation Measurement (GPM) mission. The framework is based on the Weather Research and Forecasting (WRF) model and its four-dimensional variational data assimilation options. Preliminary results of assimilating six-hour NCEP Stage IV precipitation of a spatial resolution of ∼20 km are discussed. Section 2.1 illustrates the relevant research and the motivation of the study. Section 2.2 provides a brief description of the models used in this study. Section 2.3 presents the numerical experiment setup. Section 2.4 shows the results of three experiments, and Section 2.5 summarizes the entire chapter. The majority of the work presented in this chapter has been published in *Lin et al.* (2015).

2.1 Introduction

Precipitation is an important component of global and regional hydrologic cycles. Since December 1997, the Tropical Rainfall Measuring Mission (TRMM) has been providing a wealth of spaceborne precipitation data. Among these, the TRMM multi-satellite precipitation analysis (TMPA) has provided 3B42 rainfall products at resolutions as fine as $0.25°$ $\times$ $0.25°$ in space and three hours in time over the tropics, which covers $50°$ N-S (*Huffman et al.*, 2007). The success of the TRMM has led to the Global Precipitation Measurement (GPM) mission, which consists of a core observatory and a complementary set of existing and new satellites that will be cross-calibrated and operated as a constellation. As a successor of TRMM, GPM will provide spaceborne observations of precipitation with unprecedented resolutions that may reach up to 0.1×0.1 degree every 30 minutes in the future for a merged product that combines GPM core observations with measurements provided by other partner radiometers and infrared instruments (*Hou et al.*, 2014).

From a hydrologic point of view, evolution of hourly high intense rain cells typically occurs at a spatial scale smaller than 10 km, which may not be fully resolved in satellite-based products. To enhance the resolution of satellite-based precipitation for hydrologic applications, such as flash flood forecasting and landslide prediction, numerous downscaling approaches have been studied. The two most common families of methodologies are dynamical and statistical downscaling approaches. Statistical methods consist of a large group of methodologies that use empirical multi-scale statistical relationships, parameterized by observations or other environmental predictors, to reproduce realizations of multi-scale precipitation fields (*Fowler et al.*, 2007). This family of downscaling approaches is not typically capable of resolving the complex underlying dynamics of precipitation processes and thus is unable to produce realistic and sufficiently accurate precipitation at high spatiotemporal resolutions (*Gutmann et al.*, 2012). On the other hand, dynamical downscaling approaches are computationally more demanding than their statistical counterparts (*Hellstrom et al.*, 2001) but able to resolve the inherent precipitation dynamics (*Schmidli et al.*, 2007). In addition, the family of dynamical downscaling methods is also able to provide hydrometeorological variables (e.g., downward radiation, surface temperature, and surface wind speed) that are physically consistent with the downscaled precipitation and required by many hydrological models. To this end, this work attempts to use a physically-based mesoscale weather forecasting model together with a variational data assimilation (DA) scheme for producing high-resolution hourly precipitation products with a spatial scale of less than 10 km in grid spacing.

Data assimilation—a mathematical approach integrating observations into a dynamic model—is used to dynamically downscale satellite precipitation products with an atmospheric prediction system for hydrologic applications (*Zupanski et al.*, 2011; *Zhang et al.*, 2013). Together with data assimilation, dynamical downscaling approaches that use a physically-based model can integrate satellite observations with underlying physics to spatially and temporally downscale coarse-scale precipitation data and other meteorological variables. To provide improved precipitation analysis, some studies have focused on the assimilation of precipitation into atmospheric models using variational data assimilation

techniques. For example, the four-dimensional variational data assimilation (4D-Var) of precipitation has been implemented in operational regional climate models, including those of the Japan Meteorological Agency (JMA) and the United Kingdom's Met Office (*Bauer et al.*, 2011a). The 4D-Var technique has been shown to improve short-term (i.e., one to three days) precipitation forecasts (*Tsuyuki*, 1996a,b, 1997; *Zupanski and Mesinger*, 1995). *Koizumi et al.* (2005) used the JMA 4D-Var system to assimilate one-hour radar-based precipitation data at a spatial resolution of 20 km and found improved precipitation forecasts up to 18 hours ahead. *Mesinger et al.* (2006) assimilated hourly precipitation observations into the North American Regional Reanalysis system, which provides 32-km spatial resolution products every three hours, and demonstrated improvements in the precipitation analysis compared to the reference monthly observations. Furthermore, *Lopez* (2011) and *Lopez and Bauer* (2007) assimilated the National Centers for Environmental Prediction (NCEP) Stage IV gauge-corrected radar precipitation into the global integrated forecasting system of the European Centre for Medium-Range Weather Forecasts (ECMWF) and found substantial improvement in the short-term (i.e., up to 12 hours) precipitation forecasts.

As an alternative to direct assimilation of precipitation, the assimilation of satellite radiances into atmospheric models is also frequently used to improve precipitation forecasts. The assimilation of radiances, however, requires a radiative transfer model, which simulates radiances at the top of the atmosphere based on simulated atmospheric (and sometimes land) states. Compared to precipitation assimilation, radiance assimilation is more straightforward, partly because of the non-zero and space-time continuous nature of radiances that better conform to the Gaussian assumption in data assimilation. However, radiance assimilation can be challenging because of the difficulty of resolving cloud water in an atmospheric data assimilation system. *Bauer et al.* (2006a,b) implemented a 1D+4D-Var algorithm into the ECMWF system to assimilate radiances under rainy conditions, while *Bauer et al.* (2010) and *Geer et al.* (2010) used a 4D-Var algorithm to assimilate all-sky radiances. *Zupanski et al.* (2011), *Zhang et al.* (2013), and *Chambon et al.* (2013) used an ensemble data assimilation system to assimilate precipitation-affected radiances such as those from the Advanced Microwave Scanning Radiometer-EOS (AMSR-E), the

6

TRMM Microwave Imager (TMI), and the Microwave Humidity Sounder (MHS) for improving precipitation forecasts and providing downscaled precipitation estimates relevant to the GPM products. *Zhang et al.* (2013) found that the precipitation forecasts can be improved by radiance assimilation, and this improvement becomes more pronounced when precipitation intensity decreases and the spatial scale of analysis coarsens. *Chambon et al.* (2013) showed that the radiance assimilation reduces the root-mean-square error (RMSE) of two-day accumulated precipitation at a 9-km resolution by 8.1% and improves the correlation of spatial rainfall patterns from 0.57 to 0.63, when compared to the results without assimilating radiances.

The Weather Research and Forecasting (WRF) model data assimilation system (WRFDA) is an open-source system that has been widely used to improve precipitation forecasting. Because of the growing interest in the WRFDA system and associated community-based developments, the WRFDA system has been equipped with extensive capability to assimilate various types of observations. The WRFDA system has DA options such as three-dimensional variational data assimilation (3D-Var), 4D-Var, and hybrid variational-ensemble DA that permit assimilating a wide range of observations including in-situ measurements, Doppler radar reflectivity, precipitation, and radiances (*Barker et al.*, 2012; *Wang et al.*, 2013). For example, the 3D-Var assimilation of conventional ground-based data and radiance observations has been used for improving precipitation forecasts at various spatial resolutions (*Ha et al.*, 2011; *Ha and Lee*, 2012; *Hsiao et al.*, 2012; *Liu et al.*, 2012b; *Routray et al.*, 2010; *Schwartz et al.*, 2012; *Xu and Powell*, 2012).

This chapter uses version 3.4 of the WRF model (see *Skamarock et al.* (2008)) and the WRFDA system (*Barker et al.*, 2004, 2012; *Huang et al.*, 2009). Note that, the WRFDA system is currently not fully capable of assimilating precipitation-affected radiances (*Barker et al.*, 2012) and thus we only focus on the assimilation of precipitation for our dynamical downscaling experiments using the 4D-Var module. Specifically, we first focus on assimilating a point-scale observation at a single site to shed light on the sensitivity of dynamical downscaling to precipitation assimilation. Afterwards, in real case experiments, we study the impact of outlier removal and seasonality on dynamical precipitation downscaling. It is

important to note that unlike classic data assimilation studies, which focus on improving the forecast skill of a model, we use the WRF model and the WRFDA system to improve the spatiotemporal resolution of remotely-sensed rainfall observations. In this work, we use an upscaled (20-km grid boxes) version of six-hour NCEP Stage IV precipitation (see *Lin and Mitchell* (2005) for the original version of Stage IV data) as a general surrogate for a coarse-scale remotely-sensed precipitation product and compare the downscaled results with the reference Stage IV data at a gridded spatial resolution of 9 km. Although the spatial scale of the surrogate input precipitation is chosen to be close to the current TRMM 3B42 product, we assimilated six-hour precipitation to be consistent with the default assimilation window of the WRF 4D-Var system. It is worthwhile noting that *Lopez* (2011) reported that assimilating six-hour Stage IV precipitation in their ECMWF system exhibited better behavior than assimilating one- or three-hour precipitation. In addition, we need to note that the chosen surrogate precipitation may not be fully consistent with the envisaged future space-time resolution of the GPM products. However, as we use a physically-based model for downscaling, the promising results of this attempt can be considered as a proof of concept for possible downscaling of GPM precipitation to the hydrologic scales of interest.

2.2   Model Description

2.2.1   WRF Model

The WRF model is a next-generation mesoscale forecast system designed for both research and operational applications. The model, developed collaboratively by several agencies, is currently maintained and made available by the U.S. National Center for Atmospheric Research (NCAR). The WRF model contains two dynamics solvers: the Advanced Research WRF (ARW) solver and the Non-hydrostatic Mesoscale Model (NMM) solver. This study uses the ARW solver to numerically solve atmospheric prognostic equations for three-dimensional wind velocities, potential temperatures, geopotentials, air pressure, and moisture. The ARW solver uses a third order Runge-Kutta scheme for the time integration and second- to sixth-order advection schemes for spatial discretization. The WRF model offers optional parameterization in five major areas: microphysics, cumulus clouds, land

surface, planetary boundary layer physics, and atmospheric radiation physics. Detailed documentation can be found in *Skamarock et al.* (2008).

2.2.2 WRFDA 4D-Var System

The WRFDA 4D-Var system of version 3.4 is used in this study. 4D-Var is superior to 3D-Var for (1) using observations at or nearly at the time of the measurements, (2) constraining the analysis by the model dynamics, and (3) implicitly describing the flow-dependent forecast error covariance. The WRFDA 4D-Var system makes use of the incremental 4D-Var formulation to solve for the analysis increments by minimizing a prescribed cost function. The incremental 4D-Var includes tangent linear and adjoint models derived from a simplified version of the full nonlinear WRF model. The standard control variables (CVs) of the WRFDA 4D-Var system are the stream function, unbalanced velocity potential, unbalanced temperature, pseudo relative humidity, and unbalanced surface pressure (*Barker et al.*, 2004). Prior to the minimization process, the background error covariance of the control variables has to be estimated. More detailed can be found in *Huang et al.* (2009). Below we use WRF 4D-Var to represent the modeling framework that includes both the WRF model and the WRFDA 4D-Var system.

2.3 Model Configurations and Experiment Design

This study configured the WRF model with a nested domain as shown in Figure 2.1, covering an outer 160×100 domain with a 36-km resolution and an inner 121×101 domain with a 9-km resolution. One-way nesting was used in order to support assimilation of coarse-scale precipitation and facilitate dynamical downscaling. The top pressure level of the experimental domain is set at 50 hPa with 40 vertical levels extending to the ground surface. The WRF model physics options used in this study include schemes of the WRF single-moment three-class microphysics (*Hong et al.*, 2004), the rapid radiative transfer model for longwave radiation (*Mlawer et al.*, 1997), the Dudhia shortwave radiation (*Dudhia*, 1989), the MM5 similarity surface layer, the Noah land surface model (*Chen and Dudhia*, 2001), the Yonsei University (YSU) planetary boundary layer (*Hong et al.*, 2006), and the Kain-Fritsch cumulus parameterization (*Kain and Fritsch*, 1990).
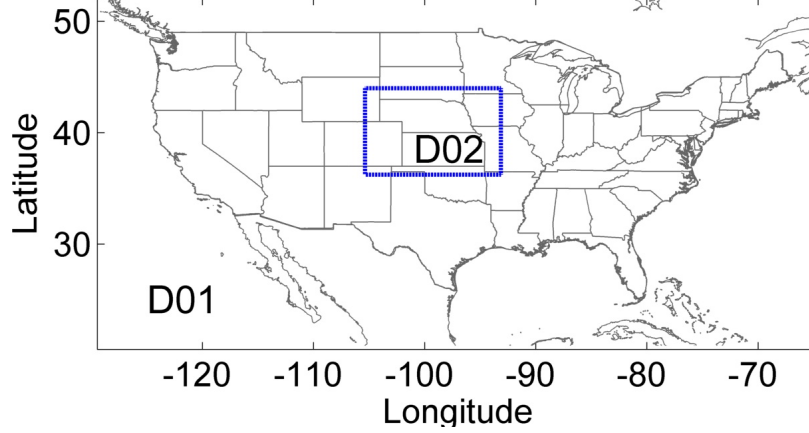
Figure 2.1: Model domain configuration with an outer domain of 160 × 100 grid cells with a 36-km resolution and an inner domain of 121 × 101 grid cells with a 9-km grid resolution.

Figure 2.2 shows our experiment flowchart. We conducted three sets of experiments over three different periods: (1) a synthetic experiment that investigates the assimilation of a point-scale precipitation observation over 1800 UTC 10 June to 0000 UTC 11 June 2009, (2) winter experiments on 11 February 2009, and (3) summer experiments from 1800 UTC 10 June to 1800 UTC 15 June 2009. In these experiments, we use a six-hour analysis cycle and thus each set of experiments contains one, four, and twenty analysis cycles, respectively. The purpose of the point-scale experiment is to understand the sensitivity of precipitation assimilation in the WRFDA system. In both the winter and summer experiments, we investigate the improvement of precipitation analyses resulting from the quality control on outlier observations. In contrast to the winter experiments, the summer experiments are important for evaluating the ability of our dynamical downscaling approach to reproduce precipitation at fine space-time resolutions during convective events.
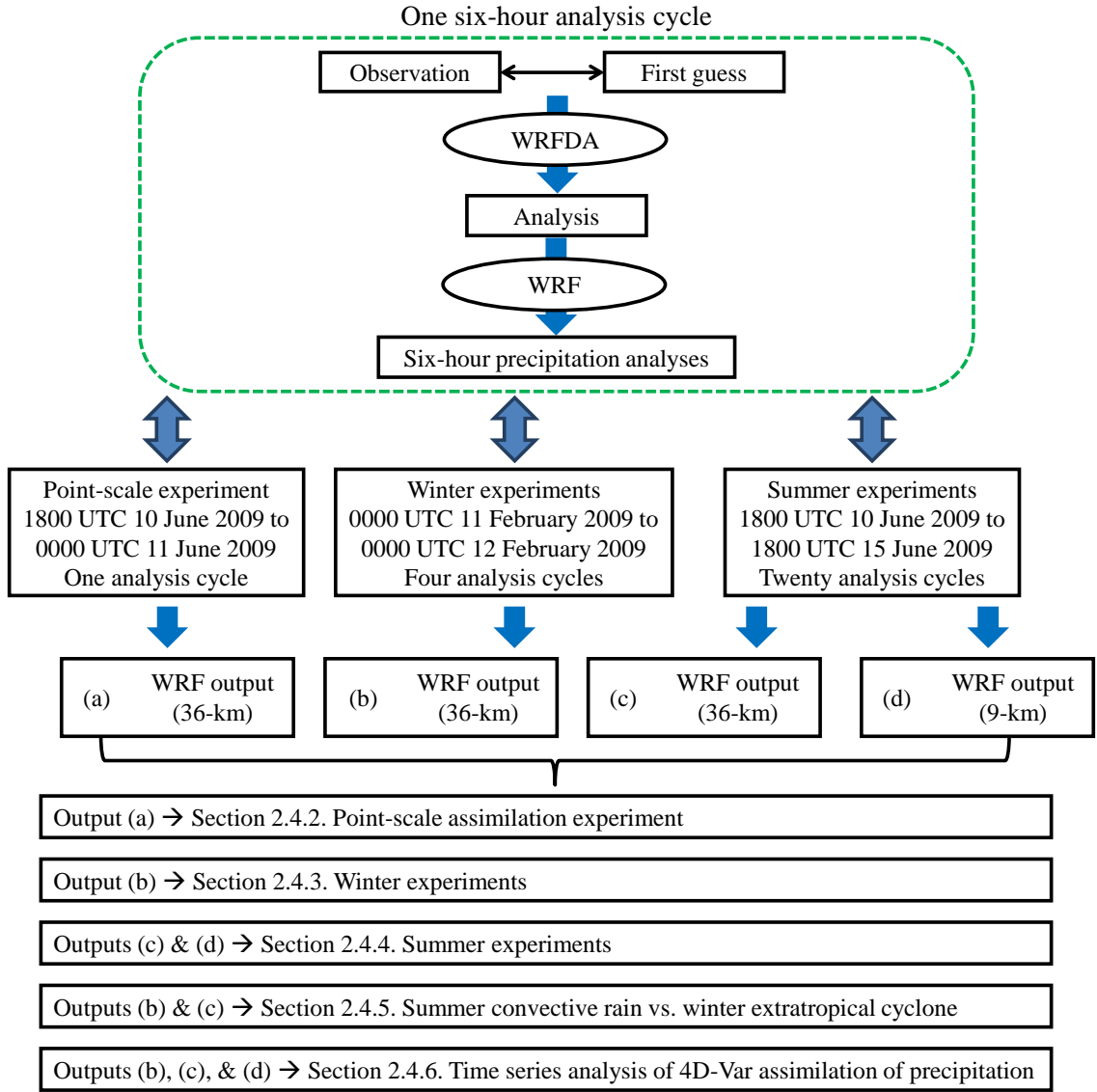
Figure 2.2: Flowchart of this study.

For all WRFDA experiments, we specify several general settings, including the specifications of the assimilation domain, first guesses, cycling mode, and background error covariance estimation. First, the DA process is employed only on the outer domain as all experiments use one-way nesting. Second, all experiments use the NCEP FNL operational global analysis dataset with six-hour 1×1 degree resolutions to generate first guesses or "background states." Third, this study designs a non-cycling process, in which the first guesses are generated based on NCEP FNL data, while the first guesses in the cycling mode are typically obtained from short-range (typically 1-6 hours) forecasts (*Skamarock et al.* (2008), p.88). Fourth, the background error covariance was obtained by computing the average difference between 12- and 24-hour forecasts valid at the same time using the National Meteorological Center (NMC) method (*Parrish and Derber*, 1992). The NMC method generates domain-dependent, static background error covariance matrices, referred to as CV5 in the WRFDA system.

In addition to the above general WRFDA settings, we have two specific settings for the WRF 4D-Var assimilation of precipitation. These include optional use of the quality control of innovation (observation minus background) and constructing the thinning mesh. First, in some experiments, we employ the quality control of innovation (QCI) to reject outlier observations for which the innovation exceeds five times the specified observation error of 2 mm per six hours. Both of these two numbers are the default settings of the WRFDA system. However, it is noted that errors of satellite precipitation observations likely depend on the grid resolution and observation magnitude, which requires further research. Moreover, we use a 20-km thinning mesh to reduce overlapping observations at a given spatial resolution.

To understand how point-scale rainfall assimilation affects WRF primary state variables, we first conduct the 4D-Var synthetic experiment involving assimilation of only one perturbed precipitation observation at an arbitrary location (34.27N, 98.16W). The selected location is associated with approximately 26 mm of accumulated precipitation over a six-hour period in the open-loop forecasts, which represent WRF forecasts without any assimilation in this study. As is evident, the position of this point is carefully selected as it

is surrounded by a strong precipitation forecast. Using the explained experiment settings, we assimilate a synthetic observation, which is generated by adding a small (1 mm) positive increment to the six-hour precipitation forecast at the selected location.

The winter and summer seasons are characterized by different precipitation patterns and mechanisms. The winter experiments focus on a large-scale extratropical cyclone over the United States dominated by stratiform precipitation that lasted almost one day over our study domain. On the other hand, the summer experiments include strong and local convective storms over five days. Since the resolution of the assimilated precipitation does not capture the local nature of these intense summertime convective events, recovering of these small-scale high-intensity activities using the dynamical downscaling approach is challenging. To study the effects of large innovations in dynamical downscaling, we also investigate two scenarios, with and without the QCI, in both winter and summer experiments.

2.4 Results

2.4.1 Statistical Basis for the Comparison of Experiments

We use three main metrics to quantify the performance of the proposed dynamical downscaling approach, namely: 1) root mean squared error (RMSE), 2) mean absolute error (MAE), and 3) correlation (ρ) between modeled (downscaled) and observed (reference) precipitation. The RMSE is defined as

$$RMSE = \sqrt{\frac{1}{nm}\sum_{i=1}^{n}\sum_{j=1}^{m}[R_M(i,j) - R_O(i,j)]^2}, \qquad (2.1)$$

where R_M and R_O are the m-by-n modeled and observed precipitation 2D fields, respectively. The MAE is defined as follows:

$$MAE = \frac{1}{nm}\sum_{i=1}^{n}\sum_{j=1}^{m}|R_M(i,j) - R_O(i,j)|. \qquad (2.2)$$

Note that the RMSE markedly penalizes large anomalies compared to the MAE that uniformly penalizes all anomalies. Furthermore, to explore the predictive skill of the proposed dynamical downscaling approach, we also use normalized differences between the performance metrics of the open-loop and 4D-Var results, as follows:

$$\frac{RMSE_{openloop} - RMSE_{DA}}{RMSE_{openloop}}. \qquad (2.3)$$

and

$$\frac{MAE_{openloop} - MAE_{DA}}{MAE_{openloop}}. \qquad (2.4)$$

To evaluate the correlation between the downscaled and reference precipitation fields, the classic Pearson cross-correlation coefficient (ρ) is used.

2.4.2 Point-scale Assimilation Experiment

Figure 2.3 shows the analysis increments (i.e., analyses minus the first guesses) of zonal wind, meridional wind, surface dry air mass pressure, surface pressure, potential temperature, and specific humidity at the lowest model level. These figures are meant to demonstrate how a small (1 mm) perturbation in the assimilated precipitation propagates into the WRF state variables via the 4D-Var algorithm. As a result of assimilation, maximum analysis

14
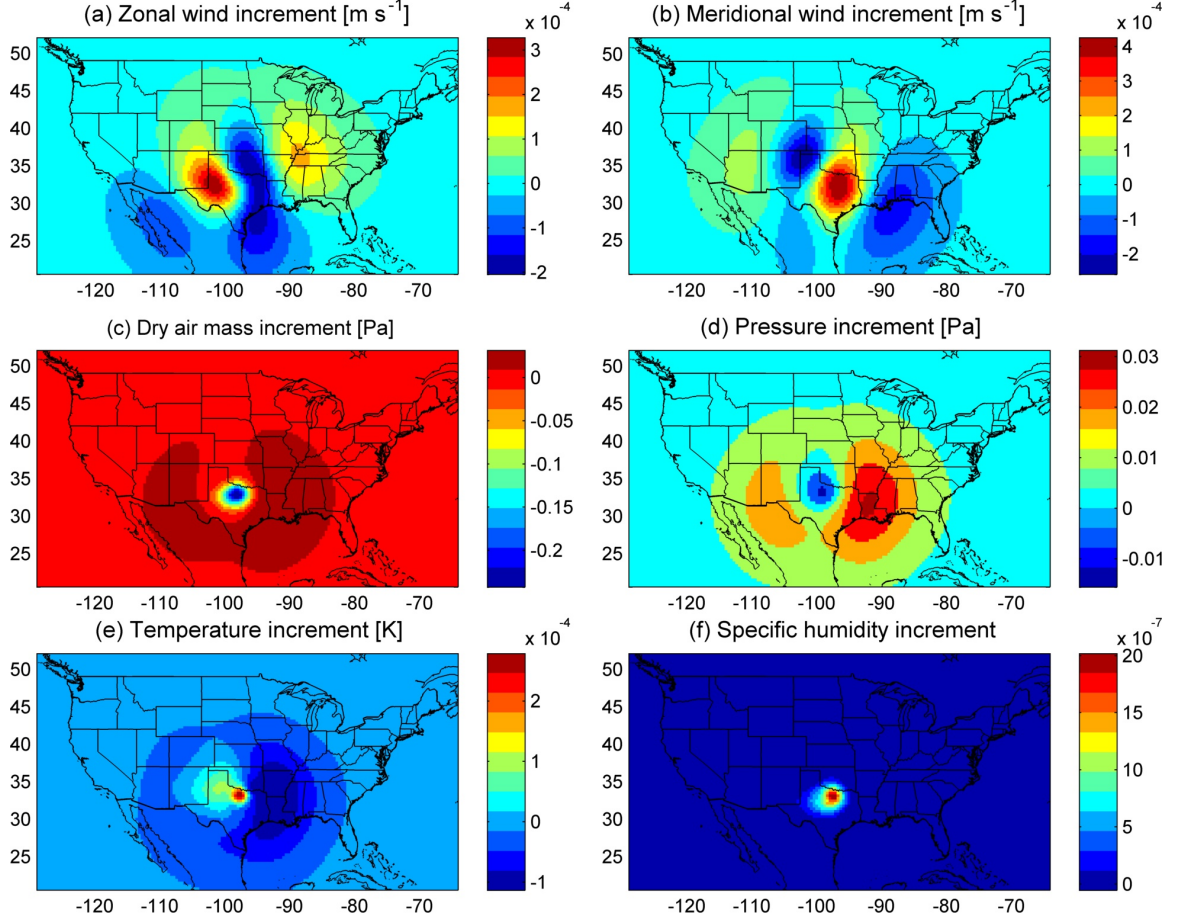
Figure 2.3: The increments of several variables defined as the analyses minus the first guesses at the lowest model level from the synthetic experiment of the 4D-Var assimilation of a six-hour accumulated precipitation observation at a single site. (a) zonal wind (m s^{-1}), (b) meridional wind (m s^{-1}), (c) dry air mass pressure (Pa), (d) air pressure (Pa), (e) potential temperature (K), and (f) specific humidity (kg kg^{-1}).

increments are 3.28×10^{-4} [m s^{-1}] for zonal wind, 4.25×10^{-4} [m s^{-1}] for meridional wind, 0.24 [pa] for surface dry air mass pressure, 0.031 [pa] for surface pressure, 2.7×10^{-4} [K] for surface temperature, and 2.01×10^{-6} [kg kg^{-1}] for specific humidity. While the maximum absolute increments are small, it is interesting to note that the 4D-Var algorithm in the WRFDA system affects the primary state variables over a relatively large area, which may be partly due to the smoothing effects of the background error covariance. For a larger correlation length in the error covariance, the data assimilation involves a larger number of neighboring pixels and thus leads to smoother results. Unlike other state variables with wide-spread increments, specific humidity shows a limited spatial spread.

Despite the fact that the small magnitude of the assimilated perturbation did not substantially affect the magnitude of WRF primary state variables, we found that the influence on the analysis rainfall is substantial. Figure 2.4a shows the open-loop forecasts of the rainfall field from 1800 UTC 10 to 0000 UTC 11 June 2009 covering the contiguous United States, while Figure 2.4b shows the six-hour accumulated rainfall analyses minus the open-loop forecasts. A total of 116 pixels out of 160,000 pixels have six-hour deviation (analysis minus forecast) greater than 1 mm with the maximum value of 9.17 mm. Note that those pixels usually correspond to rainy pixels of the open-loop forecast (Figure 2.4b). After six hours of nonlinear model integration, the small rainfall perturbation not only is propagated throughout the entire domain but also causes a significant deviation much larger than the perturbation itself over a significant surrounding area. The results clearly suggest that the 4D-Var rainfall analysis are markedly sensitive to assimilated rainfall observations.

2.4.3   Winter Experiments

In this subsection, we focus on the winter experiments and devote special attention to comparing the results of multiple assimilation scenarios. As the NCEP stage IV data are only available over land, we selected a rectangular region of interest that corresponds to 66 × 41 grid cells (2706 pixels total) within the outer domain. The winter experiments consist of the following three scenarios:

1. OpL: WRF forecasts without DA.

2. P-noQCI: assimilation of 20 km, six-hour accumulated precipitation using the 4D-Var algorithm without the QCI.

3. P-QCI: same as (ii) but with the QCI.

Figure 2.5a–d shows one-day precipitation accumulations from the NCEP Stage IV data, the open-loop forecasts, and the two precipitation assimilation scenarios. The analysis fields show a good visual agreement with the reference field, which is also well reflected in the computed statistical metrics (see Figure 2.5d). Moreover, the improvement is more
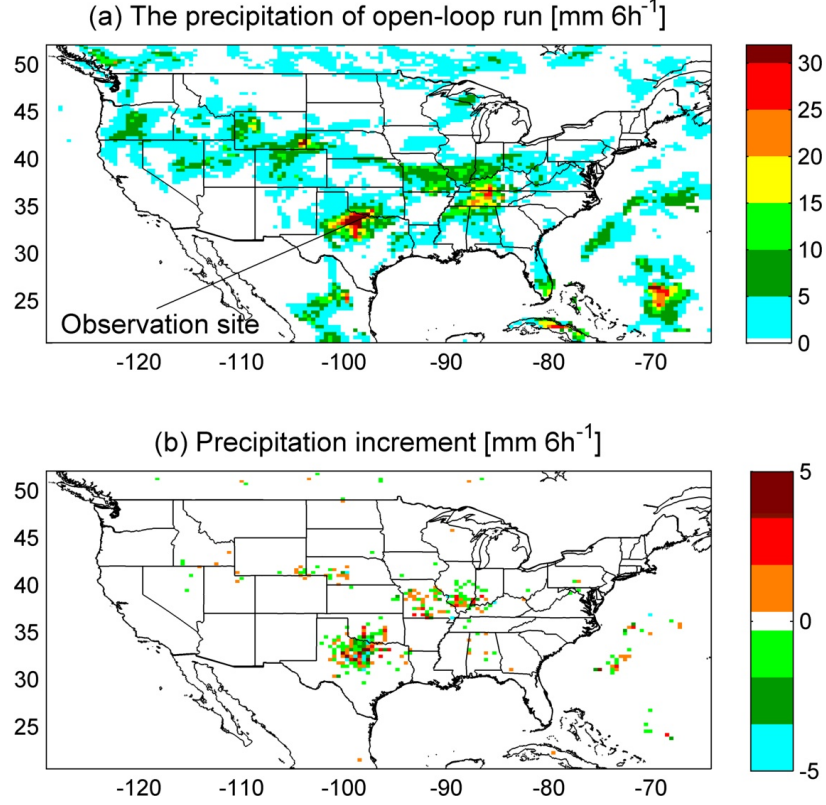
Figure 2.4: Precipitation analysis and forecast (mm 6h^{-1}) in the point-scale assimilation experiment from 1800 UTC 10 to 0000 UTC 11 June 2009. (a) The six-hour accumulated precipitation of the open-loop experiment. (b) The deviation of six-hour accumulated precipitation computed as the precipitation of the DA experiment minus that of the open-loop experiment with a constrained scale from -5 to 5 (mm 6h^{-1}).

significant when we use the built-in QCI. Note that, in each analysis cycle during the one-day experiments, the P-noQCI scenario used the entire 29,996 precipitation data points within the outer domain, while the P-QCI experiment filtered out 431, 444, 279, and 338 data points in four analysis cycles, respectively. About 1% of the observations are removed in the analysis cycle and ultimately lead to a significant improvement in the precipitation analysis. Note also that, although P-noQCI leads to a close visual agreement with the reference data, the quantitative improvements are marginal, compared to the OpL scenario. In contrast, the P-QCI scenario shows the best RMSE (4.98 mm) and MAE (2.43 mm), which are equivalent to 29% and 28% relative improvements, respectively. This finding suggests that the removal of outliers can be a key element for successful implementation of the proposed dynamical downscaling via precipitation assimilation during the winter.
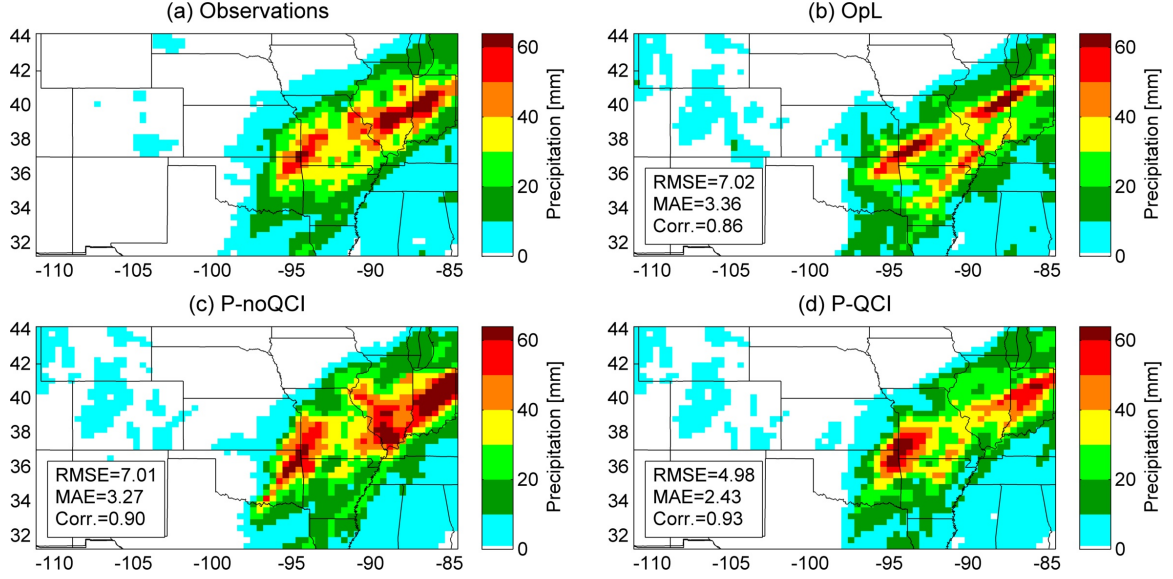
Figure 2.5: One-day accumulated precipitation (mm) at the 36-km resolution for the winter experiments: (a) reference data from NCEP Stage IV precipitation observations, (b) open-loop scenario, (c) P-noQCI scenario, and (d) P-QCI scenario. The RMSE (mm day^{-1}), MAE (mm day^{-1}), and correlation of modeled and observed precipitation are reported in (b)-(d).

2.4.4 Summer Experiments

In this subsection, we study the performance of dynamical downscaling for the summer experiments over both 36-km (outer domain) and 9-km (inner domain) resolutions. Figure 2.6 shows the five-day precipitation accumulations at the 36-km resolution for the same scenarios described in Section 2.4.3. The 4D-Var with the QCI scenario shows the most improved downscaled precipitation (Figure 2.6d), while the 4D-Var without the QCI scenario shows significant overestimation (Figure 2.6c). When compared to the reference data set and OpL forecasts, the assimilation with the QCI scenario markedly improves the spatial patterns of precipitation analyses. For instance, the P-QCI scenario captures a band of rainfall that extends from northeastern Colorado, through Kansas, northern Oklahoma, and northern Arkansas, to northern Georgia while the OpL scenario does not. In addition, the P-QCI scenario produced lower intensity of rainfall around Indiana, leading to a closer agreement with the reference data. Statistics of the five-day precipitation accumulations also confirm that the 4D-Var assimilation with the QCI can substantially improve the spatial distributions of precipitation. However, as is apparent, the assimilation experiment produces too
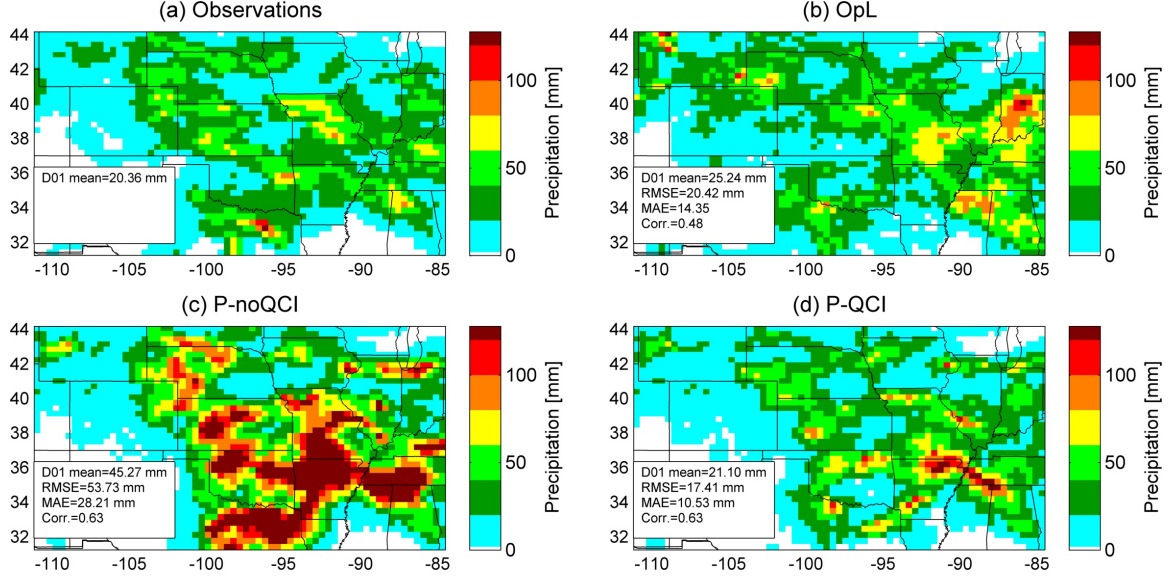
Figure 2.6: Five-day surface accumulated summer precipitation (mm) from the outer domain within 1800 UTC 10-15 June 2009: (a) reference data from NCEP Stage IV precipitation observations, (b) open-loop scenario, (c) P-noQCI scenario, and (d) P-QCI scenario. The domain means are expressed in (a)-(d), while the RMSE, MAE, and correlation of modeled and observed precipitation are reported in (b)-(d).

much precipitation over northeastern Arkansas and western Tennessee. In addition to five-day accumulations, we also compare the hourly domain means of the reference data with those of the P-QCI and the OpL scenarios at the 36-km resolution over the study region introduced in Section 2.4.3 (Figure 2.7). The results demonstrate that the hourly domain means of the P-QCI scenario are closer to those of the reference data than those for the OpL forecasts (Figures 2.7a and 2.7b), showing the effectiveness of the QCI in our dynamical downscaling approach. In the sections below, we will only analyze the winter and summer assimilation experiments using the QCI.

The results for a selected region of interest in the inner domain (101×81 pixels at 9-km resolution) are shown in Figure 2.8, which compares five-day precipitation accumulations from the 4D-Var and the open-loop experiments with the reference data. This region excludes a ten-grid space of each side of the inner domain for convenience of analysis and to avoid any boundary effect. A closer scrutiny of Figure 2.8 clearly shows that the dynamical downscaling approach improves the estimation of rainfall spatial distribution. In particular, four distinct features confirm that the 4D-Var experiment outperforms the open-loop
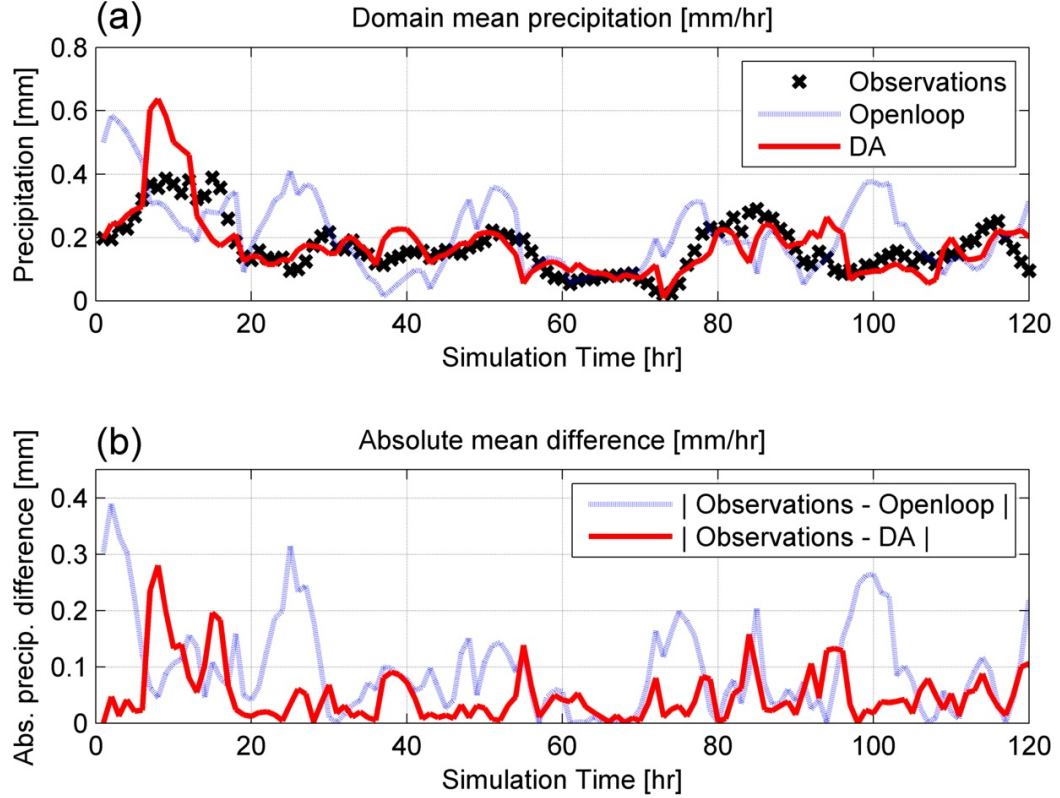
Figure 2.7: The comparison of the domain means of hourly observed summer precipitation, the open-loop, and the DA experiments from the outer domain within 1800 UTC 10-15 June 2009. (a) Domain means and (b) the absolute value of the difference between the domain means of the reference data and open-loop forecasts and those between the reference data and the 4D-Var analyses.

experiment. First, a rainband from about 104W and 42N to 99W and 37N (a white-line parallelogram in Figure 2.8) is captured by the 4D-Var experiment, which is in agreement with the reference data, but not captured well by the open-loop experiment. Second, along latitude 39N to 40N and within longitude 95W to 99W, the open-loop experiment predicted heavy rain of 40 mm to 80 mm, which is corrected with the data assimilation. Third, the WRF 4D-Var system successfully recovers a narrow strip with heavy precipitation along latitude 40N and within longitude 95W to 96W (a white-line rectangle), which is missing in the open-loop experiment. Finally, all the statistics—the domain means, the RMSE, the MAE, and the correlation—demonstrate that the WRF 4D-Var assimilation produces precipitation analyses in closer agreement with the reference data than the open-loop experiment.
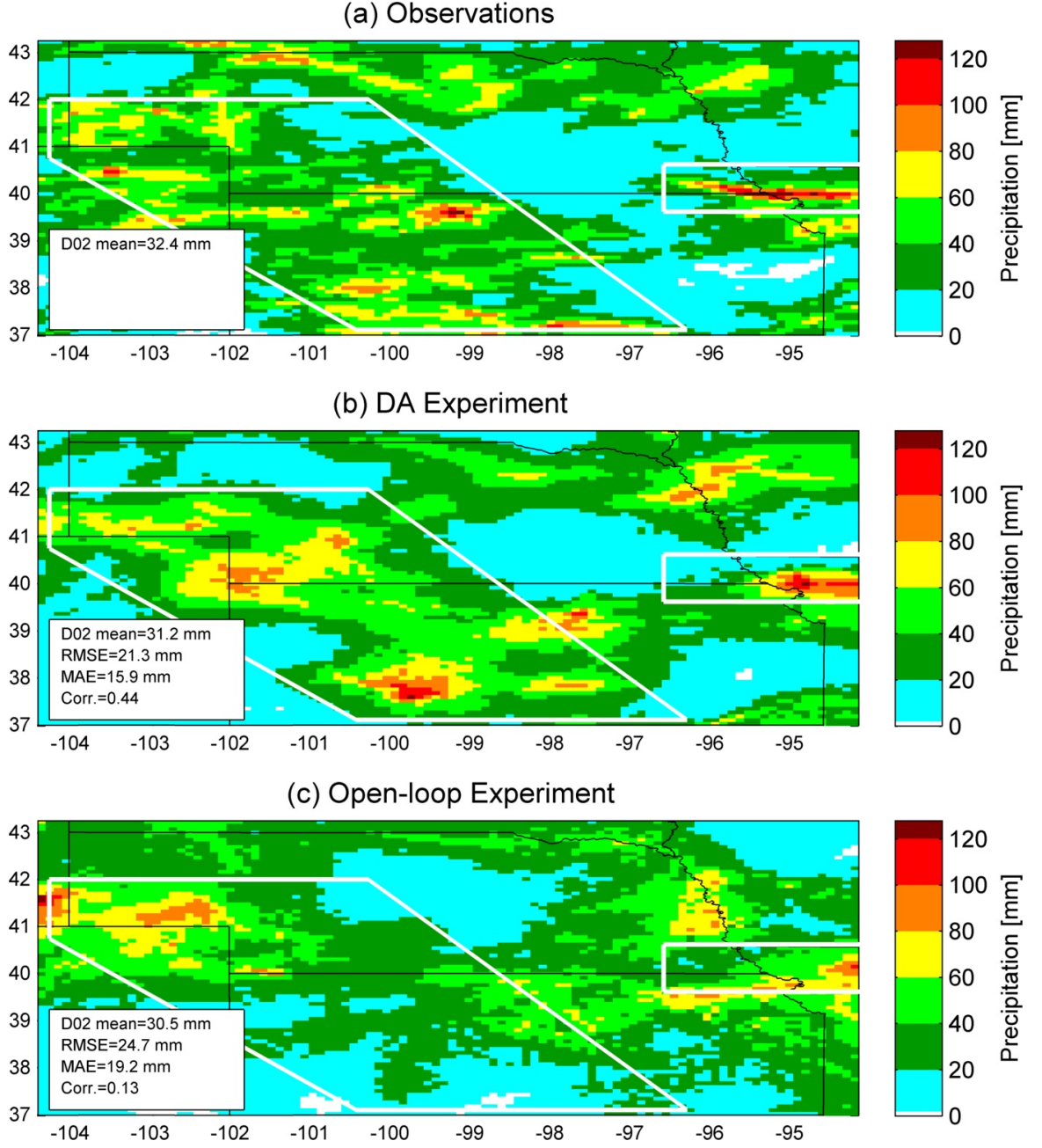
Figure 2.8: Five-day surface accumulated precipitation (mm) from the inner domain of the summer experiments during 1800 UTC 10-15 June 2009: (a) NCEP Stage IV precipitation data, (b) 4D-Var experiment, and (c) open-loop experiment. The RMSE, MAE, and correlation are computed between the modeled accumulated precipitation and observed data. The white-line regions are described in Section 2.4.4.

For each pixel within the region of interest in the inner domain, Figure 2.9 compares the MAEs, correlations, and RMSEs between forecasts, analyses, and the reference data obtained from the hourly rainfall time series over the entire 8,181 pixels. Figure 2.9a shows the MAE for the 4D-Var and open-loop experiments. A total of 60% of the MAE values fall below the diagonal line, indicating that the dynamical downscaling with 4D-Var performed better than the open-loop forecasts in 60% of pixels. For the correlation coefficients, Figure 2.9b shows that the 4D-Var significantly outperforms the open-loop experiment as 66% of the points fall above the diagonal line. The RMSE also shows that 55% of the pixels in the 4D-Var experiment have better performance than the open-loop experiment. Note that the above assimilation experiments were only performed in the outer domain, and analysis outputs from the outer domain were used as the initial and lateral boundary conditions for the inner domain. Therefore, we concluded that assimilation in the outer domain (36-km grid cells) produces improved initial and lateral boundary conditions for the inner domain (9-km grid cells) that ultimately lead to high-resolution and improved estimates of precipitation. We also tested the significance of the difference between the population means of the paired experiments (i.e., open-loop vs. DA) for each statistical metric using the classic two-sample t-test with a significance level of 0.05. The results indicate that the improvement of fine-scale precipitation estimates is significant in terms of MAE and correlation, but not for the RMSE. The statistical significance of the hypothesis can further be tested through bootstrap methods (*Livezey and Chen*, 1983).

2.4.5 Summer Convective Rain vs. Winter Extratropical Cyclone

The purpose of this comparison is to understand the performance of the proposed dynamical downscaling approach for different seasons and rainfall mechanisms. The performance of assimilating six-hour accumulated precipitation in each DA analysis cycle of the one-day winter experiments is compared with that of the five-day summer experiments over the region of interest at the outer domain resolution. As mentioned in Section 2.3, the winter experiments are associated with an extratropical cyclone while the summer experiments consist of many convective storms. Figure 2.10 shows the correlation between the modeled
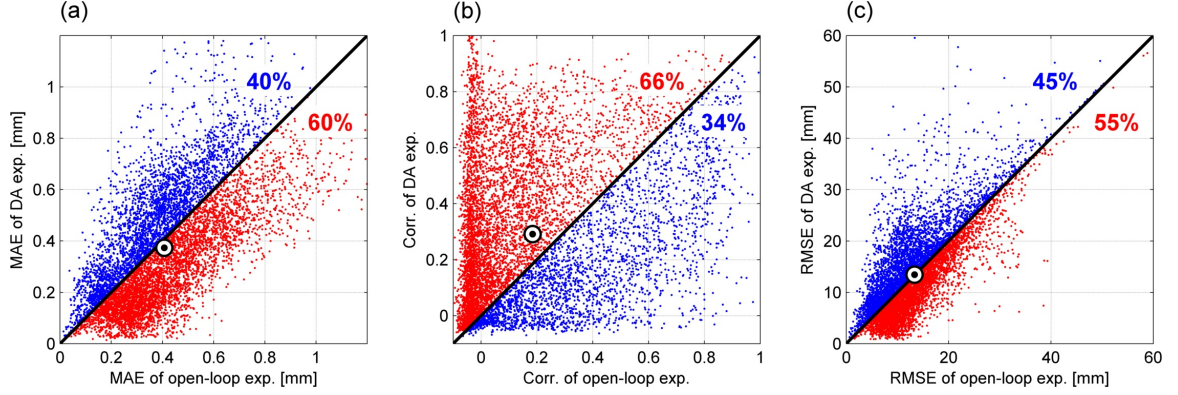
Figure 2.9: The comparison of the MAEs, correlations, and RMSEs of hourly precipitation for each grid of the open-loop experiment versus the DA experiment over the inner domain in the summer experiments. (a) MAEs, (b) correlations, and (c) RMSEs. Higher density of the red dots compared to the blue dots shows that the 4D-Var experiment outperforms the open-loop experiment. The black double-circle markers refer to the mean values.

and the observed precipitation and the predictive skill measured by RMSE and MAE, respectively, for every six-hour analysis cycle in both summer and winter experiments. For the winter experiments, the average correlation between the open-loop forecasts and the reference data is higher than that between the 4D-Var analyses and reference data from the summer experiments (Figure 2.10a). This shows that the precipitation forecasts for the winter, even without using data assimilation, are in closer agreement with the reference data than the corresponding data assimilation experiment in the summer. It is reported in Figure 2.10 that assimilation of precipitation increases the correlation between model output and reference data on average by 0.19 for the summer and 0.13 for the winter. In other words, data assimilation improves the summertime precipitation analyses more than the wintertime in terms of correlation. However, the end results are closer to the reference data in the winter because of better quality of the open-loop forecasts during the winter.

In addition, the skill measured by RMSE is relatively consistent for the analysis cycles during the winter, but varies substantially and degrades sometimes during the summer. Figure 2.10b shows the skills measured by RMSE for the winter and summer experiments are 34% and 3%, respectively. Since RMSE penalizes large errors substantially, the poor summer skill may be due to over- or under-estimation of localized extreme precipitation intensities by the data assimilation scheme. This suggests that in a convection dominant

regime, precipitation extremes may not be well captured by the employed data assimilation system. Surprisingly, the skill of the 4D-Var measured by MAE shows an increase in skill of on average 31% and 29% for the winter and summer experiments, respectively (Figure 2.10c). While both the summer and winter experiments have similar average MAE, the improvement in downscaled precipitation exhibits more spatial variability during the summer than winter. Note that the second analysis cycle in the summer experiment is associated with a large degradation in RMSE and MAE, and the sixteenth analysis cycle shows a large degradation measured by RMSE while no degradation measured by MAE. The reasons for these differences are explored next.
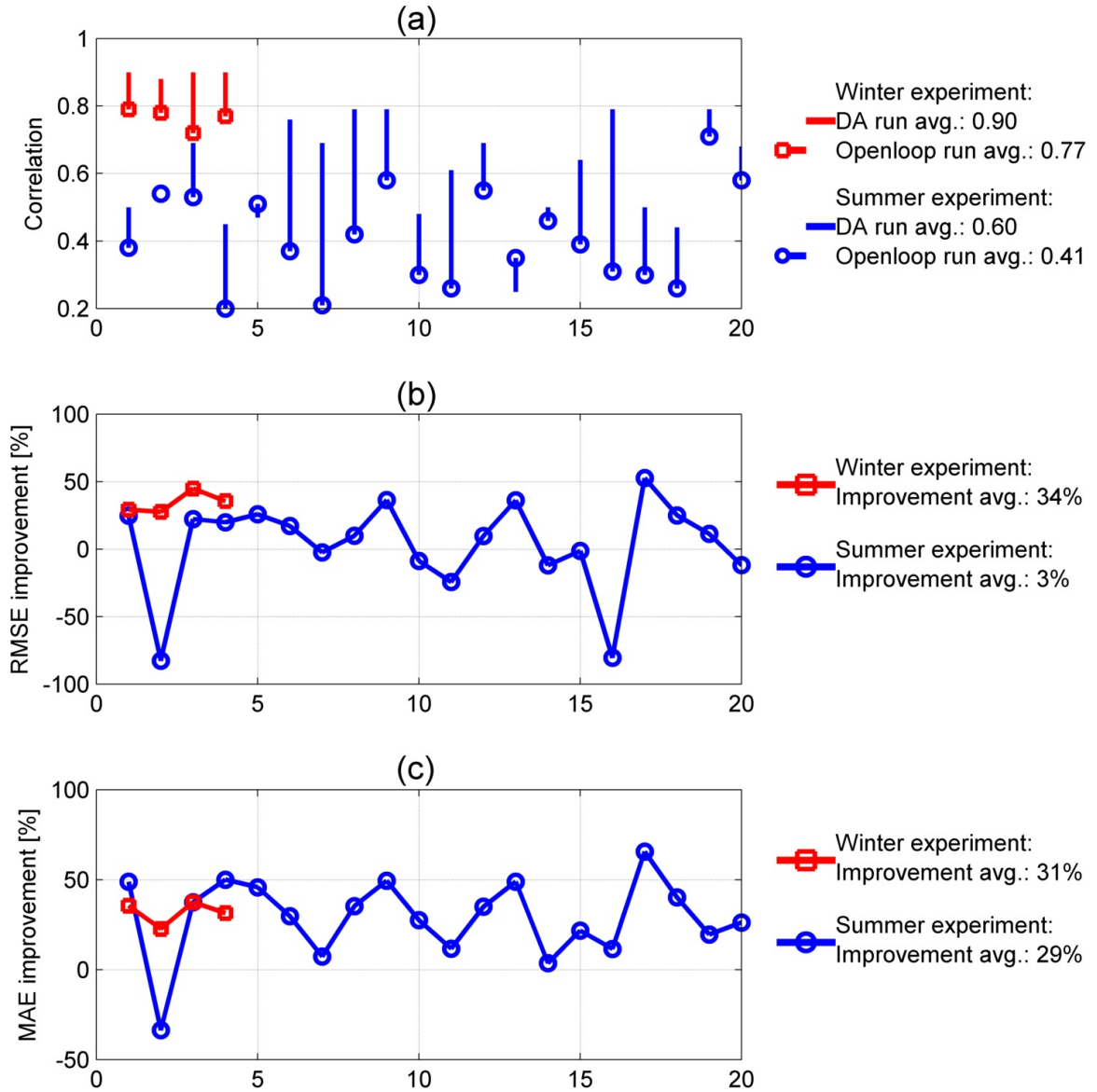
Figure 2.10: The statistics of the summer experiments (blue) and the winter experiments (red): (a) correlations between the six-hour accumulation of modeled and observed precipitation. The hollow circles and squares represent the correlations between the open-loop experiment and reference data. The other end of each line without a circle or a square represents the correlation between the DA experiment and reference data; (b,c) the skill of modeling improvement in terms of RMSE and MAE, respectively.

Figure 2.11 shows six-hour precipitation of assimilation cycles 1, 2, 3, and 16 from the summer experiments, while Figure 2.12 shows six-hour precipitation of cycles 1 to 4 from the winter experiments. These figures give more detail of the impact of non-assimilated observations due to the QCI. As discussed previously, cycles 2 and 16 in the summer experiments do not exhibit good assimilation skill as measured by RMSE (Figure 2.10b). Figures 2.11j and 2.11l show where the WRF 4D-Var system significantly overestimates precipitation in comparison to the reference data in Figures 2.11f and 2.11h, respectively, which is the major source of large RMSE. Note that this region is mainly dominated by convective activity for which its spatial extent is largely estimated correctly, but its precipitation intensities are overestimated by the 4D-Var algorithm. This situation happens much more frequently in the summer than in the winter mainly because (1) the difference between the observed and forecasted precipitation can be very large for the cases of convective rainfall events and thus the observations may not be used in the DA experiment because of the QCI and (2) the prescribed background error covariance can affect model states at a large spatial extent and may not benefit our proposed downscaling approach in capturing local precipitation extremes. The gray regions in northern Texas (Figure 2.11b) and in Tennessee, Alabama, and Mississippi (Figure 2.11d) are those areas where the observations are considered to be outliers in the QCI module and have not been used in the 4D-Var algorithm. Notice that these areas are typically surrounded by relatively large positive innovations in the studied convective dominant storm. As a result, the positive innovations and the large spatial footprint of the background error covariance typically lead to overestimation in those gray regions where no observations are assimilated to properly constrain the overestimation through the cost function of 4D-Var algorithm. In contrast, since winter open-loop forecasts are relatively accurate, the innovation magnitudes mainly remain within the acceptable bounds of the QCI. Thus, the WRFDA typically assimilates a major fraction of heavy precipitation observations within the storm. In Figures 2.12a–d, it can be seen that the wintertime 4D-Var assimilates relatively more areas of heavy precipitation observations than that of the summertime experiments and thereby do not exhibit significant over-estimation. This problem further manifests itself in summertime experiments when

open-loop forecasts completely miss the observed small-scale convective cells. In this case, the 4D-Var with the QCI typically ignores the observations and totally misses information content of important convective precipitation features of the storm. Figure 2.11g shows a small but heavy precipitation patch in Texas that was observed but not assimilated (Figure 2.11c). Therefore, over this heavy rainfall patch, data assimilation does not alter the precipitation analyses significantly compare to the forecasts (Figure 2.11o), and the analysis rainfall intensities remain almost unchanged (Figure 2.11k). However, it can be seen that the WRF 4D-Var system effectively reduces precipitation errors when the open-loop forecasts produce heavy rain over the areas where the observations suggest no rain or light rain. Figure 2.11m shows heavy rain forecasts within longitudes 85 to 95W, while we see little or very light rainfall in Figures 2.11e and 2.11i. Even though Figure 2.11a has a gray region of non-assimilated observations, the assimilated observations surrounding the gray region ultimately reduce forecast errors significantly and lead precipitation analyses in a good agreement with the reference data. Therefore, the QCI seems very effective when the open-loop experiment falsely predicts rainfall, while giving rise to misleading results when the open-loop forecasts miss observed localized precipitation events.
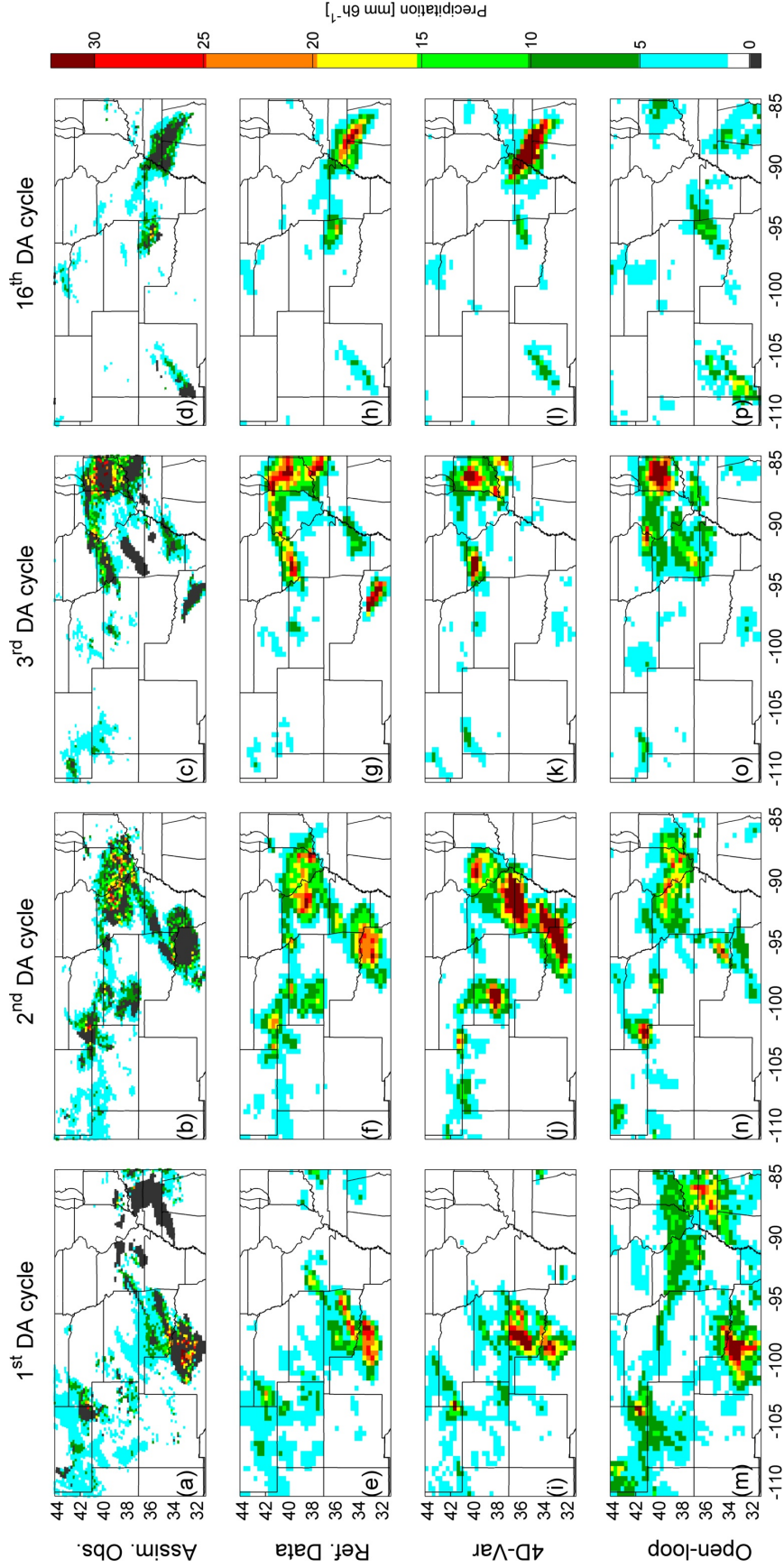
Figure 2.11: Six-hour precipitation (mm) of cycles 1, 2, 3, and 16 from the summer experiments using the QCI. (a)-(d) The assimilated observations at 20-km resolution of the four selected cycles, respectively. Those gray regions denote the locations where observations were filtered by the QCI and not assimilated. (e)-(h) The reference data at 36-km resolution. (i)-(l) The 4D-Var analyses with using the QCI at 36-km resolution. (m)-(p) The open-loop forecasts at 36-km resolution.

28
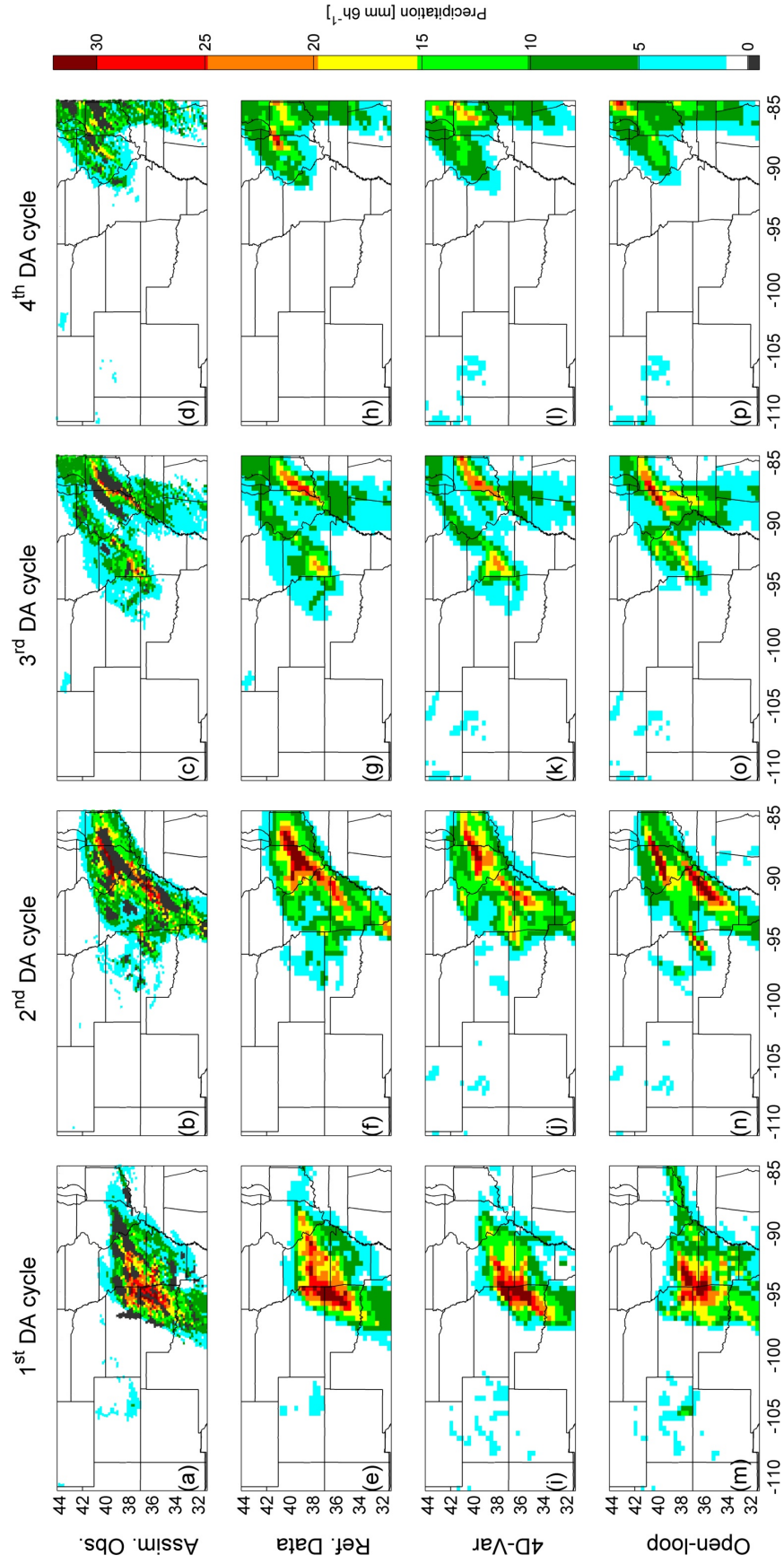
Figure 2.12: Same as Fig. 2.11, except for cycles 1, 2, 3, and 4 from the winter experiments.

29

2.4.6   Time Series Analysis of 4D-Var Assimilation of Precipitation

In this section, we focus on understanding how the 4D-Var scheme impacts wintertime and summertime precipitation analyses at hourly and pixel scales (the smallest simulation unit) within the experimental domain. We select a set of pixels over the study domain where the accumulated precipitation exceeds certain thresholds and discuss the temporal aspects of the proposed dynamical downscaling in those locations.

2.4.6.1   Time Series of One-day Winter Experiments (36-km Resolution)

Figure 2.13a shows the one-day accumulated precipitation from the reference data and the location of six selected sites for hourly time series analysis. The precipitation time series at the sites are shown in Figures 2.13b–g with the corresponding statistics presented in Table 2.1. To study the effects of the dynamical downscaling approach on capturing high-intensity precipitation over the studied domain, we select six individual locations based on the following criteria: (1) Sites B and C exhibit accumulated precipitation within the top 10% of the reference data (>30 mm/day) and the highest modeling skill measured by MAE defined in Equation (2.4); (2) Sites D and E exhibit similar behavior as sites B and C, except that their accumulated precipitation is within the top 10% of the open-loop experiment (>25 mm/day); and (3) Sites F and G exhibit accumulated precipitation within the top 10% of the reference data but exhibit the lowest modeling skill measured by MAE.

Figures 2.13b–e demonstrate that the downscaling approach effectively disaggregates six-hour winter precipitation to the hourly scale, particularly for the case that the open-loop experiment falsely forecasts heavy rainfall. At sites B to E, it can be seen that the time series of 4D-Var analyses are in closer agreement with the reference data than those of open-loop forecasts. For those time intervals in which the open-loop forecasts have intense rainfall but the reference data do not, the WRF 4D-Var significantly reduces overestimation of the open-loop forecast. We see similar behaviors at all sites, especially in time intervals 15:00 to 20:00 UTC at site B; 14:00 to 17:00 UTC at site C; 00:00 to 06:00 UTC at site D; and 16:00 to 18:00 UTC at site E.

Figures 2.13f and 2.13g show that the downscaling approach occasionally overestimates

Table 2.1: The statistics of selected sites in Figures 2.13-2.15. Units are in mm.

	B	C	D	E	F	G
One-day experiments for the winter (D01)						
Accumulated precipitation (OBS)	39	65	11	34	33	34
Accumulated precipitation (OpL)	98	41	29	59	30	25
MAE (DA vs. OBS)	1.47	1.28	0.38	0.84	1.70	1.79
MAE (OpL vs. OBS)	3.51	2.48	1.09	1.88	0.95	0.96
Five-day experiments for the summer (D01)						
Accumulated precipitation (OBS)	58	54	7	16	49	89
Accumulated precipitation (OpL)	77	66	102	81	17	10
MAE (DA vs. OBS)	0.37	0.41	0.10	0.17	0.75	0.99
MAE (OpL vs. OBS)	0.86	0.76	0.80	0.91	0.39	0.68
Five-day experiments for the summer (D02)						
Accumulated precipitation (OBS)	52	60	17	62	10	108
Accumulated precipitation (OpL)	126	17	80	64	70	71
MAE (DA vs. OBS)	0.54	0.33	0.19	0.53	0.07	0.73
MAE (OpL vs. OBS)	1.17	0.60	0.60	0.87	0.64	1.07

precipitation analyses when the rainfall patterns in the open-loop forecasts and reference data are drastically different. In some sense, the overestimation problem is related to issues previously discussed in Section 2.4.5. At these two sites, the WRF 4D-Var reproduces down-scaled precipitation over the time intervals in which the open-loop forecasts are rainy and remains dry when the open-loop forecasts are dry. In other words, the 4D-Var assimilation only increases the rainfall estimates over those time intervals where the open-loop forecast is raining rather than reproducing rainfall temporal patterns similar to the reference data. For example, it can be seen that the behavior of hourly precipitation is different between the reference data and the open-loop forecasts within the second assimilation cycle (hours 07:00 to 12:00 UTC). In this cycle, the reference data show moderate rain from 07:00 to 08:00 UTC, with rainfall effectively stopping at 09:00 UTC; however, the open-loop experiment only forecasts a small amount of precipitation at 10:00 UTC. Assimilating six-hour rainfall observations, the WRF 4D-Var algorithm apparently increases the volume of precipitation analysis during the time intervals in which the open-loop forecasts are raining. As a result, we can see that the precipitation intensities at 10:00 UTC for the reference data, DA experiment, and open-loop experiment are 0, 14 and 2 mm, respectively. These findings suggest

that the proposed dynamical downscaling approach may be less effective in those analysis cycles within which the observed rainfall exhibits strong intermittency.

2.4.6.2 Time Series of Five-day Summer Experiments (36-km Resolution)

In the summer experiments, similar assimilation effects are found as discussed in the previous subsection except the fact that the effect is more drastic. In other words, the 4D-Var analyses still outperform the open-loop forecasts in a temporal sense at the hourly scale. However, because the temporal patterns of open-loop forecasts and assimilated observations are typically very different during the summer, the assimilation results are not as good as the winter experiments in terms of the examined quality metrics. Figure 2.14a shows the accumulated precipitation during the five-day summer experiments with the location of the six selected sites. Figures 2.14b–g show the hourly precipitation time series at each site with the corresponding statistics reported in Table 2.1. The selection criteria for the six sites are the same as Section 2.4.6.1, except that the top 10% of the reference data and open-loop experiment are now 46 and 54 mm over five days, respectively. For sites B to E, it is clear that the DA was quite effective and improved the results of precipitation analyses with respect to the reference data compared to those of open-loop forecasts. On the other hand, the sites F and G show lowest downscaling performance. It can be seen that the DA experiment overestimates precipitation during very short periods of time such as the hour 00:00 UTC 11 June and the time interval from 13:00 to 18:00 UTC 12 June at site F and underestimates from 07:00 to 18:00 UTC 11 June at site G. As discussed in Section 2.4.5, we suspect that the difficulty of precipitation downscaling is related to the imprecise forecast of summer-time convective precipitation and the smoothing effect of the prescribed background error covariance.

2.4.6.3 Time Series of Five-day Summer Experiments (9-km Resolution)

The hourly precipitation time series of six selected sites within the inner domain are also presented in Figure 2.15 with the corresponding statistics reported in Table 2.1. The domain in Figure 2.15a was divided into six regions, each containing a site with significant improvement measured by the MAE metric. Figures 2.15b–g demonstrate that in all cases

the 4D-Var outperforms the open-loop experiment. However, both the open-loop forecasts and 4D-Var analyses occasionally missed high intense precipitation in the reference data (Figure 2.15e). We can see that the assimilation scheme is fairly effective at reducing or removing rainfall intensities appearing in the open-loop forecasts that do not appear in the reference data. As a result, we conclude that the dynamical downscaling framework is sufficiently effective not only in improving precipitation accumulation measured by the described statistical metrics but also in precipitation estimation at hourly time and pixel scales.
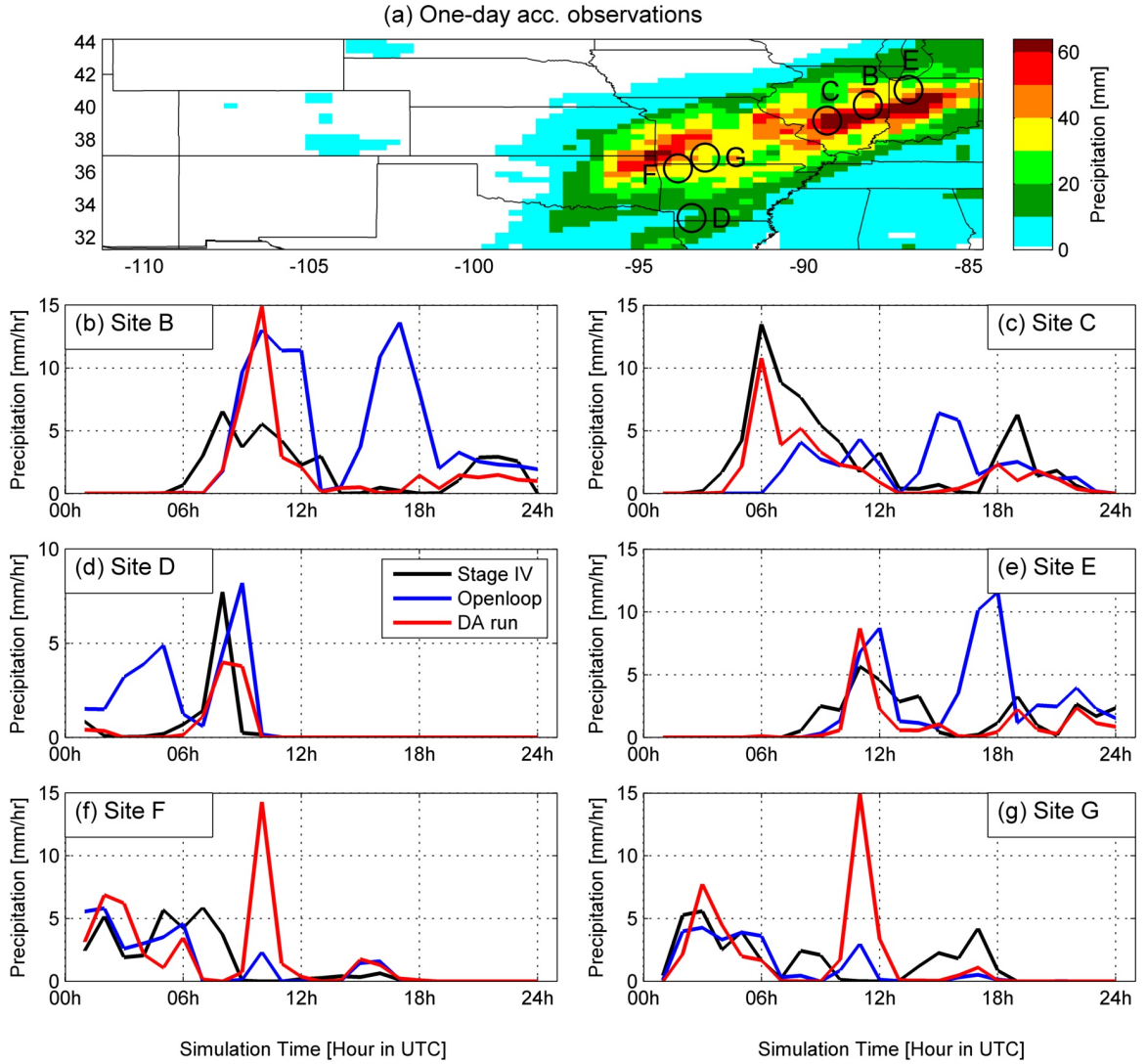
Figure 2.13: (a) Observed accumulated precipitation and the locations of selected sites (black circles) from the outer domain of the one-day winter experiments. (b)-(g) the time series of hourly precipitation of Stage IV reference data (black), the open-loop experiment (blue), and the 4D-Var experiment (red) for sites B to G, respectively.
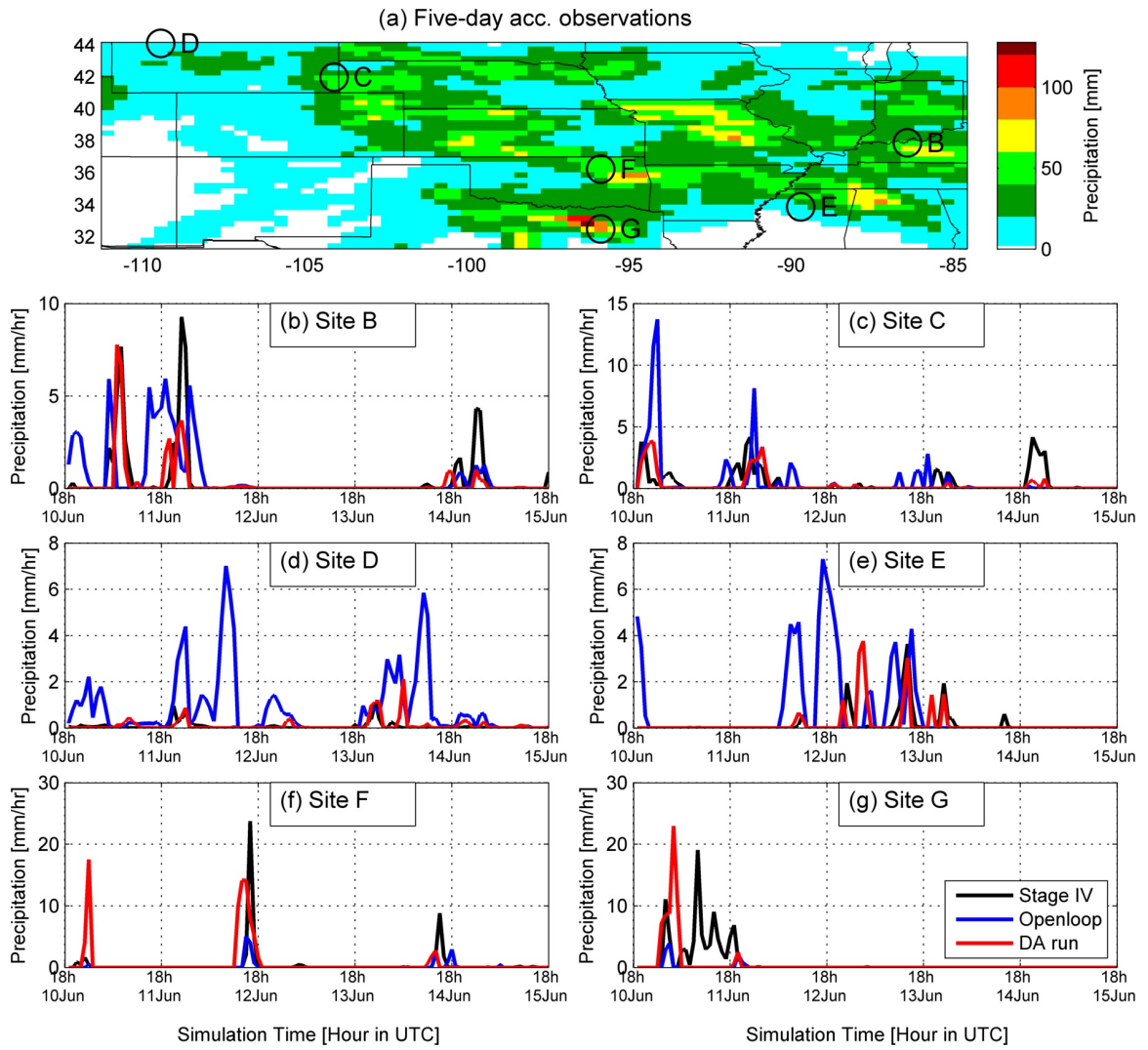
Figure 2.14: Same as Fig. 2.13, except for the outer domain of the summer experiments.
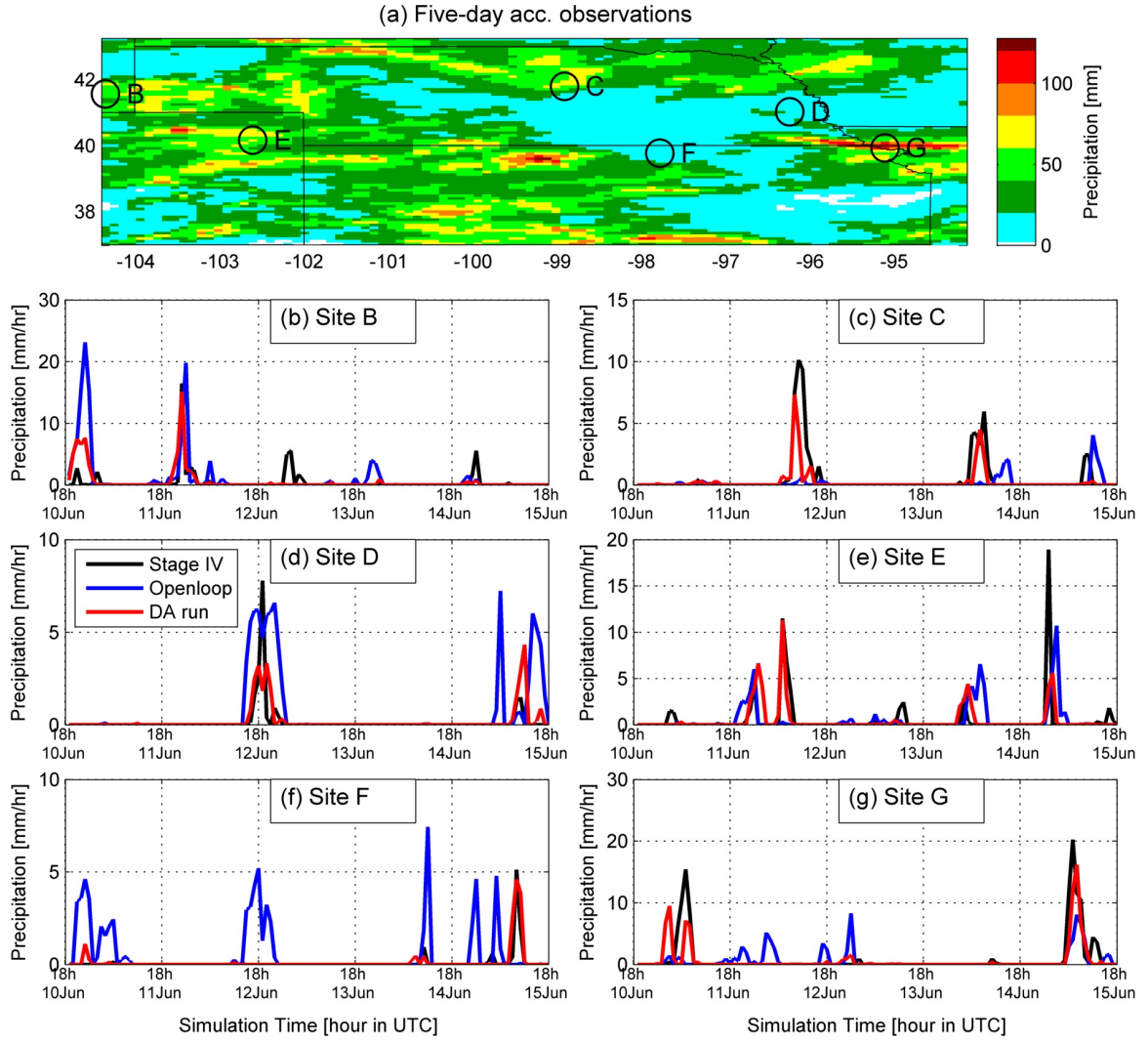
Figure 2.15: Same as Fig. 2.13, except for the inner domain of the summer experiments.

2.5   Summary of the Chapter

The objective of this chapter was to develop and preliminarily test a framework for dynamically downscaling spaceborne precipitation products using the Weather Research and Forecasting (WRF) model with four-dimensional variational data assimilation (4D-Var). Numerical experiments have been conducted to (1) understand the sensitivity of precipitation downscaling through point-scale precipitation data assimilation and (2) investigate the impact of seasonality and associated changes in precipitation-generating mechanisms on the quality of spatiotemporal downscaling of precipitation. The point-scale experiment suggests that assimilating precipitation can significantly affect the precipitation analysis, forecast, and thus downscaling. Because of occasional overestimation or underestimation of small-scale summertime precipitation extremes, our numerical experiments demonstrate that the wintertime assimilation produces downscaled precipitation estimates that are in closer agreement with our reference data set than similar summertime experiments. This leads to the conclusion that the WRF 4D-Var system is able to effectively downscale a six-hour precipitation product with a spatial resolution of 20 km to hourly precipitation with a spatial resolution of less than 10 km in grid spacing—relevant to fine-scale hydrologic applications for the era of the Global Precipitation Mission.

CHAPTER III

PRECIPITATION DATA ASSIMILATION AND DOWNSCALING II: ASSIMILATION OF TRMM 3B42 DATASET

In the previous chapter, a framework of precipitation assimilation and downscaling based on the WRF 4D-Var system has been described and demonstrated as a proof of concept. This chapter extends the applications by assimilating Tropical Rainfall Measuring Mission (TRMM) 3B42 precipitation data into the WRF model and studies its impacts on precipitation analyses and forecasts. The work also enables the joint data assimilation of soil moisture and precipitation (Chapter 5) and paves the way for applying downscaled precipitation analyses resulting from the WRF 4D-Var system in streamflow predictions (see Appendix A). The rest of the chapter is organized as follows. Section 3.1 briefly describes relevant research and the main goals of the chapter. Section 3.2 provides the details of the data sets, the model and experiment configuration, and the statistical basis for performance evaluation. Section 3.3 presents the results and discussions, and Section 3.4 summarizes the findings of the study.

3.1 Introduction

The inaccuracy of precipitation estimates from current numerical weather predictions is typically attributed to the significant uncertainty of initial conditions of the models. Summertime convective precipitation is largely driven by local-scale updrafts resulting from surface heating rather than large-scale synoptic weather systems, and therefore it is particularly challenging to be predicted (*Case et al.*, 2011). In contrast, satellite merged products typically outperform the models when convective rain dominates (*Gottschalck et al.*, 2005; *Ebert et al.*, 2007; *Kubota et al.*, 2009; *Sapiano and Arkin*, 2009; *Kidd et al.*, 2012). Hence, to better capture fine-scale summertime cloud and precipitation processes, *Ebert et al.* (2007) suggested integrating satellite observations into high-resolution numerical models.

Direct assimilation of satellite and gauge precipitation into numerical weather prediction

models has been studied for more than a decade. Rain rates retrieved from the Special Sensor Microwave Imager (SSM/I) were assimilated into the Florida State University global spectral model (*Tsuyuki*, 1997). Rain rates and total precipitable water retrieved from the TRMM Microwave Imager (TMI), SSM/I, and the Advanced Microwave Scanning Radiometer for Earth Observing System (AMSR-E) were assimilated into the Goddard Earth Observing System (GEOS) (*Hou et al.*, 2000b,a, 2001, 2004; *Pu et al.*, 2002; *Lin et al.*, 2007). In addition, surface rain rates and retrieved total precipitable water were assimilated into the European Centre for Medium-Range Weather Forecasts (ECMWF) operational system, and results showed that rainfall forecasts of up to 12 hours improved (*Lopez and Bauer*, 2007; *Geer et al.*, 2008; *Lopez*, 2011, 2013). More recently, TRMM 3B42 precipitation is assimilated into the low-resolution National Centers for Environmental Prediction (NCEP) Global Forecast System (GFS) (*Lien et al.*, 2016). On a regional scale, studies have assimilated total precipitable water and rain rates into models, including the WRF model, the Japanese Meteorological Agency (JMA) system, and the National Meteorological Center (NMC) ETA model, and showed improved rainfall forecasts over various spatiotemporal resolutions (*Zupanski and Mesinger*, 1995; *Pu and Tao*, 2004; *Koizumi et al.*, 2005; *Chen et al.*, 2008; *Rakesh et al.*, 2009; *Kumar et al.*, 2014; *Lin et al.*, 2015). However, the assimilation of clouds and precipitation has several remaining issues: (1) quick decay of the influence of assimilated information; (2) non-Gaussian error characteristics of the model; (3) the inconsistency between full physics parameterization and its linearized representation, particularly for the atmospheric moist parameterization; and (4) the mismatch between observations and background states (*Errico et al.*, 2007; *Lopez*, 2007; *Bauer et al.*, 2011b). The last two issues may be exacerbated when data assimilation are performed within a domain of high resolutions.

Building on Chapter 2, this study assimilate both NCEP Stage IV and TRMM 3B42 rainfall datasets into the WRF model with a 4D-Var scheme to re-visit several remaining issues in precipitation assimilation. With a focus on high-resolution summertime precipitation data assimilation and downscaling, the work addresses issues raised in several review studies (*Errico et al.*, 2007; *Lopez*, 2007; *Bauer et al.*, 2011b) and the issue of under- or

over-estimation of summertime precipitation discussed in Chapter 2. Specifically, the study attempts to answer the following questions: (1) what is the effect of the quality control for removing observation outliers and the linearized parameterization model used in the data assimilation process on precipitation analyses, (2) how much can the assimilation of TRMM precipitation improve precipitation analyses compared to the assimilation of NCEP Stage IV data, (3) how much can the information of assimilated rainfall at the outermost domain penetrate into finer-resolution domains, and (4) how much can the assimilation of TRMM precipitation improve forecasts beyond the assimilation window (i.e., six hours in this work).

3.2 Methodology

In this section, we provide an overview of the datasets, the experimental configuration and design, and statistical metrics used in this study. Section 3.2.1 describes (1) two datasets to be assimilated, NCEP Stage IV precipitation and TRMM 3B42 version 7 and (2) the NCEP final (FNL) analysis for deriving the initial and lateral boundary conditions of the WRF numerical experiments. Section 3.2.2 describes the setup of the WRF 4D-Var system and the design of ten experiments. Section 3.2.3 presents statistical metrics for evaluating the performance of the experiments.

3.2.1 Data Sets

3.2.1.1 NCEP Stage IV Precipitation

The NCEP Stage IV precipitation data set, available in the contiguous United States, is a ground-based radar-derived product with gauge correction and manual quality control procedures performed by the River Forecast Centers of the National Weather Service (*Lin and Mitchell*, 2005). The hourly precipitation of the data set has a gridded spatial resolution of 4 km and is publicly available online (see http://data.eol.ucar.edu/codiac/dss/id=21.093).

3.2.1.2 TRMM 3B42

The TRMM 3B42 product is retrieved from multiple satellite sensors with a temporal resolution of 3 hours and a spatial resolution of $0.25° \times 0.25°$ covering 50°S to 50°N latitudes

(*Huffman et al.*, 2007). This product uses all available microwave-based precipitation esti-
mates from TMI, AMSR-E, SSM/I, and the Advanced Microwave Sounding Unit-B (AMSU-
B) with the adjustment to the TRMM 2B31 imager/radar combined product. For filling
the fields without microwave observations, the product uses microwave-calibrated infrared
precipitation estimates. Finally, the product is rescaled for matching Global Precipita-
tion Climatology Project (GPCP) monthly rain gauge analysis. The TRMM 3B42 data is
publicly available online (see http://pmm.nasa.gov/data-access/downloads/trmm).

3.2.1.3   NCEP FNL

The NCEP FNL product, available on $1°\times1°$ grids every 6 hours, is produced by the NCEP
Global Data Assimilation System (GDAS) with a delay one-to-two hours compared to the
Global Forecast System product in order to integrate more observations ($\sim10\%$ more). The
dataset is publicly available online (see http://rda.ucar.edu/datasets/ds083.2/).

3.2.2   Model and Experiment Setup

3.2.2.1   Model Setup

In this chapter, the WRF configurations and model setup are described in Table 3.1 with
the corresponding domain configuration shown in Figure 3.1. One-way nesting (i.e., no
feedback from a child domain to a parent domain) is used for all experiments having nested
domains. The setup of the WRF 4D-Var system is similar to that used in Chapter 2,
including (1) the employment of the National Meteorological Center (NMC) method for
estimating a domain-dependent, static background error covariance matrix, referred to as
option 5 for control variables (CV5), (2) the use of the quality control for innovations (QCI)
that rejects outlier observations when the observations with the corresponding innovations
exceed a multiplier multiplied by a specified observation error, which is set to be 2 mm
$6hr^{-1}$, and (3) the employment of a default six-hour assimilation window.
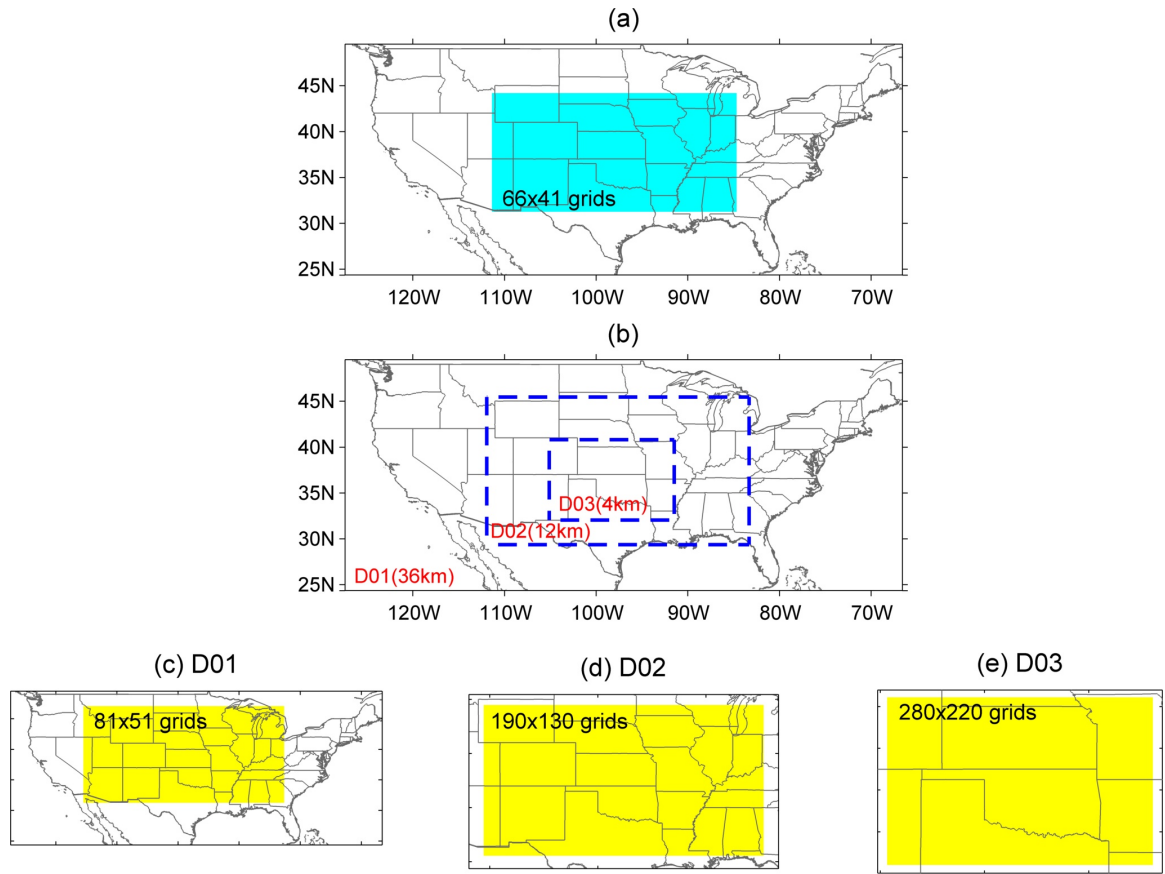
Figure 3.1: (a,b) Domain configuration with respect to settings A and B, respectively, in Table 1. The blue box denotes the region of interest for precipitation analysis. (c-e) The domains with a region of interest shown in yellow boxes from subplot (b).

Table 3.1: Settings and WRF physics parameterization.

	Setting A	Setting B
General		
WRF version	3.4	3.6.1
WRFDA version	3.4	3.6.1
Experiment period	1800UTC 10-15 June 2009	0000UTC 16-26 July 2013
Domain geometry		
Feedback between domains	-	One-way nested
Top of atmosphere (hPa)	50	50
Vertical levels	41	41
Domain 01 (D01)		
Grid size	149×79	149×79
Grid resolution (km)	36	36
Domain 02 (D02)		
Grid size	-	210×150
Grid resolution (km)	-	12
Domain 03 (D03)		
Grid size	-	300×240
Grid resolution (km)	-	4
WRF model physics		
Microphysics	WRF single-moment 3-class scheme (*Hong et al.*, 2004)	WRF single-moment 6-class scheme (*Hong and Lim*, 2006)
Land surface scheme	Noah model (*Chen and Dudhia*, 2001)	Noah model
Cumulus	Kain-Fritsch (*Kain*, 2004)	Kain-Fritsch scheme, except none for domain 03
Longwave radiation	Rapid Radiative Transfer Model (*Mlawer et al.*, 1997)	RRTMG scheme (*Iacono et al.*, 2008)
Shortwave radiation	Dudhia scheme (*Dudhia*, 1989)	RRTMG scheme
Surface layer	MM5 similarity	Revised MM5 similarity (*Jimenez et al.*, 2012)
Planetary boundary layer	Yonsei University scheme (*Hong et al.*, 2006)	Yonsei University scheme

3.2.2.2   Experiment Design

To address the questions previously mentioned in Section 3.1, we conduct a series of numerical experiments with the detailed settings and the study domains shown in Table 3.1 and Figure 3.1. Five experiments use setting A, while the other five use setting B (see Table 3.2). The data assimilation experiments assimilate precipitation retrievals at only the 36-km domain. The experiments using setting A are used for understanding the sensitivity of precipitation analyses to the given multiplier of the QCI, while those with setting B are designed for quantifying the impact of TRMM precipitation data assimilation on precipitation analyses and forecasts. The thinning process is employed so that the spatial density of the assimilated observations for both NCEP Stage IV and TRMM data is similar and comparable. Furthermore, for the experiments using setting B, the updated states from the 36-km domain are used for deriving the initial and lateral boundary conditions of the inner domains, including both 12- and 4-km domains. As in Chapter 2, this study uses a cold start mode (non-cycling mode) for every six-hour assimilation cycle. The first guesses or "background states" are obtained from global model outputs rather than from the previous six-hour WRF integration. Figure 3.2 illustrates the flowchart of the simulations in each assimilation cycle (i.e., those starting at 00, 06, 12, and 18 UTC). In each cycle, six-hour precipitation observations valid at the end of the cycle are assimilated. For all the experiments except B_OL_24 and B_TRMM_24, we study six-hour precipitation analyses of each run initialized every six hours. In contrast, we analyze the daily precipitation forecasts of each run initialized every six hours for the B_OL_24 and B_TRMM_24 experiments.
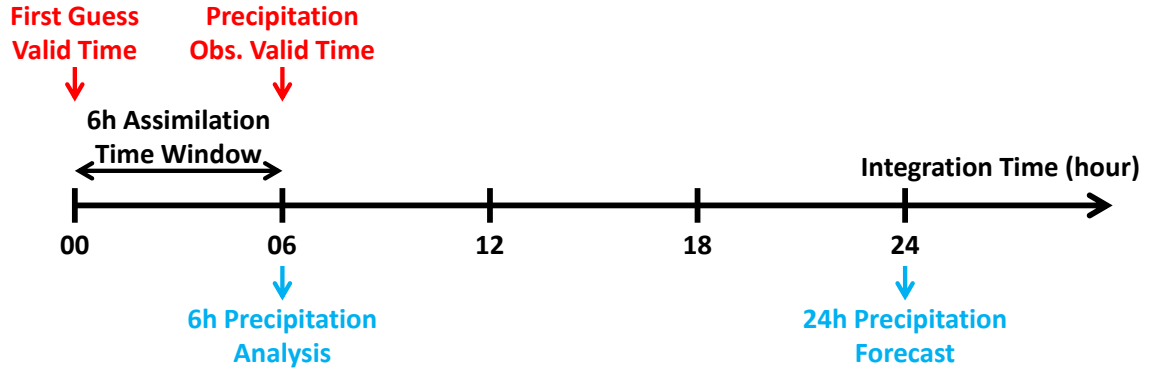
Figure 3.2: Schematics of precipitation assimilation, analysis, and forecast in this study.

Table 3.2: List of experiments.

Experiment	Setting (Table 3.1)	Assimilated observations	Thinning mesh	QCI	Integration hours	Relevant sections
A_OL	A	-	-	-	6	3.3.1
A_QCI4	A	6h Stage IV	20 km	4	6	3.3.1
A_QCI6	A	6h Stage IV	20 km	6	6	3.3.1
A_QCI8	A	6h Stage IV	20 km	8	6	3.3.1
A_QCI10	A	6h Stage IV	20 km	10	6	3.3.1
B_OL	B	-	-	-	6	3.3.2, 3.3.3
B_ST4	B	6h Stage IV	20 km	6	6	3.3.2
B_TRMM	B	6h TRMM	-	6	6	3.3.2, 3.3.3
B_OL_24	B	-	-	-	24	3.3.4
B_TRMM_24	B	6h TRMM	-	6	24	3.3.4

3.2.3 Performance Metrics

We compute five metrics, namely the mean absolute error (MAE), correlation coefficient (ρ), equitable threat score (ETS), false alarm rate (FAR), and bias score (BS) to evaluate the performance of the experiments. The precipitation analyses and forecasts from the numerical experiments listed in Table 3.2 are compared to the reference NCEP stage IV precipitation at corresponding time-space resolutions. The blue box in Figure 3.2a shows the region of interest for the experiments using setting A, and the yellow boxes in Figures 3.2c-e show the regions of interest for the experiments using setting B. The metrics are computed based on the precipitation fields in the region of interest. The MAE is defined as follows:

$$MAE = \frac{1}{nm} \sum_{i=1}^{n} \sum_{j=1}^{m} |M(i,j) - O(i,j)|, \tag{3.1}$$

where $M(i,j)$ and $O(i,j)$ are the modeled and observed precipitation, respectively, at pixel (i,j) of a m-by-n 2D fields. The fields are also used for calculating ρ using the classic Pearson cross-correlation coefficient. An MAE reduction percentage is also calculated as $(MAE_{OL} - MAE_{DA})/MAE_{OL}$, in which subscript OL denotes the open-loop experiments, while subscript DA indicates the data assimilation experiments.

The ETS, FAR, and BS metrics are computed based on a classic 2-by-2 contingency table that detects whether a rain rate exceeds a certain threshold. The table includes four components: (1) the total number of correct hits a, (2) the total number of false alarms b, (3) the total number of misses c, and (4) the total number of the occasions that both forecasts and observations are under a threshold (no forecasts), as follows:

$$\begin{pmatrix} a & b \\ c & d \end{pmatrix} = \begin{pmatrix} hits & false\,alarms \\ misses & no\,forecasts \end{pmatrix}, \tag{3.2}$$

with a sample size $n = a + b + c + d$. Based on Equation (3.2), the ETS, the FAR, and the BS are defined as follows

$$ETS = \frac{a - a_r}{a + b + c - a_r}, \tag{3.3}$$

$$FAR = \frac{b}{a + b}, \tag{3.4}$$

$$BS = \frac{a+b}{a+c},\tag{3.5}$$

where a_r is the expected number of correct hits due to a random chance, as $a_r = (a+b)(a+c)/n$. In Equation (3.3), $ETS = 1$ means a perfect forecast, while $ETS \leq 0$ means no any model skills. Equation (3.5) illustrates overestimation for $BS > 1$ or underestimation for $BS < 1$.

3.3   Results and Discussions

3.3.1   The Effect of the QCI and the Linearized Model

Figure 3.3 compares the performance of precipitation data assimilation with various thresholds of the QCI: experiments A_OL, A_QCI4, A_QCI6, A_QCI8, and A_QCI10. The scatter plot shows the MAE and the correlation of modeled and observed six-hour precipitation fields of 36-km resolution for each six-hour assimilation cycle. Note that a dot below the 1:1 line in the MAE (Figures 3.3a-d) and that above the line in the correlation (Figures 3.3e-h) denotes that a data assimilation run outperforms the corresponding open-loop run. The average values of the MAE and correlation are also reported in the figure. As is evident, the six-hour precipitation estimates of the 4D-Var experiments are in closer agreement with the reference NCEP Stage IV data set than those of the open-loop experiments. We also computed the p-score of each experiment using the classic two-sample t-test. With a significance level of 0.05, the p-score indicates that for all experiments, the 4D-Var precipitation analyses are significantly improved compared to the open-loop forecasts. In terms of the MAE and correlation, using the QCI threshold equal to 6 mm 6h^{-1} appears to lead to more accurate precipitation analyses than using other QCI thresholds.

To further explain the impact of the QCI thresholds, we compare six-hour precipitation analyses of experiments A_OL, A_QCI4, A_QCI6, A_QCI8, and A_QCI10 with the observations from the reference NCEP Stage IV dataset over three selected periods (Figure 3.4), with the MAE of each period reported in Table 3.3. In cycles 2 and 8, it can be seen that overestimated precipitation relative to the reference in the assimilation experiments occurs mainly when using the default QCI threshold (see the blue arrows in Figures 3.4f

Table 3.3: Five-day domain mean values of the precipitation observations from the reference NCEP stage IV dataset and the precipitation analyses of various experiments; and the mean absolute error (MAE) of six-hour simulated precipitation relative to observed precipitation with respect to the comparison in Figure 3.4.

	Reference	A_OL	A_QCI4	A_QCI6	A_QCI8	A_QCI10
5d domain mean (mm)	20.36	25.21	16.62	16.48	18.53	21.48
MAE in Cycle 03	-	1.93	1.38	1.24	1.25	1.28
MAE in Cycle 02	-	2.01	1.56	1.58	1.91	2.71
MAE in Cycle 08	-	1.20	0.70	0.61	0.67	0.79

and 3.4l), which was also reported in Chapter 2. The issue of summertime precipitation overestimation appears to be mitigated when a relatively small QCI threshold is used. Furthermore, Figures 3.4m-r provide an example in which an observed small-scale heavy precipitation is not captured in any WRF experiments. The results provide evidences why the experiment A_QCI6 leads to better precipitation analyses shown in Figure 3.3. However, it is noted that even though more accurate six-hour precipitation analyses of 36-km resolution can be produced using the QCI threshold 6 mm 6h^{-1} in terms of MAE and correlation, the five-day domain mean of experiment A_QCI6 is underestimated (see Table 3.3). In contrast, the experiment A_QCI10 shows in close agreement with the reference in terms of five-day domain mean, which is likely due to the averaging of over- and under-estimated locations.
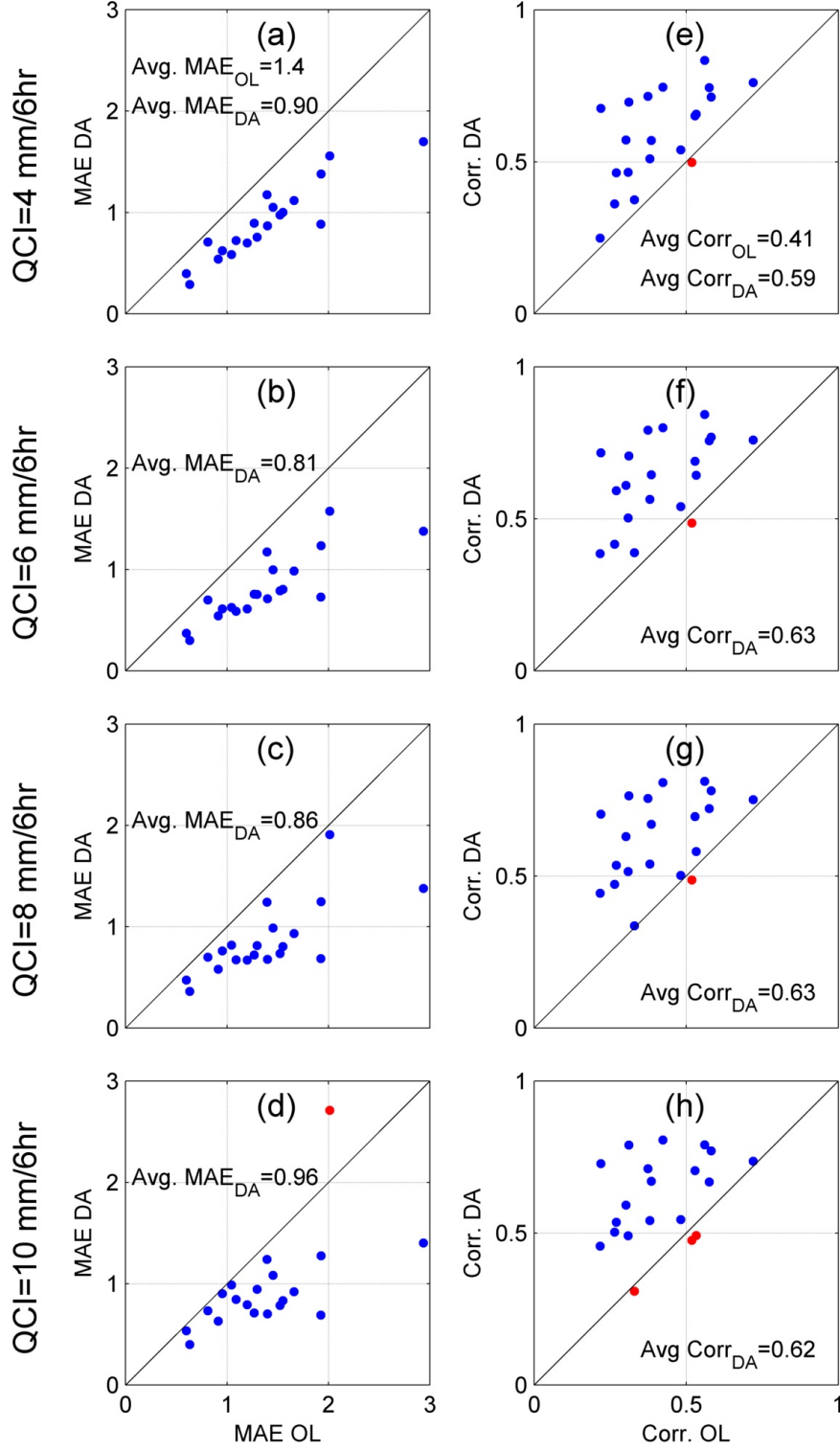
Figure 3.3: The comparison of metrics MAE and correlation of six-hour simulated precipitation at a resolution of 36 km from experiments A_OL, A_QCI4, A_QCI6, A_QCI8, and A_QCI10 relative to six-hour observed NCEP Stage IV precipitation at the same resolution. Blue dots denote a six-hour cycle in which the data assimilation experiment outperforms the open-loop experiment.
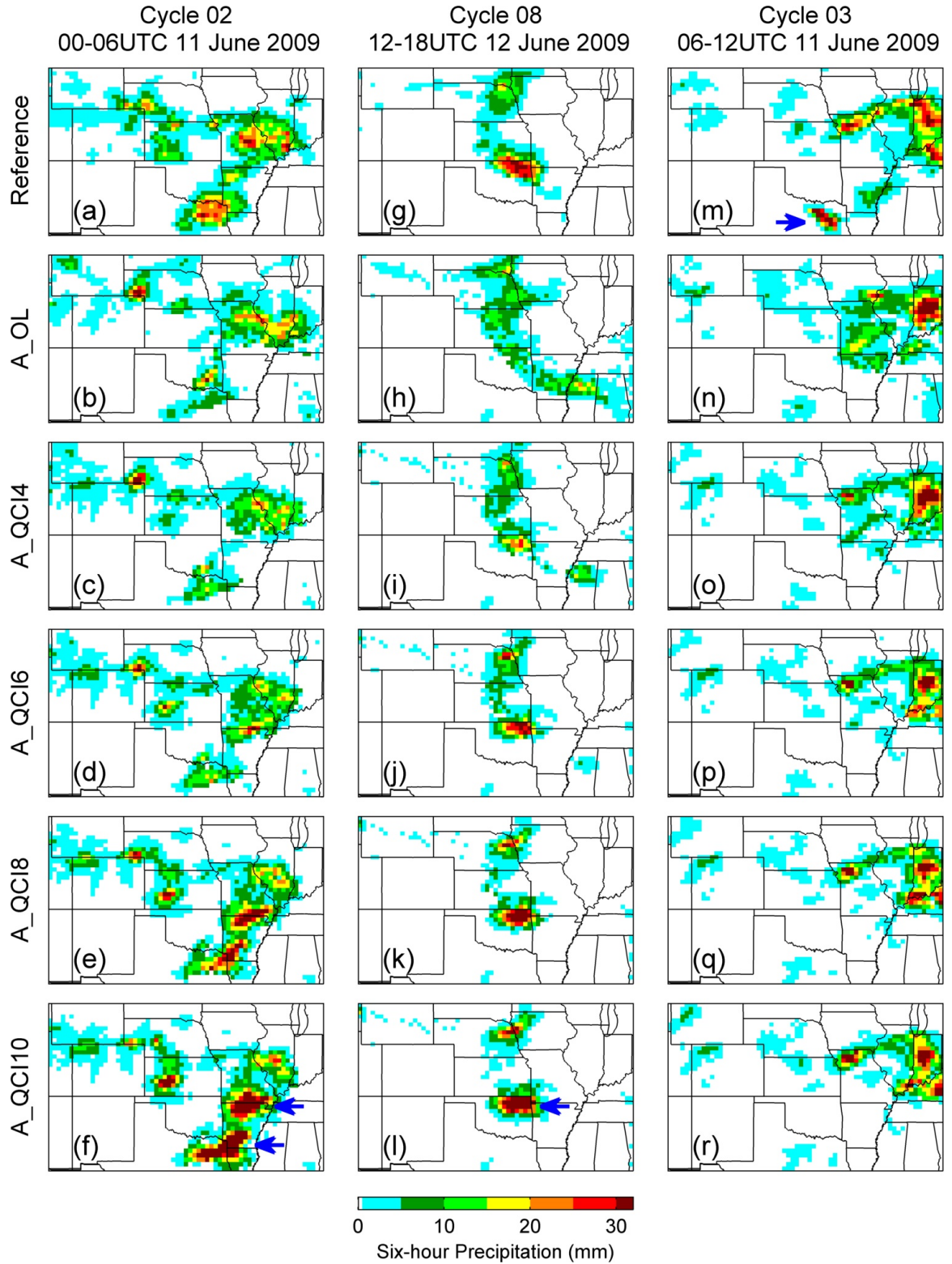
Figure 3.4: Six-hour precipitation distribution of the reference NCEP stage IV and experiments A_OL, A_QCI4, A_QCI6, A_QCI8, and A_QCI10 during three selected periods. Blue arrows denote the areas of interest with descriptions in the texts. The corresponding statistics are reported in Table 3.3

For experiments A_QCI6 and A_QCI10, Figure 3.5 compares the assimilated observations and six-hour precipitation integration produced by the tangent-linear model at the last 4D-Var optimization iteration with the corresponding analyses, open-loop forecasts, and the reference during 00-06UTC 11 June 2009 (cycle 02). Note that grid spacing in Figures 3.5c-d and 3.5f-g is 20 km while that in Figures 3.5a-b, 3.5e, and 3.5h is 36 km. By looking at the gray-color shaded pixels in Figures 3.5c and 3.5f, we can see that the A_QCI6 experiment rejects substantially more observations than the A_QCI10 experiment. For those pixels with assimilated observations, it seems that even though different QCI thresholds are used, the six-hour precipitation produced by the tangent-linear model of both the A_QCI6 and A_QCI10 experiments (Figures 3.5d and 3.5g) represent well the observations (Figures 3.5c and 3.5f). However, even if the same state analyses are used, the distribution and intensity of six-hour precipitation analyses produced by the WRF full-physics model are found to be significantly different when compared to those produced by the tangent-linear model, particularly for the A_QCI10 experiment (see Figures 3.5d-e and 3.5g-h). Similar phenomena can be seen during 12-18UTC 12 June 2009 (cycle 08; Figure 3.6) but not during 06-12UTC 11 June 2009 (cycle 3; Figure 3.7). The results suggest that the discrepancy between the linearized model and the full WRF physics model exists, and that discrepancy becomes obvious when a large QCI threshold is used. We suspect that the discrepancy could be a limitation of the WRF 4D-Var system in further improving the accuracy of the precipitation analysis and downscaling. In addition, we observe the occurrence of negative tangent-linear model precipitation estimates, the areas with which often correspond to the areas with zero-rain in the final six-hour precipitation analyses using WRF full physics (not shown). The magnitude of negative values in the A_QCI10 experiment is larger on average than that in the A_QCI6 experiment. Additional research is necessary to understand this situation. As we found that using a relatively small QCI threshold (6 mm 6hr^{-1}) produces precipitation with a smaller MAE and a higher correlation against the reference than using the default threshold (10 mm 6hr^{-1}), below we use only the threshold of 6 mm 6hr^{-1}.
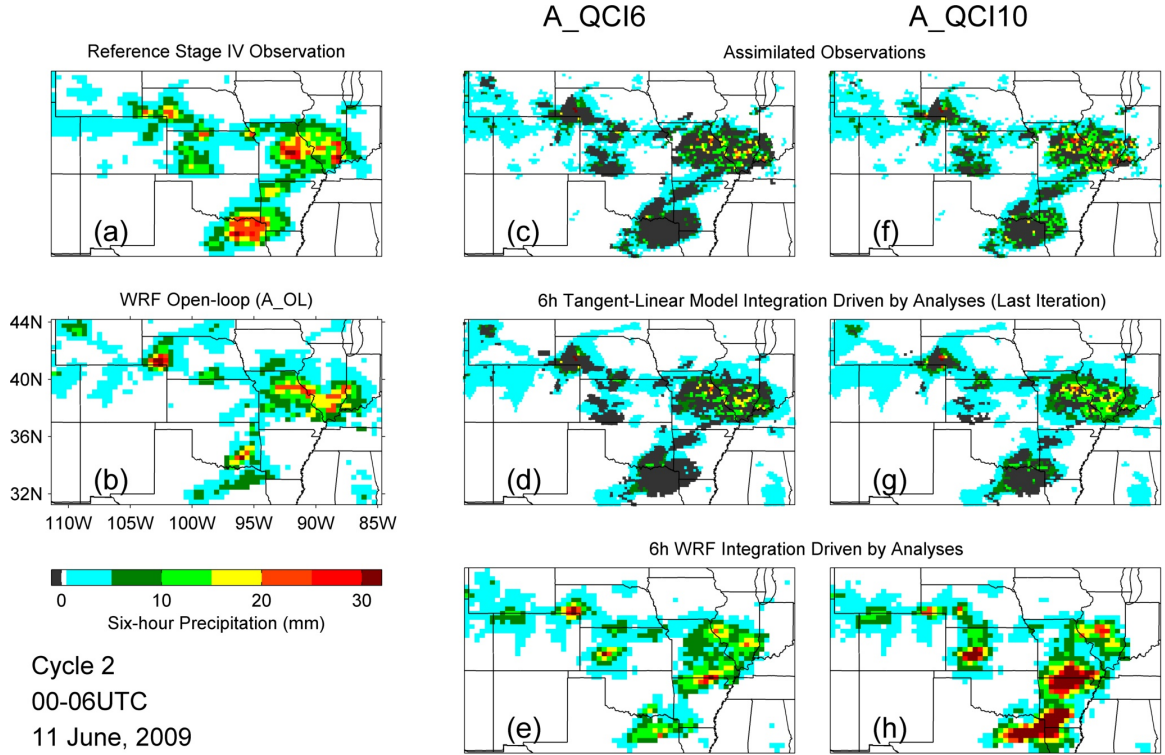
Figure 3.5: Six-hour precipitation distribution from the references NCEP stage IV (a; at a resolution of 36 km), experiment A_OL (b; 36 km), assimilated NCEP stage IV observations (c,f; 20 km), tangent-linear model integration driven by the final state analysis at the last optimization iteration (d,g; 20 km), and WRF precipitation analysis (e,h; 36 km) valid at 06UTC 11 June 2009 (cycle 2). Results of experiments A_QCI6 and A_QCI10 are reported subplots c-e and f-h, respectively. Grey grids denote areas where observations are not used in the optimization process due to the quality control procedure.
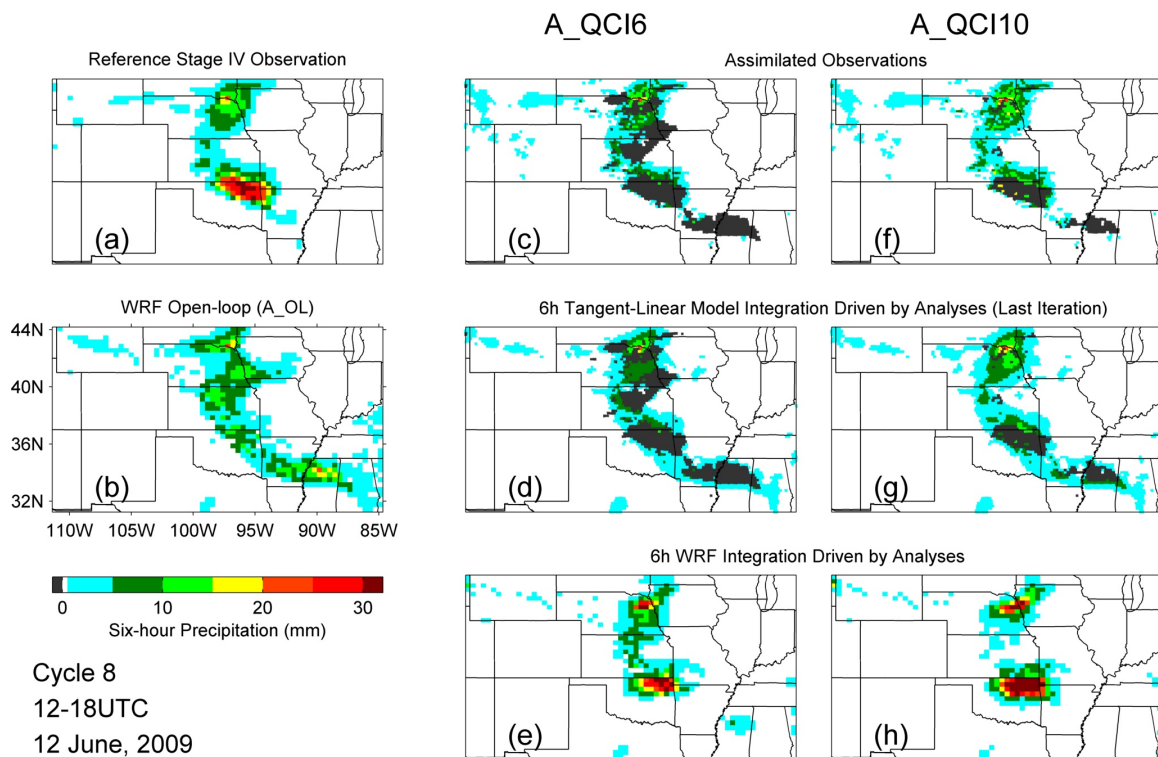
Figure 3.6: Same as Figure 3.5, except for cycle 8 during 12-18UTC 12 June, 2009.
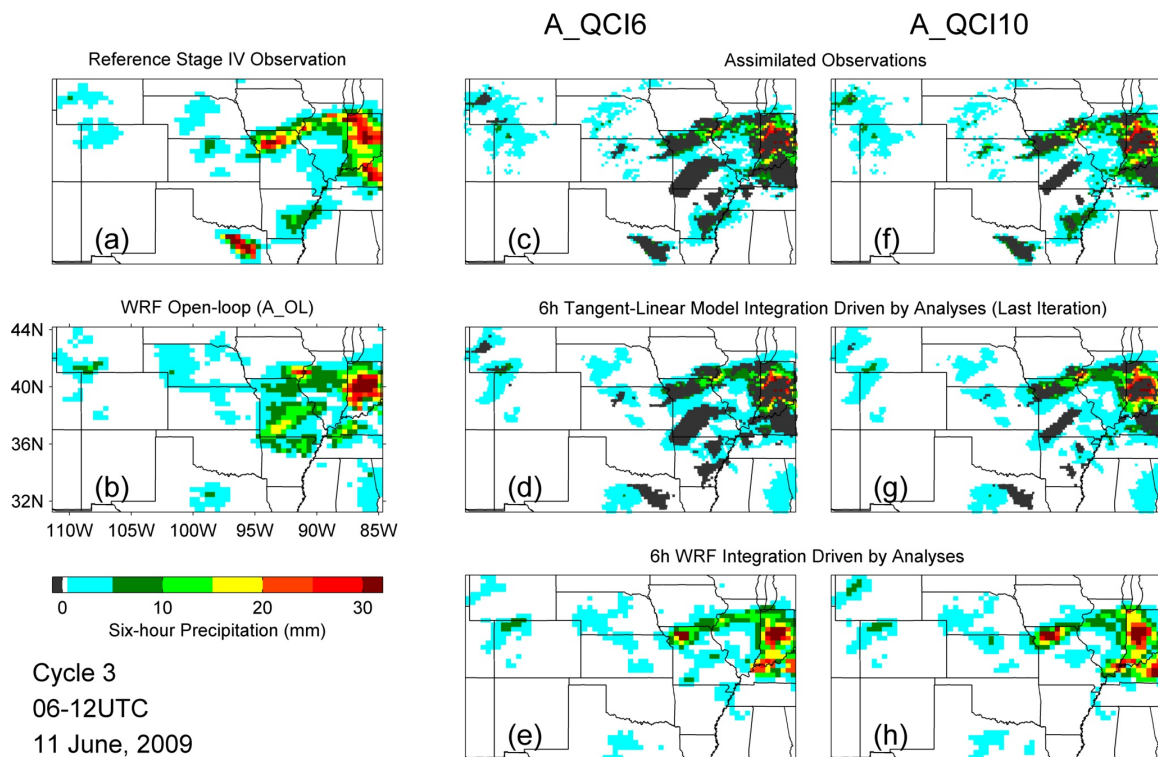
Figure 3.7: Same as Figure 3.5, except for cycle 3 during 06-12UTC 11 June, 2009.

3.3.2 Assimilation of TRMM Data versus Assimilation of NCEP Stage IV Data

In this subsection, we assess the assimilation of TRMM 3B42 precipitation assimilation along with the NCEP Stage IV precipitation assimilation and the benefits of assimilated TRMM observations in the inner domains. Figure 3.8 compares the 10-day precipitation accumulation at a resolution of 36 km from the reference NCEP Stage IV dataset, the TRMM 3B42 dataset, and the B_OL, B_ST4 and the B_TRMM experiments. The figure also includes the computed bias, MAE, and correlation coefficient of the precipitation fields in Figures 3.8b-e with respect to those in Figure 3.8a. During the summer, the TRMM 3B42 data show in a close agreement with the reference. The B_OL experiment produces over-estimated precipitation estimates with the largest MAE and the smallest correlation. In contrast, even though underestimated, the precipitation estimates from both B_ST4 and B_TRMM experiments are in closer agreement with the reference in terms of the MAE and the correlation than those from the B_OL experiment. The performance of experiments B_ST4 and B_TRMM is comparable and similar. However, the 10-day precipitation estimates from the B_ST4 and B_TRMM are still not as good as those of TRMM 3B42 dataset, which may be attributed to the discrepancy between WRF physics and its linearized representation reported in Section 3.3.1.

Figure 3.9 shows the MAE and correlation metrics of six-hour precipitation estimates at a resolution of 36 km from the B_OL, B_TRMM, and B_ST4 experiments and the TRMM dataset against those of the reference NCEP Stage IV. This comparison of six-hour precipitation at 36-km resolution re-affirms that precipitation estimates from the B_TRMM and B_ST4 experiments are comparable and improved compared those of the open-loop experiment but not as good as the TRMM 3B42 dataset. In addition, we observe that the B_OL experiment often produces overestimated precipitation during the afternoon times (i.e., cycles 4, 8, 12, ..., 40 occurring at 18-24UTC), reflected as a high MAE during those times in Figure 3.9a. During those times, data assimilation often leads to a significant reduction of the MAE for both experiments B_TRMM and B_ST4. This reduction is likely attributed to the effectiveness of the WRF 4D-Var system in mitigating false alarms
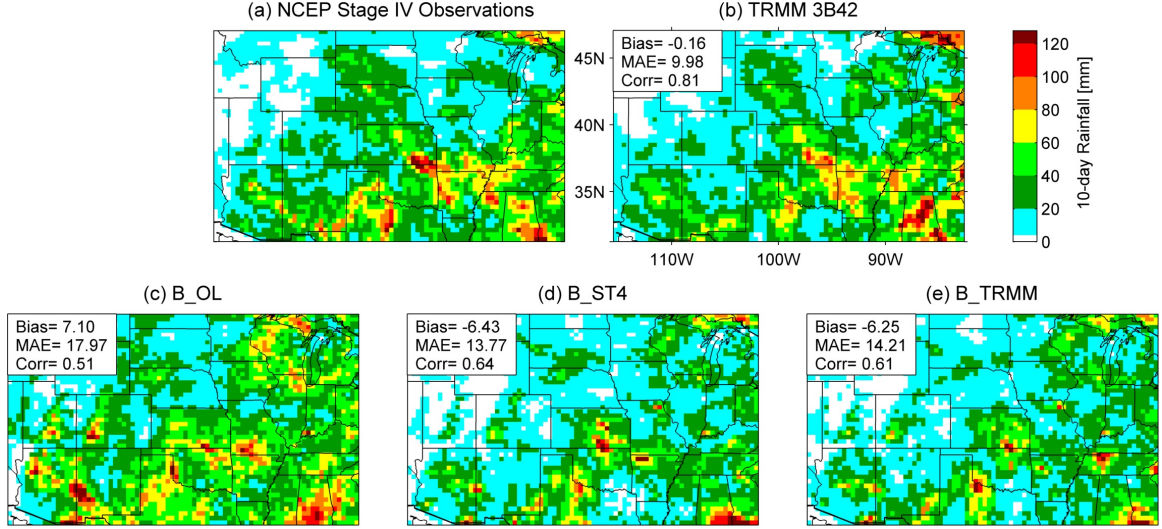
Figure 3.8: 10-day precipitation distribution at a resolution of (a) 36 km of the reference NCEP stage IV, (b) TRMM 3B42 dataset, (c) experiment B_OL, (d) experiment B_ST4, and (e) experiment B_TRMM. The bias, MAE, and correlation metrics are calculated according to the precipitation fields in subplots b-e relative to the fields in subplot a.

or overestimation, reported in Chapter 2.

Similar to Figure 3.9, Figures 3.10 and 3.11 show the comparison at a resolution of 12 and 4 km, respectively. These three figures demonstrate that the benefit of precipitation data assimilation is properly propagated into the middle domain but not seen in the inner-most domain. The assimilation of NCEP Stage IV (TRMM) precipitation leads to MAE reductions by 31%, 21%, and -2% (27%, 18%, and 0%) for the precipitation estimates at resolutions of 36, 12, and 4 km, respectively. To produce better fine-scale (i.e., 1 to 5 km) precipitation analyses, we suggest to (1) perform data assimilation at even finer domain resolutions than 36 km, (2) include other types of observations such as satellite radiances or soil moisture (see Chapter 4), or (3) assimilate observations of finer spatiotemporal resolutions. In light of recently-launched missions, the Global Precipitation Measurement (GPM; *Hou et al.* (2014)) and the Soil Moisture Active Passive (SMAP; *Entekhabi et al.* (2010)), further investigation of the WRF 4D-Var system is encouraged.
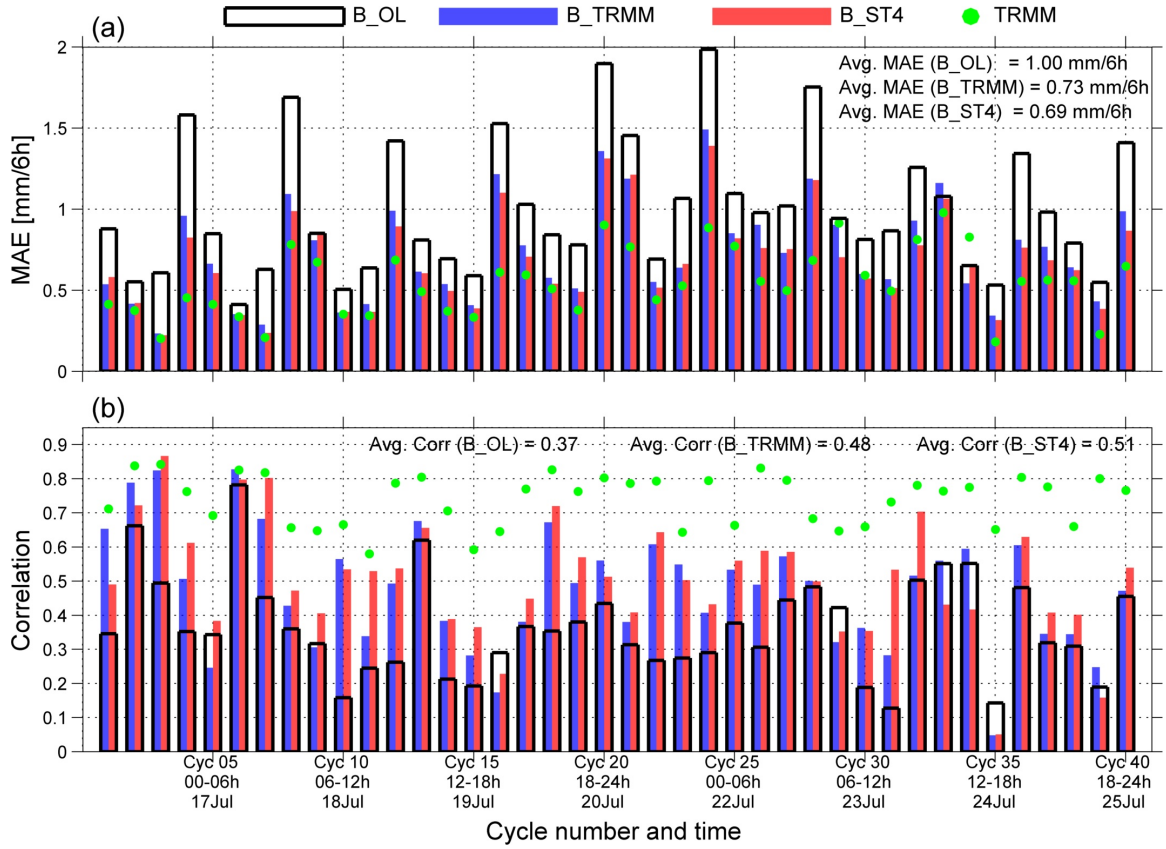
Figure 3.9: The reported mean absolute error (MAE; a) and correlation (b) of six-hour precipitation at a resolution of 36 km (the outermost domain) from experiments B_OL (black-edge-line bars), B_TRMM (blue bars) and B_ST4 (red bars) and TRMM 3B42 dataset (green dots) relative to that from the reference NCEP stage IV dataset. Average statistics from all 40 cycles are also reported.
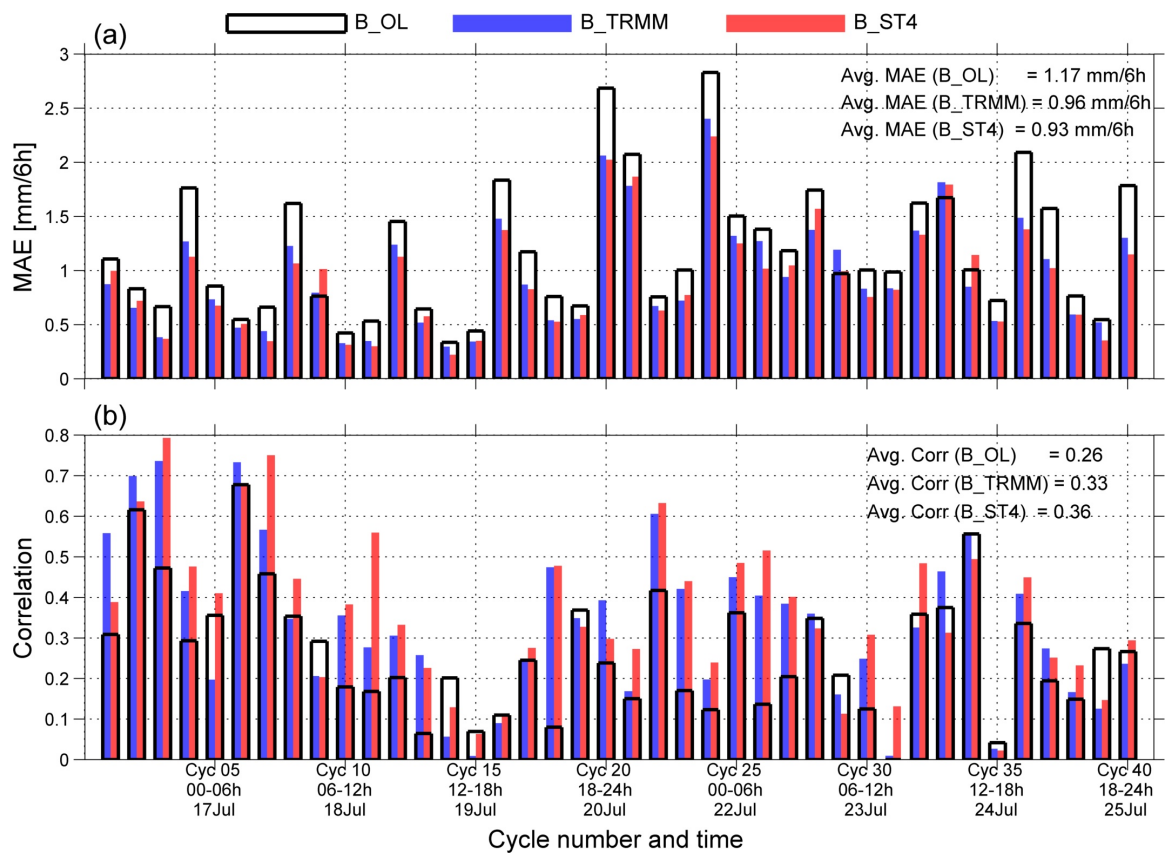
Figure 3.10: Same as Figure 3.9, except for the comparison at a resolution of 12 km (the middle domain) without the TRMM dataset.
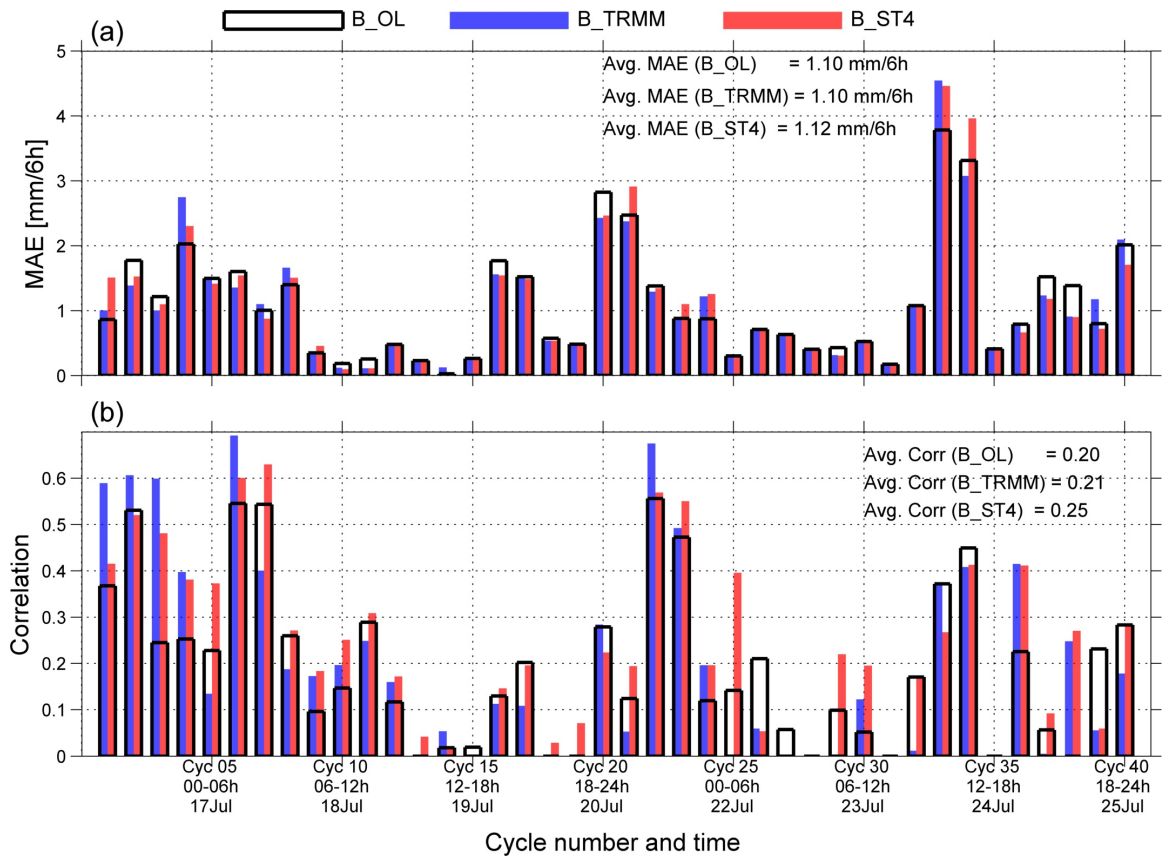
Figure 3.11: Same as Figure 3.9, except for the comparison at a resolution of 4 km (the innermost domain) without the TRMM dataset.

3.3.3 Score Analysis of Six-Hour Precipitation Analysis

In this subsection, we present the score analysis of the ETS, FAR, and BS of the B_OL and B_TRMM experiments to provide insights of TRMM precipitation data assimilation. Figure 3.12 shows the score calculated according to the six-hour precipitation analyses of 36-km resolution during 16-26 July 2013 within the region of interest (see the yellow region in Figure 3.1c). The ETS demonstrates that assimilation of TRMM precipitation observations is useful in providing better six-hour precipitation analyses (Figure 3.12a). The FAR points out that such assimilation is particularly useful in false alarm reduction. However, the assimilation of TRMM 3B42 data often leads to an underestimation, while the open-loop WRF forecasts are overestimated, particularly for a BS threshold less than 10 mm 6h^{-1} (figure 3.12c).

Since the mechanism of summertime precipitation occurrence may be different sub-diurnally, we present a similar score analysis but for four times (i.e., 00-06, 06-12, 12-18, and 18-24 UTC) to characterize the performance of precipitation assimilation at different times (Figure 3.13). Note that below we include the Central Standard Time in brackets to show the corresponding local time information. First, as the gap between the ETS of the B_TRMM experiment and that of the B_OL experiment during 06-18UTC is much larger than the gap during other times, the ETS demonstrates that precipitation assimilation is particularly useful during 06-18UTC (midnight to noon local time). In addition, it can
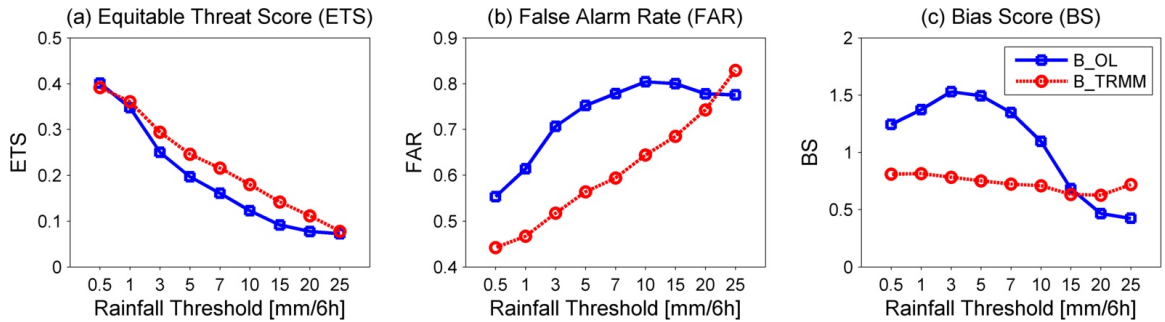
Figure 3.12: The equitable threat score (a), false alarm rate (b), and bias score (c) computed according to the six-hour simulated precipitation at a resolution of 36 km from experiments B_OL and B_TRMM relative to the six-hour observed precipitation from NCEP stage IV dataset with various precipitation thresholds in mm 6h-1 during 16-25 July 2013.
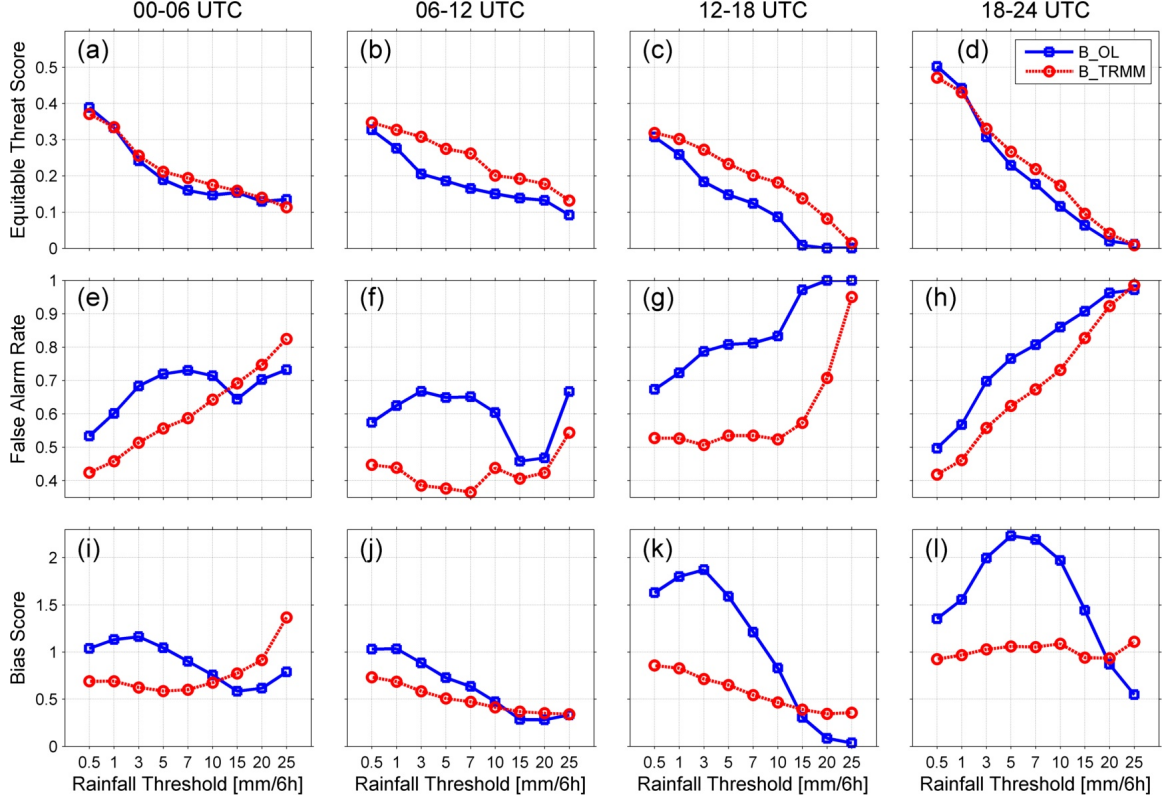
Figure 3.13: Same as Figure 3.12, except the score analyses are separated into four time periods 00-06, 06-12, 12-18, and 18-24UTC for the ETS (a-d), FAR (e-h), and BS (i-l).

be seen that throughout various times, the WRF 4D-Var system is effective in reducing falsely-estimated precipitation. However, assimilation of TRMM data often leads to underestimation except during 18-24UTC (local afternoon time, 12-6 p.m.), while open-loop overestimation is significant during 12-24UTC (local day time, 6 a.m. to 6 p.m.).

3.3.4 Forecast Skills

Above we mainly analyzed the impact of precipitation data assimilation within the assimilation window. In this subsection, we present the results from the B_OL_24 and B_TRMM_24 experiments to quantify the impact of TRMM data assimilation on one-day precipitation forecasts. Figure 3.14 shows the MAE of six-hour precipitation estimates of 36-km resolution initialized during 16-24 July 2013 with various leading times from the experiments relative to six-hour observations from the reference NCEP Stage IV dataset.

As is evident, the benefit of assimilated TRMM data is quickly lost beyond the six-hour as-similation window. The loss of information can also be seen in the computed correlation of model precipitation against the reference precipitation (Figure 3.15). Figure 3.16 compares the ETS, FAR, and BS of the B_OL_24 and B_TRMM_24 experiments with different precipitation thresholds. The ETS and FAR indicate that beyond the assimilation window, the impact of TRMM data assimilation is marginal. In terms of the BS, the B_TRMM_24 experiment produces nearly as much precipitation as the B_OL_24 experiment after 12 hours (see Figures 3.16i-j).

3.4   Summary of the Chapter

Assimilation of cloud- or precipitation-affected data into the national weather prediction (NWP) system is critical for improving precipitation predictions, but several issues related to model parameterization and resolution remain. To better understand those issues on a regional scale, this chapter uses the Weather Research and Forecasting (WRF) four-dimensional variational data assimilation (4D-Var) system to directly assimilate rainfall retrievals and conducts a series of numerical experiments with a focus on summertime precipitation analyses and forecasts at high resolutions (e.g., 36/12/4 km and six hourly). The rain retrievals used in the experiments include six-hour precipitation accumulations from the upscaled 20 km×20 km National Centers for Environmental Prediction (NCEP) Stage IV and $0.25°×0.25°$ Tropical Rainfall Measuring Mission (TRMM) 3B42 data sets. The study identified a discrepancy between six-hour precipitation integration from the WRF full-physics model and that from the linearized model used in the 4D-Var algorithm. Such discrepancy is sensitive to the quality control threshold for removing observation outliers during the summer and likely to limit the model performance in precipitation analysis, forecast, and downscaling. Assimilation of TRMM observations into a model space at a resolution 36 km is able to improve six-hour precipitation analyses at a resolution of 36 and 12 km by 27% and 18%, respectively, measured by the mean absolute error, but has little impact at a 4-km resolution. Nevertheless, the benefits of assimilated TRMM observations are quickly lost beyond the six-hour assimilation window.
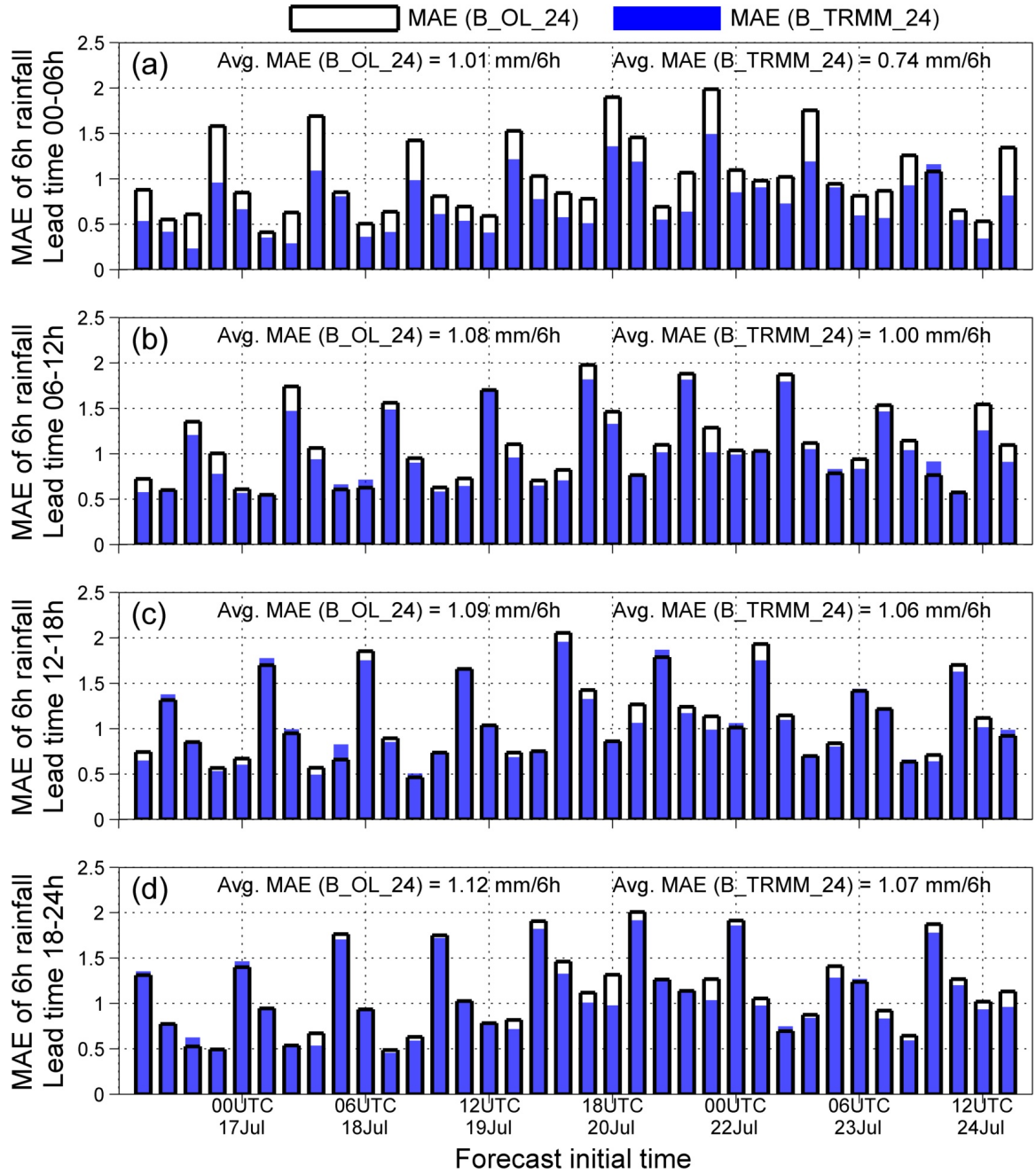
Figure 3.14: The MAE of six-hour simulated precipitation at a resolution of 36 km from experiments B_OL_24 and B_TRMM_24 with various lead times relative to the reference NCEP stage IV dataset.
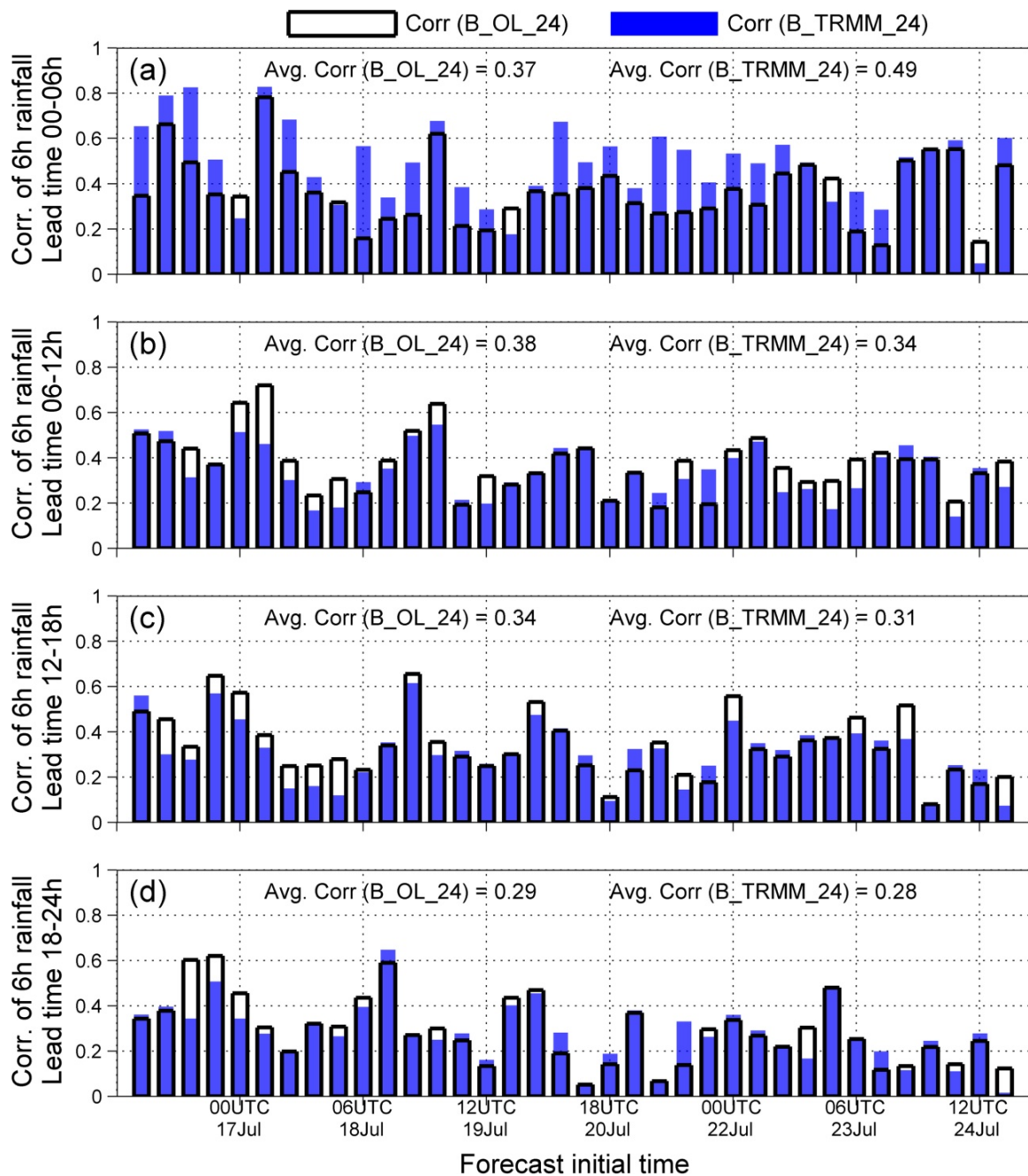
Figure 3.15: Same as Figure 3.14, except for the correlation comparison.
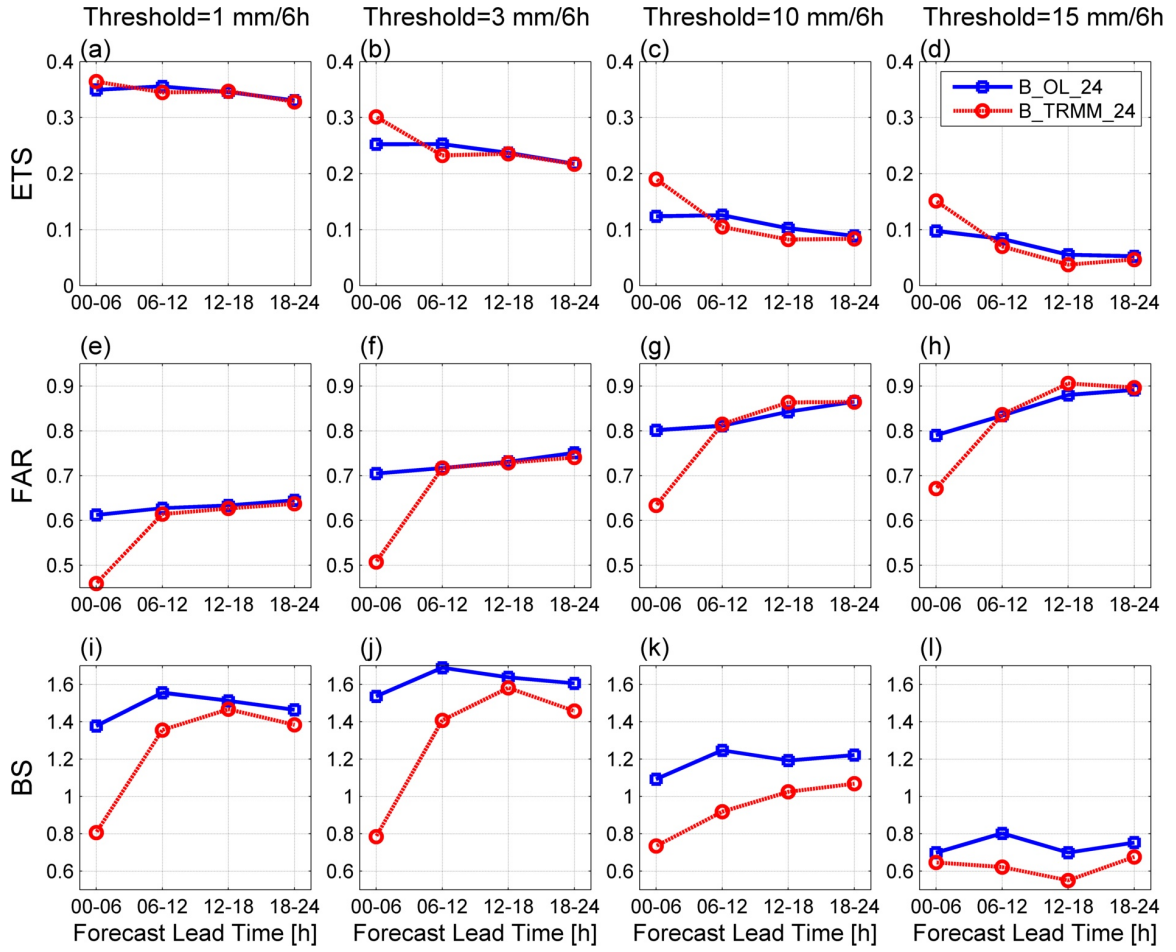
Figure 3.16: The ETS (a-d), FAR (e-h), and BS (i-l) computed based on six-hour precipitation forecasts at a resolution of 36 km of experiments B_OL_24 and B_TRMM_24 relative to six-hour precipitation observations from the NCEP stage IV dataset with various precipitation thresholds.

CHAPTER IV

SOIL MOISTURE BACKGROUND ERROR COVARIANCE AND VARIATIONAL DATA ASSIMILATION

This chapter describes the development of a soil moisture data assimilation system using a land-atmosphere coupled model, WRF-Noah, and presents a one-month experiment over the contiguous United States by assimilating Soil Moisture and Ocean Salinity (SMOS) soil moisture retrievals. The development is in preparation for the joint data assimilation applications of precipitation and soil moisture that will be discussed in Chapter 5. The rest of the chapter are organized as follows. Section 4.1 provides literature review relevant to soil moisture data assimilation and states the goals of the chapter. Section 4.2 briefly explains the WRF and Noah land surface model. In Section 4.3, we present the formulation of the data assimilation system. The spatiotemporal properties of the soil moisture background error and its climatological variability are presented in Section 4.4. Section 4.5 discusses a case study of data assimilation experiments using SMOS data. Section 4.6 summarizes this chapter. The work presented in this chapter is described in *Lin et al.* (2016) in revision and the text comes from that source.

4.1 Introduction

Soil moisture is key to land-atmosphere interactions. Surface soil moisture markedly impacts land-surface emissivity, especially in microwave bands (*Grody*, 1988). This affects weather forecasts through its impacts on radiative transfer modeling and radiance data assimilation systems. Numerous studies using mesoscale weather forecasting models have also shown that the prediction of precipitation is sensitive to the soil moisture variability (*Sutton et al.*, 2006; *Aligo et al.*, 2007; *Trier et al.*, 2008; *Hohenegger et al.*, 2009; *Quintanar and Mahmood*, 2012; *Zaitchik et al.*, 2013).

The two most common methods of data assimilation are variational and filtering approaches (see *Ebtehaj et al.* (2014)). The former typically uses a static background error

covariance matrix and minimizes a cost function to assure that the analysis state is close to both observation and background state. The latter uses a time-varying forecast error covariance matrix to recursively assimilate observations into the model. A majority of land surface data assimilation systems relies on ensemble filtering methods (e.g., EnKF: the ensemble Kalman filter), which use a Monte Carlo approach for estimating the background error covariance. In light of the availability of remotely-sensed soil moisture data (*Dorigo et al.*, 2012), many studies have shown improved simulations by assimilating satellite-based soil moisture observations into land surface models (*Reichle and Koster*, 2005; *Reichle et al.*, 2007, 2008a; *Kumar et al.*, 2009; *Liu et al.*, 2011; *Peters-Lidard et al.*, 2011; *Draper et al.*, 2012; *Flores et al.*, 2012; *Li et al.*, 2012; *Sahoo et al.*, 2013; *Yin et al.*, 2014). However, most of the previous studies focused on an off-line data assimilation scheme using a land surface model not coupled with an atmospheric model.

Atmospheric data assimilation studies often use variational approaches, which require accurate estimation of the background error covariance. The background field, also known as the "first guess" or the "prior information," is often derived from short-range forecasts (*Daley*, 1991; *Kalnay*, 2003). *Parrish and Derber* (1992) estimated the background error with the difference between forecasts with different lead times but valid at the same time (see an example in Figure 4.1). This procedure, known as the National Meteorological Center (NMC) method, has been adopted in global operational data assimilation systems of the National Centers for Environmental Prediction (NCEP) and the United Kingdom's Met Office for estimating the background error of primary control variables such as the stream function, velocity potential, temperature, pressure, and relative humidity (*Parrish and Derber*, 1992; *Lorenc et al.*, 2000; *Ingleby*, 2001; *Wu et al.*, 2002). The NMC method is also used in the Weather Research and Forecast (WRF) model data assimilation (WRFDA) system (*Barker et al.*, 2004, 2012; *Huang et al.*, 2009), in which the background error is obtained using the difference between 12- and 24-hour forecasts initialized 12 hours apart for regional-scale simulations (Figure 4.1). Climatological estimates of the atmospheric background error covariance, using the NMC method, have been widely used in many data assimilation studies (*Barker*, 2005; *Zhang et al.*, 2006; *Meng and Zhang*, 2007, 2008; *Wu*
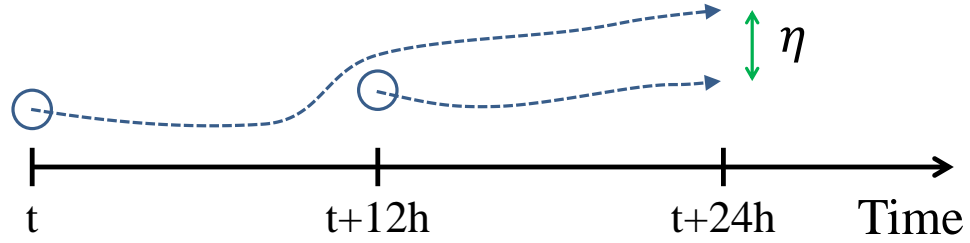
Figure 4.1: Schematic diagram of the National Meteorological Center (NMC) method showing the forecast error (η) between forecasts with 12- and 24-hour leading times

et al., 2010; *Rakesh and Gowsami*, 2011; *Liu et al.*, 2012a, 2013). However, as soil moisture is not commonly considered a control variable in atmospheric data assimilation systems, its direct assimilation has not yet been thoroughly studied in the global and regional weather models.

In this work, we develop a variational data assimilation system for direct assimilation of soil moisture using the WRF model with the Noah land surface scheme. Unlike recent studies using ensemble filtering for soil moisture data assimilation with a coupled model (*Rasmy et al.*, 2012; *Williams et al.*, 2013; *Schneider et al.*, 2014), this study has the following unique features: (1) estimation of spatiotemporally-varying soil moisture background error covariance using the NMC method and (2) development of a one-dimensional variational data assimilation (1D-Var) scheme to assimilate remotely-sensed soil moisture retrievals into the WRF-Noah model. We use the NCEP final analysis (FNL) dataset to derive the initial conditions for the WRF-Noah model. Note that the accuracy and applicability of our analyses are certainly subject to the selected models and datasets. To our knowledge, no previous research has studied the variability of the soil moisture background error covariance to the extent that we do in this work. We identify an apparent discrepancy between the soil moisture estimates of the NCEP FNL data and those of our WRF-Noah experiments, which is significant over the Southeastern United States. The sensitivity of the soil moisture background error to the WRF physics parameterizations is also investigated. It is shown that the assimilation of soil moisture data from the Soil Moisture Ocean Salinity (SMOS) satellite with a space-time varying background error can significantly improve hourly soil

moisture simulations at a resolution of 4 km while have a marginal impact on the quality of precipitation modeling.

4.2 WRF-Noah Model

This study uses WRF version 3.4, compiled with the GNU compiler 4.4.5. Brief model description can be found in Section 2.2, while detailed documentation can be see in *Skamarock et al.* (2008). To provide land surface heat and moisture fluxes, the land surface models need to communicate with different modules and schemes in the WRF model. In particular, the land surface models are forced with atmospheric boundary conditions, downward radiation fluxes, and precipitation supplied by the schemes of the surface layer, radiation, and microphysics and sub-grid convections, respectively. In WRF version 3.4, the available land surface models include the MM5 5-layer soil temperature model, the Noah model, the rapid update cycle (RUC) model, and the Pleim-Xiu model. Among these models, the Noah model simulates soil moisture at four consecutive soil layers, with 10-, 30-, 60-, and 100-cm thickness from top to bottom. Given the initial conditions such as soil moisture content and temperatures and information of vegetation, land-use, and soil texture, the Noah model provides heat and moisture fluxes throughout the soil column by numerically solving the governing heat and moisture transport equations (*Chen and Dudhia*, 2001). In the Noah model, soil evaporation only takes places in the top soil layer, while moisture uptake due to plant transpiration is parametrized throughout the three uppermost soil layers.

4.3 Implementation of 1D-Var

4.3.1 1D-Var Algorithm

This study uses a 1D-Var assimilation system to find the optimal estimate (or analysis state) of the soil moisture profiles throughout the soil column, by minimizing the following cost function $\mathcal{J}(\mathbf{x})$ (*Lorenc*, 1986; *Ide et al.*, 1997):

$$\mathcal{J}(\mathbf{x}) = \frac{1}{2}(\mathbf{x} - \mathbf{x}^b)^T \mathbf{B}^{-1}(\mathbf{x} - \mathbf{x}^b) + \frac{1}{2}\left(\mathbf{y}^o - H(\mathbf{x})\right)^T \mathbf{R}^{-1}\left(\mathbf{y}^o - H(\mathbf{x})\right), \qquad (4.1)$$

where the m-element vectors $\mathbf{x}$ and $\mathbf{x}^b$ are the control and the background soil moisture state variables, respectively; $\mathbf{B}$ is an m-by-m background error covariance matrix; $\mathbf{y}^o$ is an

n-element observation vector; $H(\cdot)$ denotes the observation operator that maps the control state variables onto the observation space; and $\mathbf{R}$ is an n-by-n observation error covariance matrix. The cost function $\mathcal{J}(\mathbf{x})$ in Equation (4.1) has two components: one associated with the background error covariance matrix $\mathbf{B}$ and the other one with the observation error covariance matrix $\mathbf{R}$. The structure of the $\mathbf{B}$-matrix depends on the model error which often exhibits space-time variability. In practice, the $\mathbf{R}$-matrix is generally considered to be diagonal and space-time invariant.

Equation (4.1) can be reformulated in an incremental form as follows (*Courtier et al.*, 1998):

$$\mathcal{J}(\delta\mathbf{x}) = \frac{1}{2}\delta\mathbf{x}^T\mathbf{B}^{-1}\delta\mathbf{x} + \frac{1}{2}\left(\mathbf{d} - \mathbf{H}\delta\mathbf{x}\right)^T\mathbf{R}^{-1}\left(\mathbf{d} - \mathbf{H}\delta\mathbf{x}\right), \tag{4.2}$$

where $\delta\mathbf{x} = \mathbf{x} - \mathbf{x}^b$ is the analysis increment, $\mathbf{d} = \mathbf{y}^o - H(\mathbf{x}^b)$ is the innovation (observational increment), and $\mathbf{H}$ is the Jacobian of the observation operator. Setting the gradient of the cost function $\mathcal{J}(\delta\mathbf{x})$ with respect to $\delta\mathbf{x}$ to zero (i.e., $\nabla_{\delta\mathbf{x}}\mathcal{J}(\delta\mathbf{x}) = 0$) leads to the following analysis state $\mathbf{x}^a$:

$$\mathbf{x}^a = \mathbf{x}^b + \mathbf{B}\mathbf{H}^T\left(\mathbf{H}\mathbf{B}\mathbf{H}^T + \mathbf{R}\right)^{-1}\mathbf{d}. \tag{4.3}$$

4.3.2 Background Error Covariance

This study uses the NMC method to compute the $\mathbf{B}$-matrix as the expected value of differences between 12- and 24-hour forecasts initialized 12 hours apart but valid at the same time as follows (Figure 4.1):

$$\mathbf{B}_b = \overline{\eta\eta^T} = \overline{\left[\mathbf{x}^f_{t+24|t} - \mathbf{x}^f_{t+24|t+12}\right]\left[\mathbf{x}^f_{t+24|t} - \mathbf{x}^f_{t+24|t+12}\right]^T}, \tag{4.4}$$

where η is the vector of forecast differences and the over-bar denotes the expectation operator. In the computation of the background error covariance, it is typically assumed that forecast differences are unbiased (*Bannister*, 2008). However, as pointed out by *Lorenc et al.* (2000), the calculation of the $\mathbf{B}$-matrix using Equation (4.4) does not explicitly account for potential biases. Without an explicit bias removal, bias can be deemed as a large-scale unknown error in the background error covariance, which may even lead to an improved performance of data assimilation from a practical standpoint. To quantify the biases in the

B-matrix, using the terminology by *Dee* (2005), we call $\mathbf{B}_b$ a bias blind estimate, while a bias-aware approximation is as follows:

$$\mathbf{B}_a = \overline{(\eta - \bar{\eta})(\eta - \bar{\eta})^T}, \tag{4.5}$$

where $\bar{\eta}$ is the expected value (bias) of η.

As $\mathbf{B}_a = \mathbf{B}_b - \bar{\eta}\bar{\eta}^T$, the diagonal elements of $\mathbf{B}_a$ are always less than or equal to those of $\mathbf{B}_b$. Note that a bias-aware estimate is more consistent with the statistical interpretation of the cost function in Equation (4.1), which assumes that the background error can be explained by a zero-mean normal distribution. In the context of the 1D-Var, this study estimates the background errors for all land grid cells of the study domain independently, without considering the impacts of the neighboring cells. Therefore, for the four-soil-layer Noah model, the estimated background error covariance matrix of each grid cell is a 4-by-4 matrix that can be decomposed as follows (*Ide et al.*, 1997; *Kalnay*, 2003; *Bannister*, 2008):

$$\mathbf{B} = \begin{bmatrix} \sigma_1 & 0 & 0 & 0 \\ 0 & \sigma_2 & 0 & 0 \\ 0 & 0 & \sigma_3 & 0 \\ 0 & 0 & 0 & \sigma_4 \end{bmatrix} \begin{bmatrix} 1 & \rho_{12} & \rho_{13} & \rho_{14} \\ \rho_{21} & 1 & \rho_{23} & \rho_{24} \\ \rho_{31} & \rho_{32} & 1 & \rho_{24} \\ \rho_{41} & \rho_{42} & \rho_{43} & 1 \end{bmatrix} \begin{bmatrix} \sigma_1 & 0 & 0 & 0 \\ 0 & \sigma_2 & 0 & 0 \\ 0 & 0 & \sigma_3 & 0 \\ 0 & 0 & 0 & \sigma_4 \end{bmatrix}, \tag{4.6}$$

where σ_1 to σ_4 are the standard deviations of error for soil layers from top to bottom, and ρ_{ij} denotes the cross-layer error correlation between layers i and j.

4.4 Computation of the Soil Moisture Background Error

In this section, we explain details of the NMC method for the estimation of monthly soil moisture background error and provide some insights into the space-time variability of the background error with respect to the spatial patterns of soil moisture and precipitation (Sections 4.4.2 and 4.4.3). We also discuss the bias characteristics, particularly over the Southeast United States, where the bias shows a large magnitude and variability (Section 4.4.4). The rest of this section is devoted to sensitivity analysis of the background error to different WRF physics options (Section 4.4.5).

4.4.1 Experiment Setup

We use one WRF domain (D01) configured with 149×79 grids of 36-km resolution (Figure 4.2a). Figure 4.2b gives the soil types over the domain based on the 1-km soil characteristics dataset from the United States Department of Agriculture's State Soil Geographic Database (*Miller and White*, 1998). The pressure level configuration and physics options used in this study are shown in Table 4.1 (see the column of main experiment). To generate initial and lateral boundary conditions for the WRF simulations, we employ the six-hour $1° \times 1°$ NCEP FNL operational global analysis dataset produced by the Global Data Assimilation System (GDAS) for the period of 2006 to 2013. This period is chosen because the NCEP FNL dataset prior to 2006 has only two soil layers, while the current configuration of the Noah model has four layers. We use all differences of 12- and 24-h forecasts, initialized at 0000 and 1200 UTC, for computing monthly climatological background error covariance matrices according to Equations (4.4) and (4.5). In addition, we conduct a sensitivity analysis to understand the effects of WRF physics on the soil moisture background error matrices during July 2013 by using various combinations of microphysics, cumulus parameterization, and land surface model schemes.

Table 4.1: Model configuration and physics schemes used in this study.

	Main Experiment (Sections 4.4.2-4.4.4 and 4.5)	Sensitivity Experiment (Sections 4.4.5)
General		
WRF version	3.4	3.4
Domain geometry		
Atmosphere top (hPa)	50	50
Vertical levels	41	41
Domain 01 (D01)		
Grid size	149×79	149×79
Grid resolution (km)	36	36
Only for the experiments in Section 4.5		
Domain 02 (D02)		
Grid size	210×150	-
Grid resolution (km)	12	-
Domain 03 (D03)		
Grid size	300×240	-
Grid resolution (km)	4	-
WRF model physics		
Microphysics	WRF single-moment 6-class (WSM6) scheme (*Hong and Lim*, 2006)	1. The scheme by Lin et al. (*Lin et al.*, 1983) 2. WRF single-moment 3-class (WSM3) scheme (*Hong et al.*, 2004) 3. WSM6 scheme 4. Goddard scheme (*Tao et al.*, 1989) 5. Thompson scheme (*Thompson et al.*, 2008)
Cumulus	Kain-Fritsch (*Kain*, 2004)	1. Kain-Fritsch scheme 2. Betts-Miller-Janjic scheme (*Janjic*, 1994, 2000) 3. Grell-3D scheme (*Grell and Devenyi*, 2002)
Land surface scheme	Noah model (*Chen and Dudhia*, 2001)	1. Noah model 2. Rapid Update Cycle model (*Smirnova et al.*, 2000)
Longwave radiation	Rapid Radiative Transfer Model (*Mlawer et al.*, 1997)	Rapid Radiative Transfer Mode
Shortwave radiation	Dudhia scheme (*Dudhia*, 1989)	Dudhia scheme
Surface layer	MM5 similarity	MM5 similarity
Planetary boundary layer	Yonsei University scheme (*Hong et al.*, 2006)	Yonsei University scheme
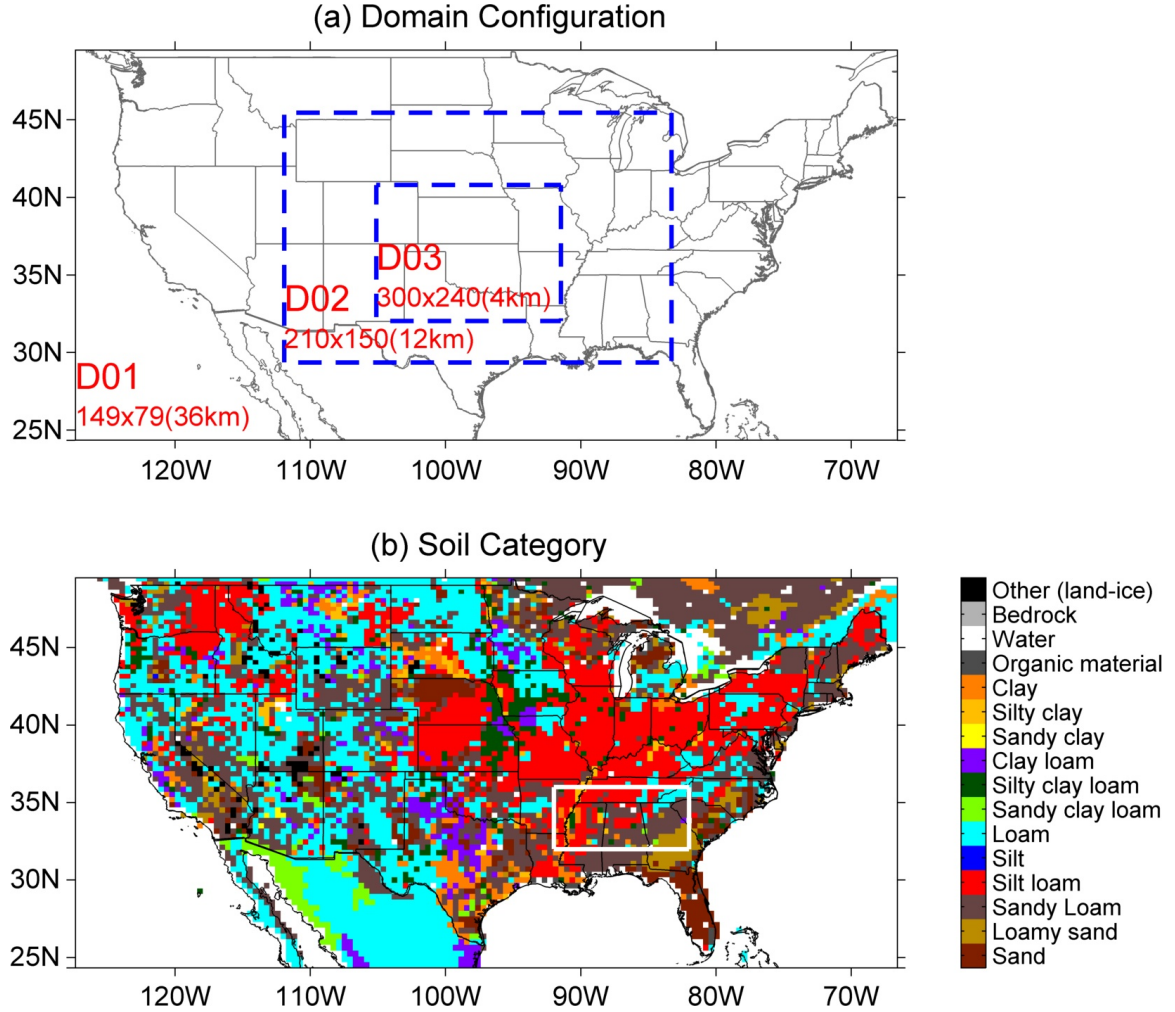
Figure 4.2: Top panel: three-nested study domain configuration, including an outermost domain (D01), a middle domain (D02), and an innermost domain (D03). Bottom panel: the dominant soil texture of the study domain. The white box denotes a region of interest used in Figure 4.13 for analyzing the biases in soil moisture background error.

4.4.2 Space-time Structure of the Background Error

Figure 4.3 shows monthly average soil moisture background error in calendar years 2010 to 2013 for January, April, July, and October. Specifically, the maps show the bias-blind standard deviation of the background error for the top-soil layer (i.e., the square root of the first diagonal element of $\mathbf{B}_b$). We can see that the monthly background error exhibits strong intra-annual space-time variability while the inter-annual variability is relatively weak. In January and April, large errors occur over the Pacific Coast Ranges where snow melting occurs and air temperature fluctuates around the freezing point. In July, large background
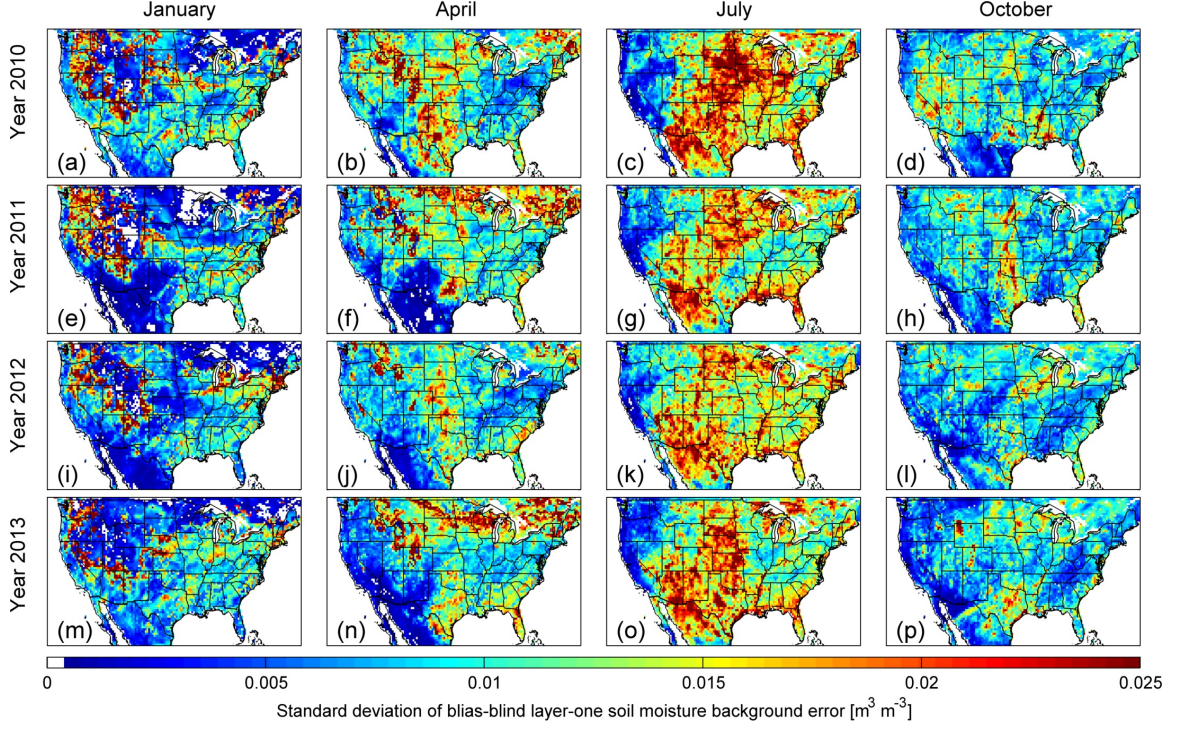
Figure 4.3: The bias-blind standard deviation of layer-one soil moisture background error in January, April, July, and October from years 2010 to 2013.

errors can be seen over a wide area, spreading from the Midwest through Colorado, Texas, New Mexico, Arizona, and Northern Mexico. The coherent spatial structure of monthly error justifies the use of spatially varying background error covariance on a monthly scale for variational soil moisture data assimilation. Estimates of the background error on a shorter timescale (e.g., weekly) may not be sufficiently accurate due to insufficient sample sizes. We empirically observed that the characterization of the background error on a weekly scale often results in incoherent patterns in the spatial structure of the error (not shown here). Therefore, throughout this section, we focus on a monthly average representation of the background error. Specifically, we study: (1) domain-average monthly values of the biases ($\overline{\eta}$) and error standard deviations and (2) spatial patterns of seasonal biases and error standard deviations for both $\mathbf{B}_a$ and $\mathbf{B}_b$.

Figure 4.4 shows the eight-year average values of domain-mean monthly biases (left column) and the bias-aware (σ_a) and -blind (σ_b) standard deviations of soil moisture background error (right column). Figures 4.4a-d show that the domain-mean bias is negative,

on average, in the upper three layers but is positive in the bottom layer. The absolute values of the bias do not differ substantially throughout the soil column, falling between 0.0005 and 0.002 [m^3 m^{-3}]. This behavior is mainly due to the initialization of WRF-Noah experiments (see Section 4.4.4 for more details). The monthly standard deviation values decrease from the top to bottom soil layers, consistent with the results of some previous studies (e.g., see Table 1 in *Kumar et al.* (2009)). This pattern seems also to align with the fact that the soil moisture exhibits more diurnal variability in surface layers than the bottom layers, which makes the simulations prone to larger errors. The results show a relatively constant bias and decreasing standard deviations from top to bottom layers. As a consequence, the gaps between the bias-aware and -blind background error increase in deeper soil layers (Figures 4.4e-f). Moreover, we can see strong seasonal variability in the background error with the largest values found during the summer in the two uppermost soil layers (Figures 4.4e and 4.4f). For better understanding the seasonal variability, we have to explore the spatial patterns of the background error.

Figures 4.5-4.8 show the spatial distribution of seasonal biases (a-d) and bias-blind (σ_b) and -aware (σ_a) standard deviations (e-l) of each Noah soil layer obtained from the eight-year WRF-Noah experiments. The maps show three notable spatial features. First, the bias is large over the Southeast United States, particularly during the winter and the spring (Figures 4.5a-b, 4.6a-b, 4.7a-b, and 4.8a-b), typically leading to a visible difference between σ_b and σ_a over this region (Figures 4.5e-f, 4.5i-j, 4.6e-f, 4.6i-j, 4.7e-f, 4.7i-j, 4.8e-f, and 4.8i-j). This pattern appears to be correlated with the spatial distribution of sandy loam soil type (see Figure 4.2b) and mainly caused by the initialization of the WRF-Noah model (see Section 4.4.4 for more details). Second, like in Figure 4.3, there are large background errors over the Pacific Coast Ranges during the winter and the spring (Figures 4.5e-f, 4.6e-f, 4.7e-f, and 4.8e-f). These areas are likely to be affected by frequent freezing/thawing processes, leading to large uncertainties in soil moisture simulations. Third, during the summer, the background error is relatively large around the Midwest and the Great Plains for the top two soil layers (Figures 4.5g, 4.5k, 4.6g, and 4.6k), which might be largely due to uncertainties in precipitation forcings (see Section 4.4.3 for more discussions).
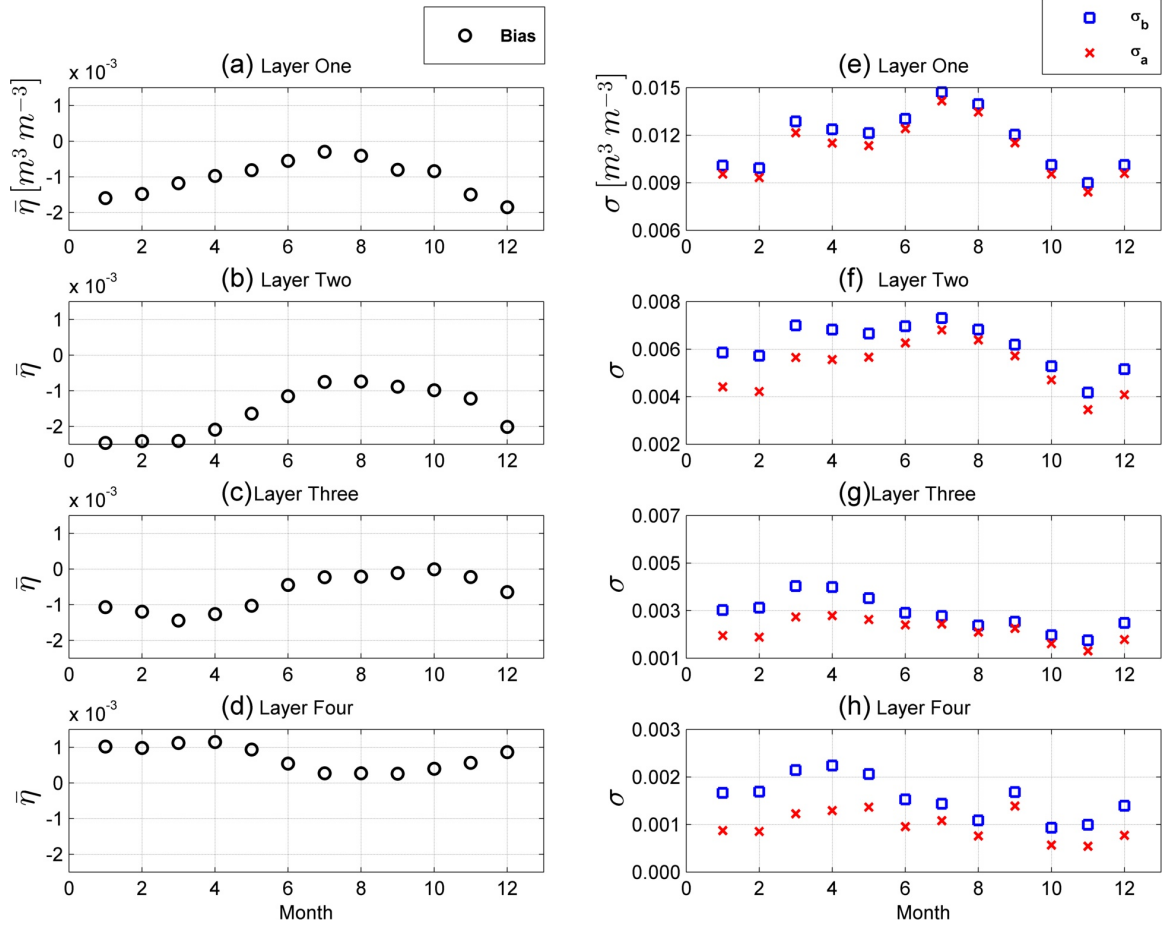
Figure 4.4: The domain-mean values of the biases (a-d) and standard deviations of the bias-blind (σ_b) and -aware ($sigma_a$) soil moisture background error (e-h) throughout the soil depth. The units are in m^3 m^{-3}.
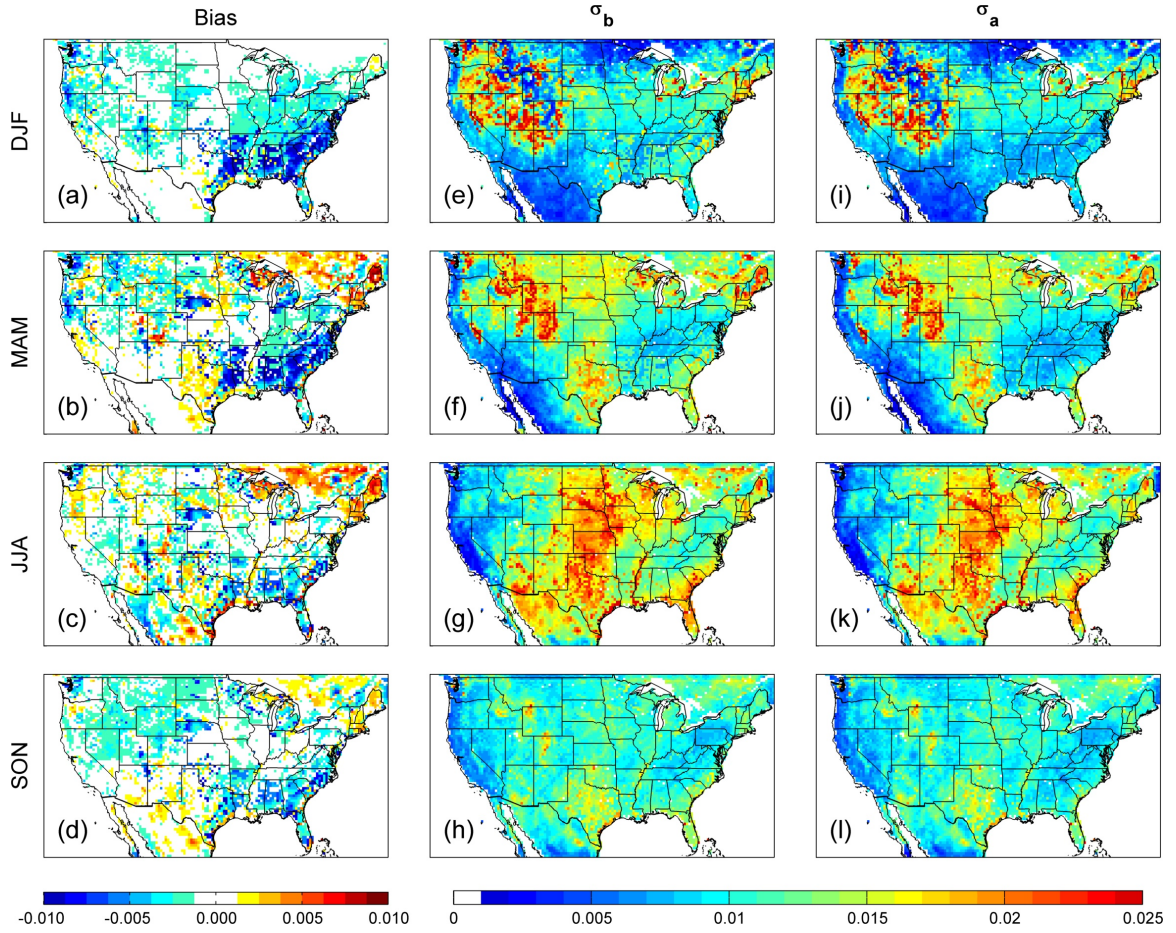
Figure 4.5: The seasonal bias (a-d) and the bias-blind (e-h) and -aware (i-l) standard deviations of the background error of the top soil layer during the winter (December, January, February, as DJF), the spring (March, April, and May, as MAM), the summer (June, July, and August, as JJA), and the fall (September, October, and November, as SON) based on the eight-year WRF simulations. The bias and standard deviations are in m^3 m^{-3}.
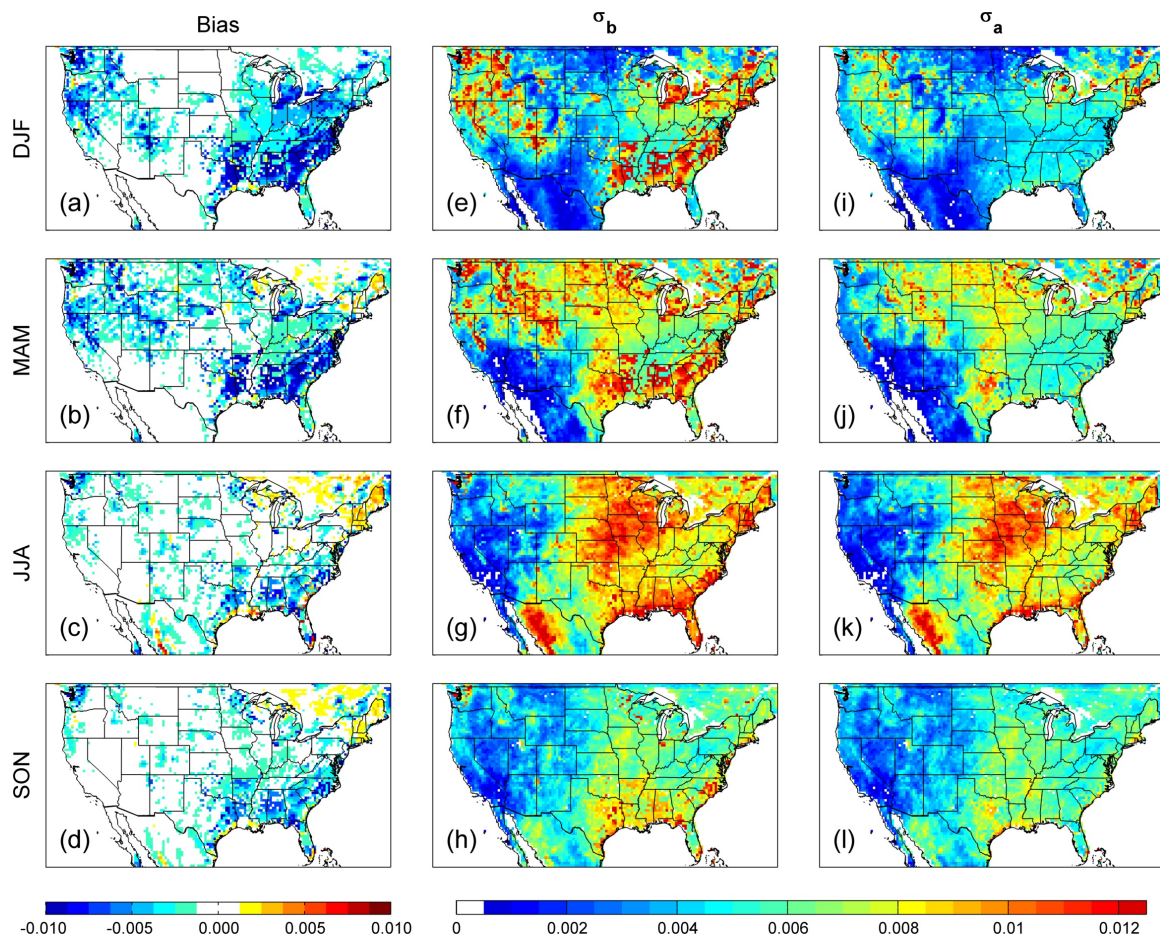
Figure 4.6: Same as Figure 4.5, except for the second soil layer.
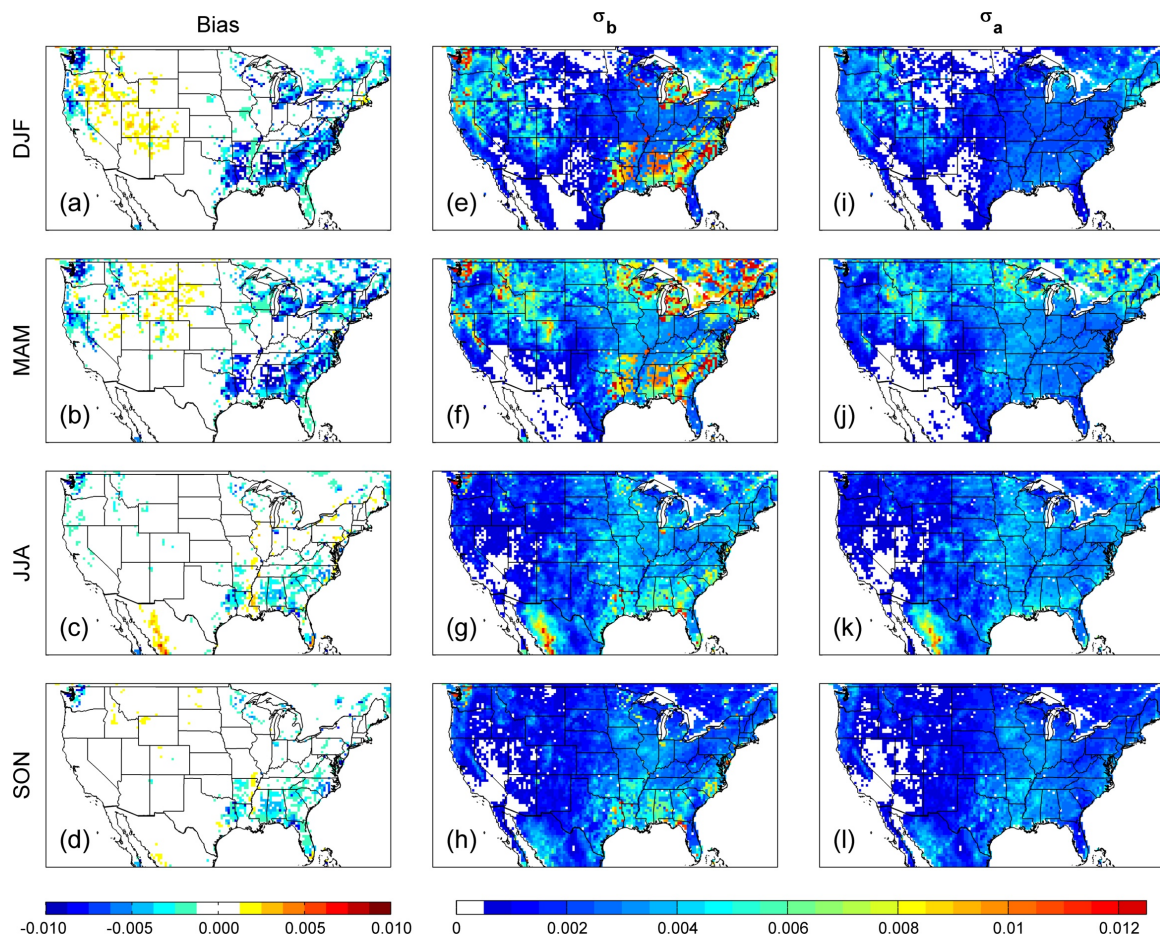
Figure 4.7: Same as Figure 4.5, except for the third soil layer.

79
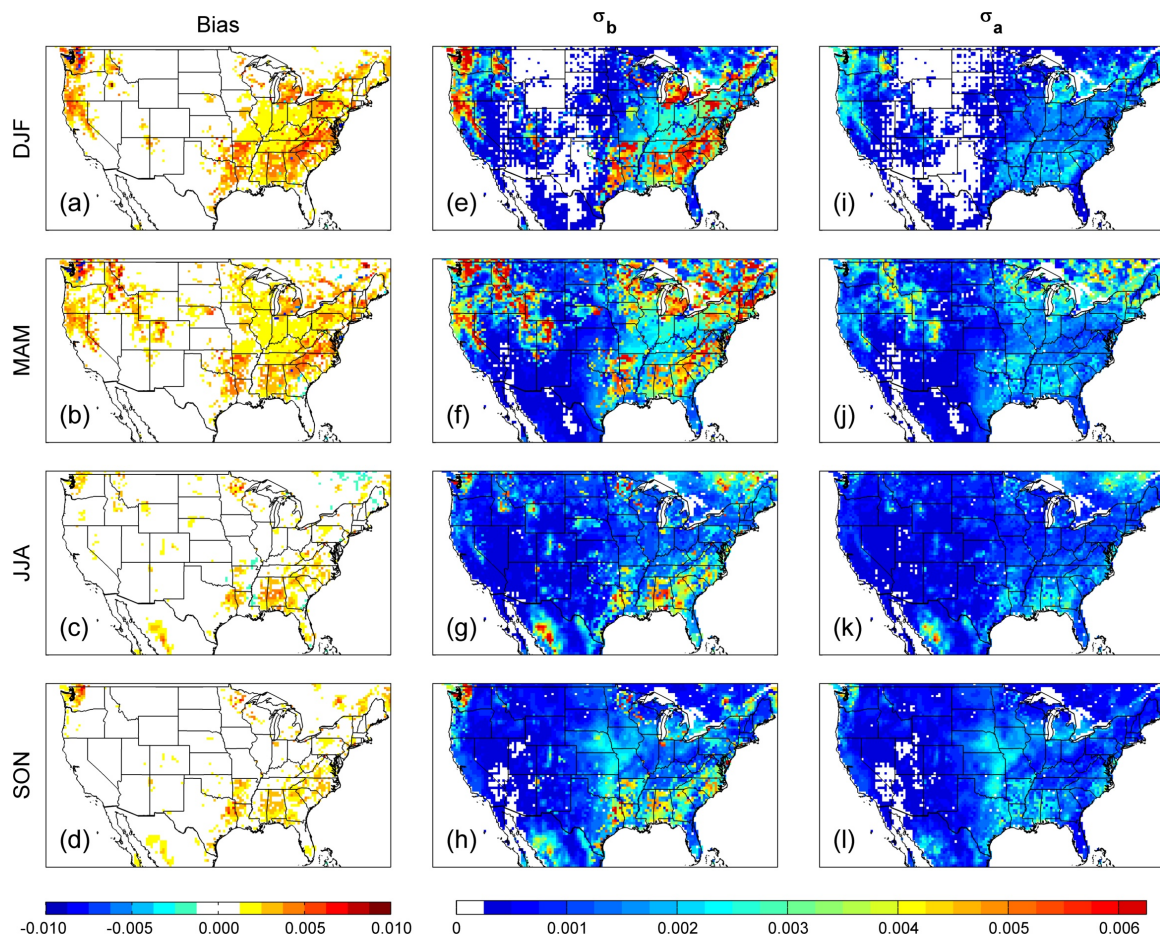
Figure 4.8: Same as Figure 4.5, except for the fourth soil layer.
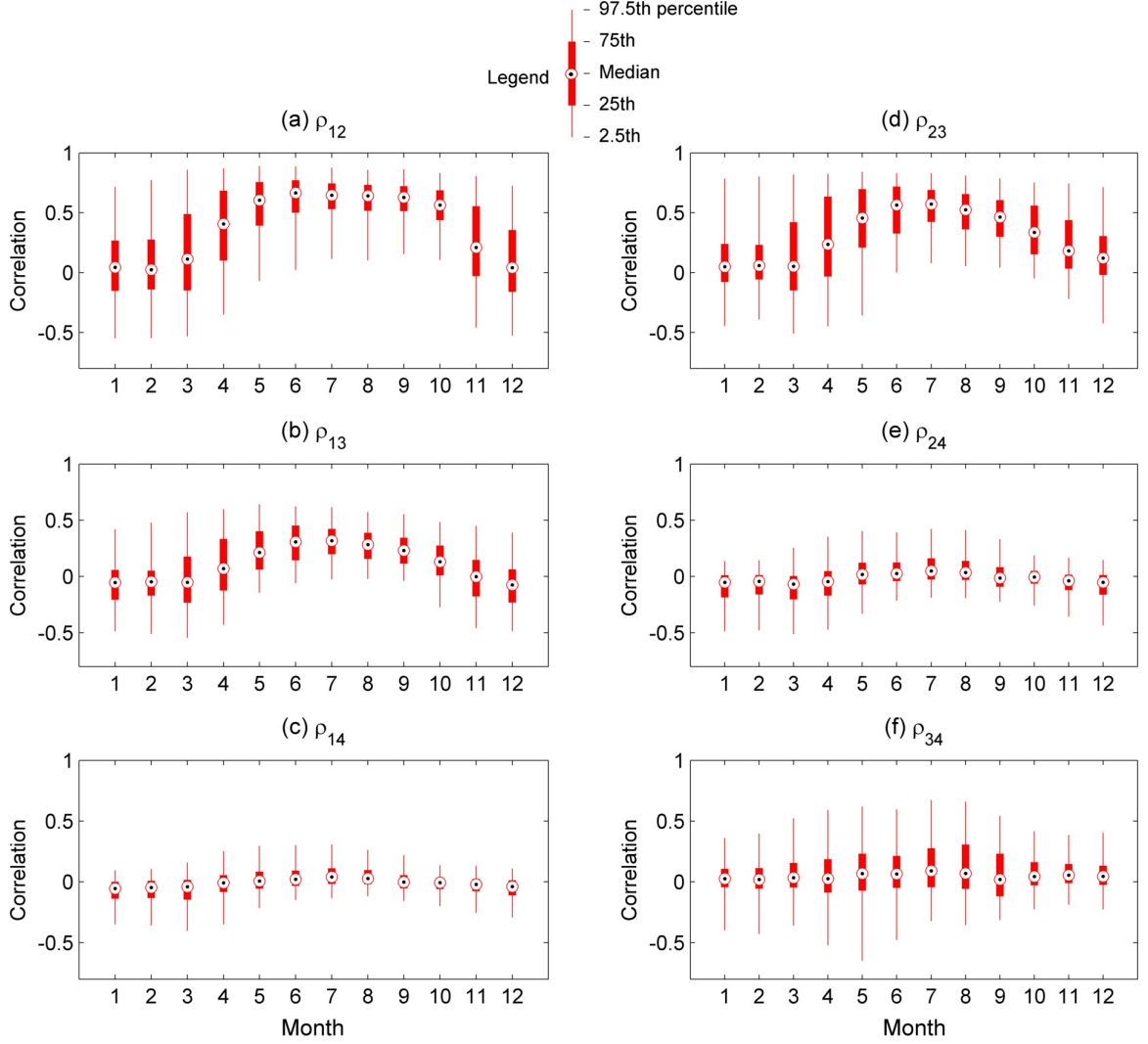
Figure 4.9: The box plot of the monthly estimates of the background error cross-layer correlations obtained from the eight-year simulations. The estimates of each month have a sample size of 7,860 (total land pixels).

Figure 4.9 shows cross-layer correlation of the background error in each month. Like the error standard deviations, the correlations also exhibit monthly variability throughout the soil column. The highest correlation ($\sim$0.6) is found between the first and second layers during the summer (Figure 4.9a) while the correlation between the top and bottom layers is close to zero for all months (Figure 4.9c). Note that weak cross-layer correlation between the top and the lower soil layers implies that the soil moisture content in the lower layers may not be significantly influenced by the assimilation of surface soil moisture measurements.
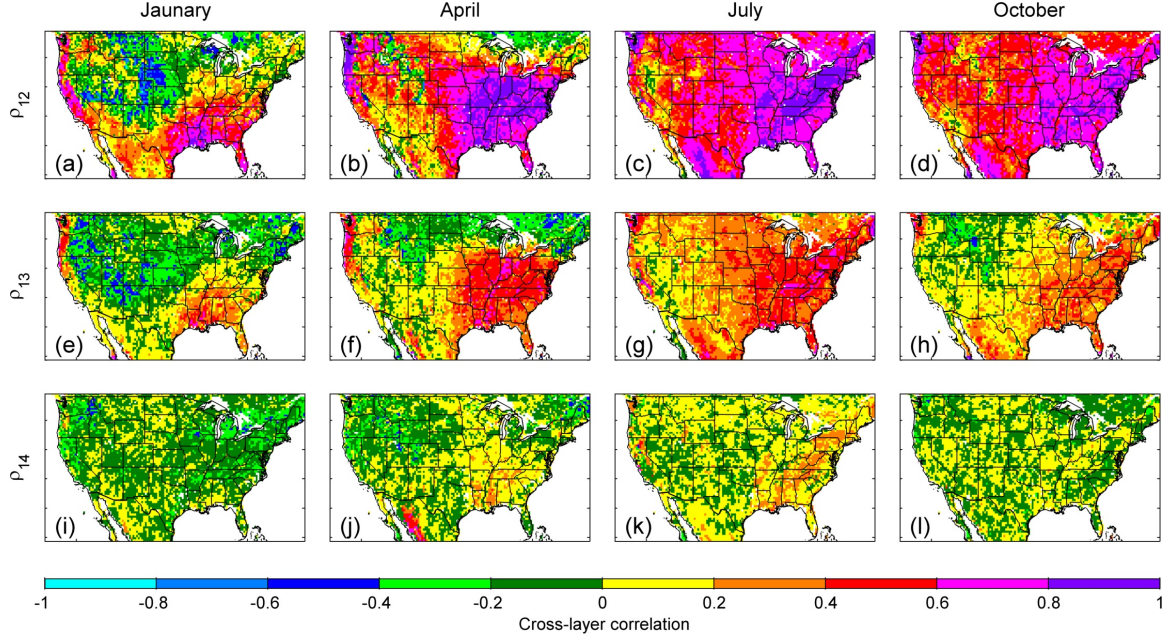
Figure 4.10: Cross-layer correlations between layer one and two (a-d; ρ_{12}), layer one and three (e-h; ρ_{13}), and layer one and four (i-l; ρ_{14}) in January, April, July, and October.

Figure 4.10 compares the spatial distribution of monthly error correlations between the top and lower soil layers in January, April, July, and October. In January, negative correlations between the top two layers can be found over areas subject to freezing/thawing processes, while positive correlations are revealed over the Southeast and the West coast. In April, high correlations (≥ 0.4) are often found in areas with monthly precipitation greater than 30 mm and non-frozen top soil layer. Throughout all seasons, over land surfaces with non-frozen soil, the error correlation between the top two layers is the highest, while it decays sharply as the vertical lag increases. In addition, we notice that the spatial patterns of cross-layer correlations are not necessarily similar to those of the layer's standard deviations. For example, the highest correlations are found over the Eastern United States (see Figures 4.10b-d), where the magnitude of the standard deviation is relatively insignificant (see Figures 4.5g and 4.6g). These areas generally have relatively high soil moisture (≥ 0.3 m^3 m^{-3}) during the summer, which is almost close to the saturation level, leading to reduced uncertainty in modeled soil moisture.

4.4.3 Error vs. Physical Variables

To further understand the spatial patterns of the background error, we analyze the regional relationship between the soil moisture background error, soil moisture, and precipitation using the WRF-Noah simulations during January and July 2013. We map frozen and non-frozen soil pixels based on the monthly mean values of the top-layer soil temperature simulations and select regions of interest within the study domain that are not subject to freezing and thawing processes. Figure 4.11a shows two selected regions with different monthly precipitation and soil moisture amount in January. The blue (red) region has relatively low (high) monthly precipitation (Figure 4.11b) and surface soil moisture (Figure 4.11c). For the selected regions, we also compare the error standard deviations of the first layer with the monthly precipitation and soil moisture values (Figures 4.11d and 4.11e). The mean values indicate that the error magnitude is apparently an increasing function of precipitation and soil moisture content up to some thresholds. Over the dry region (blue box), the magnitude of the background error shows a positive correlation with the precipitation and soil moisture, while this correlation becomes negative over the wet region (red box). Significance analysis indicates that the correlations are statistically significant ($p \leq 0.05$), except the negative correlation between the background error and the precipitation over the wet region.

Like in Figure 4.11, in July, we selected three regions in the western (blue), middle (black), and eastern (red) parts of the United States (Figure 4.12a) based on different regimes of precipitation, which increases from the West to the East (Figure 4.12b). It seems that the magnitude of the background error increases as the soil moisture and precipitation increase up to some thresholds and then begins to decrease. This observation is consistent with our previous findings indicating that the soil moisture background error decreases under abundant precipitation and saturated soil moisture condition. Specifically, it seems that the soil moisture background error increases when monthly precipitation and volumetric soil moisture content are below 100 mm and 0.25 $\text{m}^3 \text{ m}^{-3}$, respectively, while above those thresholds this trend is downward (Figures 4.12d and 4.12e). Obviously, further in-depth investigations are needed for fully verifying this observation.
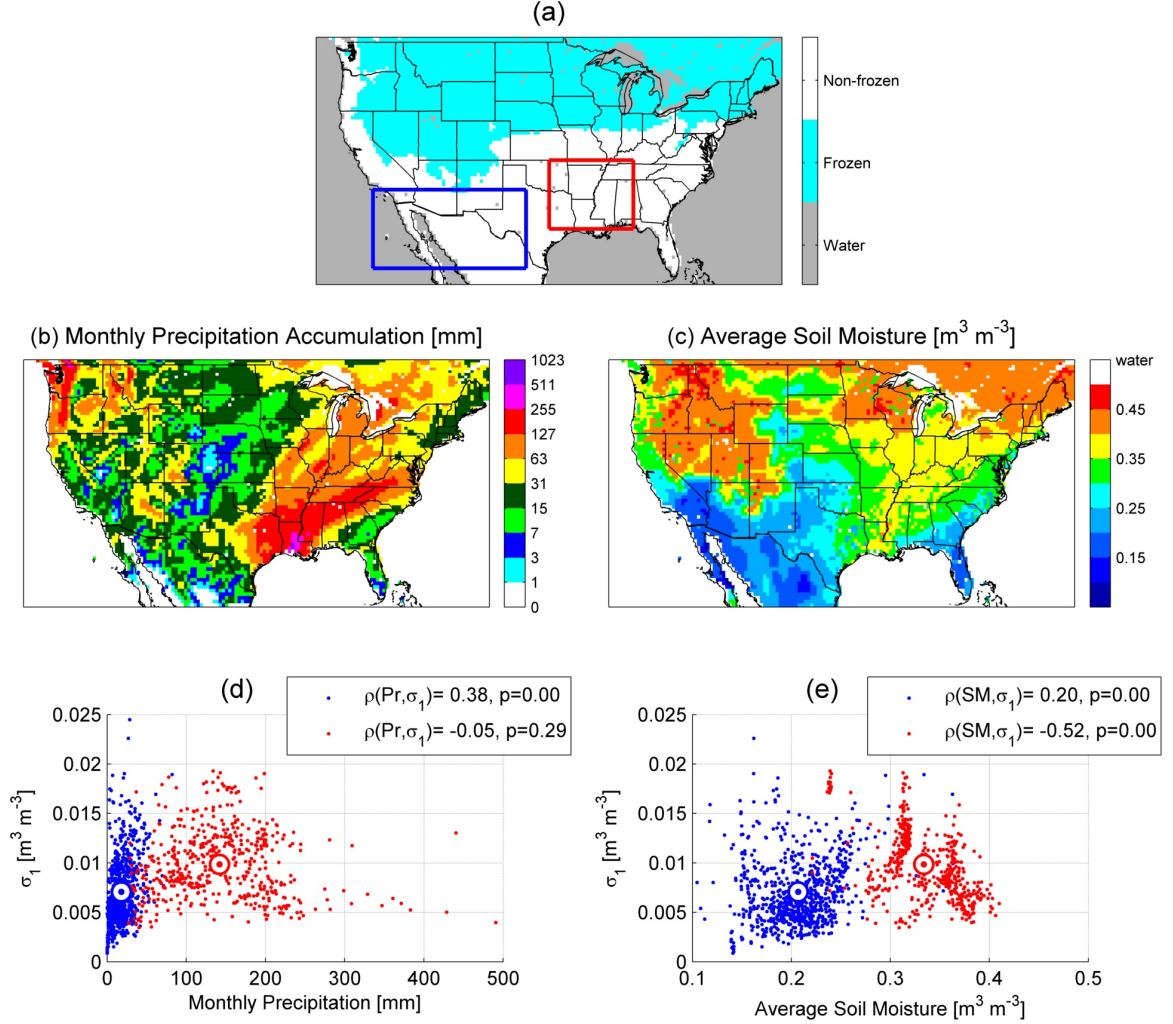
Figure 4.11: Regional analysis of the soil moisture background error against soil moisture content and precipitation in January 2013. (a) Two selected regions in the study domain, in which the frozen top soil layer is shown in shaded light blue. (b) Monthly precipitation accumulation [mm]. (c) Monthly top-layer soil moisture [m^3 m^{-3}]. (d-e) A comparison of monthly precipitation (Pr) and layer-one soil moisture content (SM) versus layer-one standard deviation of the background error (σ_1). The blue and red dots correspond to the shown regions in (a), while the large circles refer to the mean values. The correlations (ρ) and their significance p-values (p) are reported in (d-e).
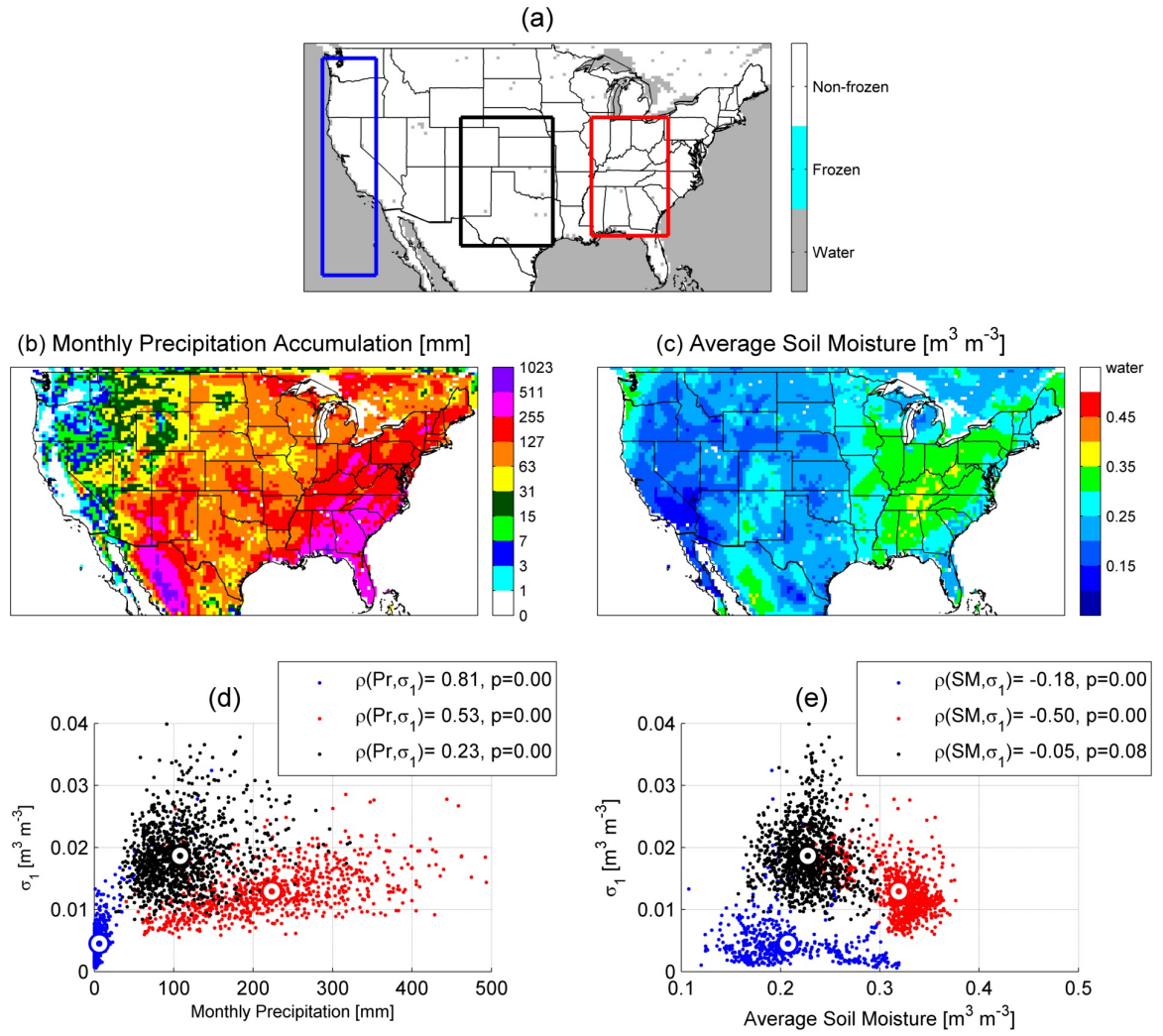
Figure 4.12: Same as Figure 4.11, except for three delineated regions in July 2013.

4.4.4 Bias Analysis over the Southeastern United States

For explaining the large bias ($\overline{\eta}$) of the soil moisture background error over the Southeastern United States, we analyze soil moisture time series over that region during January 2013. Figure 4.13a shows the map of dominant soil texture within a selected region of interest shown in Figure 4.2b. Looking closely at the southeastern areas in the subplots a-b in Figures 4.5-4.8, we can see that areas with large biases overlap with the pixels of the sandy loam soil type shown in Figure 4.13a. Thus, we focus on the sandy loam pixels of the region to study the bias of each soil layer (Figures 4.13b-e) together with the spatially-averaged volumetric soil moisture of the initial conditions, 12-hour forecasts, and 24-hour forecasts (Figures 4.13f-i). In the three upper layers, the WRF-Noah soil moisture forecasts tend to be drier than the given initial soil moisture from the NCEP FNL dataset, while the opposite trend is seen in the bottom soil layer. This tendency persists after 12-h model integrations. Consequently, positive biases are found in the three upper layers and negative biases in the bottom layer. We suspect that the discrepancy of soil moisture estimates between the WRF-Noah forecasts and the NCEP FNL dataset may be attributed to the errors of the FNL soil moisture data or the land surface parameterization deficiencies of the WRF-Noah model, especially for the soil type of sandy loam.

4.4.5 Sensitivity to Physical Parameterizations of Clouds and Land Surfaces

Figure 4.14 shows the top soil-layer error standard deviations during July 2013 corresponding to different schemes of the model physics. Note that the control run (shown at the top-left panel) uses the schemes of WSM-6, Kain-Fritsch, and the Noah model for microphysics, cumulus parameterization, and land surface, respectively. The spatial correlation coefficients of each scheme combination with the control run are reported at the bottom left of each subfigure. The results show that the soil moisture background errors are more influenced by the change in land surface schemes than the microphysics and cumulus parameterization. We do not see significant differences among the spatial patterns of the background error using various WRF physics.
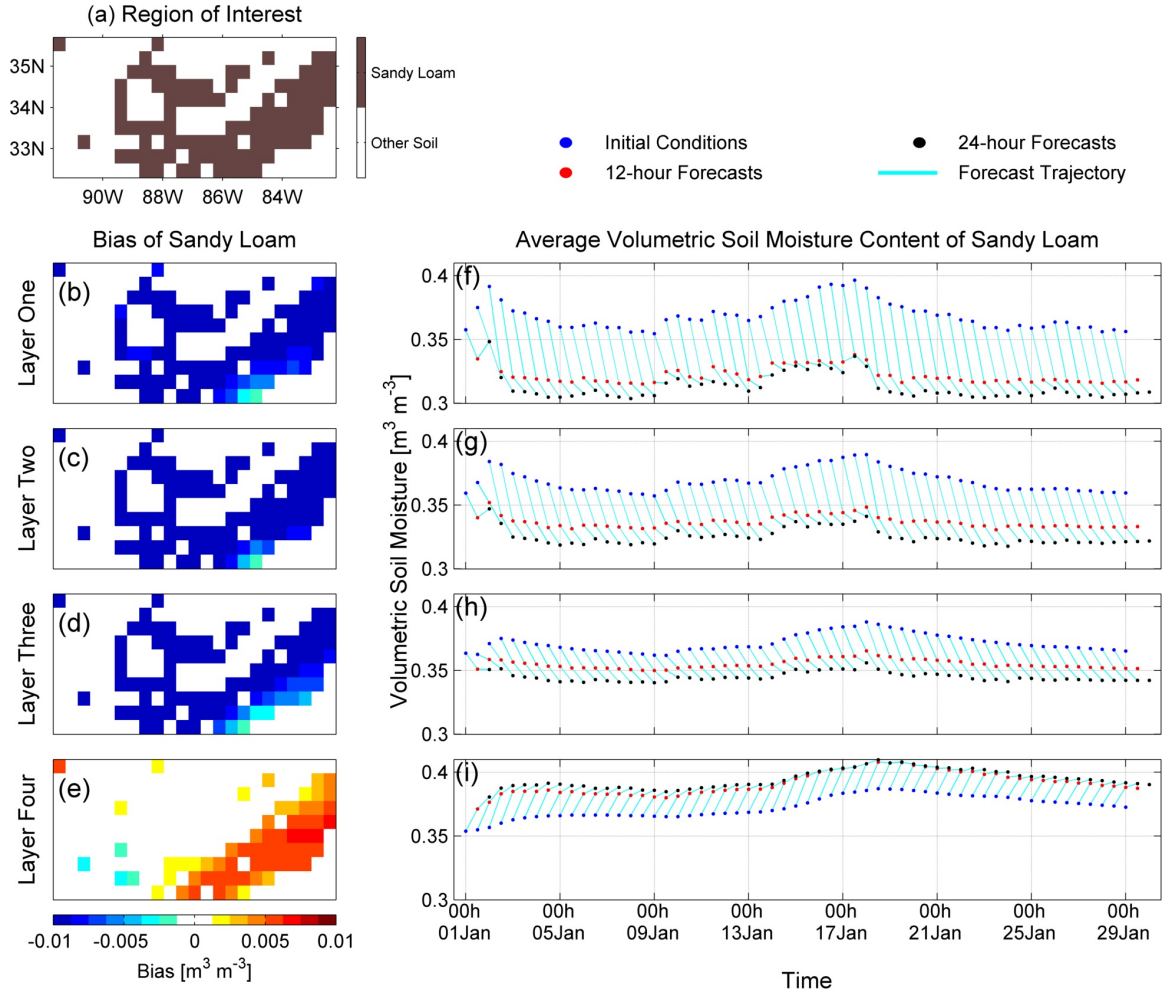
Figure 4.13: (a) The sandy loam soil texture in the sub-region of interest shown in Figure 2b; (b-e) its bias ($\bar{\eta}$); and (f-i) averaged volumetric soil moisture content throughout the soil depth for the initial conditions (blue dots) and 12- and 24-hour forecasts (red and black dots, respectively).
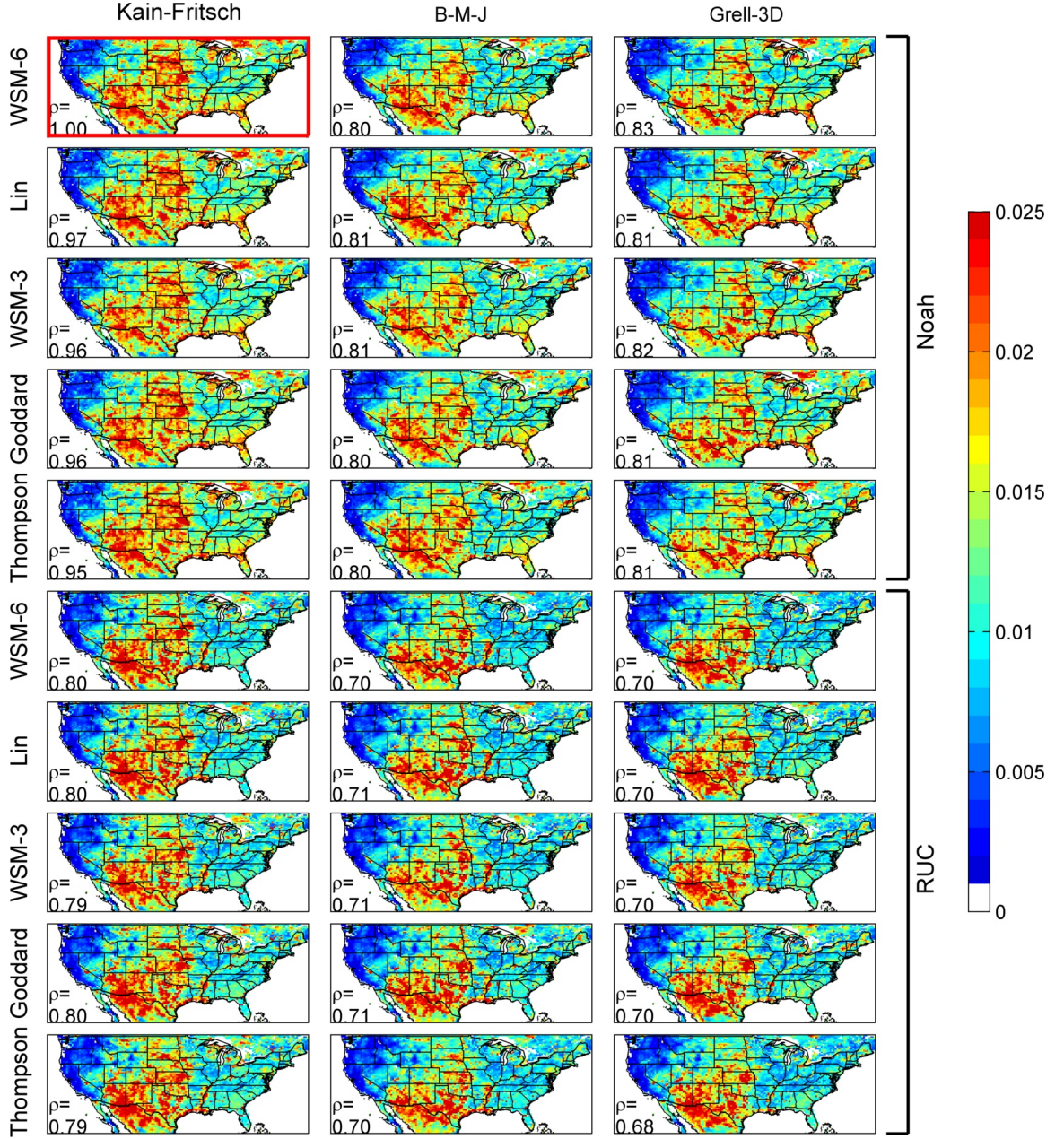
Figure 4.14: The bias-blind standard deviations of layer-one soil moisture background error [m³ m⁻³] in July 2013 using different combinations of the WRF physics options, including the microphysics schemes (Lin, WSM-3, WSM-6, Goddard, and Thompson), the cumulus parameterization schemes (Kain-Fritsch, B-M-J, and Grell-3D), and the land surface models (Noah and RUC). The correlation coefficient of the error fields of each scheme combination against the fields of the control run (top left subfigure) is reported at the bottom left of each subfigure.

4.5 SMOS Assimilation Experiment

We have previously shown that the soil moisture background error is relatively large over the Great Plains during the summer. This implies that the soil moisture data assimilation is expected to be more effective over this region than other areas with smaller background errors. Therefore, focusing on this region, we conduct experiments during July 2013 that assimilate soil moisture retrievals from the Soil Moisture and Ocean Salinity (SMOS) satellite into the WRF-Noah coupled model. We study the impacts of the estimated background error covariance matrices not only on soil moisture but also on precipitation simulations. We also demonstrate the advantages of using a space-time varying soil moisture background error in comparison with its space-time invariant characterization.

4.5.1 Experiment Setup

We conducted three experiments for the period of 3-26 July 2013:

(a) OL: the open-loop experiment that does not include any data assimilation.

(b) DA: the 1D-Var data assimilation experiment using the soil moisture bias-aware background error ($\mathbf{B}_a$) described in Section 4.4 for assimilating the daily soil moisture retrievals obtained from the SMOS Barcelona Expert Centre.

(c) DA-AVG: same as (b), except using the domain-mean time-invariant values of the background error (i.e., averages of monthly estimate of $\mathbf{B}_a$ over the entire domain, see Table 4.2).

The experiments use a three-nested domain configuration (Figure 4.2) with one-way nesting and the same WRF physics as described in Section 4.4.1 and Table 4.1. Figure 4.15 shows the schematic of the assimilation cycle. A cycling mode, in which the first guesses

Table 4.2: The space-time averaged values of the monthly bias-aware soil moisture background error covariance matrix.

Variable	Standard deviation ($\mathrm{m}^3 \ \mathrm{m}^{-3}$)	Cross correlations			
		sm_1	sm_2	sm_3	sm_4
Layer-one soil moisture (sm_1)	$1.2{\times}10^{-2}$	1	0.34	0.04	-0.04
Layer-two soil moisture (sm_2)	$6.0{\times}10^{-3}$	0.34	1	0.26	-0.07
Layer-three soil moisture (sm_3)	$2.7{\times}10^{-3}$	0.04	0.26	1	-0.06
Layer-four soil moisture (sm_4)	$1.3{\times}10^{-3}$	-0.04	-0.07	-0.06	1
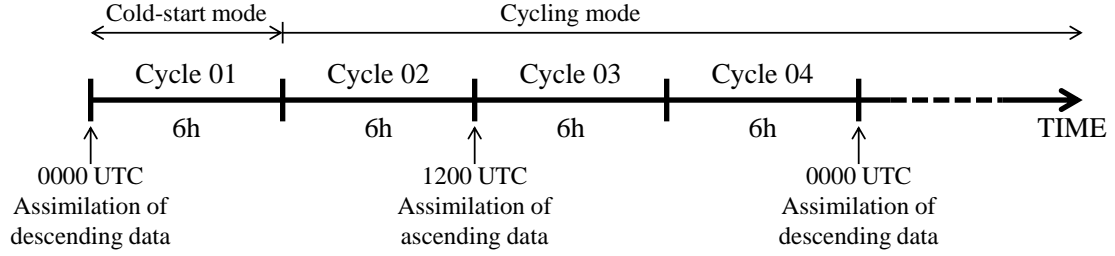
Figure 4.15: A schematic flowchart that shows the assimilation timing and cycles of descending and ascending SMOS orbital retrievals used in the conducted data assimilation experiments.

are obtained from previous short-range forecasts, is used after the first six hours of the experiment. Because the descending and ascending overpasses of the SMOS radiometer occur at approximately 6 p.m. and 6 a.m. local time, respectively, we assimilate descending orbital observations at 0000 UTC and ascending observations at 1200 UTC (Figure 4.15). To assign the SMOS observation error, one option is to use space-time varying observation error (see, *Lievens et al.* (2015)), ranging between 0.02 and 0.1 m^3 m^{-3} with an average of 0.049 m^3 m^{-3} (ascending) and 0.043 m^3 m^{-3} (descending). For simplicity, this study uses the overall SMOS soil moisture retrieval accuracy 0.04 m^3 m^{-3} (*Kerr et al.*, 2010) as a constant standard deviation of observation error. We emphasize that any potential systematic model and/or observational biases are not explicitly taken into account in our data assimilation experiments (see *Dee* (2005)).

Prior to data assimilation practices, SMOS daily orbital soil moisture retrievals are re-gridded onto the numerical grids of the study domain using the nearest-neighbor interpolation method. Note that the SMOS original retrievals have a gridded spatial resolution of 25 km while our study domain is configured with regular 36-km grids. The interpolated SMOS soil moisture data are treated as measurements of the top 10-cm layer, equivalent to the depth of first layer in the Noah Model. The observations are assimilated only over the outermost domain. Figure 4.16 shows a sample of SMOS observations, in which the gray pixels represent where the SMOS data are available but not used in our experiments. Due to the time difference between the descending overpasses over the eastern United States and the assimilation time (i.e., 0000 UTC), we do not assimilate those descending orbital
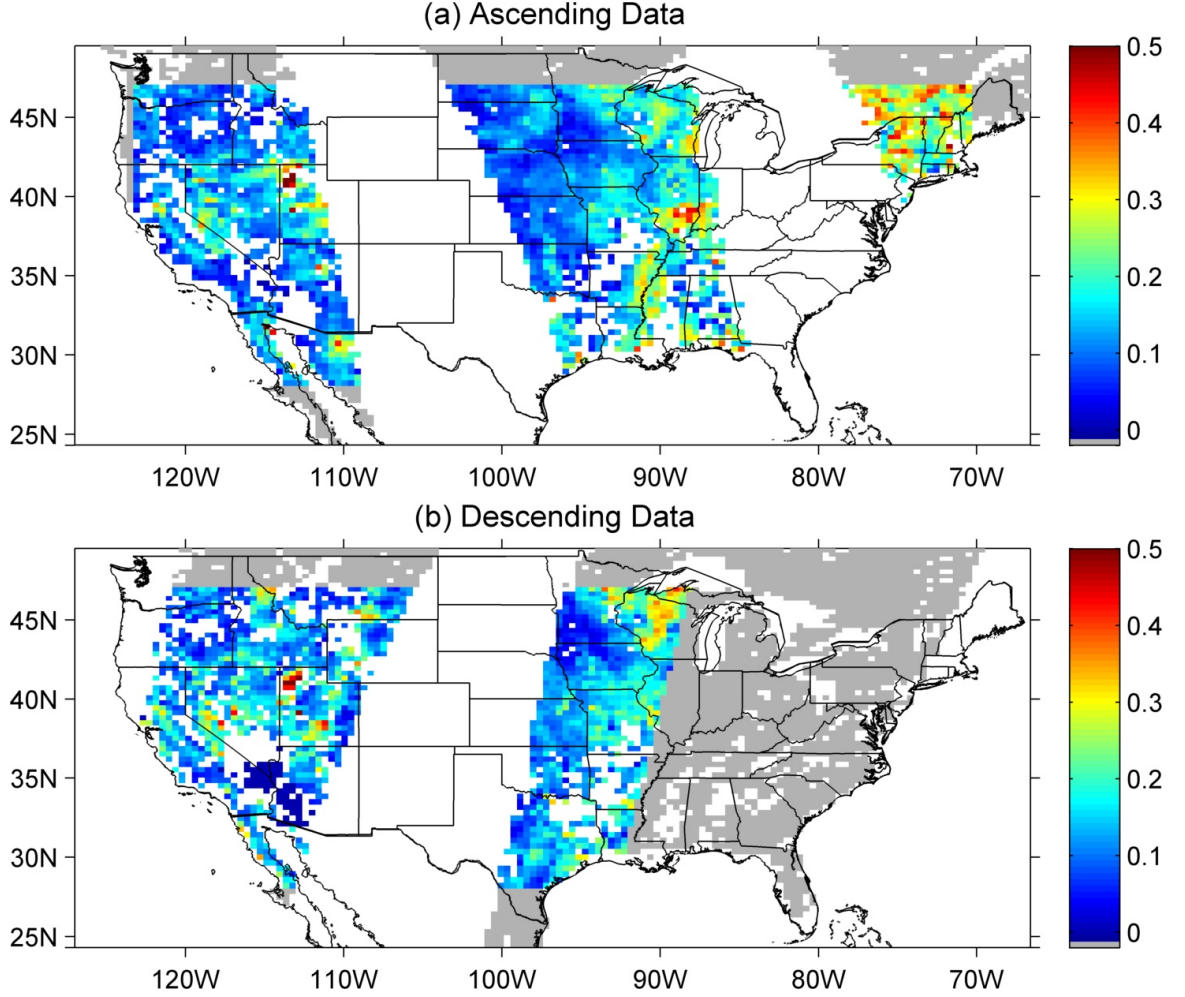
Figure 4.16: Assimilated SMOS soil moisture orbital observations [m³ m⁻³] with 36-km grid-size on 5 July 2013. The retrievals are not used over the gray areas in our assimilation experiments, mainly due to significant difference between the analysis time and the measurement sampling time. See Section 4.5.1 for more details of SMOS data pre-processing.

observations over eastern United States in the DA and DA-AVG experiments.

4.5.2 Ground-based Data and Metrics for Comparison

To compare the results of our experiments, we consider the soil moisture observations from the ground-based Soil Climate Analysis Network (SCAN) and precipitation observations from the NCEP stage IV dataset as reference datasets. The SCAN has approximately 200 stations over the United States in 2015 and uses the Stevens Water Hydra Probe to measure a dielectric constant at soil depths of 5, 10, 20, 51, and 102 cm (*Schaefer et al.*, 2007). Derived from dielectric constants, SCAN soil moisture measurements have accuracy
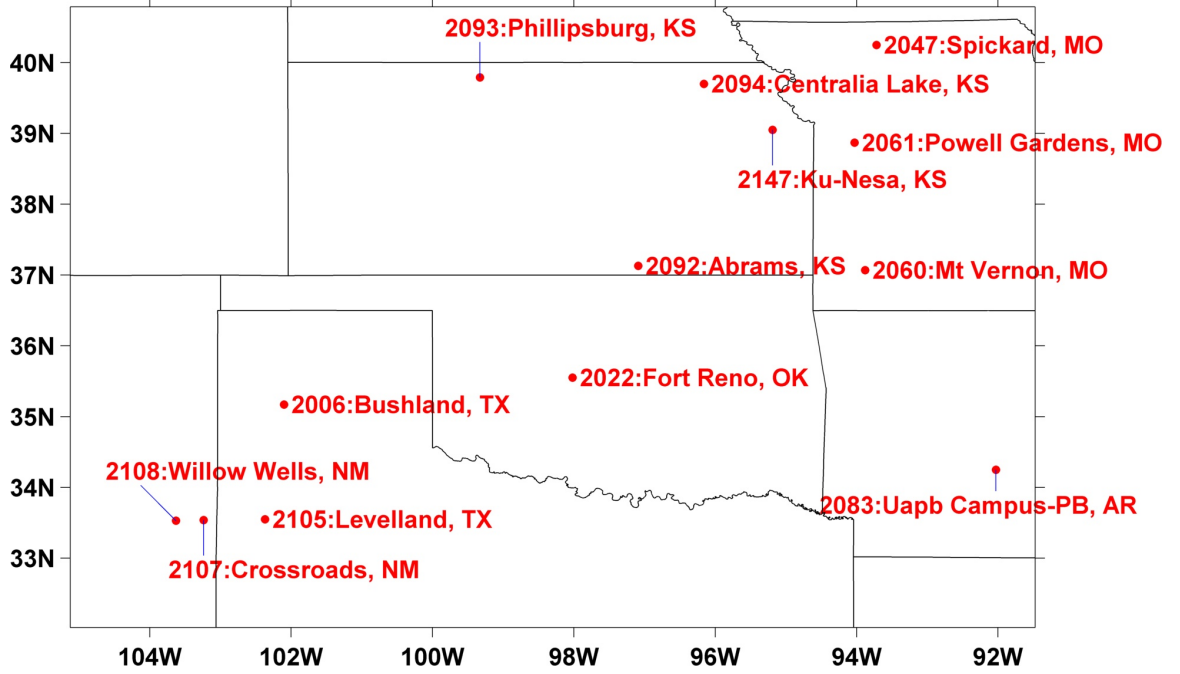
Figure 4.17: The standard IDs and the names of the selected SCAN stations within the study domain.

around 0.03 m^3 m^{-3}. We selected all available 13 stations within the innermost study domain for validation purposes (see a map of the 13 stations in Figure 4.17). Note that the number of selected SCAN stations is limited, and the SCAN data are not free of error. Therefore, the accuracy of our conclusions is certainly subject to above constraints. For precipitation, the NCEP stage IV dataset is a rain-gauge corrected radar product covering the contiguous United States since 2002 and has a gridded spatial resolution of 4 km (*Lin and Mitchell*, 2005).

To quantify the performance of the data assimilation system, we use four metrics, namely the bias, mean absolute error (MAE), root mean square error (RMSE), and correlation coefficient (R). The MAE and RMSE are calculated as follows:

$$MAE = \frac{1}{N} \sum_{i=1}^{N} |M_i - O_i|, \tag{4.7}$$

$$RMSE = \sqrt{\frac{1}{N} \sum_{i=1}^{N} (M_i - O_i)^2}, \tag{4.8}$$

where O_i and M_i are the N-by-1 vectors of the observed references and modeled outputs,

respectively. To quantify the impact of data assimilation, we compute the following normalized performance percentages (NPP):

$$NPP_{MAE} = \frac{MAE_{OL} - MAE_{DA}}{MAE_{OL}} \times 100\%, \qquad (4.9)$$

$$NPP_{RMSE} = \frac{RMSE_{OL} - RMSE_{DA}}{RMSE_{OL}} \times 100\%, \qquad (4.10)$$

$$NPP_{R} = \frac{R_{DA} - R_{OL}}{1 - R_{OL}} \times 100\%, \qquad (4.11)$$

where OL and DA refers to the open-loop and data assimilation experiments, respectively.

4.5.3   Comparison of Soil Moisture and Precipitation Simulations

We compare the spatially-averaged soil moisture and precipitation simulations of 36-km resolution within the innermost domain relative to the reference datasets during 6-26 July 2013. Figure 4.18b shows the domain-mean values of the top-10-cm soil moisture simulations versus those of the reference SCAN data at a depth of 5 cm. In this figure, the mean values of SMOS observations are also included when more than 50% of the innermost domain is covered by the satellite overpasses. The results indicate that SMOS observations are almost unbiased and in closer agreement with the reference dataset than the simulations. The model simulations are relatively biased in the top soil layer. Although we do not explicitly account for the model or observation bias, due to the least squares minimization process, it is apparent that the 1D-Var scheme implicitly results in analysis states with reduced biases compared to the open-loop simulations. By inspection, we can see that the model bias is reduced more in the DA experiment with the space-time varying error covariance compared to the data assimilation experiment with an invariant background error representation (DA-AVG). Specifically, the NPP_{MAE} (NPP_{RMSE}) in the top-10-cm soil moisture time series is 40% and 22% (38% and 21%) for the DA and DA-AVG experiments, respectively, showing more than 20% relative reduction.

In Figure 4.18c, similar results for the lower 10-to-40-cm soil layer are shown. As is evident, in the lower layer, the soil moisture simulations are less biased with respect to
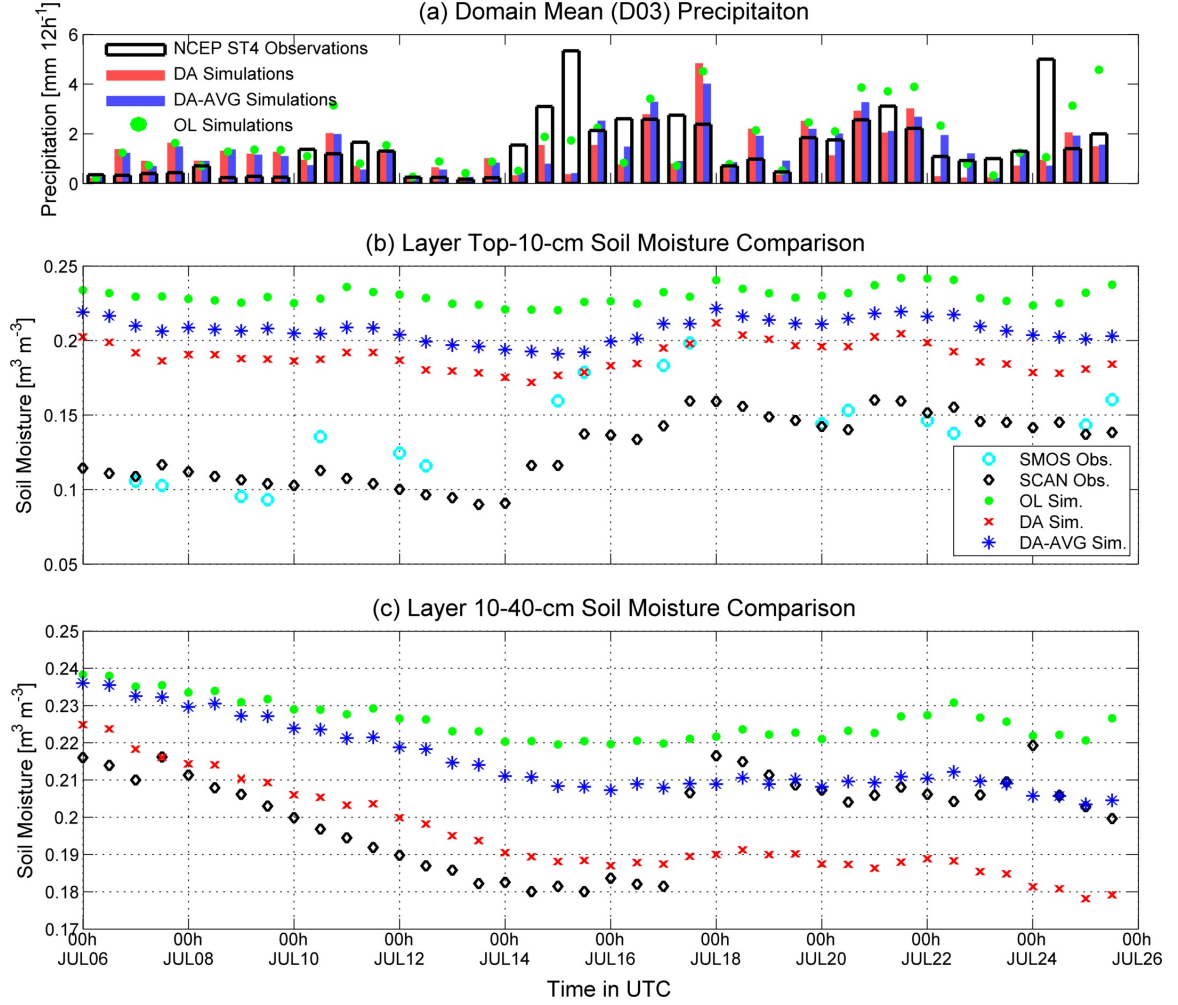
Figure 4.18: (a) Innermost domain-mean precipitation (mm/12h) from the data assimilation experiments and the NCEP Stage IV observations. (b-c) Innermost domain-mean soil moisture simulations of 36-km resolution versus the SCAN observations at depths of 5 and 20 cm.

the SCAN data, leading to an improved assimilation results compared to the top layer. We can also see that the DA outperforms the DA-AVG experiment. Specifically, the DA experiment shows a reduction of 47% and 43% in the MAE and RMSE, respectively, while 36% and 28% reduction is observed for the DA-AVG. However, an anomalous deviation between the model simulations and the SCAN data is seen in the lower layer after July 18. This anomaly is mainly due to moisture infiltration after a major precipitation event around July 15, which is not properly captured by the WRF-Noah simulations (Figure 4.18a).

Table 4.3 represents the quality metrics obtained by comparing the hourly SCAN soil

moisture observations at a depth of 5 cm with the top-10-cm simulations of the nearest 4-by-4-km numerical grid during 6-26 July 2013. Since soil moisture exhibits significant spatial heterogeneity, to obtain robust statistics, we evaluate the performance metrics averaged over all gauges. The results show that the assimilation of SMOS data markedly improves soil moisture simulations, leading to 35% and 33% reduction in the MAE and RMSE, respectively. However, we need to emphasize that this reduction might be largely due to an implicit impact of data assimilation on reduction of the local open-loop biases. However, regardless of the bias impacts, the average correlations are increased more than 19% as a result of data assimilation. Table 4.4 presents similar statistics obtained by comparing the simulations in the lower 10-to-40-cm soil layer with the SCAN observations at the depth of 20 cm. In terms of the quality metrics, the results demonstrate that the assimilation of SMOS data into the surface layer does not alter significantly simulations in the lower layers. However, more than 8% reduction in MAE and RMSE is observed for the DA experiment, while correlation increases up to 25%. Overall, the results imply that proper incorporation of a space-time varying background error can tangibly improve the results of fine-scale soil moisture simulations.

Table 4.3: The normalized performance percentages (see, Equations (4.9)-(4.11)) of the employed quality metrics, obtained by comparing the reference hourly SCAN soil moisture observations at a depth of 5 cm with the top-10-cm soil moisture simulations of nearest 4-by-4-km numerical grid during 6-26 July 2013.

Station ID	Bias			MAE			RMSE			Correlation		
	OL	DA	DA-AVG	OL	DA	DA-AVG	OL	DA	DA-AVG	OL	DA	DA-AVG
2006	0.103	0.036	0.060	0.105	0.051	0.070	0.116	0.063	0.083	0.399	0.465	0.205
2022	-0.033	-0.041	-0.034	0.117	0.097	0.104	0.122	0.107	0.111	-0.029	0.669	0.512
2047	0.069	-0.009	0.015	0.069	0.033	0.015	0.075	0.038	0.017	0.367	0.207	0.978
2060	0.114	0.080	0.097	0.121	0.097	0.108	0.131	0.102	0.115	-0.212	0.000	-0.028
2061	0.051	0.007	0.036	0.051	0.019	0.036	0.055	0.021	0.043	0.344	0.799	0.386
2083	0.215	0.190	0.211	0.215	0.190	0.211	0.216	0.191	0.211	0.176	0.035	-0.077
2092	0.028	0.015	0.027	0.058	0.042	0.045	0.066	0.049	0.053	-0.188	0.522	0.552
2093	0.107	0.063	0.084	0.107	0.064	0.084	0.110	0.072	0.091	0.531	0.316	0.456
2094	0.072	0.016	0.053	0.084	0.053	0.065	0.089	0.065	0.071	0.531	0.061	0.628
2105	0.098	0.035	0.049	0.098	0.057	0.058	0.117	0.073	0.078	0.413	0.441	0.507
2107	0.094	0.034	0.056	0.095	0.047	0.059	0.105	0.061	0.071	0.369	0.139	0.371
2108	0.159	0.086	0.113	0.159	0.086	0.113	0.164	0.090	0.116	-0.066	0.450	0.427
2147	0.157	0.095	0.133	0.157	0.095	0.133	0.160	0.096	0.137	-0.167	0.364	-0.103
Mean	0.095	0.047	0.069	0.111	0.071	0.085	0.117	0.079	0.092	0.190	0.344	0.370
NPP					35%	23%		33%	22%		19%	22%

Table 4.4: Same as Table 4.3, except for the comparison of simulated soil moisture at depth of 10-to-40 cm with the observed soil moisture at a depth of 20 cm.

Station ID	Bias			MAE			RMSE			Correlation		
	OL	DA	DA-AVG	OL	DA	DA-AVG	OL	DA	DA-AVG	OL	DA	DA-AVG
2006	-0.117	-0.158	-0.139	0.117	0.158	0.139	0.130	0.168	0.151	-0.028	0.151	-0.199
2022[1]	-	-	-	-	-	-	-	-	-	-	-	-
2047	-0.046	-0.099	-0.064	0.046	0.099	0.064	0.051	0.100	0.066	0.979	0.974	0.974
2060	0.093	0.057	0.080	0.094	0.069	0.085	0.101	0.071	0.090	0.249	0.359	0.292
2061	-0.097	-0.141	-0.106	0.097	0.141	0.106	0.098	0.141	0.108	0.701	0.930	0.714
2083	0.213	0.188	0.209	0.213	0.188	0.209	0.213	0.188	0.209	0.171	0.283	0.165
2092	-0.017	-0.030	-0.017	0.048	0.037	0.045	0.054	0.049	0.050	-0.756	0.400	-0.594
2093	0.035	0.012	0.034	0.035	0.016	0.034	0.038	0.022	0.037	0.364	0.406	0.297
2094	-0.199	-0.232	-0.208	0.199	0.232	0.208	0.200	0.233	0.209	0.606	0.023	0.287
2105	0.110	0.055	0.073	0.110	0.062	0.076	0.120	0.071	0.086	0.563	0.778	0.886
2107	0.107	0.040	0.069	0.107	0.044	0.069	0.112	0.054	0.075	0.038	-0.356	-0.162
2108	0.170	0.104	0.136	0.170	0.104	0.136	0.172	0.105	0.136	-0.318	0.852	0.897
2147	0.044	-0.004	0.032	0.044	0.020	0.033	0.047	0.024	0.035	0.686	0.661	0.775
Mean	0.025	-0.017	0.008	0.107	0.097	0.100	0.111	0.102	0.104	0.271	0.455	0.361
NPP					9%	6%		8%	6%		25%	12%

[1]The site has no observation at a depth of 20 cm during our experiment
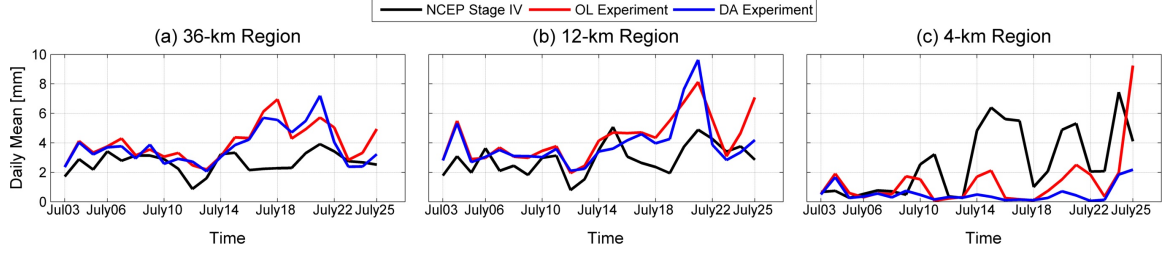
Figure 4.19: The daily domain-mean precipitation estimates for the selected regions within the three nested domains (see the domain configuration in Figure 2). The three regions are a box ranging from 115.5°W and 31.2°N (bottom left corner) to 82.6°W and 47.1°N (top right corner) for the outermost domain (a) and a rectangular box excluding a ten-grid strip at the boundary for the middle and innermost domains (b-c).

Table 4.5: The quality metrics obtained by comparing the time series of simulated precipitation against that of the reference NCEP Stage IV observations in Figures 4.19.

		Bias	MAE	RMSE	Correlation
D01	OL	1.33	1.34	1.76	0.35
	DA	1.09	1.20	1.59	0.41
D02	OL	1.40	1.51	1.86	0.61
	DA	1.01	1.32	1.73	0.54
D03	OL	-1.35	2.04	2.80	0.30
	DA	-2.15	2.25	3.07	0.23

To evaluate the impact of soil moisture assimilation on precipitation simulations, the NCEP stage IV dataset is used as a reference over three regions within the three nested domains (D01, D02, and D03 in Figure 4.2a). Since soil moisture is a key to the formation of intense but short summertime precipitation, any improvements in the estimation and forecast of soil moisture may directly impact the precipitation simulation skill of a coupled model. Figure 4.19 shows the domain mean values of the daily precipitation over the three nested domains for the open-loop experiment, the DA experiment, and the NCEP stage IV dataset, while the quality metrics for the domain-mean values are reported in Table 4.5. The results of the outermost and middle domains indicate that both the open-loop and assimilation experiments tend to overestimate precipitation during July 2013, while the pattern is opposite in the innermost domain. Overall, it can be seen that assimilation of SMOS soil moisture shows a marginal impact on precipitation simulations. Within the outermost and middle domains, the results indicate appreciable improvements in the bias

(28%), MAE (13%), RMSE (10%), and correlation (9%). However, no tangible improvement in quality metrics is observed for the innermost domain. It seems that the noise and error in high-resolution model simulations and data are large enough to prevent the data assimilation scheme lead to an appreciable improvement in precipitation simulations.

4.6   Summary of the Chapter

This study characterizes the space-time structure of soil moisture background error covariance and paves the way for the development of a soil moisture variational data assimilation system for the Noah land surface model coupled to the Weather Research and Forecasting (WRF) model. We show that the soil moisture background error covariance over the contiguous United States exhibits strong seasonal and regional variability with the largest values occurring in the uppermost soil layer during the summer. Large background error biases were identified, particularly over the Southeastern United States, caused mainly by the discrepancy between the WRF-Noah simulations and the initial conditions derived from the used operational global analysis dataset. The assimilation of orbital retrievals of the Soil Moisture and Ocean Salinity (SMOS) satellite results in significant reduction in the error of soil moisture simulations and in marginal improvements on precipitation simulations. On average, data assimilation results in 33% and 35% reduction in the root-mean-square error and the mean absolute error, respectively, in the simulation of hourly top-10-cm soil moisture.

CHAPTER V

JOINT ASSIMILATION OF PRECIPITATION AND SOIL MOISTURE

In Chapter 3, the effect of TRMM data assimilation on the analysis, forecast, and downscaling during the summer was studied. Additionally, Chapter 4 explained the developed 1D-Var WRF-Noah soil moisture data assimilation system. In order to study the relative impact of precipitation and soil moisture data assimilation on the model estimates of precipitation, soil moisture, and other meteorological variables such as temperature and humidity, this chapter presents the development of a data assimilation system that is able to simultaneously assimilate remotely-sensed precipitation and soil moisture observations into the WRF-Noah model and includes the preliminary results of TRMM precipitation and SMOS soil moisture data assimilation. The rest of this chapter is organized as follows. Section 5.1 briefly illustrates relevant research studies and the main goals of the chapter. Section 5.2 explains the design of joint data assimilation system and the configuration of the numerical experiments. Section 5.3 verifies the simulations of precipitation, soil moisture, and near-surface hydrometeorological variables against ground-based measurements and briefly discusses the error characteristics between the soil moisture and atmospheric states. Section 5.4 summarizes the entire chapter.

5.1   Introduction

National weather prediction (NWP) models have been used for providing weather forecast for decades. A NWP model typically includes the physics of microphysics and clouds to provide direct rainfall forecasts falling on the land surface and a land surface model having states such as soil moisture and temperature to provide lower-boundary heat flux estimates. For improving weather forecasts, a common practice is to assimilate observations from in-situ gauges, radiosondes, and satellite measurements into the NWP model. Such data assimilation practices often correct control states such as the wind, temperature, pressure, and specific humidity (*Parrish and Derber*, 1992; *Derber and Bouttier*, 1999; *Barker et al.*,

2004; *Wang et al.*, 2013). In contrast, even though rainfall predictions at a regional scale are sensitive to soil moisture (*Jimenez et al.*, 2014; *Feng and Houser*, 2015), up to now, a modern NWP data assimilation system typically does not include soil moisture in the analysis procedure. Therefore, the relative usefulness of integrating observations into atmospheric states and land surface soil moisture on weather predictions remains largely unknown. To better understand such relationship, this chapter attempts to develop a regional data assimilation system that includes the analysis of conventional atmospheric states as well as soil moisture states and is able to integrate remotely-sensed precipitation and soil moisture observations into the model.

Many studies have assimilated all kinds of synthetic and real observations into land surface and hydrologic models to improve the estimates of soil moisture, soil temperature, and streamflow. To test data assimilation algorithms with various models, many studies have conducted observation system simulation experiments (OSSE) and identical twin experiments (*Margulis and Entekhabi*, 2001; *Reichle et al.*, 2001a,b, 2002a,b, 2008a,b; *Dunne and Entekhabi*, 2005; *Zhou et al.*, 2006; *Kumar et al.*, 2009; *Pan and Wood*, 2010; *Chen et al.*, 2011; *Flores et al.*, 2012, 2014; *Kumar et al.*, 2012; *Nagarajan et al.*, 2012; *Pauwels et al.*, 2013; *Pedinotti et al.*, 2014). In addition, studies have tested the assimilation of various real data such as ground-based and remotely-sensed observations into land surface models. For instance, the assimilation of ground-based measurements from long-term datasets or short-term field campaigns was conducted in the studies of *Margulis et al.* (2002); *Dunne and Entekhabi* (2006); *DeLannoy et al.* (2007a,b); *Ghent et al.* (2010); *Hoppe et al.* (2014); *Parrens et al.* (2014); *Draper et al.* (2015). As satellite observations often provide a global coverage, previous studies also tested the assimilation of soil moisture products derived from the Advanced Microwave Scanning Radiometer for the Earth Observing System (AMSR-E) (*Reichle et al.*, 2007; *Liu et al.*, 2011; *Draper et al.*, 2012; *Li et al.*, 2012; *Sahoo et al.*, 2013; *Peters-Lidard et al.*, 2011; *Alvarez-Garreton et al.*, 2015), the Advanced Scatterometer (ASCAT) (*Brocca et al.*, 2012; *Draper et al.*, 2012; *Schneider et al.*, 2014; *Alvarez-Garreton et al.*, 2015), the Scanning Multi-channel Microwave Radiometer (SMMR) (*Reichle and*

Koster, 2005; *Reichle et al.*, 2007), and the Soil Moisture and Ocean Salinity (SMOS) mission (*Ridler et al.*, 2014; *Alvarez-Garreton et al.*, 2015; *Lievens et al.*, 2015). Recently, studies have tested data assimilation algorithms with the merged soil moisture products from multiple satellite sensors, such as the Essential Climate Variable (ESV) product and the Soil Moisture Operational Products System (SMOPS) (*Kumar et al.*, 2014; *Yin et al.*, 2014, 2015). The aforementioned studies focus largely on the effect of data assimilation on land surface or hydrologic predictions. Nevertheless, building on these studies, there has been some progress in coupling land-atmosphere data assimilation and studying the feedback of land surface data assimilation on weather predictions.

In recent years, several studies have coupled various land data assimilation schemes with regional-scale numerical weather prediction systems. For instance, *Mahfouf et al.* (2009) developed a land data assimilation system semi-coupled to the Météo-France's Aire Limitée Adaption Dynamique développement InterNational (ALADIN) weather system that is capable of assimilating near-surface temperature, humidity, and soil moisture every six hours using an extended Kalman filter (EKF) algorithm. The system was tested in an off-line mode for assimilating soil moisture retrievals from the ASCAT and AMSR-E (*Draper et al.*, 2009, 2011a,b). The system was also tested together with the atmospheric component with the assimilation of ASCAT soil moisture, and the results show that the assimilation has a positive impact on the forecasts of near-surface humidity and precipitation (*Mahfouf*, 2010; *Schneider et al.*, 2014). Several data assimilation systems have been developed based on the Weather Research and Forecasting (WRF) model. *Williams et al.* (2013) used the ensemble Kalman filter (EnKF) algorithm of the Data Assimilation Research Testbed (DART) to couple the ParFlow hydrologic model with the WRF model to improve wind speed forecasting. *Rasmy et al.* (2011, 2012) developed a coupled atmosphere and land data assimilation system (CALDAS) capable of updating the states of soil moisture, cloud liquid water, water vapor, rain, and snow through the assimilation of AMSR-E radiances. *Peters-Lidard et al.* (2015) proposed the NASA Unified-Weather Research and Forecasting (NU-WRF) data assimilation system building on the Land Information System (LIS; *Kumar et al.* (2008)) with an ensemble data assimilation component and the WRF ensemble data

assimilation system (WRF-EDAS; *Zupanski et al.* (2011)).

In this chapter, we design a framework that combines the soil moisture data assimilation algorithm built in Chapter 4 and the WRF four-dimensional variational data assimilation (4D-Var) system tested in Chapters 2 and 3 in order to directly assimilate soil moisture and precipitation observations. This work is also motivated by the availability of data from the Global Precipitation Measurement mission (GPM; *Hou et al.* (2014)) and the Soil Moisture Active and Passive mission (SMAP; *Entekhabi et al.* (2010)). We conduct a series of numerical summertime experiments that assimilate TRMM 3B42, the predecessor of GPM; and SMOS, which has a similar data resolution as SMAP. Specifically, this chapter attempts to answer a scientific question: What are the relative impacts of the assimilation of precipitation and soil moisture observations on the estimation of surface precipitation and soil moisture? Because of computational constraints, we focus mainly on the data assimilation on a domain of 36-km gridded resolution over the contiguous United States and use a nested domain of 9-km for the downscaling of precipitation, soil moisture and other meteorological variables. The results show that the assimilation of SMOS soil moisture does not improve on the six-hourly precipitation analysis resulting from the assimilation of TRMM precipitation data. In contrast, both the assimilation of TRMM and SMOS data is able to improve soil moisture forecasts of the top-10-cm and the lower 10-to-40-cm soil layers. In addition, assimilation of TRMM and SMOS data does not improve the six-hour forecasts of soil temperature, air temperature at 2 m, and humidity at 2 m.

5.2 Methodology

This section presents the configuration of the WRF model and the framework of the joint data assimilation system. We also describe the experiment design (Section 5.2.2), the observation pre-processing (Section 5.2.3), the observational error characteristics (Section 5.2.3), and the background states (Section 5.2.4).

5.2.1 WRF Model Setup

This study uses version 3.6.1 of the WRF model, a mesoscale forecast system currently maintained by the United States Center for Atmospheric Research (NCAR) (*Skamarock*

et al., 2008). Figure 5.1a shows the domain configuration, with a parent domain of 36-km resolution and a child domain of 9-km resolution. Our inner domain is chosen according to *Koster et al.* (2004, 2006), in which the Great Plains was identified as a hot spot where the response of atmospheric states to land surface conditions, or so-called land-atmosphere interactions coupling, is strong. Several studies have also focused on the Great Plains to understand the strength of local land-atmosphere interactions (*Santanello et al.*, 2009, 2011). The configurations of the number of vertical levels, the top of atmosphere level, the feedback option, and the physics are included in Table 5.1.

(a)

(b) D01

(c) D02
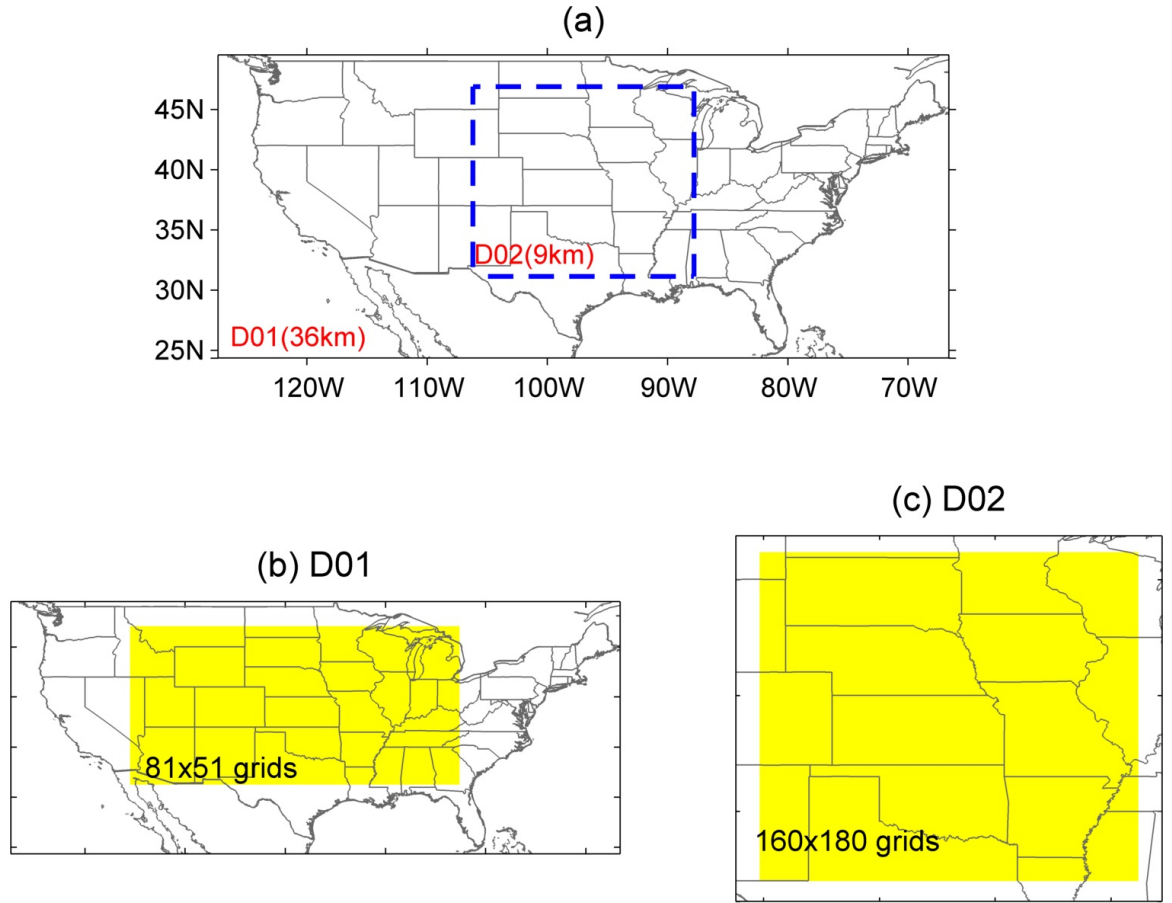
Figure 5.1: (a) Domain configuration. (b-c) The region of interest shown in yellow boxes for the precipitation analysis of the parent (D01) and the child (D02) domains, respectively.

Table 5.1: Model setup and WRF physics parameterization.

	WRF Configuration
General	
WRF version	3.6.1
Experiment period	3-26 July 2013
Domain geometry	
Feedback between domains	One-way nested
Top of atmosphere level (hPa)	50
Vertical levels	41
Domain 01 (D01)	
Grid size	149×79
Grid resolution (km)	36
Domain 02 (D02)	
Grid size	180×200
Grid resolution (km)	9
WRF model physics	
Microphysics	WSM single-moment 6 (*Hong and Lim*, 2006)
Longwave radiation	RRTMG (*Iacono et al.*, 2008)
Shortwave radiation	RRTMG (*Iacono et al.*, 2008)
Surface layer	Revised MM5 similarity
Land surface scheme	Noah model (*Chen and Dudhia*, 2001)
Planetary boundary layer	Yonsei University scheme (*Hong et al.*, 2006)
Cumulus	Kain-Fritsch (*Kain*, 2004)

5.2.2 Data Assimilation Framework and Experiment Design

Figure 5.2 shows the framework of the joint data assimilation system. The framework uses the 4D-Var component built in the WRF Data Assimilation (WRFDA) system (hereafter: WRF 4D-Var system) to assimilate precipitation data and the WRF-Noah 1D-Var soil moisture data assimilation system to assimilate soil moisture data. We have presented the assimilation of NCEP Stage IV and TRMM 3B42 precipitation datasets and discussed relevant issues in Chapters 2 and 3; and reported the development of the WRF-Noah 1D-Var soil moisture data assimilation system and its preliminary test in Chapter 4. To directly answer the scientific question posted in Section 5.1, we conduct three experiments:

- OL, which is the open-loop experiment without any data assimilation;

- PrDA, which includes the assimilation of TRMM 3B42 precipitation data every six hours; and

- PrSMDA, which includes the assimilation of TRMM 3B42 precipitation data every six hours and SMOS soil moisture data every 12 hours.

It is noted that our experimental design is different from operational weather forecast systems, which typically use short-term (e.g., six hours) forecasts as the first guess at the time of data assimilation analysis. In our study, 24-day experiments are separated into 96 six-hour analysis cycles. The first guesses of the first cycle are directly derived from the NCEP FNL dataset, so-called a cold-start mode. For the rest of the analysis cycles, the first guesses of soil moisture are obtained from the six-hour forecasts of previous analysis cycle, while those of other states variables are derived from NCEP FNL dataset. This design is motivated by Chapter 3, which describes that the benefit of TRMM data assimilation does not last beyond the six-hour analysis window and by Chapter 4, which indicates that the effect of SMOS data assimilation is long lasting by the system. Similar to previous chapters, the data assimilation is only performed on the outermost 36-km domain.
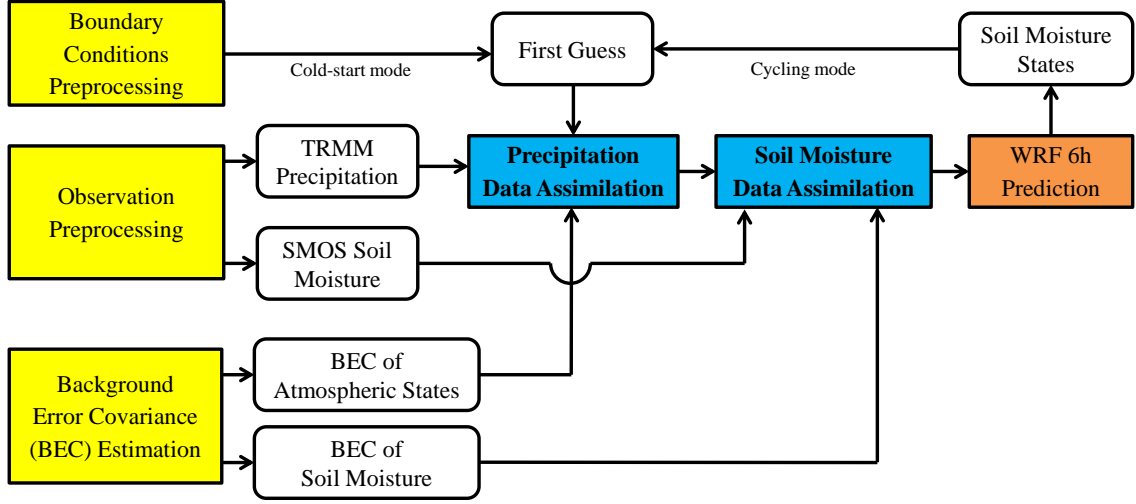
Figure 5.2: The framework of the precipitation and soil moisture data assimilation system.

5.2.3 Observation preprocessing and error

We use the TRMM 3B42 version 7 precipitation dataset, which has a spatial resolution of $0.25° \times 0.25°$ and a time resolution of three hours; it has been available since 1998 (*Huffman et al.*, 2007). Six-hour precipitation obtained from the accumulation of three-hour original TRMM data is used in the data assimilation experiments. Same as Chapters 2 and 3, a constant observation error equal to 2 mm $6h^{-1}$ is employed. According to Chapter 3, we use a threshold of 6 mm $6h^{-1}$ for the quality control procedure that removes observation outliers.

In the PrSMDA experiment, we assimilate the soil moisture retrieval from the Barcelona Expert Centre (available online: http://cp34-bec.cmima.csic.es/). The original SMOS data with a spatial resolution of 25 km is interpolated onto the parent domain of 36-km resolution. The experiment assimilates descending and ascending soil moisture observations at 00 and 12 UTC time, respectively. Note that the observations over boundary pixels and those occurring over Northeast, Southeast, and East North Center States of the United States are not assimilated. In addition, we employ a constant observation error of 0.04 m^3 m^{-3}. The aforementioned processes and procedures of soil moisture data assimilation are the same as the experiments in Chapter 4, where rationales of the processes can be found.

5.2.4   Background Error

This study computes the background error covariance separately for the assimilation of precipitation and soil moisture (see Figure 5.2). The default atmospheric control variables (CVs) of the WRF 4D-Var system are the stream function; the unbalanced components of velocity potential, temperature, and surface pressure; and pseudo relative humidity (*Barker et al.*, 2004). For these variables, we obtain domain-dependent, static background error covariance by computing the average difference between 12-h and 24-h forecasts valid at the same time based on the National Meteorological Center (NMC) method (*Parrish and Derber*, 1992), referred to the CV5 option of the GEN_BE tool in the WRF 4D-Var system. Regarding soil moisture, we also use the NMC method to estimate the background error covariance. Unlike the background error covariance for the atmospheric control variables, the soil moisture background error covariance of each pixel is computed independently without the consideration of neighboring effect. Detailed formulation and characteristics of the soil moisture background error can be found in Chapter 4. Figure 5.3 shows the error standard deviation of each Noah soil layer (i.e., layers configured with thicknesses of 10, 30, 60, and 100 cm from top to bottom) and the error correlation between the top-10-cm layer and the other layers from the monthly bias-aware background error covariance. The figure provides the first order information about the sensitivity of soil moisture analysis to the assimilated soil moisture observations at different locations. For example, the Great Plains show a large magnitude of the error standard deviation and correlation, which implies that the soil moisture analysis increment (i.e., analysis minus background) over the Great Plains is likely to show more variability than that in other areas. The results also justify the choice of inner domain (see Figure 5.1) for studying the role of land atmosphere interaction in soil moisture and precipitation data assimilation.
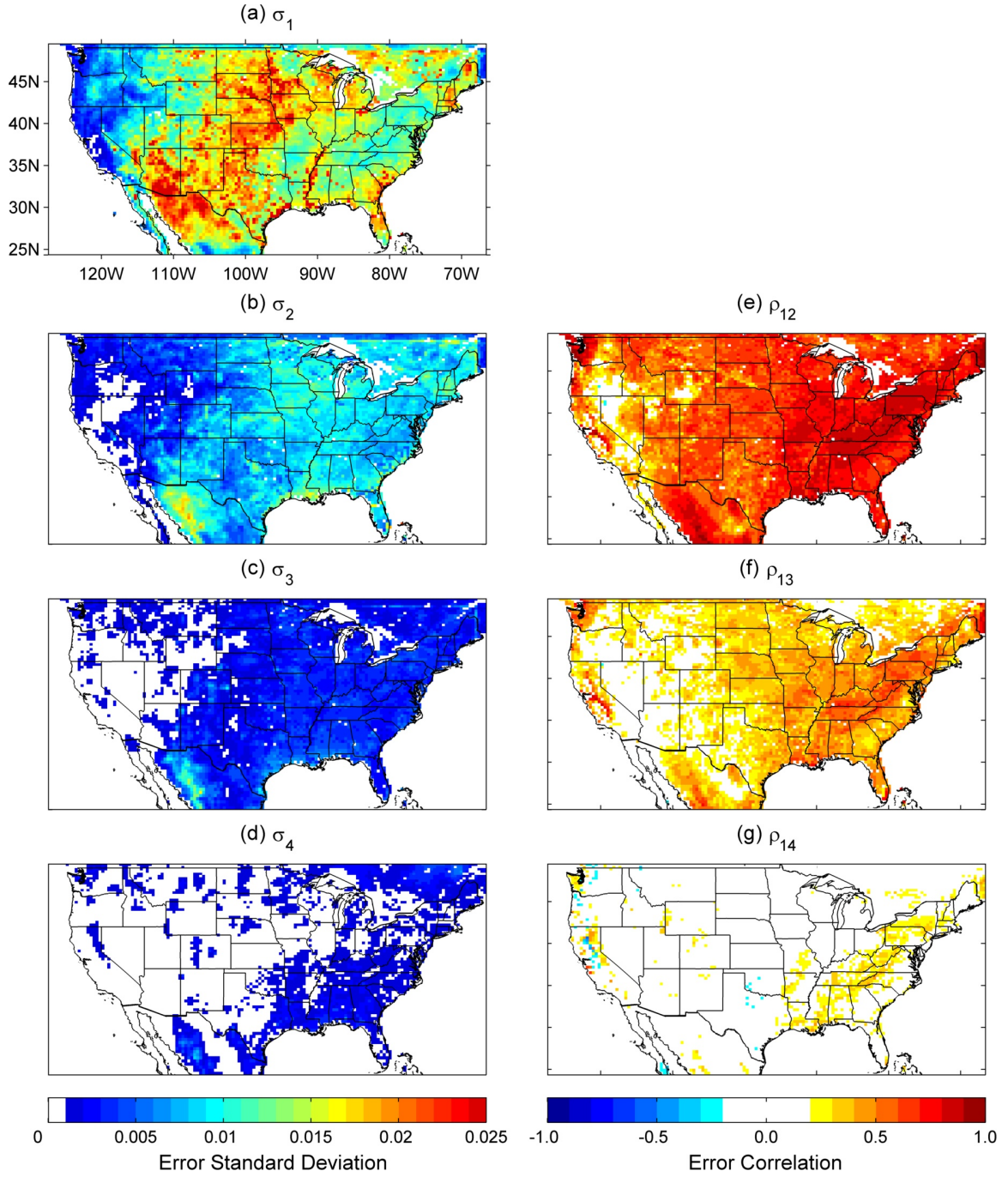
Figure 5.3: The estimates of soil moisture background error statistics for July. (a-d) Error standard deviation for layers one (top) to four (bottom). (e-g) Error correlation between the errors of the top soil layer and the other soil layers.

5.3 Results and Discussion

We compare the output of the numerical experiments to (1) precipitation from the NCEP stage IV dataset, (2) soil moisture observations at depths of 5 and 20 cm from the Soil Climate Analysis Network (SCAN), and (3) observations including the air temperature at 2 m, relative humidity at 2 m, soil moisture at a depth of 5 cm, and soil temperature at a depth of 5 cm from the Climate Reference Network (CRN). To support the analysis, we calculate the bias, mean absolute error (MAE), and correlation coefficient between the model output and the reference datasets at various scales. We focus on understanding the relative impact of the assimilation of TRMM precipitation and SMOS soil moisture retrievals on the short-term simulations (i.e., six hours). Moreover, we empirically discuss the correlation between the forecast errors of soil moisture in the top 10-cm layer and those of atmospheric states at different vertical levels.

5.3.1 Precipitation Verification Against NCEP Stage IV Data

Figures 5.4 and 5.5 show the accumulated precipitation during 3-26 July 2013 of the NCEP Stage IV dataset and experiments OL, PrDA, and PrSMDA for the regions of interest of the outer and inner domains (see Figures 5.1b and 5.1c, respectively). The results from experiment PrDA and those from experiment PrSMDA exhibit a marginal difference. Figures 5.6 and 5.7 show the MAE and correlation of the six-hour precipitation estimates of the experiments relative to the reference NCEP Stage IV dataset at resolutions of 36 and 9 km. Overall, assimilation of SMOS soil moisture provides little additional benefit in the six-hour precipitation analysis upon the assimilation of TRMM precipitation data.
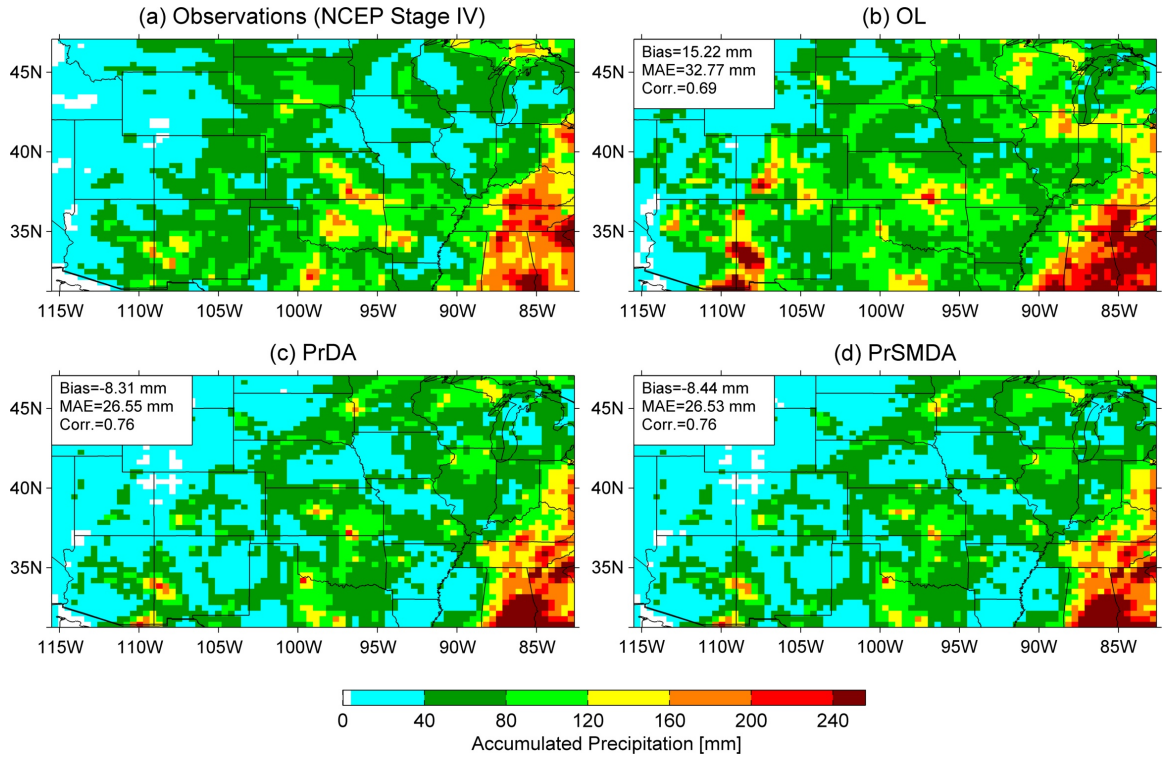
Figure 5.4: The accumulated precipitation fields at a gridded 36-km resolution of the reference NCEP Stage IV dataset and the experiments OL, PrDA, and PrSMDA during 3-26 July 2013. The bias, mean absolute error (MAE), and correlation coefficient of the 2D fields from the experiments relative to those from the reference are reported in (b-d).
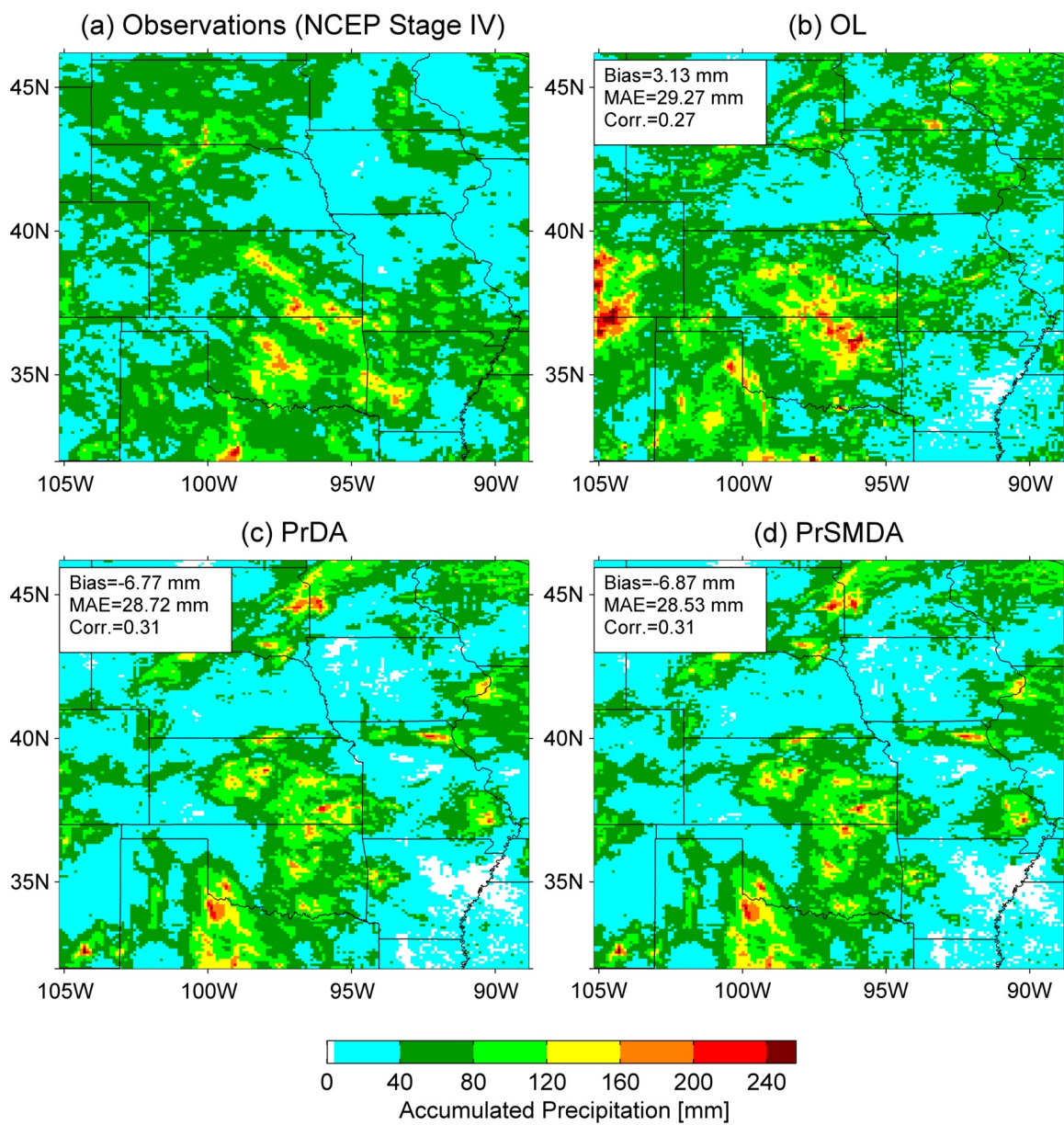
Figure 5.5: Same as Figure 5.4, except for the precipitation fields of 9 km resolution.
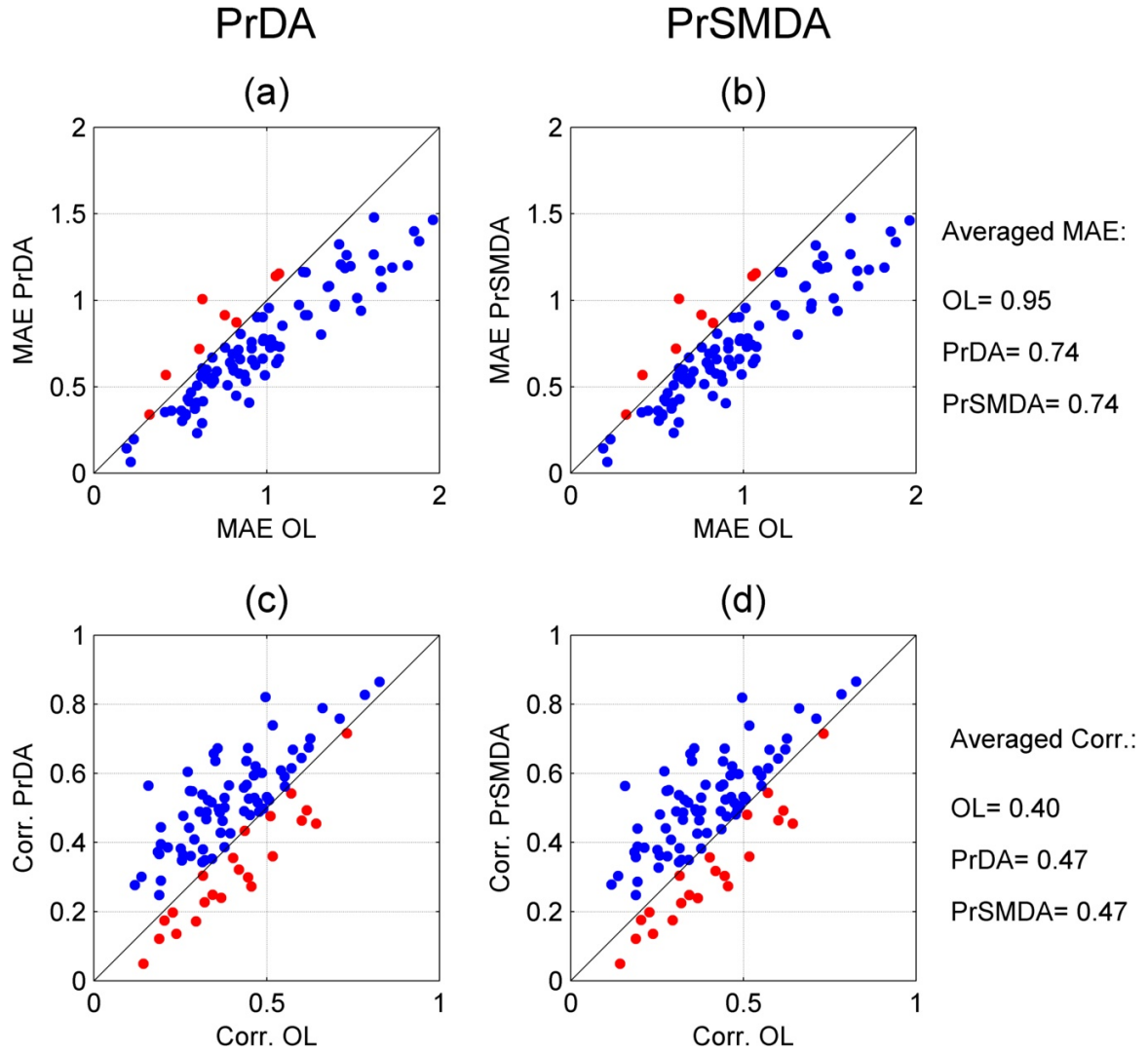
Figure 5.6: The comparison of the mean absolute error (MAE) and the correlation of six-hour precipitation fields of 36-km resolution for the open-loop experiment versus the assimilation experiments during 3-26 July 2013. The blue dots indicate an improvement after data assimilation.
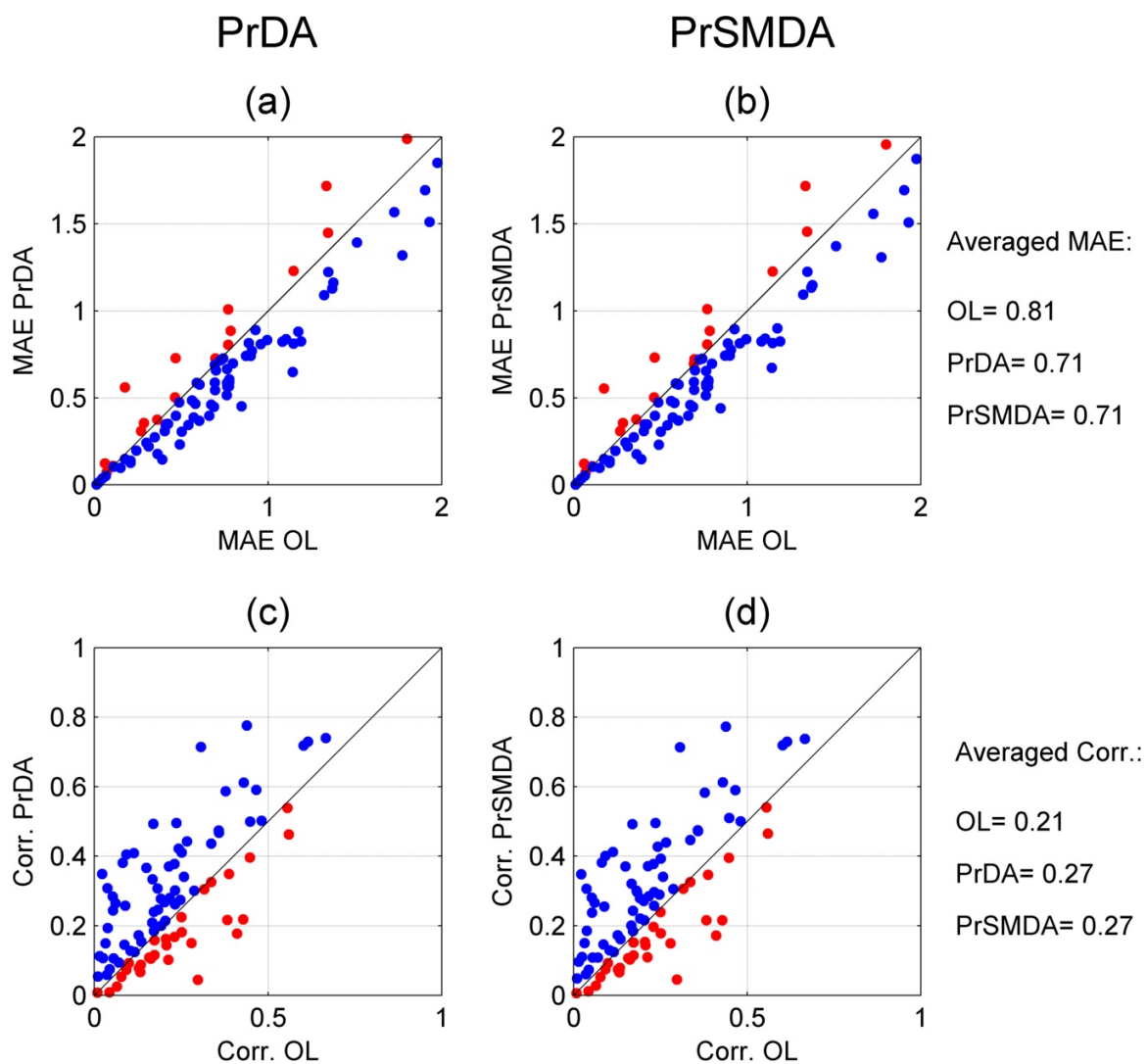
Figure 5.7: Same as Figure 5.6, except for the precipitation fields of 9 km resolution.

5.3.2 Soil Moisture Verification against SCAN Data

We compare the hourly soil moisture estimates from 16 selected SCAN stations (see a map in Figure 5.8a) to those of the nearest 9-by-9-km grids. Figures 5.8b-c shows the MAE of hourly top-10-cm and 10-to-40-cm Noah soil moisture simulations from experiments OL, PrDA, and PrSMDA relative to SCAN observations at a 5- and 20-cm depth, respectively, from the corresponding SCAN stations. We also highlight the stations according to the computed MAE reduction ratio (MRR), defined as follows:

$$MRR = \frac{MAE_{OL} - MAE_{DA}}{MAE_{OL}}, \tag{5.1}$$

where subscripts OL and DA denote the MAE of the corresponding open-loop and data assimilation experiments, respectively, at each station. Stations with MMR<0 are highlighted with yellow while those with MMR>40 are highlighted with cyan. It can be seen that assimilation of both precipitation and soil moisture significantly impacts the top-layer soil moisture simulations, resulting in reduced MAE in most of the stations, while it has a relatively-small impact in the lower soil layers. In addition, the average values of the MAE of all stations reported in Table 5.2 show that the assimilation of TRMM precipitation reduces the MAE of top-10-cm soil moisture simulations by 10% while the addition of SMOS soil moisture data assimilation further reduces the MAE by 25%. For the lower soil layer, assimilation of TRMM precipitation data reduces MAE by 4%, while adding the assimilation of SMOS soil moisture data reduces MAE by an additional 2%.

Table 5.2: The average mean absolute error (MAE) of hourly modeled soil moisture estimates relative to the reference SCAN observations. The MAE reduction ratio according to Equation (5.1) is reported in brackets.

	OL	PrDA	PrSMDA
MAE for the top-10-cm soil moisture comparison	0.109	0.098 (10%)	0.071 (35%)
MAE for the 10-to40-cm soil moisture comparison	0.098	0.094 (4%)	0.091 (6%)

(a) SCAN Stations

2001: Rogers Farm, Nebraska
2006: Bushland, Texas
2047: Spickard, Missouri
2060: Mt Vernon, Missouri
2061: Powell Gardens, Missouri
2068: Shagbark Farm, Iowa
2072: Eros Data Center, South Dekota
2083: Uapb Campus-PB, Arkansas
2092: Abrames, Kansas
2093: Phillipsburg, Kansas
2094: Centralia lake, Kansas
2105: Levelland, Texas
2107: Crossroads, New Mexico
2108: Willow Wells, New Mexico
2147: Ku-Nesa, Kansas
2194: Journagan Ranck, Missouri

(b) MAE for Top-10-cm Soil Moisture Comparison

(c) MAE for 10-to-40-cm Soil Moisture Comparison

Figure 5.8: The locations and the standard IDs of the selected SCAN stations. (b-c) The mean absolute error (MAE) of hourly top-10-cm and 10-to-40-cm WRF-Noah soil moisture simulations at 9-by-9-km grids nearest to the selected SCAN stations within the inner study domain relative to the hourly SCAN gauge measurements at depths of 5 and 20 cm, respectively. Stations with the MAE reduction ratio according to Equation (1) less than 0 or greater than 0.4 are highlighted for later analysis in Figures 5.9 and 5.10.

For detailed comparison, we selected five stations with MMR<0 in the lower 10-to-40-cm soil layer (yellow highlight in Figure 5.8c) to show soil moisture time series. Figure 5.9 shows the time series of soil moisture in the top-10-cm and 10-to-40-cm soil layers as well as the assimilated SMOS soil moisture. Note that simulated soil moisture has a spatial resolution of 9 km while the SMOS observations are at a spatial resolution of 36 km. For such pixel to point comparison, we underscore that the accuracy of conclusions is subject to the resolution difference of the compared soil moisture products and the spatial heterogeneity of soil texture. For the latter one, the Noah model uses a homogeneous soil moisture texture throughout the soil column, which would not be true in the reality. At a point scale, we can see how precipitation and soil moisture data assimilation corrects the error in the OL experiments. For example, in Figures 5.9c and 5.9d, the orange arrows point out several anomalies occurring in the OL experiment but not in both the PrDA and PrSMDA experiments and the SCAN observations. Since the top soil layer responds to the falling rainfall quickly, it is likely that the OL experiments falsely produces precipitation, but the assimilation of TRMM data corrects it. SMOS observations typically agree with the SCAN observations, except station 2068. As a result, the PrSMDA experiment produces soil moisture simulations that are in closer agreement with the reference SCAN dataset (except station 2068) than experiments OL and PrDA.

Figures 5.9f-j show the comparison of the 10-to-40-cm soil moisture layer. Here, we have to emphasize again that the overall lower-layers soil moisture estimates are improved after data assimilation (see Figure 5.8 and Table 5.2), but we present the time series with negative MRR in order to elucidate how the WRF-Noah model performs at a fine scale. It is first noted that the open-loop soil moisture simulations underestimate the reference SCAN data, while the PrSMDA experiment produces even drier soil moisture. Since the innovations (SMOS observations minus the first guesses) are often negative (Figures 5.9a-e), and the error correlation values are positive over the study areas (Figure 5.3e), it is expected to see drier soil moisture in the lower layer after data assimilation. Such degradation in the assimilation experiments is also relevant to the bias in the initial conditions. For stations 2006, 2047, 2061, and 2094, it can be seen that the soil moisture estimates from the

SCAN stations are wetter in the lower layers than in the top layer in the beginning of the experiment. Such variability is not captured well by the simulations. The results suggest that the large-scale assimilation of remotely-sensed soil moisture is sometimes not able to reproduce the fine-scale lower-layer soil moisture variability, arguably due to previously mentioned limitations (i.e., data resolution and soil heterogeneity).

Figure 5.10 shows the soil moisture time series at the stations with MRR>0.4 in the lower soil layer (see the blue highlight in Figure 5.8c). This figure reaffirms the effectiveness of both precipitation and soil moisture data assimilation at a fine scale. The hourly time series indicate that the assimilation of TRMM precipitation data removes spurious precipitation reflected in the open-loop experiment (see the orange arrows in Figure 5.10), which also results in a reduction of soil moisture in the lower 10-to-40-cm layer (Figures 5.10f-j). Assimilation of SMOS soil moisture further reduces the error and ultimately leads to the simulations in better agreement with the reference data for both the top and lower soil layers for all experiments. It is worthwhile to note that the difference of SCAN soil moisture time series between the top-10-cm and the 10-to-40-cm layers is on average much smaller in Figure 5.10 than in Figure 5.9. This implies that those areas shown in Figure 5.10 may have soils with less vertical heterogeneity, resulting in more effective soil moisture data assimilation.
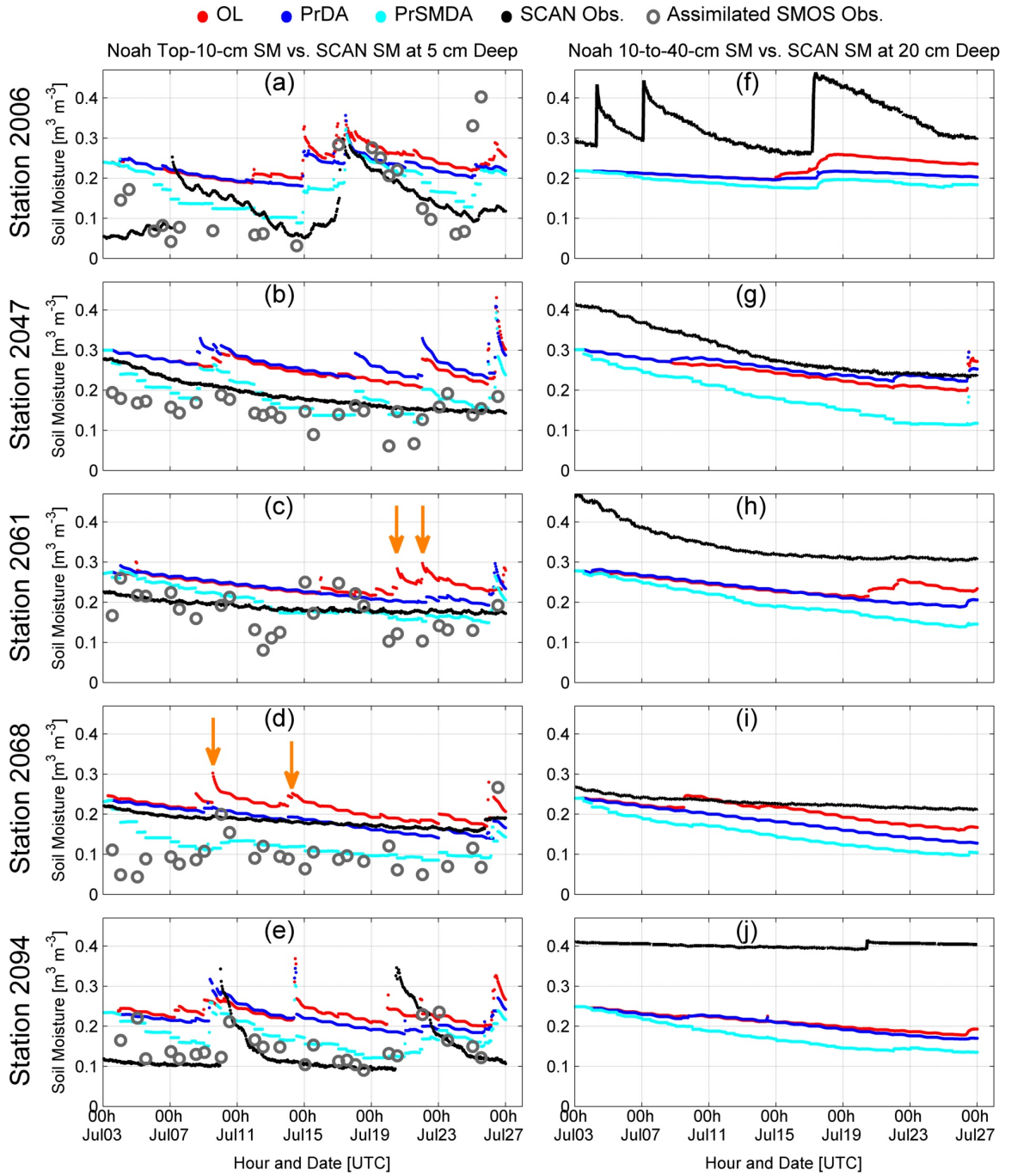
Figure 5.9: The comparison of the hourly soil moisture estimates from the selected SCAN stations with a negative MAE reduction ratio (MRR) (see yellow highlights in Figure 5.8c) and those from 9-by-9-km grids including the SCAN stations. The SCAN observations at a depth of 5 cm and the WRF simulations in the top 10-cm layer are shown in (a-e), while the SCAN observations at a depth of 20 cm and the WRF simulations in the 10-to-40-cm layer are shown in (f-j). Assimilated SMOS observations nearest to the selected SCAN stations are presented in (a-e).
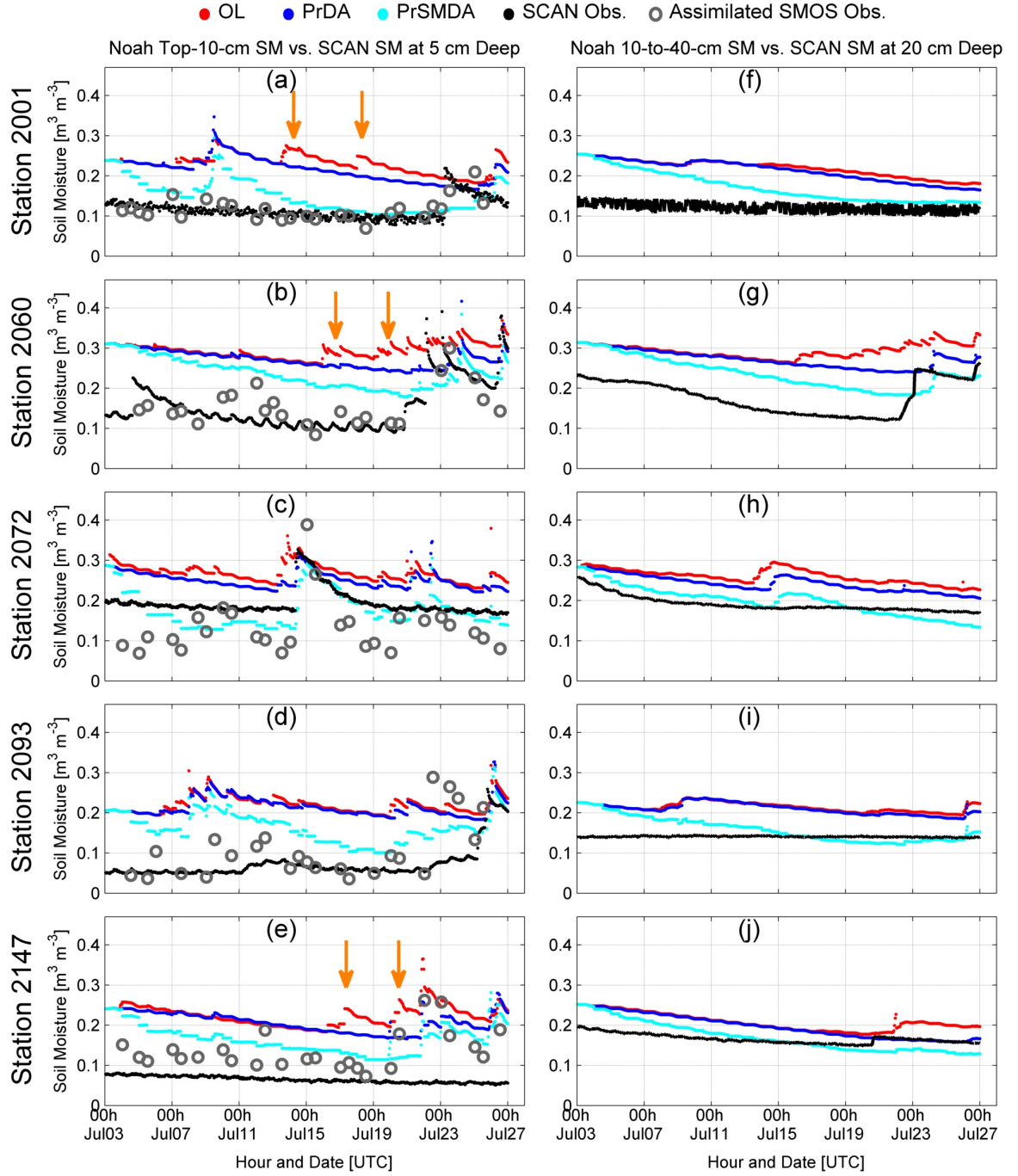
Figure 5.10: Same as Figure 5.9, except for stations with $MRR > 0.4$ (see blue highlights in Figure 5.8c).

5.3.3 Near-Surface Variables Verification against the CRN Data

This section compares the temperature at 2 m, the relative humidity at 2 m, the top-10-cm soil moisture, and the top-layer soil temperature of the WRF forecasts with those from the Climate Reference Network (CRN) dataset (see a map of 17 selected stations within the inner domain in Figure 5.11). Since the WRF model does not directly output the relative humidity at 2 m, we use the WRF outputs of specific humidity at 2 m, temperature at 2 m, and surface pressure to compute the relative humidity at 2 m based on the following equations (*Dingman*, 2002):

$$e^* = 611 \cdot exp\left(\frac{17.3 \cdot T}{T + 237.3}\right), \tag{5.2}$$

$$RH = \frac{q}{0.622 \cdot \frac{e^*}{P}} \cdot 100\%, \tag{5.3}$$

where e^* is the saturation vapor pressure in Pa, T is the temperature in °C, q is the specific humidity, and P is the pressure in Pa. We compare hourly observations from the 17 CRN stations to simulations of the 9-by-9-km grids that include them. Figure 5.12 shows the MAE of the comparison. Figure 5.12a demonstrates again that the assimilation of TRMM and SMOS data is helpful in reducing the error of soil moisture forecasts. However, such assimilation has only a marginal effect on soil temperature forecasts (Figure 5.12b), and results in degradation in the forecasts of the temperature and relative humidity at 2 m.

To explore the above results, we compare results of hourly top-10-cm soil moisture and soil temperature (a-b) and air temperature and humidity at 2 m (c-d) with observations at Des Moines, Iowa during 19-26 July 2013 (Figure 5.13). Note that because of the experiment design, it is possible to see discontinuity every six hours in the forecasts of soil temperature, air temperature, and relative humidity. As is evident, the results demonstrate the usefulness of precipitation and soil moisture data assimilation, reducing the systematic soil moisture bias occurring in the open-loop experiment (Figure 5.13a). Data assimilation often leads to higher soil temperature forecasts before the peak time (hours approximately prior to 00UTC) than that of open-loop forecasts (Figure 5.13b). However, since such change of soil temperature forecasts in the assimilation experiments corresponds to improvement in some
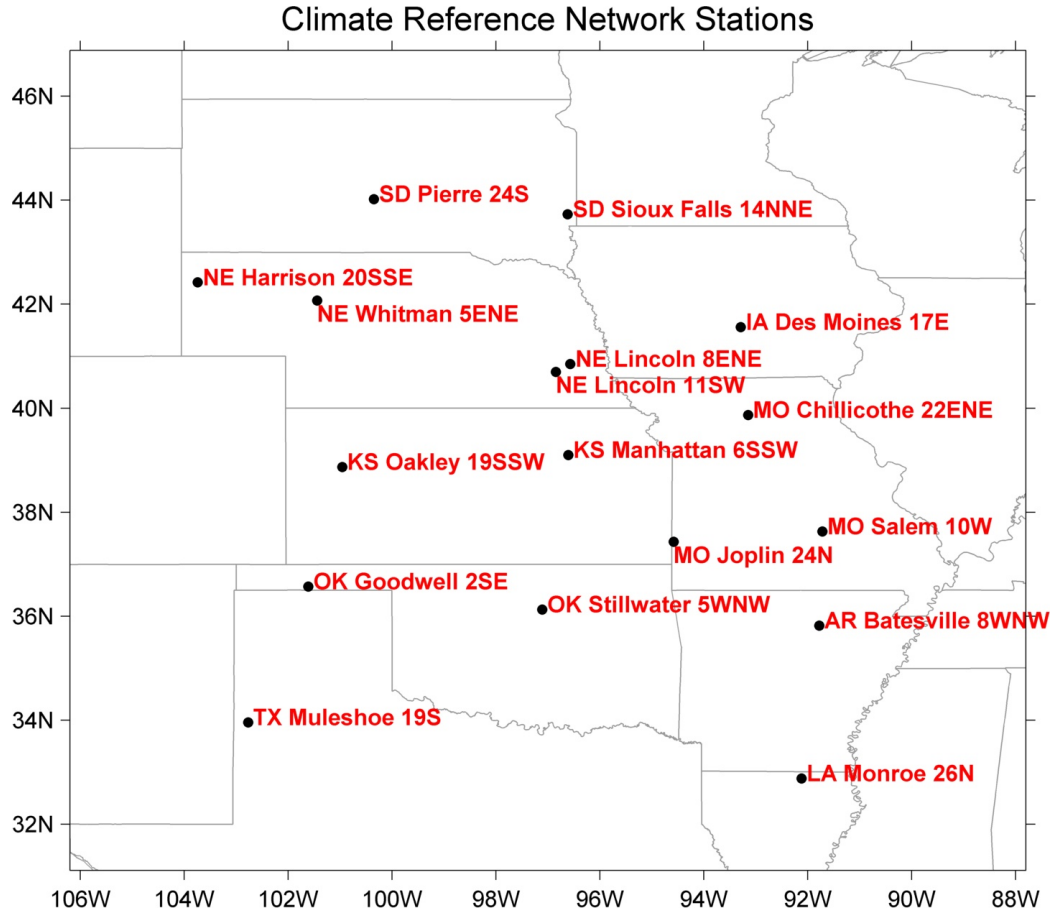
Figure 5.11: The locations and the standard IDs of the selected United States CRN stations.

of the days but overestimation in some other days, the effect of data assimilation on soil temperature estimates is on average marginal. For the air temperature and humidity, data assimilation often results in higher temperature and lower humidity during the daytime (i.e., the peak time of air temperature), which is likely due to reduced availability of soil moisture supply in the assimilation experiments (Figures 5.13c-d). Since we see a close agreement between the air temperature and humidity estimates from the open-loop experiment and those of the reference CRN dataset, except in July 21, data assimilation ultimately leads to degradation in the forecasts of near-surface temperature and humidity. The above results also indicate that the initial conditions obtained from the NCEP FNL dataset are more accurate for the estimates of near-surface air temperature and humidity than those of soil temperature and moisture; this is likely due to the fact that the NCEP Global Data Assimilation System (GDAS) that produces the FNL data corrects only atmospheric states.
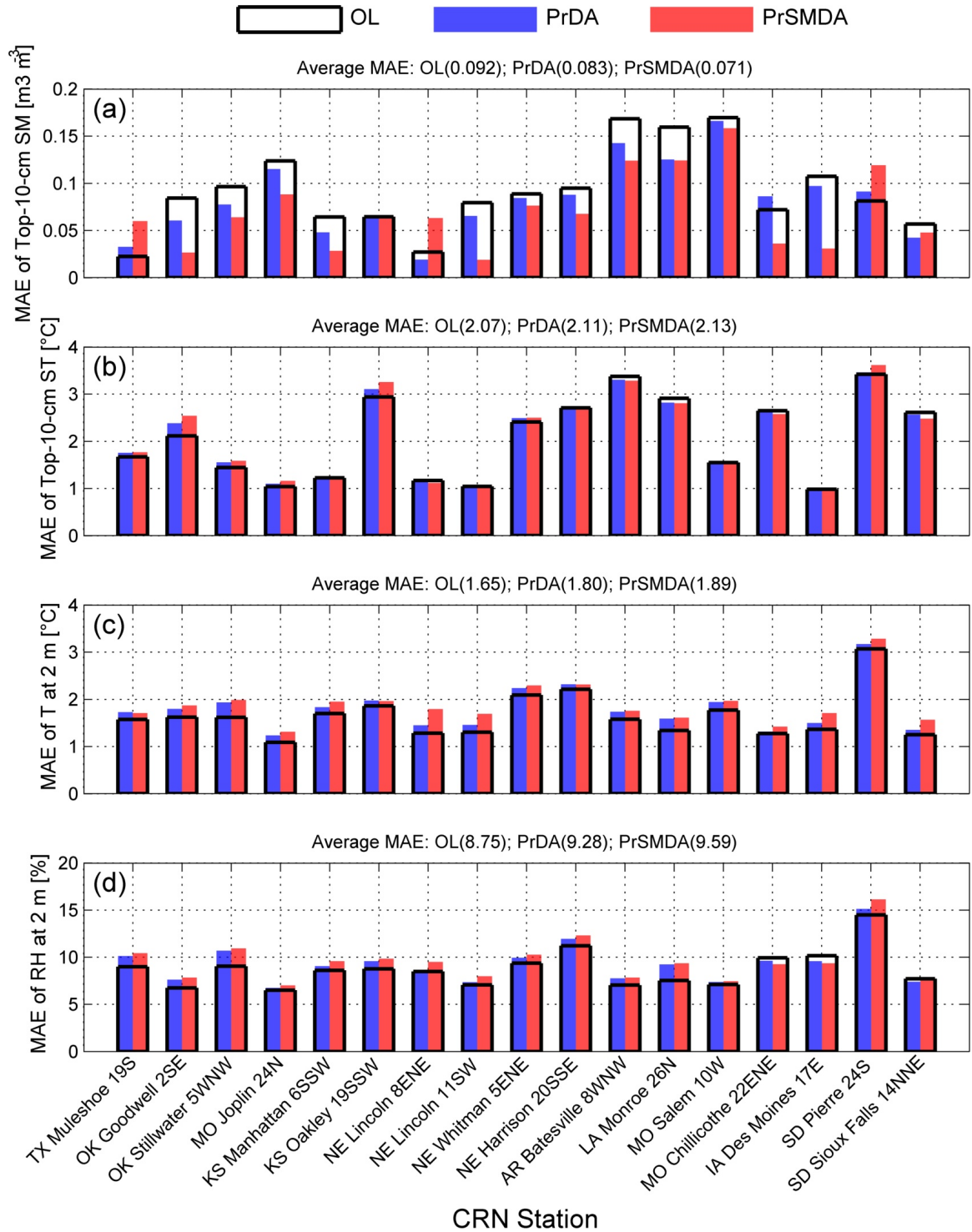
Figure 5.12: The mean absolute error (MAE) of hourly estimates from the CRN stations to those of the 9-by-9-km grids that include them. The comparisons of top-10-cm layer soil moisture and soil temperature are shown in (a-b), while those of air temperature and humidity at 2 m are shown in (c-d).
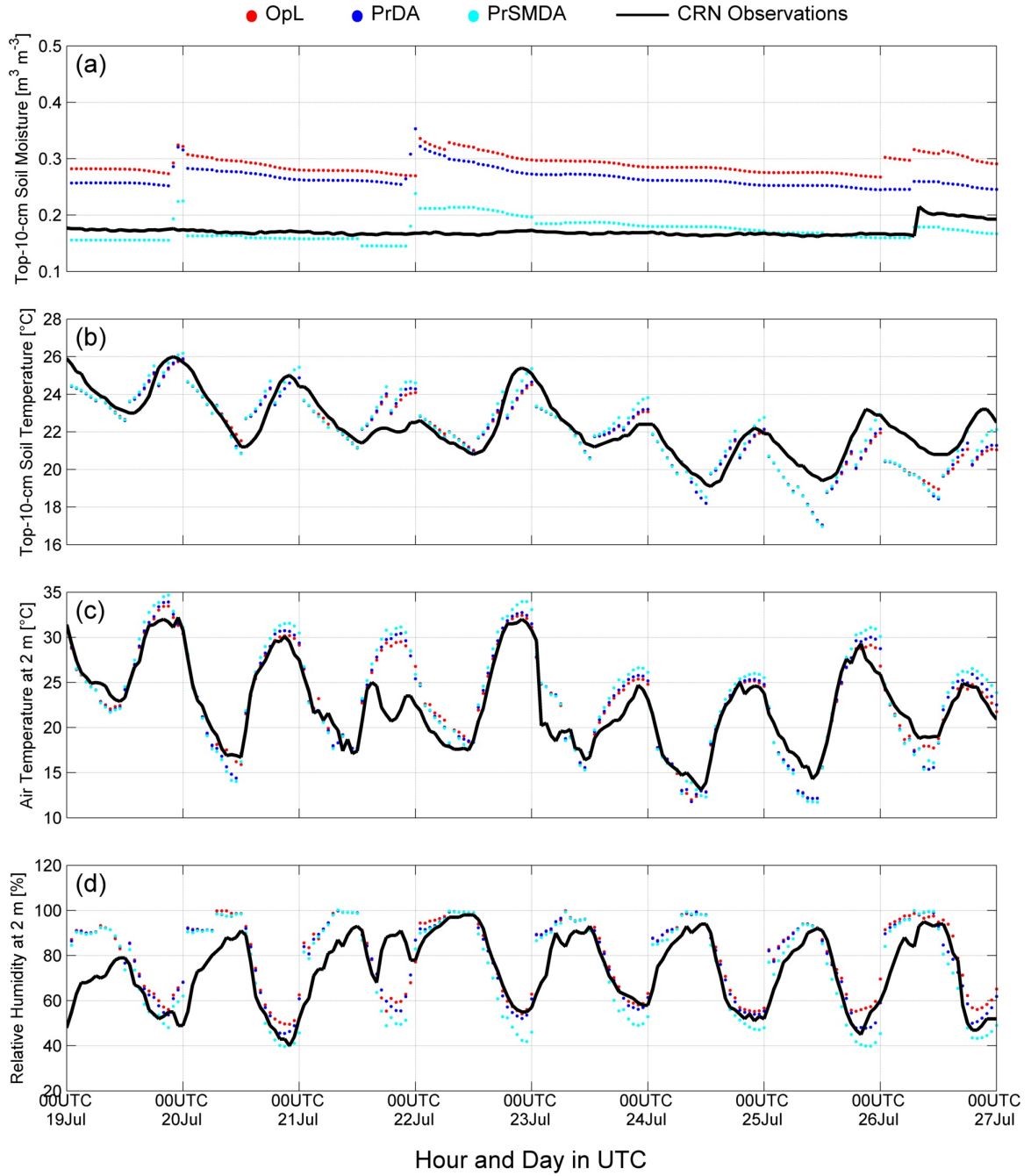
Figure 5.13: (a-b) Hourly top-10-cm soil moisture and temperature simulations of a 9-by-9-km numerical grid nearest to the selected station versus hourly CRN observations at 5 cm in station Des Moines, Iowa. (c-d) Hourly air temperature and relative humidity observations at 2 m of the Des Moines station with the corresponding simulations at its nearest 9-by-9-km grid.

5.3.4 Discussion of the Error Correlation between Soil moisture and Atmospheric States

This subsection discusses possible consequence if we include the error correlation between soil moisture and atmospheric states in the analysis procedure. Figure 5.14 shows the correlation between the forecast errors (η; see more detailed description and computation in Chapter 4) of the top-10-cm soil moisture and those of atmospheric states (i.e., the potential temperature, zonal wind, meridional wind, and specific humidity) at different pressure levels based the WRF-Noah simulations during 2013. The results show that the error correlation values are the highest during the summer, particularly large between potential temperature and specific humidity. It can be seen that the error correlation between the soil moisture and the potential temperature is negative near the surface, while that between the soil moisture and the specific humidity is positive with values approximately 0.1 from the surface up to the top of tropopause. These values imply that if such error correlation is considered in a data assimilation system, the assimilation of conventional data (e.g., radiosondes) may affect soil moisture analyses, and in reverse, the assimilation of soil moisture measurements may change the analysis of atmospheric states. The correlation values seem small, but the accumulated effect could be significant. More investigation is needed in order to better understand the error correlations and to use those in a fully-coupled data assimilation system.

5.4 Summary of the Chapter

This chapter bridges the efforts of previous chapters to study the relative impact of precipitation (Chapters 2 and 3) and soil moisture (Chapter 4) data assimilation on the predictions of precipitation, soil moisture, and other near-surface meteorological variables. The NMC method is used to estimate the background error for the atmospheric states including the stream function, velocity potential, temperature, pseudo relative humidity, and surface pressure; and the soil moisture states. Using the obtained background error covariance, several numerical experiments were performed for assimilating $0.25° \times 0.25°$ TRMM 3B42 precipitation every six hours and 36-by-36-km SMOS soil moisture observations every 12 hours
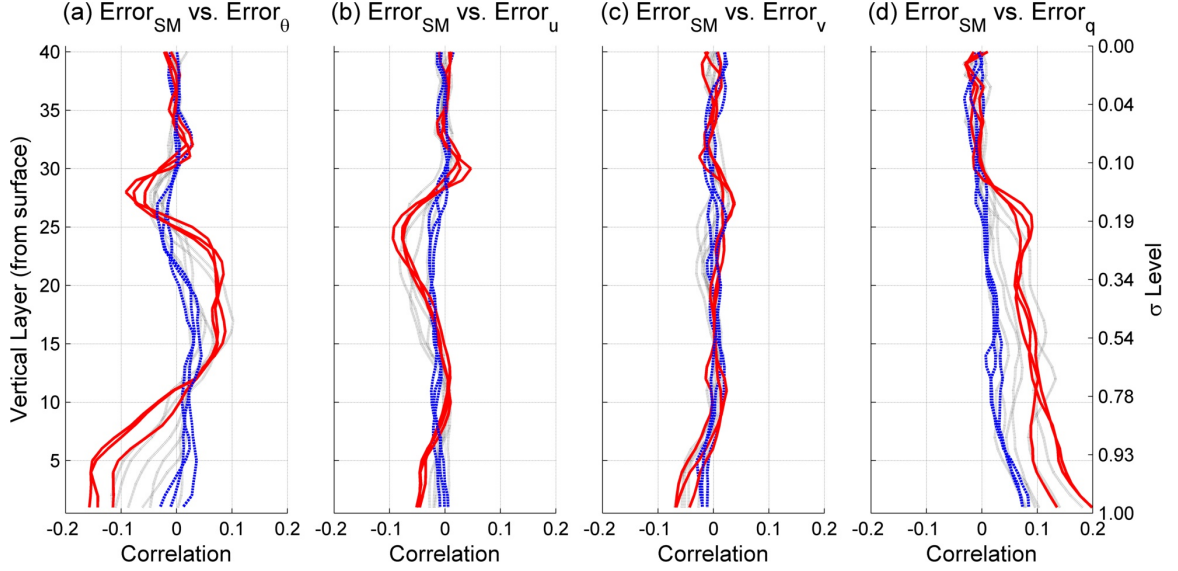
Figure 5.14: The correlation coefficient values of top-10-cm soil moisture (SM) forecast error relative to the forecast error of the potential temperature (θ; a), the zonal wind (u; b), the meridional wind (v; c), and the specific humidity (q; d) at different levels. The values are obtained based on the WRF-Noah simulations in each month of 2013. The red lines denote the results for the summer time (i.e., June, July, and August), the blue lines show the results for the winter season (i.e., December, January, and February), and the gray lines the results for the rest of the months.

into the WRF-Noah model.

The results show that adding SMOS data assimilation to the assimilation of TRMM data does not benefit the six-hour precipitation analysis compared to only assimilating the TRMM data. In contrast, the assimilation of TRMM and SMOS data is able to improve short-term soil moisture forecasts (relative to the Soil Climate Analysis Network dataset). In terms of mean absolute error (MAE), assimilation of TRMM data improves hourly 9-by-9-km soil moisture estimates of the top 10-cm and lower 10-to-40-cm soil layers by 10% and 4%, respectively. Inclusion of SMOS data assimilation with the TRMM data assimilation reduced MAE by an additional 25% and 2% for the top and the lower soil layers, respectively. We also compared the top-10-cm soil temperature and near-surface air temperature and relative humidity from the WRF-Noah experiments to those from the Climate Reference Network dataset. The comparison indicates that the joint data assimilation of TRMM and SMOS data has a marginal effect on the soil temperature simulations but degrades the simulations of temperature and humidity at 2 m, relative to those without any data

126

assimilation. The degradation is partially attributed to the quality of initial conditions derived from the NCEP FNL dataset, which is already very close to temperature and humidity of the ground-based reference CRN dataset.

CHAPTER VI

CONCLUSIONS AND RECOMMENDATIONS

6.1   Research Contributions and Findings

This thesis has introduced a modeling framework capable of assimilating and downscaling satellite precipitation and soil moisture data for the Global Precipitation Measurement (GPM) and Soil Moisture Active Passive (SMAP) missions. The focus is over the contiguous United States. Following are some conclusions.

Precipitation data assimilation and downscaling

Chapters 2 and 3 developed a framework for dynamically downscaling satellite precipitation data using a sophisticated mesoscale atmospheric model, the Weather Research and Forecasting (WRF) model, together with a recently-available (since 2012) precipitation assimilation component with four-dimensional variational data assimilation (4D-Var) in the WRF Data Assimilation (WRFDA) system. The chapters aim to produce fine-scale (i.e., hourly and less than 10 km) precipitation estimates for hydrological applications. This kind of work also re-visited several remaining challenges in direct assimilation of precipitation such as non-Gaussian error characteristics of precipitation, the discrepancy between full physics and it linearized representation, and inaccurate first guesses obtained from global climate models, often magnified at fine modeling resolutions (*Errico et al.*, 2007; *Lopez*, 2007; *Bauer et al.*, 2011b). We conducted experiments of assimilating precipitation data from the National Centers for Environmental Prediction (NCEP) Stage IV and Tropical Rainfall Measuring Mission (TRMM) 3B42 datasets on a study domain of 36-km grid spacing and utilized nested domains to provide downscaled precipitation. The results demonstrated that data assimilation is useful in improving precipitation analyses of resolutions as fine as 9 km but has only a marginal effect on the precipitation analyses of 4 km. We have identified a limitation of the WRFDA 4D-Var linearized model and illustrated the information loss of

assimilated TRMM data beyond the six-hour assimilation window.

In Appendix A, we preliminarily examined the impact of several precipitation products on streamflow simulations using a distributed hydrologic model, the TIN (Triangular Irregular Network)-based Real-time Integrated Basin Simulator (tRIBS) over the Turkey River basin, Iowa. Hourly 9-by-9-km precipitation estimates from the TRMM 3B42 dataset and the WRF simulations with and without assimilation of TRMM 3B42 data were used as inputs in tRIBS simulations. Despite improvement of precipitation analyses shown in Chapters 2 and 3, the precipitation resulting from WRF 4D-Var system led to significantly underestimated streamflow simulations. The employment of a quality control procedure for removing observation outliers and a constant precipitation error seems not "smart" enough to identify good and bad observations. Even though the data assimilation settings used in this appendix often produced precipitation analyses with better spatio-temporal variability, these precipitation analyses are underestimated and therefore led to the poor tRIBS streamflow simulations.

Soil moisture background error, data assimilation, and downscaling

Chapter 4 introduces the development of a variational data assimilation system using a state-of-art coupled land-atmosphere model for assimilating satellite soil moisture data. While most of the land surface data assimilation research were largely tested and reported with off-line applications without coupled to atmospheric models, this chapter proposes a system that obtains that soil moisture background error covariance based on the difference of 12- and 24-hour forecasts valid at the same time, which is commonly used in the community of atmospheric data assimilation and known as the National Meteorological Center (NMC) method. Using the Noah land surface model coupled to the WRF model, we characterized soil moisture background error and showed strong space-time variability of the error, with large magnitude occurring in the upper soil layers over the Great Plains during the summer. Our experiments also demonstrated that the variability of the soil moisture background error is not sensitive to the WRF parameterization of microphysics, cumulus clouds, and land surface. We also identified large biases in the background error over the

southeastern United States, caused by discrepancy between the WRF-Noah model and the NCEP final analysis (FNL) dataset. Finally, we examined the system by assimilating soil moisture data of 36-km resolution obtained from the Soil Moisture and Ocean Salinity (SMOS) satellite into the WRF-Noah model every 12 hours. SMOS data assimilation is able to improve hourly fine-scale (4×4 km) soil moisture simulations during the summer. With data assimilation, the simulations at a top 10-cm depth show a reduction of mean absolute error (MAE) and root-mean-square error (RMSE) of 35% and 33%, respectively, while those at the lower 10-to-40-cm layer have a MAE reduction of 9% and a RMSE reduction of 8%.

Joint assimilation of TRMM precipitation and SMOS soil moisture

Chapter 5 bridges the work of previous chapters to present a joint data assimilation system and quantifies the impact of precipitation and soil moisture data assimilation on the estimates of precipitation, soil moisture, and other meteorological variables such as temperature and humidity. This chapter conducted one-month experiments during July 2013 with assimilation TRMM 3B42 precipitation and SMOS soil moisture into the WRF-Noah model. Unlike operational weather forecasts systems that commonly use previously short-term forecasts as first guesses, the first guesses of the atmospheric states in this chapter are obtained from the NCEP FNL directly, while those of the soil moisture states use the six-hour forecasts from the previous cycle. This design indicates that the benefit of TRMM data assimilation on atmospheric states is marginal beyond the assimilation cycle, while the information of SMOS observations can be memorized by the WRF-Noah model. Our results show that SMOS data assimilation does not produce additional improvement of six-hour precipitation beyond TRMM data assimilation. In terms of MAE, TRMM data assimilation improves top-10-cm and 10-to-40-cm hourly 9-by-9-km soil moisture simulations by 10% and 4%, respectively, while SMOS data assimilation contributes an additional 25% and 2%, respectively. The assimilation of TRMM and SMOS data shows a marginal effect on six-hour forecasts of top-10-cm soil temperature and near-surface relative humidity but degrades those of near-surface temperature, partially attributed to good quality of the used

initial conditions derived from the NCEP FNL dataset.

6.2   Recommendations for Future Work

This work can be further extended by (1) assimilating various observations at a fine scale and (2) using fine-scale global datasets as first guesses. As the WRFDA system is capable of assimilating conventional data (e.g., in-site, radiosonde, and radiance observations), it would be worthwhile to assimilate additional available observations into the WRF model for analyzing the relative contribution of these additional observations in improving precipitation and soil moisture predictions. Assimilation of additional satellite soil moisture products (e.g., the Soil Moisture Active Passive (SMAP; *Entekhabi et al.* (2010); *Brown et al.* (2013)) and the Soil Moisture Operational Product System (SMOPS; *Zhan et al.* (2011)) could also improve the spatio-temporal coverage of data in land surface data assimilation. Another potential research direction is to study how soil moisture data assimilation affects low-frequency microwave radiative transfer modeling and its consequential impact on precipitation forecasts via radiance data assimilation. In addition, this work tested mainly NCEP FNL $1° \times 1°$ dataset as first guesses and conducted data assimilation experiments only with a domain of 36-km grid spacing. We suggest that data assimilation experiment needs to be further tested in a fine-resolution domain with first guesses obtained from high-resolution datasets such as NCEP Global Forecast System $0.25° \times 0.25°$ dataset and NCEP FNL $0.25° \times 0.25°$ dataset.

To capture nonlinear characteristics of precipitation, further research on the error structures is needed. Despite improvements in precipitation analyses reported in Chapters 2 and 3, we have noticed that the WRF 4D-Var system experienced difficulties in reproducing heavy rain at pixels with no- or low-precipitation background forecasts and had a tendency to overestimate convective rain, particularly for summertime small-scale precipitation extremes. We suggest that the linearized model in the 4D-Var algorithm and the smoothing effect of the background error covariance are the primary reasons behind the inability of the WRF 4D-Var system to represent the discontinuous in space and sporadic in time nature of convective precipitation. Rain and no rain classifier has been the key to statistical rainfall

estimation methods. Such classifier, if implemented, in conjunction with the 4D-Var optimization technique (i.e., assimilation is only implemented over rainy cells) has the potential to improve the performance of WRF 4D-Var simulations. The quality control procedure designed to filter out observational outliers, with a constant precipitation error, rejected many extreme observed precipitation that contained information particularly useful for hydrologic applications. Therefore, for assimilating more extreme values, it is suggested to logarithmically transform precipitation prior to data assimilation. The present data assimilation effort can also be extended by relaxing the assumption of a constant precipitation error and using a more realistic error characterization scheme that properly accounts of uncertainty in observations. Unlike assimilation of remotely-sensed observations that have mixed distribution (e.g., rainfall), assimilation of observations such as satellite radiances with a continuous distribution has the potential to improve the WRF 4D-Var simulations. Furthermore, inclusion of additional control variables such as vertical wind velocity, cloud water, and rain water in estimating atmospheric background error covariance, made available since 2013 (*Wang et al.*, 2013), also has potential to further extend the present study.

In this work, the soil moisture initial conditions obtained from the NCEP FNL dataset show apparent biases. Therefore, it is important to test the developed soil moisture data assimilation system with the WRF-Noah model using bias-corrected soil moisture initial conditions. In addition, a preliminary investigation reported in Chapter 5 indicated a weak correlation between the errors of the soil moisture states and those of the temperature and humidity states within the troposphere. We suggest to estimate a background error covariance matrix for atmospheric states and land surface states simultaneously and to study the effect of this matrix on the assimilation of precipitation and soil moisture. Since soil moisture contains some memory of most recent rainfall, this comprehensive error covariance would also provide an opportunity for studying how atmospheric states are corrected in response to the assimilation of soil moisture and then whether precipitation predictions can be improved.

The other potential future direction includes analyzing the role of land surface information in the performance of data assimilation system. For instance, moist air parcels traveling

through mountainous areas often lead to enhanced precipitation extremes, and soil textures have strong control on soil moisture variability. Therefore, it is advisable to account for characteristics such as topography and soil texture while evaluating the performance of the assimilation of precipitation and soil moisture, respectively.

APPENDIX A

COMPARISON OF PRECIPITATION PRODUCTS AND THEIR USE IN STREAMFLOW PREDICTION OVER THE TURKEY BASIN, IOWA

A.1 Overview of the Chapter

To explore the usefulness of the WRF precipitation estimates with and without 4D-Var assimilation, we use them as inputs to a simulation of the Turkey River basin, Iowa ($\sim$4000 km2). We compare to other precipitation products available at the site, particularly observations made during the NASA Iowa Flood Studies (IFloodS) field campaign (April to June 2013). Simulations of the Turkey River basin are made with the distributed hydrologic TIN (Triangular Irregular Network)-based Real-time Integrated Basin Simulator (tRIBS) (*Ivanov et al.*, 2004a,b). The precipitation products used include the WRF open-loop simulation, WRF 4D-Var simulation, the TRMM 3B42 dataset, and 20 IFloodS rainfall gauges. The rest of this appendix is organized as follows. Section A.2 describes the study area and the precipitation products. Section A.3 presents the precipitation comparison and streamflow simulations using the tRIBS. Section A.4 summarizes this appendix and major findings.

A.2 Methodology

In this section, we describe the study area, the Turkey River basin, the Iowa Flood Studies (IFloodS) campaign, the tRIBS, and the datasets used for analysis and simulations.

A.2.1 Turkey River Basin

The Turkey River basin, located in northeastern Iowa, has an average annual precipitation roughly 910 mm and a drainage area around 4000 km^2. The elevation of the basin ranges between 190 and 424 m with a flatter upper watershed and deeply-carved valleys downstream (Figure A.1a). The upper watershed, identified as the Iowan Surface, is dominated
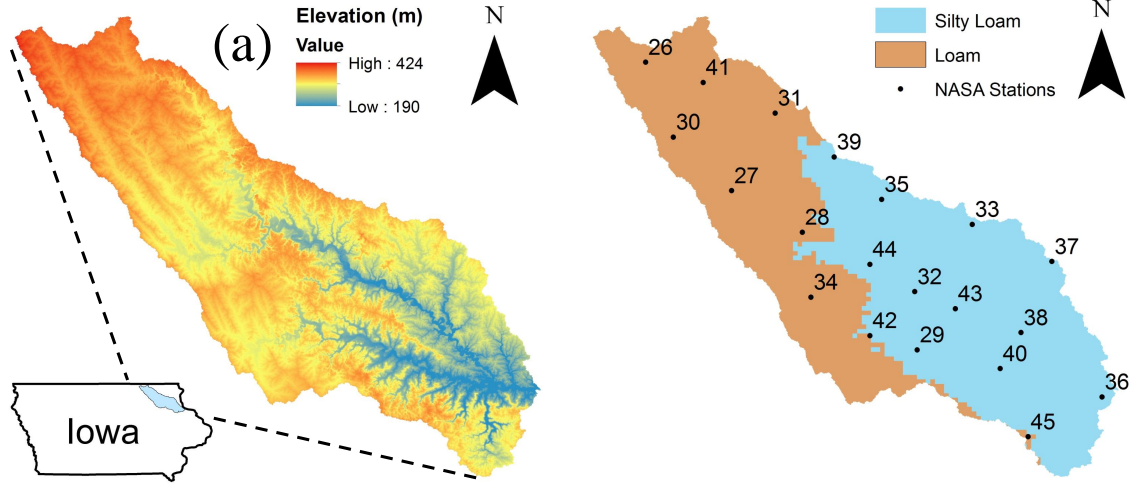
Figure A.1: The digital elevation model (DEM) (a) and soil types (b) in the Turkey River basin. The western part of the basin is characterized as loamy soil (the Iowan Surface), while the eastern part is silty loam soil (the Paleozonic Plateau). Location of the twenty rain gauges during the NASA IFloodS campaign is shown in (b).

by loamy soil, while the lower part of the basin, known as the Paleozoic Plateau, is dominated by silty loam (Figure A.1b). The primary land use is agricultural with approximately 56% coverage of the basin, followed by grass/pasture at 25% and forest at 16%. More details can be found in *Iowa Flood Center* (2014). The United States Geology Survey (USGS) operates a streamflow gauge located at Garber (#05412500), near the outlet of the basin. This gauge station is also included in the USGS Hydro-Climatic Data Network 2009 and described as not very much impacted by human control (*Lins*, 2012).

A.2.2 IFloodS Campaign

The IFloodS (http://pmm.nasa.gov/ifloods) took place in northeastern Iowa during April to June 2013. IfloodS is the first integrated hydrologic campaign to support ground validation activities for the Global Precipitation Measurement (GPM) mission (*Hou et al.*, 2014). The campaign employed numerous instruments, including multi-frequency polarimetric radar, disdrometers, rain gauges, and soil moisture sensors (*Hou et al.*, 2014; *Cunha et al.*, 2015). Among the instruments, 20 rain gauges were installed over the Turkey River basin (see a map of gauges in Figure A.1b). The measurements, at a frequency of 15 minutes, are available at http://iowafloodcenter.org/projects/ifloods/.

A.2.3 Hydrologic Model: tRIBS

The TIN (Triangular Irregular Network)-based Real-time Integrated Basin Simulator (tRIBS) (*Ivanov et al.*, 2004a,b) is used in this study. tRIBS is a physically-based spatially-distributed hydrological model that accounts for the effects of heterogeneous and anisotropic soil and the spatial variability of precipitation and near-surface meteorological (e.g., pressure, temperature, humidity, wind speed, and incoming solar radiation) fields. It has also been used as a framework for simulating shallow landslides and sediment fluxes (*Arnone et al.*, 2011; *Francipane et al.*, 2012). A modified modeling framework with dynamic vegetation component, known as tRIBS-VEGGIE, has also been used in many research studies (*Ivanov et al.*, 2008a,b; *Flores et al.*, 2009, 2012, 2014; *Lepore et al.*, 2013; *Sivandran and Bras*, 2012, 2013; *Arnone et al.*, 2014). The tRIBS model can simulate at fine temporal (minutes to hourly) and spatial (10-100 m) scales. The employment of irregular TIN meshes allows for variable grid sizes and the reduction of the number of computational elements without losing information significantly (*Vivoni et al.*, 2004). The tRIBS model includes physical parameterizations of precipitation interception, surface energy balance, evapotranspiration, infiltration, groundwater dynamics, lateral moisture transfer in the unsaturated and saturated soils, and runoff routing. The total surface runoff is computed as the accumulation of four runoff processes, including infiltration runoff, saturation runoff, perched runoff, and groundwater exfiltration runoff.

Static maps of a TIN mesh and soil texture were prepared for the Turkey River basin prior to the computation (Dr. Satish Bastola, personal communication). Based on 1-arc-second elevation data from the National Elevation Dataset, we use the hydrological similarity-based approach developed by *Vivoni et al.* (2004) to derive the TIN meshes. Figure A.2 shows the TIN mesh with 16,517 Voronoi polygons. Large Voronoi polygons are created in the western part of the basin (the Iowan Surface), because of the relatively flat topography, while dense and small polygons can be seen in the eastern part of the basin (the Paleozonic Plateau). For soil texture, we use the soil characterization from the United States Department of Agriculture (http://websoilsurvey.nrcs.usda.gov) to assign two dominant soil types (i.e., loam and silty loam) over the Turkey River basin (Figure A.1b).
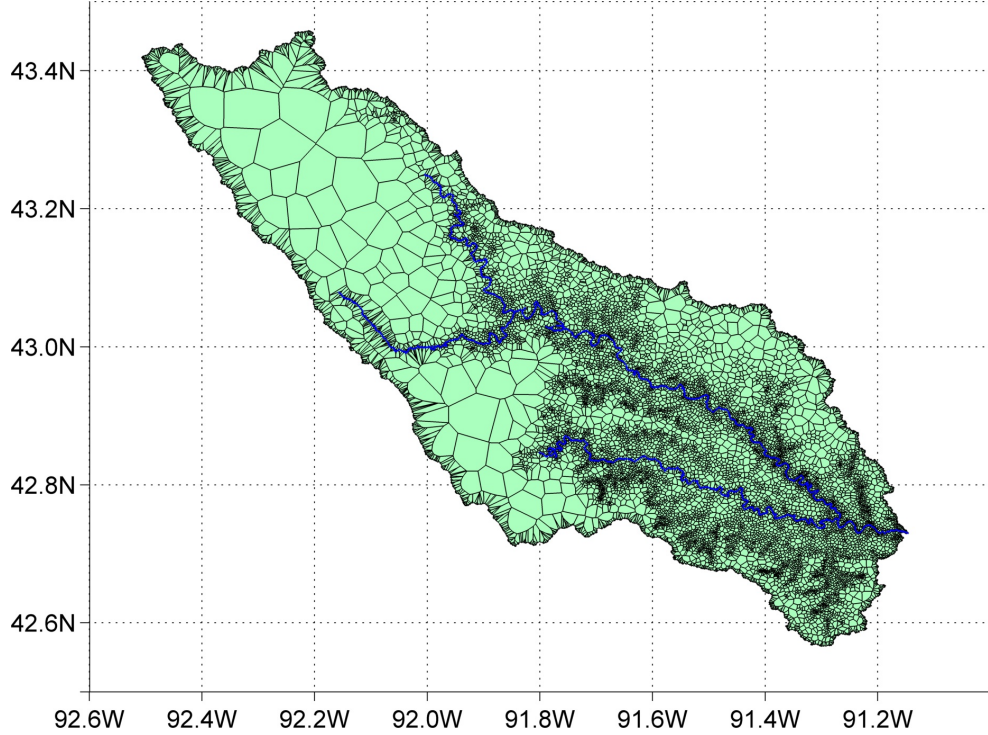
Figure A.2: The Voronoi polygon network of the Turkey River basin.

A.2.4 Dataset Description and Processing

In this subsection, we describe the datasets used for rainfall analysis and tRIBS simulations. Those datasets include the hourly precipitation obtained from the 20 IFloodS gauges (see Figure A.1b), TRMM 3B42, the WRF simulations with and without precipitation assimilation. Also used are the hourly meteorological data from the NLDAS. We discretize the Turkey River basin into 57 9-by-9-km grids (Figure A.3), on which all the precipitation and meteorological data are interpolated or simulated. Brief descriptions of each dataset are as follows:

- IFLOODS: Hourly precipitation from 20 IFloodS gauges are interpolated onto 57 9-by-9-km grids using the nearest neighbor approach.

- TRMM: We employ the TRMM 3B42 version 7 precipitation dataset at a spatial resolution of $0.25°\times0.25°$ and a temporal resolution of three hours (*Huffman et al.*, 2007). The data are linearly-interpolated onto the 57 grids.

- WRFOL: We use the 9-by-9-km precipitation outputs corresponding to the 57 grids
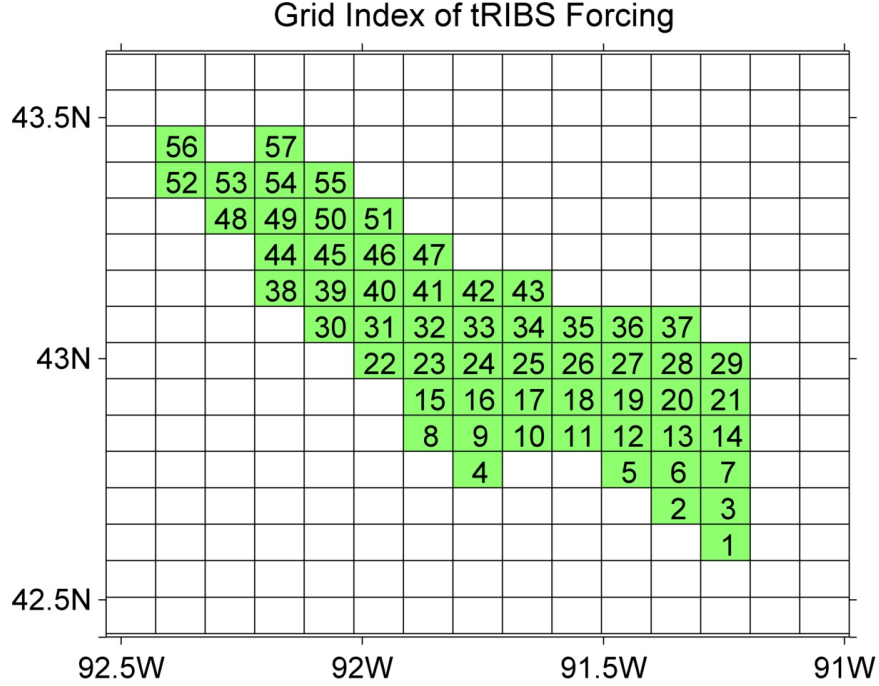
Figure A.3: The 9-by-9-km grids of the Turkey River basin for the comparison of precipitation products and the forcing of tRIBS.

from the WRF open-loop experiments from May to June, 2013. The experiment setting and model configurations of this run is the same as the open-loop experiment in Chapter 5.

- WRFDA: same as WRFOL, with assimilation of six-hour TRMM 3B42 precipitation. Detailed data assimilation experiment settings can be found in Chapter 5.

- NLDAS: NLDAS uses the atmospheric forcing from the North American Regional Reanalysis (NARR) to drive four land surface and hydrologic models. The precipitation is adjusted and disaggregated to an hourly scale according to the National Oceanic and Atmospheric Administration (NOAA) Climate Prediction Center (CPC) unified precipitation analysis, the monthly Parameter-elevation Regressions on Independent Slopes Model (PRISM), and the NCEP Stage II radar data (*Xia et al.*, 2012). We interpolate the surface pressure, humidity, temperature, wind, and incoming solar radiation from the NLDAS onto the 57 grids using the Earth System Modeling Framework (ESMF) software.

A.3 Results and Discussions

A.3.1 Rainfall Product Analysis

To understand the spatial variability of each precipitation product at a sub-basin scale, we compare hourly 9-by-9-km precipitation estimates during May 1 to June 25, 2013 from TRMM, WRFOL, and WRFDA relative to those of IFLOODS as a reference dataset. Figure A.4 shows the bias over 57 grids of each product during the two periods: May 1 to May 28 and May 29 to June 25. We observe that TRMM precipitation during the first half of the period underestimates IFLOODS data, while the situation is reversed during the second half (see Figure A.4a and A.4d). It turns out that WRFOL has the smallest bias on average among all the three products, but large positive biases are seen locally (see the eastern part of basin in Figure A.4b and the middle part in Figure A.4e). These local biases are reduced after assimilation of TRMM data. However, the domain-mean bias of WRFDA is very negative (see Chapter 3 for relevant discussions). In terms of the mean absolute error (MAE), the hourly 9-by-9-km precipitation estimates from WRFOL have on average the poorest agreement with the reference IFLOODS (Figure A.5). Assimilation of TRMM data significantly reduces the MAE. For the first period, WRFDA even shows the lowest MAE among all three products. Furthermore, in terms of correlation, the temporal variability of precipitation is fairly captured by TRMM, while it is not captured well by WRFOL (Figure A.6).
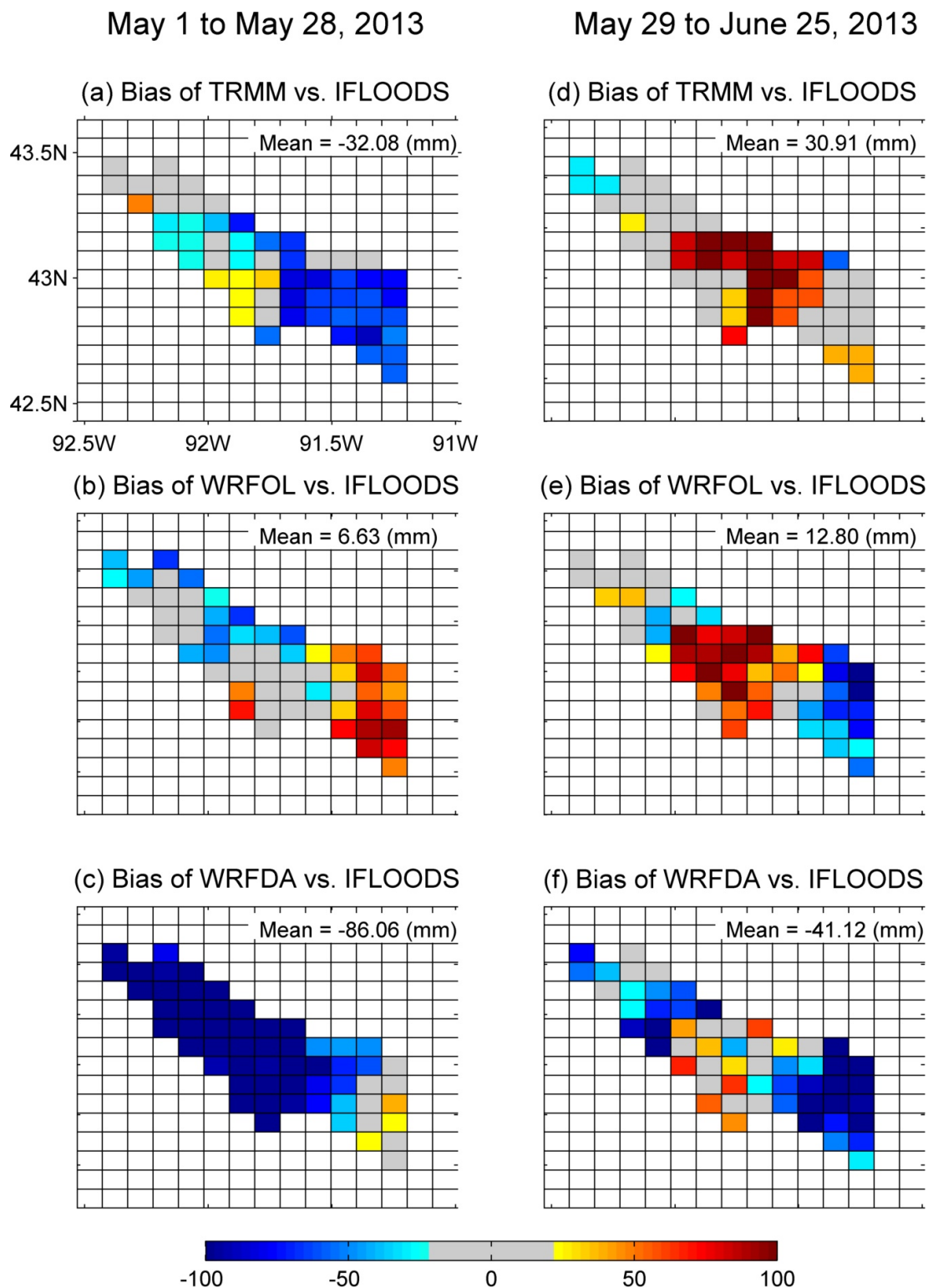
Figure A.4: The bias of hourly 9-by-9-km precipitation estimates from TRMM, WRFOL, and WRFDA relative to those from IFLOODS during May 1 to May 28, 2013 (a-c) and during May 29 to June 25, 2013 (d-f). The mean values of the bias over the Turkey River basin are also reported.
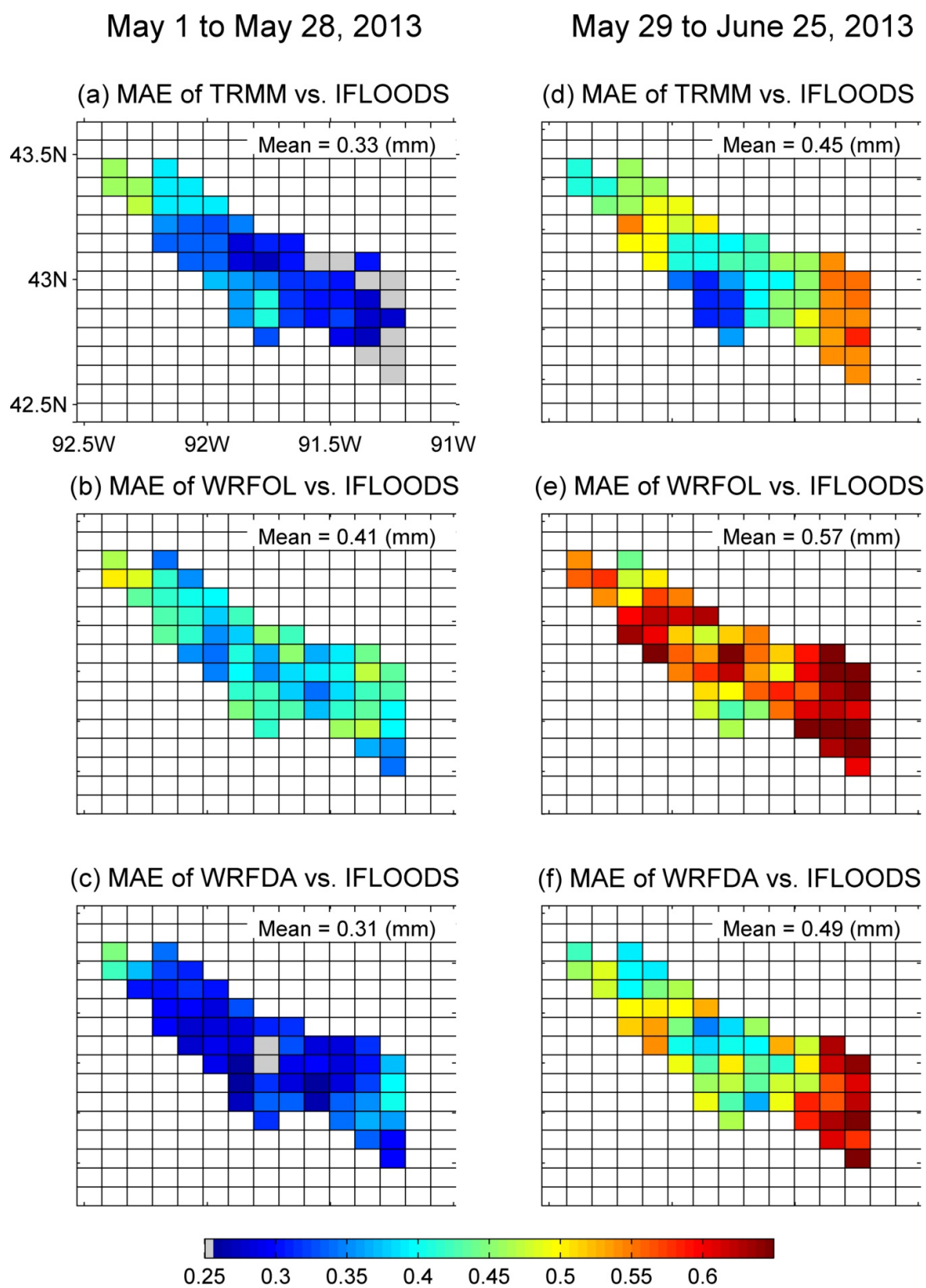
Figure A.5: Same as Figure A.4, except for metric mean absolute error (MAE).
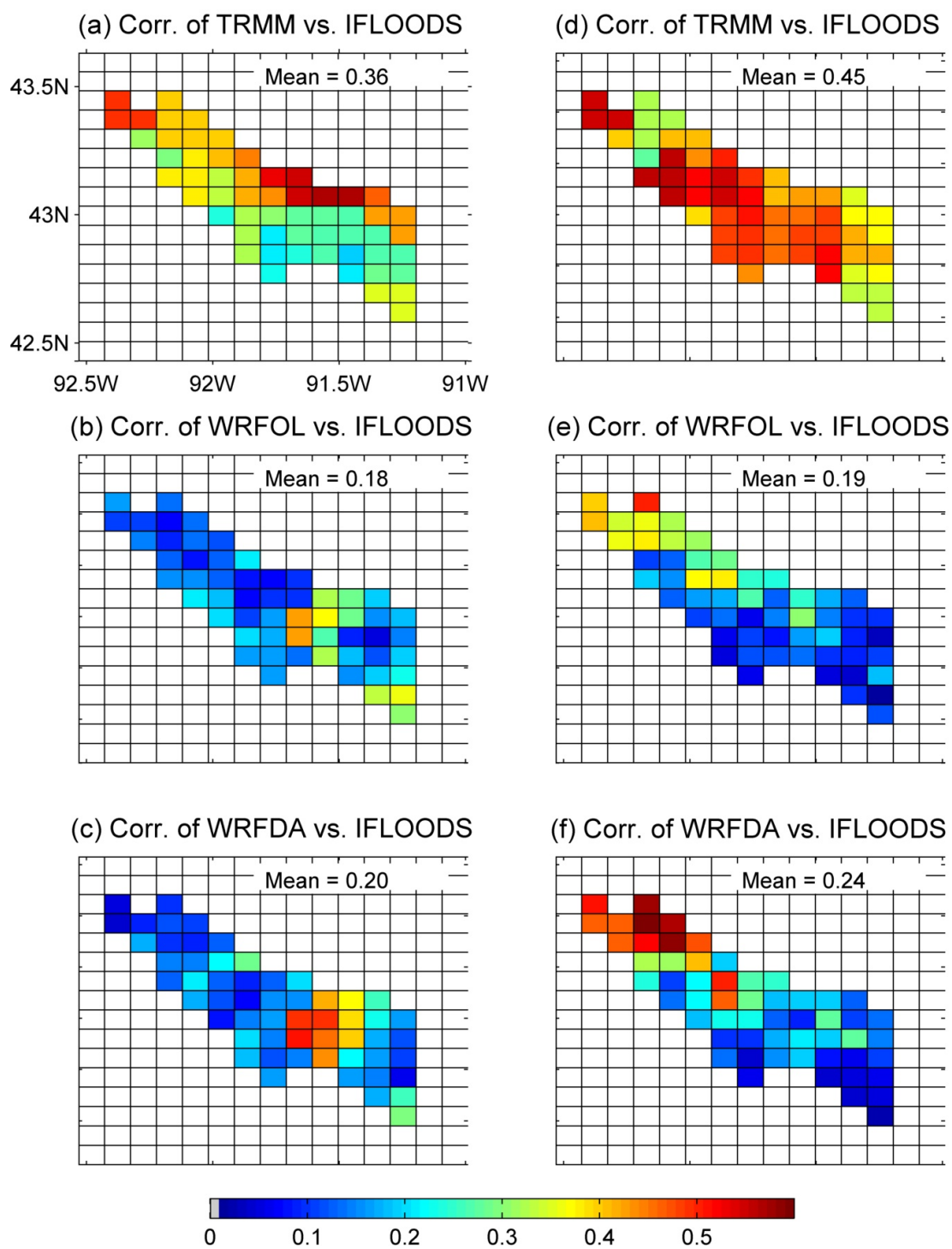
Figure A.6: Same as Figure A.4, except for metric correlation coefficient.

A.3.2 tRIBS streamflow sensitivity and calibration

A hydrologic model typically requires calibration and validation prior to applications. According to *Ivanov et al.* (2004a,b), important tRIBS calibration variables include the saturated hydraulic conductivity (K_s; mm h^{-1}), conductivity decay parameter (f), and anisotropy ratio of hydraulic conductivity; and the Manning's channel roughness (n_e) and the hillslope velocity parameters for channel routing. Considering that the Turkey River basin has two dominant soil types and a relatively large drainage area, we manually calibrate the tRIBS by tuning two soil parameters (K_s and f) and n_e by comparing tRIBS streamflow simulations at the outlet relative to the USGS observations at Garber (station #05412500). IFLOODS precipitation during April 23 to June 25, 2013 is used to simulate streamflow. Synthetic 15-mm rainfall was added to the first hour of the simulation to "wet" the model, and the period of April 23-30 was used for model spin-up. A series of experiments were conducted using different combinations of K_s, f, and n_e, while fixing other soil and channel parameters calibrated and provided by Dr. Satish Bastola at the Georgia Institute of Technology. K_s=13 mm h^{-1}, f=0.7, and n_e=0.016 are considered the final calibrated parameters, and all other calibrated model parameters for the two soil types can be seen in Table A.1. Figure A.7 shows examples of the sensitivity of streamflow simulations to various combinations of parameters K_s and n_e during May 1 to June 25, 2013. The results show that a lower K_s value leads to increased streamflow simulations, and vice versa. A lower value of n_e results in an earlier occurrence of a runoff and a higher peak. It is noted that the simulated peak around June 23, 2013 is significantly underestimated, which is also the case in *Thorstensen et al.* (2016).

Table A.1: tRIBS soil parameters and their calibrated values using in this study.

Parameter	Description	Unit	Silty Loam	Loam
K_s	Saturated hydraulic conductivity	$mm\ h^{-1}$	13	13
θ_s	Saturation soil moisture content	-	0.435	0.420
θ_r	Residual soil moisture content	-	0.027	0.030
λ_0	Pore-size distribution index	-	0.22	0.20
ψ_b	Air entry bubbling pressure	mm	-111	-150
f	Conductivity decay parameter	mm^{-1}	0.7	0.7
A_s	Anisotropy ratio for saturated zone	-	200	200
A_u	Anisotropy ratio for unsaturated zone	-	200	200
n	Total porosity	-	0.484	0.452
k_s	Volumetric heat conductivity	$J\ m^{-1}\ s^{-1}\ K^{-1}$	0.214	0.214
C_s	Soil heat capacity	$J\ m^{-3}\ K^{-1}$	2,136,115	2,136,115
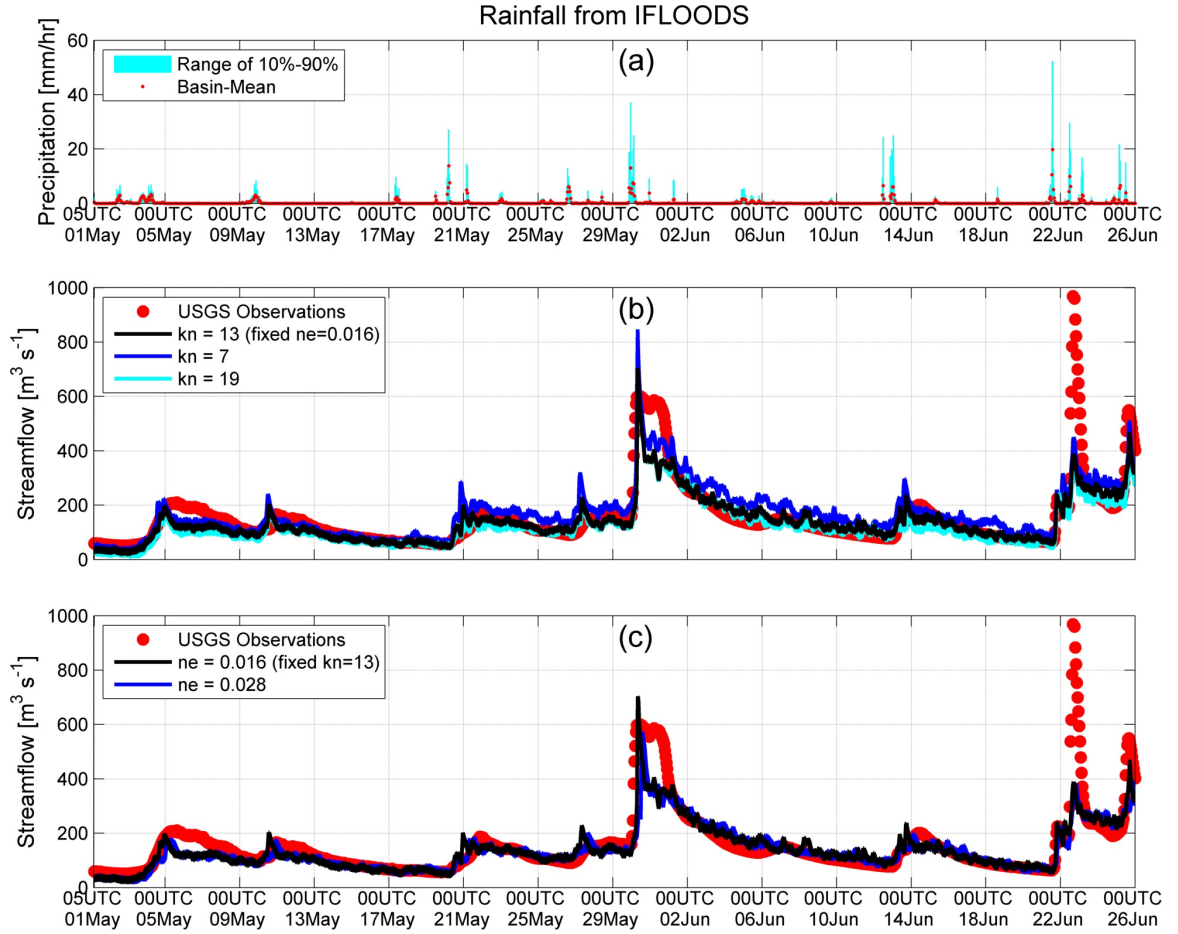
Figure A.7: (a) Hourly precipitation from IFLOODS, including the domain means (red dots) and the range (blue bars) between 10% and 90% of the precipitation fields of each hour. (b-c) The sensitivity of tRIBS streamflow simulations forced with IFLOODS precipitation to the parameterization of saturated hydraulic conductivity (K_s) and channel roughness (n_e). The hourly observations are obtained from USGS gauge 05412500.

144

A.3.3 tRIBS Simulated Streamflow with Various Rainfall Products as Inputs

This subsection presents the tRIBS streamflow simulations forced with various rainfall products as inputs, including IFLOODS, TRMM, WRFOL, and WRFDA (see Section A.2.4 for detailed description). All the scenarios have the same initial conditions starting on May 1, 2013 and run until June 25, 2013. As discussed in Section A.3.1, we arbitrarily separated the streamflow simulations into two periods: May 1 to May 28 (Figure A.8) and May 29 to June 25 (Figure A.9). The bias, MAE, root-mean-square error (RMSE), and correlation of hourly streamflow simulations forced with TRMM, WRFOL, and WRFDA relative to those with the reference IFLOODS is reported in Table A.2. For the first periods, it turns out that WRFOL streamflow simulations represent the IFLOODS results well, particularly during the first ten days. WRFDA and TRMM streamflow simulations capture a few of the peaks but underestimate for majority of the time. Even though it was reported in Section A.3.1 that WRFDA and TRMM precipitation is in closer agreement with IFLOODS precipitation, in terms of the MAE and correlation, respectively, than WRFOL precipitation, the precipitation bias appears a dominant factor in streamflow simulations. In Figure A.9, TRMM streamflow simulations seem to represent IFLOOS simulations well. However, significant streamflow overestimation using TRMM is seen during May 31 to June 12, leading to a MAE and a RMSE greater than those for WRFOL streamflow simulations (Table A.2). Because of negative precipitation bias, WRFDA streamflow simulations also show significant underestimation during the second period.

Table A.2: The metrics (the bias, mean absolute error (MAE), root-mean-square error (RMSE), and correlation coefficient (R)) obtained by comparing hourly streamflow simulations during May 1 and June 25, 2013 using various rainfall products as inputs in the tRIBS simulations to those using IFLOODS precipitation.

	May 1 to May 28, 2013				May 29 to June 25, 2013			
	Bias	MAE	RMSE	R	Bias	MAE	RMSE	R
TRMM	-48.36	56.13	64.24	0.56	87.88	90.72	128.69	0.87
WRFOL	27.84	32.64	41.09	0.76	-30.16	80.24	102.39	0.22
WRFDA	-55.30	55.64	66.86	0.26	-100.49	110.65	139.20	0.18
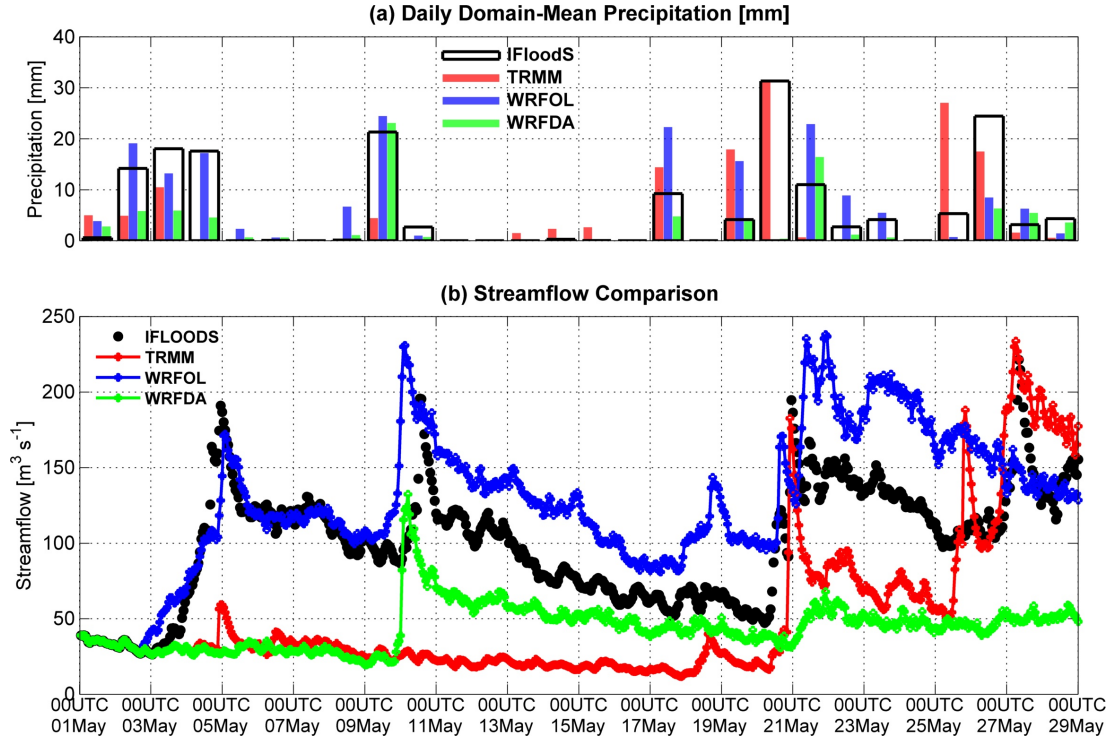
Figure A.8: (a) Daily basin-mean values of various precipitation products; (b) comparison of hourly streamflow simulated with tRIBS using various precipitation products as inputs during May 1 to May 28, 2013.
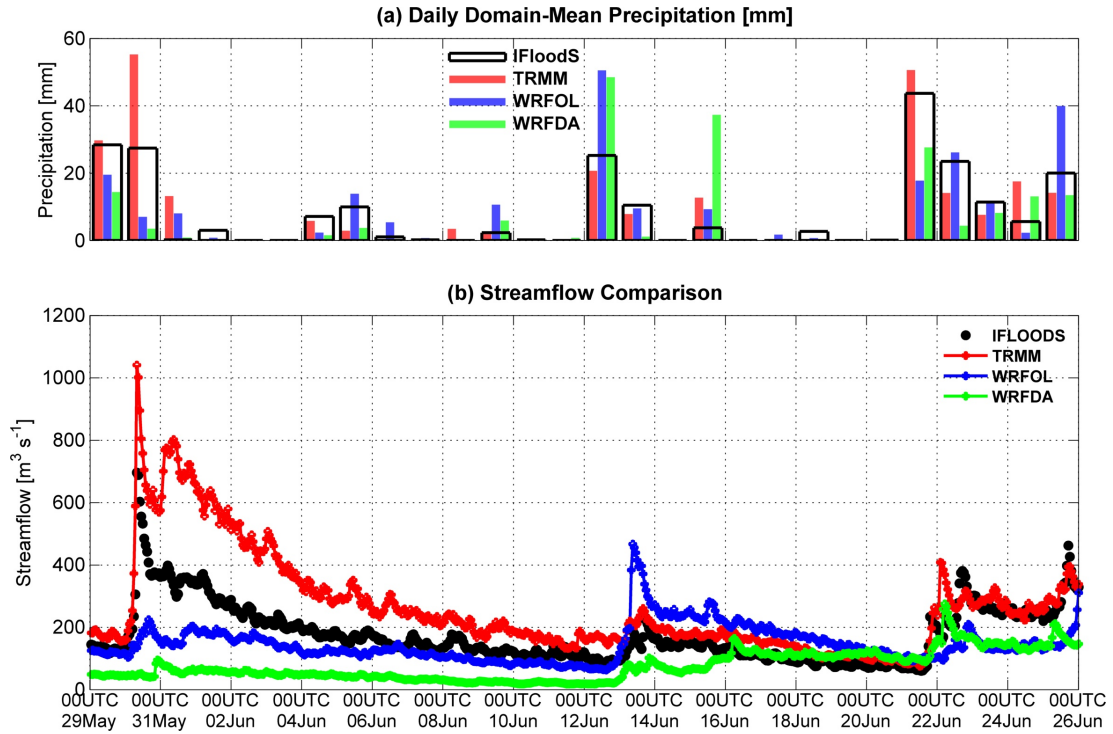
Figure A.9: Same as Figure A.8, except for the periods of May 29 to June 25, 2013.

146

Even though the 4D-Var precipitation analyses resulted in a poor performance in the streamflow simulations, we stress that the streamflow simulation results shown in this appendix is not conclusive as it only reflects performance of 4D-Var analyses over a small portion ($\sim$4000 km^2) of the WRF inner domain ($\sim$3 million km^2). The results and discussion in Chapters 2 and 3 demonstrates the capability of the WRF 4D-Var system over a large domain, covering multiples states in the contiguous United States, through a series of large- and fine-scale comparison. Figure 2.9 shows that in the majority of pixels, the WRF 4D-Var simulations outperform the open-loop simulations. However, it is apparent from the figure that at local scale the performance of 4D-Var precipitation analyses can significantly degrade and subsequently degrade streamflow simulations.

In the meanwhile, the applications in this appendix convey several key messages regarding the improvement of the proposed data assimilation and modeling framework. First, a constant observational error of the WRF 4D-Var system, assumed in this thesis, may not be the best for assimilating the TRMM data. For example, during May 2-4, WRFOL reproduced IFLOODS well, while TRMM underestimated rainfall as compared to the reference data (Figure A.8a). During these three days, instead of keeping its original background states as close as possible, the WRF 4D-Var system trusted more the TRMM observations, leading to underestimation. Unlike ground-based measurements such as the NCEP Stage IV dataset, TRMM is commonly known for its regression-based retrieval approach that often do not work well over land in a cool season as compared to a warm season (e.g, *Ebtehaj et al.* (2016)). It would make sense to use time-varying adaptive observations error for the assimilation of TRMM precipitation. Second, correction of biases in model-based precipitation is important for hydrologic applications. Third, since streamflow prediction is one of the most important hydrological applications for a precipitation product, it would be useful to include streamflow as a quantitative metric in evaluating a precipitation the performance of WRF 4D-Var precipitation analyses product.

A.4 Summary

The precipitation estimates using the WRF model with and without 4D-Var assimilation of six-hour TRMM 3B42 precipitation were compared with TRMM 3B42 as well as the reference Iowa Flood Studies (IFloodS) gauge observations during May to June 2013. Those products were also evaluated in streamflow simulations over Turkey River basin, Iowa during the NASA IFloodS campaign using a distributed hydrologic model, the distributed hydrologic TIN (Triangular Irregular Network)-based Real-time Integrated Basin Simulator (tRIBS). Over the Turkey River basin, the assimilation of TRMM into the WRF model results in hourly precipitation analyses with a lower mean absolute error than those without data assimilation. The streamflow simulations using various precipitation products as inputs indicated that the domain-mean bias is a primary factor for reproducing streamflow while the variability of precipitation seems a secondary factor. Despite the improvement of WRF precipitation estimates using the WRF 4D-Var system described in Chapters 2 and 3, the 4D-Var precipitation analyses over the Turkey River basin in both May and June, 2013 are clearly underestimated, leading to underestimated streamflow simulations. We suspect that the error structure in the data assimilation experiments are the primary factor causing underestimated precipitation analyses. Future research can be devoted to the use of adaptive precipitation observational error in the WRF 4D-Var system. In addition, it is commonly known that the uncertainty of streamflow prediction is critical information in practice. It would be useful to provide ensemble forecasts of precipitation, with and without data assimilation, and then to explore how those ensemble members affect streamflow simulations.

APPENDIX B

LIST OF ACRONYMS

1D-Var	One-dimensional Variational Data Assimilation
3D-Var	Three-dimensional Variational Data Assimilation
4D-Var	Four-dimensional Variational Data Assimilation
AMSR-E	Advanced Microwave Scanning Radiometer-Earth Observing System
AMSU	Advanced Microwave Sounding Unit
ARW	Advanced Research WRF
ASCAT	Advanced Scatterometer
BS	Bias Score
CPC	Climate Prediction Center
CRN	Climate Reference Network
DART	Data Assimilation Research Testbed
ECMWF	European Centre for Medium-Range Weather Forecasts
EnKF	Ensemble Kalman Filter
EKF	Extended Kalman Filter
ESMF	Earth System Modeling Framework
ESV	Essential Climate Variable
ETS	Equitable Threat Score
FAR	False Alarm Rate
FNL	Final Analysis
GDAS	Global Data Assimilation System
GEOS	Goddard Earth Observing System
GFS	Global Forecast System

GLDAS	Global Land Data Assimilation System
GPCP	Global Precipitation Climatology Project
GPM	Global Precipitation Measurement
GSI	Gridpoint Statistical Interpolation
HIRS	High-resolution Infrared Sounder
HUC	Hydrologic Unit Code
IFloodS	Iowa Flood Studies
JMA	Japan Meteorological Agency
LIS	Land Information System
MAE	Mean Absolute Error
MHS	Microwave Humidity Sounder
NARR	North American Regional Reanalysis
NASA	National Aeronautics and Space Administration
NCAR	National Center for Atmospheric Research
NCEP	National Centers for Environmental Prediction
NLDAS	North American Land Data Assimilation System
NMC	National Meteorological Center
NMM	Non-hydrostatic Mesocale Model
NOAA	National Oceanic and Atmospheric Administration
NPP	Normalized Performance Percentage
NU-WRF	NASA Unified Weather Research and Forecasting
NWP	National Weather Prediction
OSSE	Observation System Simulation Experiment
PRISM	Parameter-elevation Regressions on Independent Slopes Model
RMSE	Root Mean Square Error
RUC	Rapid Update Cycle

SCAN	Soil Climate Analysis Network
SMAP	Soil Moisture Active Passive
SMMR	Scanning Multi-channel Microwave Radiometer
SMOPS	Soil Moisture Operational Products System
SMOS	Soil Moisture and Ocean Salinity
SSM/I	Special Sensor Microwave Imager
TIN	Triangular Irregular Network
TMI	TRMM Microwave Imager
TMPA	TRMM Multi-satellite Precipitation Analysis
tRIBS	TIN-based Real-time Integrated Basin Simulator
TRMM	Tropical Rainfall Measuring Mission
USGS	United State Geology Survey
UTC	Coordinated Universal Time
WRF	Weather Research and Forecasting
WRFDA	WRF Model Data Assimilation System
WRF-EDAS	WRF Ensemble Data Assimilation System
YSU	Yonsei University

Bibliography

Aligo, E. A., W. A. Gallus, and M. Segal (2007), Summer rainfall forecast spread in an ensemble initialized with different soil moisture analyses, *Weather Forecast.*, *22*, 299–314.

Alvarez-Garreton, C., D. Ryu, A. W. Western, C.-H. Su, W. T. Crow, D. E. Robertson, and C. Leahy (2015), Improving operational flood ensemble prediction by the assimilation of satellite soil moisture: comparison between lumped and semi-distributed schemes, *Hydrol. Earth Syst. Sci.*, *19*, 1659–1676.

Arnone, E., L. V. Noto, C. Lepore, and R. L. Bras (2011), Physically-based and distributed approach to analyze rainfall-triggered landslides at watershed scale, *Geomorphology*, *133*, 121–131.

Arnone, E., Y. G. Dialynas, L. V. Noto, and R. L. Bras (2014), Parameter uncertainty in shallow rainfall-triggered landslide modeling at basin scale: a probabilistic approach, *Procedia Earth and Planetary Science*, *9*, 101–111.

Bannister, R. N. (2008), A review of forecast error covariance statistics in atmospheric variational data assimilation. I: characteristics and measurements of forecast error covariances, *Q. J. Roy. Meteorol. Soc.*, *134*, 1951–1970.

Barker, D., X.-Y. Huang, Z. Liu, T. Auligne, X. Zhang, S. Rugg, R. Ajjaji, A. Bourgeois, J. Bray, Y. Chen, M. Demirtas, Y.-R. Guo, T. Henderson, W. Huang, H.-C. Lin, J. Michalakes, S. Rizvi, and X. Zhang (2012), The Weather Research and Forecasting (WRF) model's community variational/ensemble data assimilation system: WRFDA, *B. Am. Meteorol. Soc.*, *93*, 831–843.

Barker, D. M. (2005), Southern high-latitude ensemble data assimilation in the Antarctic mesoscale prediction system, *Mon. Weather Rev.*, *133*, 3431–3449.

Barker, D. M., W. Huang, Y.-R. Guo, A. J. Bourgeois, and N. Xiao (2004), A three-dimensional variational data assimilation system for MM5: implementation and initial results, *Mon. Weather Rev.*, *132*, 897–914.

Bauer, P., P. Lopez, D. Salmond, A. Benedetti, S. Saarinen, and M. Bonazzola (2006a), Implementation of 1D+4D-Var assimilation of precipitation-affected microwave radiances at ECMWF. I 1D-Var, *Q. J. Roy. Meteorol. Soc.*, *132*, 2277–2306.

Bauer, P., P. Lopez, D. Salmond, A. Benedetti, S. Saarinen, and M. Bonazzola (2006b), Implementation of 1D+4D-Var assimilation of precipitation-affected microwave radiances at ECMWF. II 4D-Var, *Q. J. Roy. Meteorol. Soc.*, *132*, 2307–2332.

Bauer, P., A. J. Geer, P. Lopez, and D. Salmond (2010), Direct 4D-Var assimilation of all-sky radiances. Part I: implementation, *Q. J. Roy. Meteorol. Soc.*, *136*, 1868–1885.

Bauer, P., T. Auligne, W. Bell, A. Geer, V. Guidard, S. Heilliette, M. Kazumori, M.-J. Kim, E. H.-C. Liu, A. P. McNally, B. Macpherson, K. Okamoto, R. Renshaw, and L.-P. Riishojgaard (2011a), Satellite cloud and precipitation assimilation at operational NWP centres, *Q. J. Roy. Meteorol. Soc.*, *137*, 1934–1951.

Bauer, P., G. Ohring, C. Kummerow, and T. Auligne (2011b), Assimilating satellite observations of clouds and precipitation into NWP models, *B. Am. Meteorol. Soc.*, *92*, ES25–ES28.

Brocca, L., T. Moramarco, F. Melone, W. Wagner, S. Hasenauer, and S. Hahn (2012), Assimilation of surface- and root-zone ASCAT soil moisture products into rainfall-runoff modeling, *IEEE Trans. Geosci. Remote Sens.*, *50(7)*, 2542–2555.

Brown, M. E., V. Escobar, S. Moran, D. Entekhabi, P. E. O'Neill, E. G. Njoku, B. Doorn, and J. K. Entin (2013), NASA's Soil Moisture Active Passive (SMAP) mission and opportunities for applications users, *B. Am. Meteorol. Soc.*, *94(8)*, 1125–1128.

Case, J. L., S. V. Kumar, J. Srikishen, and G. J. Jedlovec (2011), Improving numerical weather predictions of summertime precipitation over the Southeastern United States through a high-resolution initialization of the surface state, *Weather Forecast.*, *26*, 785–807.

Chambon, P., S. Q. Zhang, A. Y. Hou, M. Zupanski, and S. Cheung (2013), Assessing the impact of pre-GPM microwave precipitation observations in the Goddard WRF ensemble data assimilation system, *Q. J. Roy. Meteorol. Soc.*, *140*, 1219–1235, doi:10.1002/qj.2215.

Chen, F., and J. Dudhia (2001), Coupling an advanced land surface-hydrology model with the Penn State-NCAR MM5 modeling system. Part I: model implementation and sensitivity, *Mon. Weather Rev.*, *129*, 569–585.

Chen, F., W. T. Crow, P. J. Starks, and D. N. Moriasi (2011), Improving hydrologic predictions of a catchment model via assimilation of surface soil moisture, *Adv. Water Resour.*, *34*, 526–536.

Chen, S.-H., Z. Zhao, J. S. Haase, and A. C. andenberghe (2008), A study of the characteristics and assimilation of retrieved MODIS total precipitable water data in severe weather simulations, *Mon. Weather Rev.*, *136*, 3608–3628.

Courtier, P., E. Anderson, W. Heckley, J. Pailleux, D. Vasiljevic, M. Hamrud, A. Hollingsworth, F. Rabier, and M. Fisher (1998), The ECMWF implementation of three-dimensional variational assimilation (3D-Var). I: Formulation, *Q. J. Roy. Meteorol. Soc.*, *124*, 1783–1807.

Cunha, L. K., J. A. Smith, M. L. Baeck, and B.-C. Seo (2015), NEXRAD NWS polarimetric precipitation product evaluation for IFloodS, *J. Hydrometeorol.*, *16*, 1676–1699.

Daley, R. (1991), *Atmospheric Data Analysis*, Cambridge, UK.

Dee, D. P. (2005), Bias and data assimilation, *Q. J. Roy. Meteorol. Soc.*, *131*, 3323–3343.

Dee, D. P., S. M. Uppala, A. J. Simmons, P. Berrisford, P. Poli, S. Kobayaski, U. Andrae, M. A. Balmaseda, G. Balsamo, P. Bauer, P. Bechthold, A. C. M. Beljaars, L. van de Berg, J. Bidlot, N. Bormann, C. Delsol, R. Dragani, M. Fuentes, A. J. Geer, L. Haimberger, S. B. Healy, H. Hersbach, E. V. Holm, L. Isaksen, P. Kallberg, M. Kohler, M. Matricardi, A. P. McNally, B. M. Monge-Sanz, J.-J. Morcrette, B.-K. Park, C. Peubey, P. de Rosnay, C. Tavolato, J.-N. Thepaut, and F. Vitart (2011), The ERA-interim reanalysis: configuration and performance of the data assimilation system, *Q. J. Roy. Meteorol. Soc.*, *137*, 553–597.

DeLannoy, G. J. M., P. R. Houser, R. N. Pauwels, and N. E. C. Verhoest (2007a), State and bias estimation for soil moisture profiles by an ensemble Kalman filter: effect of assimilation depth and frequency, *Water Resour. Res.*, *43, W06401*, doi:10.1029/2006WR005100.

DeLannoy, G. J. M., R. H. Reichle, P. R. Houser, V. R. N. Pauwels, and N. E. C. Verhoest (2007b), Correcting for forecast bias in soil moisture assimilation with the ensemble Kalman filter, *Water Resour. Res.*, *43, W09410*, doi:10.1029/2006WR005449.

Derber, J., and F. Bouttier (1999), A reformulation of the background error covariance in the ECMWF global data assimilation system, *Tellus*, *51A*, 195–221.

Dingman, S. L. (2002), *Physical Hydrology*, 2 ed., Upper Saddle River, NJ.

Dorigo, W. A., A. Xaver, M. Vreugdenhil, A. Gruber, A. Hegyiova, A. D. Sanchis-Dufau, D. Zamojski, C. Cordes, and W. Wagner (2012), Global automated quality control of in situ soil moisture data from the international soil moisture network, *Vadose Zone J.*, *12(3)*, doi:10.2136/vzj2012.0097.

Draper, C., R. Reichle, G. D. Lannoy, and B. Scarino (2015), A dynamic approach to addressing observation-minus-forecast bias in a land surface skin temperature data assimilation system, *J. Hydrometeorol.*, *16*, 449–446.

Draper, C. S., J.-F. Mahfouf, and J. P. Walker (2009), An EKF assimilation of AMSR-E soil moisture into the ISBA land surface scheme, *J. Geophys. Res.*, *114, D20104*, doi: 10.1029/2008JD011650.

Draper, C. S., J.-F. Mahfouf, J.-C. Calvet, E. Martin, and W. Wanger (2011a), Assimilation of ASCAT near-surface soil moisture into the SIM hydrological model over France, *Hydrol. Earth Syst. Sci.*, *15*, 3829–3841.

Draper, C. S., J.-F. Mahfouf, and J. P. Walker (2011b), Root zone soil moisture from the assimilation of screen-level variables and remotely sensed soil moisture, *J. Geophys. Res.*, *116, D02127*, doi:10.1029/2010JD013829.

Draper, C. S., R. H. Reichle, G. J. M. D. Lannoy, and Q. Liu (2012), Assimilation of passive and active microwave soil moisture retrievals, *Geophys. Res. Lett.*, *39, L04401*, doi:10.1029/2011GL050655.

Dudhia, J. (1989), Numerical study of convection observed during the winter monsoon experiment using a mesoscale two-dimensional model, *J. Atmos. Sci.*, *46*, 3077–3107.

Dunne, S., and D. Entekhabi (2005), An ensemble-based reanalysis approach to land data assimilation, *Water Resour. Res.*, *41, W02013*, doi:10.1029/2004WR003449.

Dunne, S., and D. Entekhabi (2006), Land surface state and flux estimation using the ensemble Kalman smoother during the Southern Great Plains 1997 field experiment, *Water Resour. Res.*, *42, W01407*, doi:10.1029/2005WR004334.

Ebert, E. E., J. E. Janowiak, and C. Kidd (2007), Comparison of near-real-time precipitation estimates from satellite observations and numerical models, *B. Am. Meteorol. Soc.*, *88*, 47–64.

Ebtehaj, A. M., M. Zupanski, G. Lerman, and E. Foufoula-Georgiou (2014), Variational data assimilation via sparse regularization, *Tellus A*, *66, 21789*, doi:10.3402/tellusa.v66.21789.

Ebtehaj, A. M., R. L. Bras, and E. Foufoula-Georgiou (2016), Evaluation of ShARP passive rainfall retrievals over snow-covered land surfaces and coastal zones, *J. Hydrometeorol.*, doi:10.1175/JHM-D-15-0164.1, in press.

Entekhabi, D., E. G. Njoku, P. E. O'Neill, K. H. Kellogg, W. T. Crow, W. N. Edelstein, J. K. Entin, S. D. Goodman, T. J. Jackson, J. Johnson, J. Kimball, J. R. Piepmeier, R. D. Koster, N. Martin, K. C. McDonald, M. Moghaddam, S. Moran, R. Reichle, J. C. Shi, M. W. Spencer, S. W. Thurman, L. Tsang, and J. V. Zyl (2010), The Soil Moisture Active Passive (SMAP) Mission, *Proc. IEEE*, *98(5)*, 704–716.

Errico, R. M., G. Ohring, P. Bauer, B. Ferier, J.-F. Mahfouf, J. Turk, and F. Weng (2007), Assimilation of satellite cloud and precipitation observations in numerical weather prediction models: Introduction to the JAS special collection, *J. Atmos. Sci.*, *64*, 3737–3741.

Feng, X., and P. Houser (2015), Quantifying the strenght of land-atmosphere coupling in the 2004 North American monsoon, *Atmos. Sci. Let.*, doi:10.1002/asl2.573.

Flores, A., V. Y. Ivanov, D. Entekhabi, and R. L. Bras (2009), Impacts of hillslope-scale organization in topography, soil moisture, soil temperature, and vegetation on modeling surface microwave radiation emission, *IEEE Trans. Geosci. Remote Sens.*, *47(8)*, 2557–2571.

Flores, A. N., R. L. Bras, and D. Entekhabi (2012), Hydrologic data assimilation with a hillslope-scale resolving model and L-band radar observations: Synthetic experiments with the ensemble Kalman filter, *Water Resour. Res.*, *48, W08509*, doi: 10.1029/2011WR011500.

Flores, A. N., D. Entekhabi, and R. L. Bras (2014), Application of a hillslope-scale soil moisture data assimilation system to military trafficability assessment, *J. Terramechanics*, *51*, 53–66.

Fowler, H. J., S. Blenkinsop, and C. Tebaldi (2007), Linking climate change modelling to impacts studies: recent advances in downscaling techniques for hydrological modelling, *Int. J. Climatol.*, *27*, 1547–1578.

Francipane, A., V. Y. Ivanov, L. V. Noto, E. Istanbulluoglu, E. Arnone, and R. L. Bras (2012), trIBS-erosion: A parsimonious physically-based model for studying catchment hydro-geomorphic response, *Catena*, *92*, 216–231.

Geer, A. J., P. Bauer, and P. Lopez (2008), Lessons learnt from the operational 1D+4D-Var assimilation or rain- and cloud-affected SSM/I observations at ECMWF, *Q. J. Roy. Meteorol. Soc.*, *134*, 1513–1525.

Geer, A. J., P. Bauer, and P. Lopez (2010), Direct 4D-Var assimilation of all-sky radiances. Part II: assessment, *Q. J. Roy. Meteorol. Soc.*, *136*, 1886–1905.

Ghent, D., J. Kaduk, J. Remedios, J. Ardo, and H. Balzter (2010), Assimilation of land surface temperature into the land surface model JULES with an ensemble Kalman filter, *J. Geophys. Res.*, *115, D19112*, doi:10.1029/2010JD014392.

Gottschalck, J., J. Meng, M. Rodell, and P. Houser (2005), Analysis of multiple precipitation products and preliminary assessment of their impact on global land data assimilation system land surface states, *J. Hydrometeorol.*, *6*, 573–598.

Grell, G. A., and D. Devenyi (2002), A generalized approach to parameterizing convection combining ensemble and data assimilation techniques, *Geophys. Res. Lett.*, *29(14)*, doi: 10.1029/2002GL015311.

Grody, N. C. (1988), Surface identification using satellite microwave radiometers, *IEEE Trans. Geosci. Remote Sens.*, *26(6)*, 850–859.

Gutmann, E. D., R. M. Rasmussen, C. Liu, K. Ikeda, D. J. Gochis, M. P. Clark, J. Dudhia, and G. Thompson (2012), A comparison of statistical and dynamical downscaling of winter precipitation over complex terrain, *J. Climate*, *25*, 262–281.

Ha, J.-H., and D.-K. Lee (2012), Effect of length scale tuning of background error in WRF-3DVAR system on assimilation of high-resolution surface data for heavy rainfall simulation, *Adv. Atmos. Sci.*, *29(6)*, 1142–1158.

Ha, J.-H., H.-W. Kim, and D.-K. Lee (2011), Observation and numerical simulations with radar and surface data assimilation for heavy rainfall over central Korea, *Adv. Atmos. Sci.*, *28(3)*, 573–590.

Hellstrom, C., D. Chen, C. Achberger, and J. Raisanen (2001), Comparison of climate change scenarios for Sweden based on statistical and dynamical downscaling of monthly precipitation, *Climate Res.*, *19*, 45–55.

Hohenegger, C., P. Brockhaus, C. S. Bretherton, and C. Schar (2009), The soil moisture-precipitation feedback in simulations with explicit and parameterized convection, *J. Climate*, *22*, 5003–5020.

Hong, S.-Y., and J.-O. J. Lim (2006), The WRF single-moment 6-class microphysics scheme (WSM6), *J. Korean Meteor. Soc.*, *42*, 129–151.

Hong, S.-Y., J. Dudhia, and S. H. Chen (2004), A revised approach to ice microphysical processes for the bulk parameterization of clouds and precipitation, *Mon. Weather Rev.*, *132*, 103–120.

Hong, S.-Y., Y. Noh, and J. Dudhia (2006), A new vertical diffusion package with an explicit treatment of entrainment processes, *Mon. Weather Rev.*, *134*, 2318–2341.

Hoppe, C. M., H. Elbern, and J. Schwinger (2014), A variational data assimilation system for soil-atmosphere flux estimates for the Community Land Model (CLM3.5), *Geosci. Model Dev.*, *7*, 1025–1036.

Hou, A. Y., D. V. Ledvina, A. M. D. Silva, S. Q. Zhang, J. Joiner, R. M. Atlas, G. J. Huffman, and C. D. Kummerow (2000a), Assimilation of SSM/I-derived surface rainfall and total precipitable water for improving the GEOS analysis for climate studies, *Mon. Weather Rev.*, *128*, 509–537.

Hou, A. Y., S. Q. Zhang, and A. M. D. Silva (2000b), Improving assimilated global datasets using TMI rainfall and columnar moisture observations, *J. Climate*, *13*, 4180–4195.

Hou, A. Y., S. Q. Zhang, A. M. da Silva, W. S. Olson, C. D. Kummerow, and J. Simpson (2001), Improving global analysis and short-range forecast using rainfall and moisture observations derived from TRMM and SSM/I passive microwave sensors, *B. Am. Meteorol. Soc.*, *42(4)*, 659–679.

Hou, A. Y., S. Q. Zhang, and O. Reale (2004), Variational continuous assimilation of TMI and SSM/I rain rates: impact on GEOS-3 hurricane analyses and forecasts, *Mon. Weather Rev.*, *132*, 2094–2109.

Hou, A. Y., R. K. Kakar, S. Neeck, A. A. Azarbarzin, C. D. Kummerow, M. Kojima, R. Oki, K. Nakamura, and T. Iguchi (2014), The Global Precipitation Measurement (GPM) Mission, *B. Am. Meteorol. Soc.*, *95*, 701–722, doi:10.1175/BAMS-D-13-00164.1.

Hsiao, L.-F., D.-S. Chen, Y.-H. Kuo, Y.-R. Guo, T.-C. Yeh, J.-S. Hong, C.-T. Fong, and C.-S. Lee (2012), Application of WRF 3DVAR to operational typhoon prediction in Taiwan: impact of outer loop and partial cycling approaches, *Weather Forecast.*, *27*, 1249–1263.

Huang, X.-Y., Q. Xiao, D. M. Barker, X. Zhang, J. Michalakes, W. Huang, T. Henderson, J. Bray, Y. Chen, Z. Ma, J. Dudhia, Y. Guo, X. Zhang, D.-J. Won, H.-C. Lin, and Y.-H. Kuo (2009), Four-Dimensional variational data assimilation for WRF: formula and preliminary results, *Mon. Weather Rev.*, *137*, 299–314.

Huffman, G. J., R. F. Adler, D. T. Bolvin, G, Gu, E. J. Nelkin, K. P. Bowman, Y. Hong, E. F. Stocker, and D. B. Wolff (2007), The TRMM multisatellite precipitation analysis (TMPA): Quasi-global, multiyear, combined-sensor precipitation estimates at fine scales, *J. Hydrometeorol.*, *8*, 38–55.

Iacono, M. J., J. S. Delamere, E. J. Mlawer, M. W. Shephard, S. A. Clough, and W. D. Collins (2008), Radiative forcing by long-lived greenhouse gases: Calculations with the AER radiative transfer models, *J. Geophys. Res.*, *113, D13103*, doi: 10.1029/2008JD009944.

Ide, K., P. Courtier, M. Ghil, and A. C. Lorenc (1997), Unified notation for data assimilation: operational, sequential, and variational, *J. Meteorol. Soc. Japan*, *75(1B)*, 181–189.

Ingleby, N. B. (2001), The statistical structure of forecast errors and its representation in the Met office global 3-D variational data assimilation scheme, *Q. J. Roy. Meteorol. Soc.*, *127*, 209–231.

Iowa Flood Center (2014), Hydrologic assessment of the Turkey River watershed, *Tech. rep.*, [Available online at http://turkeyriver.org/wp-content/uploads/2014/05/PhaseI-Hydrologic-Assessment-Turkey-River-Watershed.docx.pdf].

Ivanov, V. Y., E. R. Vivoni, R. L. Bras, and D. Entekhabi (2004a), Catchment hydrologic response with a fully distrubted triangulated irregular network model, *Water Resour. Res.*, *40, W11102*, doi:10.1029/2004WR003218.

Ivanov, V. Y., E. R. Vivoni, R. L. Bras, and D. Entekhabi (2004b), Preserving high-resolution surface and rainfall data in operational-scale basin hydrology: A fully-distributed physically-based approach, *J. Hydrol.*, *298*, 80–111.

Ivanov, V. Y., R. L. Bras, and E. R. Vivoni (2008a), Vegetation-hydrology dynamics in complex terrain of semiarid areas–Part 1: A mechanistic approach to modeling dynamic feedbacks, *Water Resour. Res.*, *44, W03429*, doi:10.1029/2006WR005588.

Ivanov, V. Y., R. L. Bras, and E. R. Vivoni (2008b), Vegetation-hydrology dynamics in complex terrain of semiarid areas–Part 2: Energy-water controls of vegetation spatiotemporal dynamics and topographic niches of favorability, *Water Resour. Res.*, *44, W03430*, doi:10.1029/2006WR005595.

Janjic, Z. I. (1994), The step-mountain eta coordinate model: further developments of the convection, viscous sublayer and turbulence closure schemes, *Mon. Weather Rev.*, *122*, 927–945.

Janjic, Z. I. (2000), Comments on "development and evaluation of a convection scheme for use in climate models", *J. Atmos. Sci.*, *57*, 3686–3686.

Jimenez, P. A., J. Dudhia, J. F. Gonzalez-Rouco, J. Navarro, J. P. Montavez, and E. Garcia-Bustamante (2012), A revised scheme for the WRF surface layer formulation, *Mon. Weather Rev.*, *140*, 898–918.

Jimenez, P. A., J. V.-G. D. Arellano, J. Navarro, and J. F. Gonzalez-Rouco (2014), Understanding land-atmosphere interactions across a range of spatial and temporal scales, *B. Am. Meteorol. Soc.*, *95*, ES14–ES17.

Kain, J. S. (2004), The Kain-Fritsch convective parameterization: An update, *J. Appl. Meteor.*, *43*, 170–181.

Kain, J. S., and J. M. Fritsch (1990), A one-dimensional entraining/detraining plume model and its application in convective parameterization, *J. Atmos. Sci.*, *47*, 2784–2802.

Kalnay, E. (2003), *Atmospheric Modeling, Data Assimilation, and Predictability*, Cambridge, UK.

Kerr, Y. H., P. Waldteufel, J.-P. Wigneron, S. Delwart, F. Cabot, J. Boutin, M.-J. Escorihuela, J. Font, N. Reul, C. Gruhier, S. E. Juglea, M. R. Drinkwater, A. Hahne, M. Martin-Neira, and S. Mecklenburg (2010), The SMOS mission: New tool from monitoring key elements of the global water cycle, *Proc. IEEE*, *98(5)*, 666–687.

Kidd, C., P. Bauer, J. Turk, G. J. Huffman, R. Joyce, K.-L. Hsu, and D. Braithwaite (2012), Intercomparison of high-resolution precipitation products over Northwest Europe, *J. Hydrometeorol.*, *13*, 67–83.

Koizumi, K., Y. Ishikawa, and T. Tsuyuki (2005), Assimilation of precipitation data to the JMA mesoscale model with a four-dimensional variational method and its impact on precipitation forecasts, *SOLA*, *1*, 45–48, doi:10.2151/sola.2005-013.

Koster, R. D., P. A. Dirmeyer, Z. Guo, G. Bonan, E. Chan, P. Cox, C. T. Gordon, S. Kanae, E. Kowalczyk, D. Lawrence, P. Liu, C.-H. Lu, S. Malyshev, B. McAvaney, K. Mitchell, D. Mocko, T. Oki, K. Oleson, A. Pitman, Y. C. Sud, C. M. Taylor, D. Verseghy, R. Vasic, Y. Xue, and T. Yamada (2004), Regions of strong coupling between soil moisture and precipitation, *Science*, *305*, 1138–1140.

Koster, R. D., Z. Guo, P. A. Dirmeyer, G. Bonan, E. Chan, P. Cox, H. Davies, C. T. Gordon, S. Kanae, E. Kowalczyk, D. Lawrence, P. Liu, C.-H. Lu, S. Malyshev, B. McAvaney, K. Mitchell, D. Mocko, T. Oki, K. W. Oleson, A. Pitman, Y. C. Sud, C. M. Taylor, D. Verseghy, R. Vasic, Y. Xue, and T. Yamada (2006), GLACE: The global land-atmosphere coupling experiment. Part I: Overview, *J. Hydrometeorol.*, *7*, 590–610.

Kubota, T., T. Ushio, S. Shige, S. Kida, M. Kachi, and K. Okamoto (2009), Verification of high-resolution satellite-based rainfall estimates around Japan using a gauge-calibrated ground-radar dataset, *J. Meteorol. Soc. Japan*, *87A*, 203–222.

Kumar, P., C. M. Kishtawal, and P. K. Pal (2014), Impact of satellite rainfall assimilation on Weather Research and Forecasting model predictions over the Indian region, *J. Geophys. Res. Atmos.*, *119*, 2017–2031, doi:10.1002/2013JD020005.

Kumar, S. V., R. H. Reichle, C. D. Peters-Lidard, R. D. Koster, X. Zhan, W. T. Crow, and P. R. H. J. B. Eylander ander (2008), A land surface data assimilation framework using the land information system: Description and applications, *Adv. Water Resour.*, *31*, 1419–1432.

Kumar, S. V., R. H. Reichle, R. D. Koster, W. T. Crow, and C. D. Peters-Lidard (2009), Role of subsurface physics in the assimilation of surface soil moisture observations, *J. Hydrometeorol.*, *10*, 1534–1547.

Kumar, S. V., R. H. Reichle, K. W. Harrison, C. D. Peters-Lidard, S. Yatheendradas, and J. A. Santanello (2012), A comparison of methods for a priori bias correction in soil moisture data assimilation, *Water Resour. Res.*, *48, W03515*, doi:10.1029/2010WR010261.

Lepore, C., E. Arnone, L. V. Noto, G. Sivadran, and R. L. Bras (2013), Physically based modeling of rainfall-triggered landslides: a case study in the Luquillo forecast, Puerto Rico, *Hydrol. Earth Syst. Sci.*, *17*, 3371–3387.

Li, B., D. Toll, X. Zhan, and B. Cosgrove (2012), Improving estimated soil moisture fields through assimilation of AMSR-E soil moisture retrievals with an ensemble Kalman filter and a mass conservation constraint, *Hydrol. Earth Syst. Sci.*, *16*, 105–119.

Lien, G.-Y., T. Miyoshi, and E. Kalnay (2016), Assimilation of TRMM multisatellite precipitation analysis with a low-resolution NCEP Global Forecasting System, *Mon. Weather Rev.*, doi:10.1175/MWR-D-15-0149.1.

Lievens, H., S. K. Tomer, A. A. Bitar, G. J. M. D. Lannoy, M. Drusch, G. Dumedah, H.-J. H. Franssen, Y. H. Kerr, B. Martens, M. Pan, J. K. Roundy, H. Vereecken, J. P. Walker, E. F. Wood, N. E. C. Verhoest, and V. R. N. Pauwels (2015), SMOS soil moisture assimilation for improved hydrologic simulation in the Murray Darling Basin, Australia, *Remote Sens. Environ.*, *168*, 146–162.

Lin, L.-F., A. M. Ebtehaj, R. L. Bras, A. N. Flores, and J. Wang (2015), Dynamical precipitation downscaling for hydrologic applications using WRF 4D-Var data assimilation: Implications for GPM era, *J. Hydrometeorol.*, *16*, 811–829, doi:10.1175/JHM-D-14-0042.1.

Lin, L.-F., A. M. Ebtehaj, J. Wang, and R. L. Bras (2016), Soil moisture background error covariance and data assimilation in a coupled land-atmosphere model, *Water Resour. Res.*, in revision.

Lin, X., S. Q. Zhang, and A. Y. Hou (2007), Variational assimilation of global microwave rainfall retrievals: physical and dynamical impact on GEOS analyses, *Mon. Weather Rev.*, *135*, 2931–2957.

Lin, Y., and K. E. Mitchell (2005), The NCEP Stage II/IV hourly precipitation analyses: development and applications, in Preprints, *19th Conf on Hydrology*, p. 1.2, Amer. Meteor. Soc., San Diego, CA, [Available online at https://ams.confex.com/ams/pdfpapers/83847.pdf.].

Lin, Y.-L., R. D. Farley, and H. D. Orville (1983), Bulk parameterization of the snow field in a cloud model, *J. Climate Appl. Meteor.*, *22*, 1065–1092.

Lins, H. F. (2012), USGS Hydro-Climatic Data Network 2009 (HCDN-2009), *U. S. Geological Survey Fact Sheet 2012-3047*, pp. –.

Liu, J., M. Bray, and D. Han (2012a), Exploring the effect of data assimilation by WRF-3Dvar for numerical rainfall prediction with different types of storm events, *Hydrol. Process*, *27*, 3627–3640.

Liu, J., M. Bray, and D. Han (2013), A study on WRF radar data assimilation for hydrological rainfall prediction, *Hydrol. Earth Syst. Sci.*, *17*, 3095–3110.

Liu, Q., R. H. Reichle, R. Bindlish, M. H. Cosh, W. T. Crow, R. D. Jeu, G. J. M. D. Lannoy, G. J. Huffman, and T. J. Jackson (2011), The contributions of precipitation and soil moisture observations to the skill moisture estimates in a land data assimilation system, *J. Hydrometeorol.*, *12*, 750–765.

Liu, Z., C. S. Schwartz, C. Snyder, and S. Ha (2012b), Impact of assimilating AMSU-A radiances on forecasts of 2008 Atlantic tropical cyclones initialized with a limited-area ensemble Kalman filter, *Mon. Weather Rev.*, *140*, 4017–4034.

Livezey, R. E., and W. Y. Chen (1983), Statistical field significance and its determination by Monte Carlo techniques, *Mon. Weather Rev.*, *111*, 46–59.

Lopez, P. (2007), Cloud and Precipitation Parameterizations in Modeling and Variational Data Assimilation: A Review, *J. Atmos. Sci.*, *64*, 3766–3784.

Lopez, P. (2011), Direct 4D-Var assimilation of NCEP Stage IV radar and gauge precipitation data at ECMWF, *Mon. Weather Rev.*, *139*, 2098–2116.

Lopez, P. (2013), Experimental 4D-Var Assimilation of SYNOP rain gauge data at ECMWF, *Mon. Weather Rev.*, *141*, 1527–1544.

Lopez, P., and P. Bauer (2007), "1D+4DVAR' assimilation of NCEP Stage-IV radar and gauge hourly precipitation data at ECMWF, *Mon. Weather Rev.*, *135*, 2506–2524.

Lorenc, A. C. (1986), Analysis methods for numerical weather prediction, *Q. J. Roy. Meteorol. Soc.*, *112*, 1177–1194.

Lorenc, A. C., S. P. Ballard, R. S. Bell, N. B. Ingleby, P. L. F. Andrews, D. M. Barker, J. R. Bray, A. M. Clayton, T. Dalby, D. Li, T. J. Payne, and F. W. Saunders (2000), The Met. Office global three-dimensional variational data assimilation scheme, *Q. J. Roy. Meteorol. Soc.*, *126*, 2991–3012.

Mahfouf, J.-F. (2010), Assimilation of satellite-derived soil moisture from ASCAT in a limited-area NWP model, *Q. J. Roy. Meteorol. Soc.*, *136*, 784–798.

Mahfouf, J.-F., K. Bergaoui, C. Draper, F. Bouyssel, F. Taillefer, and L. Taseva (2009), A comparison of two off-line soil analysis schemes for assimilation of screen level observations, *J. Geophys. Res.*, *114, D08105*, doi:10.1029/2008JD011077.

Margulis, S. A., and D. Entekhabi (2001), A coupled land surface-boundary layer model and its adjoint, *J. Hydrometeorol.*, *2*, 274–296.

Margulis, S. A., D. McLaughlin, D. Entekhabi, and S. Dunne (2002), Land data assimilation and estimation of soil moisture using measurements from the Southern Great Plains 1997 field experiment, *Water Resour. Res.*, *38(12), 1299*, doi:10.1029/2001WR001114.

Meng, Z., and F. Zhang (2007), Tests of an ensemble Kalman filter for mesoscale and regional-scale data assimilation. Part II: imperfect model experiments, *Mon. Weather Rev.*, *135*, 1403–1423.

Meng, Z., and F. Zhang (2008), Tests of an ensemble Kalman filter for mesoscale and regional-scale data assimilation. Part III: comparison with 3DVAR in a real-data case study, *Mon. Weather Rev.*, *136*, 522–540.

Mesinger, F., G. DiMego, E. Kalnay, K. Mitchell, P. C. Shafran, W. Ebisuzaki, D. Jovic, J. Woollen, E. Rogers, E. H. Berbery, M. B. Ek, Y. Fan, R. Grumbine, W. Higgins, H. Li, Y. Lin, G. Manikin, D. Parrish, and W. Shi (2006), North American Regional Reanalysis, *B. Am. Meteorol. Soc.*, *87*, 343–360.

Miller, D. A., and R. A. White (1998), A conterminous United States multilayer soil characteristics dataset for regional climate and hydrology modeling, *Earth Interact.*, *2*, 1–26.

Mlawer, E., S. Taubman, P. Brown, M. Iacono, and S. Clough (1997), Radiative transfer for inhomogeneous atmospheres: RRTM, a validated correlated-k model for the longwave, *J. Geophys. Res.*, *102(D14)*, 16,663–16,682.

Nagarajan, K., J. Judge, A. Monsivais-Huertero, and W. D. Graham (2012), Impact of assimilating passive microwave observations on root-zone soil moisture under dynamic vegetation conditions, *IEEE Trans. Geosci. Remote Sens.*, *50(11)*, 4279–4291.

Pan, M., and E. F. Wood (2010), Impact of accuracy, spatial availability, and revisit time of satellite-derived surface soil moisture in a multiscale ensemble data assimilation system, *IEEE J. Sel. Topics Appl. Earth Observ. In Remote Sens.*, *3(1)*, 49–56.

Parrens, M., J.-F. Mahfouf, A. L. Barbu, and J.-C. Calvet (2014), Assimilation of surface soil moisture into a multilayer soil model: design and evaluation at local scale, *Hydrol. Earth Syst. Sci.*, *18*, 673–689.

Parrish, D. F., and J. C. Derber (1992), The National Meteorological Center's spectral statistical-interpolation analysis system, *Mon. Weather Rev.*, *120(8)*, 1747–1763.

Pauwels, V. R. N., G. J. M. D. Lannoy, H.-J. H. Franssen, and H. Vereechen (2013), Simultaneous estimation of model state variables and observation and forecast biases using a two-stage hybrid Kalman filter, *Hydrol. Earth Syst. Sci.*, *17*, 3499–3521, doi: 10.5194/hess-17-3499-2013.

Pedinotti, V., A. Boone, S. Ricci, S. Biancamaria, and N. Mognard (2014), Assimilation of satellite data to optimize large-scale hydrological model parameters: a case study for the SWOT mission, *Hydrol. Earth Syst. Sci.*, *18*, 4485–4507, doi:10.5194/hess-18-4485-2014.

Peters-Lidard, C. D., S. V. Kumar, D. M. Mocko, and Y. Tian (2011), Estimating evapotranspiration with land data assimilation systems, *Hydrol. Process*, *25*, 3979–3992.

Peters-Lidard, C. D., E. M. Kemp, T. Matsui, J. A. S. Jr., S. V. Kumar, J. P. Jacob, T. Clune, W.-K. Tao, M. Chin, A. Hou, J. L. Case, D. Kim, K.-M. Kim, W. Lau, Y. Liu, J. Shi, D. Starr, Q. Tan, Z. Tao, B. F. Zaitchik, B. Zavodsky, S. Q. Zhang, and M. Zupanski (2015), Integrated modeling of aerosol, cloud, precipitation, and land processes at satellite-resolved scales, *Environ. Modell. Softw.*, *67*, 149–159.

Pu, Z., and W.-K. Tao (2004), Mesoscale assimilation of TMI rainfall data with 4DVAR: Sensitivity studies, *J. Meteorol. Soc. Japan*, *82(5)*, 1389–1397.

Pu, Z., W.-K. Tao, S. Braun, J. Simpson, Y. Jia, J. Halverson, W. Olson, and A. Hou (2002), The impact of TRMM data on mesocale numerical simulation of supertyphoon Paka, *Mon. Weather Rev.*, *130*, 2448–2458.

Quintanar, A. I., and R. Mahmood (2012), Ensemble forecast spread induced by soil moisture changes over mid-south and neighboring mid-western region of the USA, *Tellus A*, *64, 17156*, doi:10.3402/tellusa.v64i0.17156.

Rakesh, V., and P. Gowsami (2011), Impact of background error statistics on forecasting of tropical cyclones over the north Indian Ocean, *J. Geophys. Res.*, *116, D20130*, doi: 10.1029/2011JD015751.

Rakesh, V., R. Singh, and P. C. Joshi (2009), Intercomparison of the performance of MM5/WRF with and without satellite data assimilation in short-range forecast applications over the Indian region, *Meteorol. Atmos. Phys.*, *105*, 133–155.

Rasmy, M., T. Koike, S. Boussetta, H. Lu, and X. Li (2011), Davelopment of a satellite land data assimilation system coupled with a mesocale model in the Tibetan Plateau, *IEEE Trans. Geosci. Remote Sens.*, *49(8)*, 2847–2862.

Rasmy, M., T. Koike, D. Kuria, C. R. Mirza, X. Li, and K. Yang (2012), Development of the coupled atmosphere and land data assimilation system (CALDAS) and its application over the Tibetan Plateau, *IEEE Trans. Geosci. Remote Sens.*, *50(11)*, 4227–4242.

Reichle, R. H., and R. D. Koster (2005), Global assimilation of satellite surface soil moisture retrievals into the NASA Catchment land surface model, *Geophys. Res. Lett.*, *32, L02404*, doi:10.1029/2004GL021700.

Reichle, R. H., D. Entekhabi, and D. B. Mclaughlin (2001a), Downscaling of radio brightness measurements for soil moisture estimation: a four-dimensional variational data assimilation approach, *Water Resour. Res.*, *37(9)*, 2353–2364.

Reichle, R. H., D. B. McLaughlin, and D. Entekhabi (2001b), Variational data assimilation of microwave radiobrightness observations for land surface hydrology applications, *IEEE Trans. Geosci. Remote Sens.*, *39(8)*, 1708–1718.

Reichle, R. H., D. B. McLaughlin, and D. Entekhabi (2002a), Hydrologic data assimilation with the Ensemble Kalman filter, *Mon. Weather Rev.*, *130*, 103–114.

Reichle, R. H., J. P. Walker, and P. R. Houser (2002b), Extended versus Ensemble Kalman filtering for land data assimilation, *J. Hydrometeorol.*, *3*, 728–740.

Reichle, R. H., R. D. Koster, P. Liu, S. P. P. Mahanama, E. G. Njoku, and M. Owe (2007), Comparison and assimilation of global soil moisture retrievals from the Advanced Microwave Scanning Radiometer for the Earth Observing System (AMSR-E) and the Scanning Multichannel Microwave Radiometer (SMMR), *J. Geophys. Res.*, *112, D09108*, doi:10.1029/2006JD008033.

Reichle, R. H., W. T. Crow, and C. L. Keppenne (2008a), An adaptive ensemble Kalman filter for soil moisture data assimilation, *Water Resour. Res.*, *44, W03423*, doi:10.1029/2007WR006357.

Reichle, R. H., W. T. Crow, R. D. Koster, H. O. Sharif, and S. P. P. Mahanama (2008b), Contribution of soil moisture retrievals to land data assimilation products, *Geophys. Res. Lett.*, *35, L01404*, doi:10.1029/2007GL031986.

Ridler, M.-E., H. Madsen, S. Stisen, S. Bircher, and R. Fensholt (2014), Assimilation of SMOS-derived soil moisture in a fully integrated hydrological and soil-vegetation-atmosphere transfer model in Western Denmark, *Water Resour. Res.*, *50*, 8962–8981, doi:10.1002/2014WR015392.

Rodell, M., P. R. Houser, U. Jambor, J. Gottschalck, K. Mitchell, C.-J. Meng, K. Arsenault, B. Cosgrove, J. Radakovich, M. Bosilovich, J. K. Entin, J. P. Walker, D. Lohmann, and D. Toll (2004), The global land data assimilation system, *B. Am. Meteorol. Soc.*, *85(3)*, 381–394.

Routray, A., U. C. Mohanty, D. Niyogi, S. R. H. Rizvi, and K. K. Osuri (2010), Simulation of heavy rainfall events over Indian monsoon region using WRF-3DVAR data assimilation system, *Meteorol. Atmos. Phys.*, *106*, 107–125.

Sahoo, A. K., G. J. M. D. Lannoy, R. H. Reichle, and P. R. Houser (2013), Assimilation and downscaling of satellite observed soil moisture over the Little River experimental watershed in Georgia, USA, *Adv. Water Resour.*, *52*, 19–33.

Santanello, J. A., C. D. Peters-Lidard, S. V. Kumar, C. Alonge, and W.-K. Tao (2009), A modeling and observational framework for diagnosing local land-atmosphere coupling on diurnal time scales, *J. Hydrometeorol.*, *10*, 577–599.

Santanello, J. A., C. D. Peters-Lidard, and S. V. Kumar (2011), Diagnosing the sensitivity of local land-atmosphere coupling via the soil moisture-boundary layer interaction, *J. Hydrometeorol.*, *12*, 766–786.

Sapiano, M. R. P., and P. A. Arkin (2009), An intercomparison and validation of high-resolution satellite precipitation estimates with 3-hourly gauge data, *J. Hydrometeorol.*, *10*, 149–166.

Schaefer, G. L., M. H. Cosh, and T. J. Jackson (2007), The USDA natural resources conservation service soil climate analysis network (SCAN), *J. Atmos. Oceanic Tech.*, *24*, 2073–2077.

Schmidli, J., C. M. Goodess, C. Frei, M. R. Haylock, Y. Hundecha, J. Ribalaygua, and T. Schmith (2007), Statistical and dynamical downscaling of precipitation: an evaluation and comparison of scenarios for the European Alps, *J. Geophys. Res.*, *112, D04105*, doi:10.1029/2005JD007026.

Schneider, S., Y. Wang, W. Wanger, and J.-F. Mahfouf (2014), Impact of ASCAT soil moisture assimilation on regional precipitation forecasts: A case study for Austria, *Mon. Weather Rev.*, *142*, 1525–1541.

Schwartz, C. S., Z. Liu, Y, Chen, and X. Huang (2012), Impact of assimilating microwave radiances with a limited-area ensemble data assimilation system on forecasts of typhoon Morakot, *Weather Forecast.*, *27*, 424–437.

Sivandran, G., and R. L. Bras (2012), Identifying the optimal spatially and temporally invariant root distribution for a semiarid environment, *Water Resour. Res.*, *48, W12525*, doi:10.1029/2012WR012055.

Sivandran, G., and R. L. Bras (2013), Dynamic root distributions in ecohydrological modeling: A case study at Walnut Gulch Experimental Watershed, *Water Resour. Res.*, *49*, 3292–3305, doi:10.1002/wrcr.20245.

Skamarock, W. C., J. B. Klemp, J. Didhia, D. O. Gill, D. M. Barker, M. G. Duda, X. Huang, W. Wang, and J. G. Powers (2008), A description of the advanced research WRF version 3, *NCAR Tech. Note. NCAR/TN-475+STR*.

Smirnova, T. G., J. M. Brown, S. G. Benjamin, and D. Kim (2000), Parameterization of cold-season process in the MAPS land-surface scheme, *J. Geophys. Res.*, *105(D3)*, 4077–4086.

Sutton, C., T. M. Hamill, and T. T. Warner (2006), Will perturbing soil moisture improve warm-season ensemble forecasts? A proof of concept, *Mon. Weather Rev.*, *134*, 3174–3189.

Tao, W.-K., J. Simpson, and M. McCumber (1989), An ice-water saturation adjustment, *Mon. Weather Rev.*, *117*, 231–235.

Thompson, G., P. R. Field, R. M. Rasmussen, and W. D. Hall (2008), Explicit forecasts of winter precipitation using an improved bulk microphysics scheme. Part II: implementation of a new snow parameterization, *Mon. Weather Rev.*, *136*, 5095–5115.

Thorstensen, A., P. Nguyen, K. Hsu, and S. Sorooshian (2016), Using densely distributed soil moisture observations for calibration of a hydrologic model, *J. Hydrometeorol.*, *17*, 571–590.

Trier, S. B., F. Chen, K. W. Manning, M. A. LeMone, and C. A. Davis (2008), Sensitivity of the PBL and precipitation in 12-day simulations of warm-season convection using different land surface models and soil wetness conditions, *Mon. Weather Rev.*, *136*, 2321–2343.

Tsuyuki, T. (1996a), Variational data assimilation in the tropics using precipitation data. Part I: column model, *Meteorol. Atmos. Phys.*, *60*, 87–104.

Tsuyuki, T. (1996b), Variational data assimilation in the tropics using precipitation data. Part II: 3D model, *Mon. Weather Rev.*, *124*, 2545–2561.

Tsuyuki, T. (1997), Variational data assimilation in the tropics using precipitation data. Part III: assimilation of SSM/I precipitation rates, *Mon. Weather Rev.*, *125*, 1447–1464.

Vivoni, E. R., V. Y. Ivanov, R. L. Bras, and D. Entekhabi (2004), Generation of triangulated irregular networks based on hydrological similarity, *J. Hydrol. Eng.*, *9*, 288–302.

Wang, H., J. Sun, X. Zhang, X.-Y. Huang, and T. Auligne (2013), Radar data assimilation with WRF 4D-Var. Part I. system development and preliminary testing, *Mon. Weather Rev.*, *141*, 2224–2244.

Williams, J. L., R. M. Maxwell, and L. D. Monache (2013), Development and verification of a new wind speed forecasting system using an ensemble Kalman filter data assimilation technique in a fully coupled hydrologic and atmospheric model, *J. Adv. Model. Earth Syst.*, *5*, 785–800.

Wu, C.-C., G.-Y. Lien, J.-H. Chen, and F. Zhang (2010), Assimilation of tropical cyclone track and structure based on the ensemble Kalman filter (EnKF), *J. Atmos. Sci.*, *67*, 3806–3822.

Wu, W.-S., R. J. Purser, and D. F. Parrish (2002), Three-dimensional variational analysis with spatially inhomogeneous covariances, *Mon. Weather Rev.*, *130*, 2905–2916.

Xia, Y., K. Mitchell, M. Ek, J. Sheffield, B. Cosgrove, E. Wood, L. Luo, C. Alonge, H. Wei, J. Meng, B. Livneh, D. Lettenmaier, V. Koren, Q. Duan, K. Mo, Y. Fan, and D. Mocko (2012), Continental-scale water and energy flux analysis and validation for the North American Land Data Assimilation System project phase 2 (NLDAS-2): 1. Intercomparison and application of model products, *J. Geophys. Res.*, *117, D03109*, doi:10.1029/2011JD016048.

Xu, J., and A. M. Powell (2012), Dynamic downscaling precipitation over South Asia: Impact of radiance data assimilation on the forecasts of the WRF-ARW model, *Atmos. Res.*, *111*, 90–113.

Yin, J., X. Zhan, Y. Zheng, J. Liu, C. R. Hain, and L. Fang (2014), Impact of quality control of satellite soil moisture data on their assimilation into land surface model, *Geophys. Res. Lett.*, *41*, 7159–7166, doi:10.1002/2014GL060659.

Yin, J., X. Zhan, J. Liu, and L. Fang (2015), Enhancing model skill by assimilating SMOPS-blended soil moisture product into Noah land surface model, *J. Hydrometeorol.*, *16*, 917–931.

Zaitchik, B. F., J. A. Santanello, S. V. Kumar, and C. D. Peters-Lidard (2013), Representation of soil moisture feedbacks during drought in NASA Unified WRF (NU-WRF), *J. Hydrometeorol.*, *14*, 360–367.

Zhan, X., J. Liu, L. Zhao, and K. Jensen (2011), Soil moisture operational product system (SMOPS): algorithm theoretical basis document version 3.0, *Tech. rep.*, NOAA/NESDIS/STAR, [Available online at http://www.ospo.noaa.gov/Products/land/smops/documents.html].

Zhang, F., Z. Meng, and A. Aksoy (2006), Tests of an ensemble Kalman filter for mesoscale and regional-scale data assimilation. Part I: perfect model experiments, *Mon. Weather Rev.*, *134*, 722–736.

Zhang, S. Q., M. Zupanski, A. Y. Hou, X. Lin, and S. H. Cheung (2013), Assimilation of precipitation-affected radiances in a cloud-resolving WRF ensemble data assimilation system, *Mon. Weather Rev.*, *141*, 754–772.

Zhou, Y., D. McLaughlin, and D. Entekhabi (2006), Assessing the performance of the Ensemble Kalmn filter for land surface data assimilation, *Mon. Weather Rev.*, *134*, 2128–2142.

Zupanski, D., and F. Mesinger (1995), Four-dimensional variational assimilation of precipitation data, *Mon. Weather Rev.*, *123*, 1112–1127.

Zupanski, D., S. Q. Zhang, M. Zupanski, A. Y. Hou, and S. H. Cheung (2011), A prototype WRF-based ensemble data assimilation system for dynamically downscaling satellite precipitation observations, *J. Hydrometeorol.*, *12*, 118–134.